Organisation and dynamics of mitochondria and their RNA.

Timo Henry René REY

The most important thing to do in your life
            is to not interfere with somebody else's life.

- Frank Zappa

Abstract

The organisation of molecules into dynamic cells, and collaboration of many of those cells over a billion years led to the evolution of human life. During the last century, biologists then began to unravel the marvels of cellular organisation with ever increasing detail. We now know, single cells not only comprise a defining DNA, but also a multitude of organelles. Mitochondria are such organelles, and produce cellular energy, at the heart of cellular metabolism. For this, they transcribe their own genome into mtRNA, and assemble respiratory chains. In recent decades, novel approaches, and technology enabled biologists to shed new light on the spatial organisation of sub-cellular and mitochondrial processes. Thereby mtRNA was discovered to accumulate into small foci inside the mitochondrial matrix by fluorescence microscopy. Certain mitochondrial proteins also have also been found to conglomerate in these mitochondrial RNA granules (MRGs). However, merely nothing is known about the structural, dynamic, and biophysical properties of MRGs, and their functional importance remains elusive. The development of superresolution microscopy led to a revolution and revival of imaging methods for cell biology. This technology now allows to investigate sub-cellular biology at the nanometre scale, and to illuminate MRGs inside mitochondria.

In this thesis I investigate the organisational principles governing single cell and mitochondrial biology. I first explore the application of superresolution microscopy to study the spatial organisation of nuclear DNA domains (TADs). Here, high-throughput stochastic optical reconstruction microscopy (htSTORM) allows to monitor effects of drug treatment on spatial rearrangement of a cancer associated TAD, together with established bulk-sample analysis. I then turned to study the organisation of mitochondrial dynamics, by live-cell structured illumination microscopy (SIM). How different molecular pathways associated with mitochondrial proliferation or degradation are organised has long been a matter of debate. We discover a pattern for spatial organisation of mitochondrial fission, which distribute along the mitochondrial network in a bimodal manner. With this framework different types of fission become distinguishable, and we discover distinct molecular features associated with mitochondrial proliferation, or degradation. I find actin to be involved in proliferative midzone fission, whereas peripheral fission is associated with elevated reactive oxygen levels, and precedes mitophagy. By htSTORM, SIM and other microscopy methods I then target the elucidation of the biophysical organisation of intra-mitochondrial processes and MRGs. I discover the MRG ultrastructure consists of compacted RNA embedded within a dynamic protein cloud. Furthermore, MRGs associate with the inner mitochondrial membranes, and their distribution is governed by mitochondrial dynamics. MRGs can now be understood as nanoscopic, robust and fluid compartments, likely to influence intra-mitochondrial reaction kinetics. Finally, I also begin to unravel the spatial and biophysical organisation of mitochondrial transcription.

Together, our results contribute to a holistic and dynamic picture of mitochondrial organisation. This thesis highlights advantages of state-of-the-art microscopy to investigate spatial and temporal organisation of sub-cellular processes, and marks the onset of single organelle biology, in the context of other recent studies of sub-mitochondrial organisation.

Keywords: Mitochondria, RNA, DNA topology, microscopy, fluorescence, superresolution, phase separation, transcription, mitochondrial dynamics, fission

Zusammenfassung

Die Organisation von Molekülen in dynamische Zellen, und deren Zusammenarbeit über Milliarden Jahre erlaubte die Evolution des Menschen. Doch erst im 20. Jahrhundert haben Biologen damit begonnen die Wunder der intrazellulären Organisation zu entschlüsseln. Mittlerweile wissen wir, einzelne Zellen sind nicht nur durch ihre DNS definiert, sondern beinhalten auch eine Reihe zellulärer Organellen. Mitochondrien sind ebensolche, und verantwortlich für die Energieversorgung mit ATP durch Veratmung von Zuckern und Fetten. Dazu transkribieren sie ihr eigenes Genom als mtRNS und bauen die Atmungskette. Neue Ansätze und Technologien erlaubten in vergangenen Dekaden erste Einblicke in die räumliche und zeitliche Organisation von subzellulären und mitochondrialen Prozessen. Dabei wurde durch Fluoreszenzmikroskopie entdeckt, dass sich mtRNS in kleinen Foci innerhalb der Mitochondrien anreichert. Bestimmte Proteine konglomerieren ebenfalls in diesen Mitochondrialen RNS Körnchen (MRKs). Allerdings ist fast nichts über deren strukturelle, dynamische und biophysikalische Eigenschaften bekannt, und die Funktion der MRKs bleibt hypothetisch. Die Entwicklung von superauflösender Mikroskopie führte in letzten Jahren zu einer Revolution und erneutem Aufschwung bildgebender Methoden in der Zellbiologie. Diese Technologie erlaubt neue Untersuchungen subzellulärer Biologie im Nanometerbereich, zum Beispiel der MRKs.

In dieser Dissertation ergründe ich die organisatorischen Prinzipien von Zellen und deren Mitochondrien. Dazu benutze ich superauflösende Mikroskopie zur Untersuchung der räumlichen Organisation von nuklearen DNS Domänen (TADs) an. Dabei erlaubt hochdurchlauf, stochastische Optischerekonstruktionsmikroskopie (htSTORM) die Medikamentenwirkung auf die räumliche Organisation eines TADs abzubilden. Als nächstes benutze ich Strukturiertlichtmikroskopie (SIM) um die Organisation mitochondrialer Dynamiken zu studieren. Dabei ist bisher unklar und aktiv diskutiert, wie verschiedene molekulare Stoffwechselwege miteinander verknüpft sind um zu mitochondrialer Fortpflanzung oder Abbau zu führen. Wir entdecken ein räumliches Muster mitochondrialer Teilungen, wobei diese einer bimodalen Verteilung folgen. Dadurch schaffen wir einen Rahmen zur Ordnung verschiedener Teilungstypen und zeigen, dass unterschiedliche molekulare Indizien mit der Teilung zur Fortpflanzung oder zur Zersetzung von Mitochondrien einhergehen. Hierbei entdecke ich, dass Aktin in der proliferierenden Mittelzonenteilung eine Rolle spielt, wogegen erhöhte Sauerstoffradikale einer peripheren Teilung und späterer Zersetzung vorausgehen. Mittels htSTORM, SIM und weiterer Mikroskopiemethoden untersuche ich ausserdem die biophysikalische Organisation von intramitochondrialen Prozessen und MRKs. Dabei entdecke ich, die Ultrastruktur von MRKs, die aus komprimierter RNS und einer diese umgebenden, dynamischen Proteinwolke bestehen. Ausserdem beobachten wir MRKs in Assoziation mit der inneren mitochondrialen Membran, und dass ihre Verteilung von der mitochondrialen Dynamik abhängt. Das erlaubt uns, MRKs als nanoskopische, robuste und fluide Kompartimente zu verstehen, welche höchstwahrscheinlich die intramitochondriale Reaktionskinetik beeinflussen. Zuletzt beginne ich damit die räumliche und biophysikalische Organisation der mitochondrialen Transkription zu ergründen.

Diese Resultate tragen zu einem holistischen und dynamischen Bild mitochondrialer Organisation bei. Sie zeigen dabei die Vorteile heutiger Mikroskopie um räumliche und zeitliche Organisation subzellulärer Prozesse besser zu verstehen, und läuten den Anfang einer neuen Ära der Einzelorganellbiologie, im Kontext weiterer kürzlich erschienener Studien zur submitochondrialen Organisation, ein.

Table of content

Chapter 1: Introduction

As a biologist, I am fascinated by life. Curiosity driven, I aim to understand how life works by analysing its various forms and their behaviour. A cell is the basic unit of life, and I am most fascinated by the molecular mechanisms that underlie cellular behaviour, and enable cells to live.

In this thesis towards a doctoral degree in philosophy on the "Organisation and dynamics of mitochondria and their RNA", I will first introduce the interested reader into the topic. For this, chapter 1 introduces essential concepts for non-experts, and starts off with a general introduction into cell biology and gene expression. In chapter 1.1, fundamental concepts of mitochondrial biology are elaborated before chapter 1.2 introduces the terminology and some basic principles of key methodology used for this thesis. The aims of my research will be clearly stated, before chapter 2 presents a use-case of one particular superresolution microscopy method, htSTORM to study genome dimensions. Next, specific aspects of the current knowledge about the organisation and dynamics of mitochondria (chapter 3) and their RNA (chapter 4) are elaborated and critically assessed. These chapters comprise the main body of the experimental results obtained from the research during my doctoral training. Finally, preliminary results on the organisation of mitochondrial transcription will be presented in an outlook chapter 5, before concluding remarks, a full list of references and an appendix comprising published scientific articles in chapters 6 to 9.
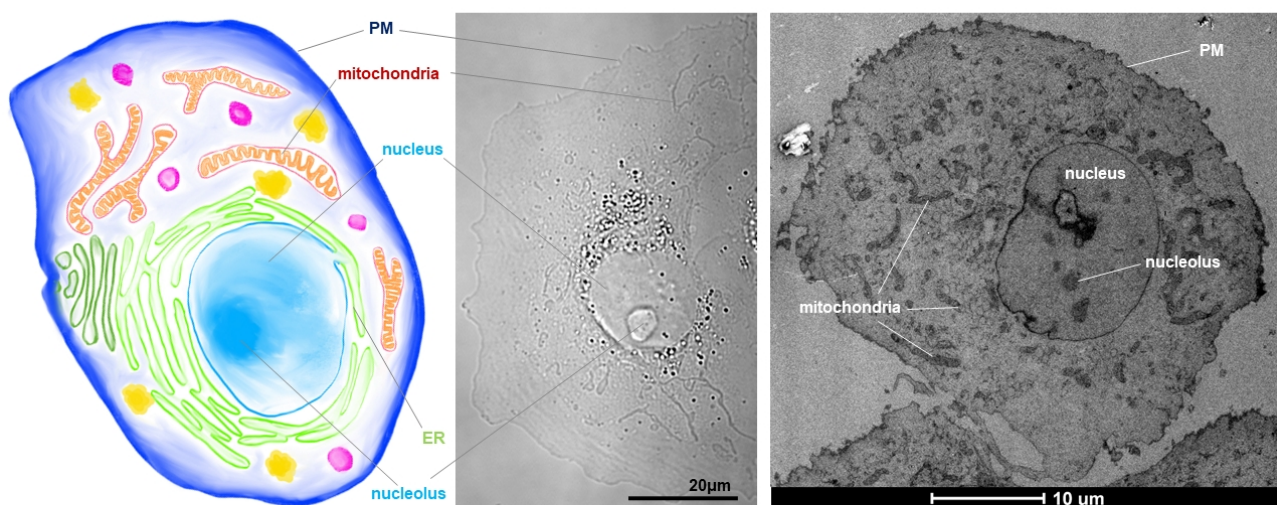
Figure 1: Typical eukaryotic cell with cell-organelles. Left, schematic of a typical cell with labelled organelles. Centre, transmission light microscopy of a Monkey kidney cell (COS7). Right, electron micrograph of a COS7 at low magnification. Abbreviations: PM = Plasma membrane, ER = endoplasmic reticulum.

Cell biology

Common to all cells is their defining boundary, the plasma membrane (PM) (Alberts, 2008). The PM consists of a bilayer of lipids and protein, though additional layers can be added to build a more sturdy cell wall in some organisms such as plants or bacteria. Modern eukaryotic organisms including animals, plants

and even corrals and bakers yeast, consist of cells which are 1'000 to 10'000 times larger than typical unicellular bacteria and contain additional membrane-encircled compartments called organelles (Alberts, 2008). Most notably, the nuclear membrane protects and segregates the eukaryotic nuclear DNA (nDNA) from the rest of the cell, and thereby tucks it away from most active processes. Mitochondria are also common to all eukaryotes. In mammals, they are the only cellular organelle that contain DNA besides the nucleus, the mitochondrial DNA (mtDNA). The remaining space between all the cellular organelles is called the cytoplasm.

Gene expression

While the original central dogma of molecular biology: "From DNA to RNA to protein" is no longer believed to be true in its absolute terms, it still serves as a good basic model to understand the internal organisation of living cells (**Fig. 2**). Long chains of 2'-deoxy-ribose-nucleotide duplexes make up a DNA molecule, and are used for long-term storage of information by all cells (WATSON & CRICK, 1953). The DNA-sequence in four-letter code is generally accepted to define a cells fundamental identity. To read the information, double-stranded DNA needs to be opened. This allows its replication by specialised molecular machines called DNA-Polymerases, and their accessory and regulatory units, which is necessary for the proliferation of a cell. But while DNA stores the information of how to replicate itself, it cannot do this autonomously. A cell first needs to transcribe its DNA's coding sequence into complementary 2'-oxygenated ribose-nucleotide chains (RNA) by a similar process using RNA-Polymerases. RNA-strings are much more versatile than DNA, and so-called ribozymes can perform and catalyse a range of molecular reactions. However, to produce replication- and transcription-polymerases, so called messenger RNA (mRNA) require translation of their sequence-information into protein. Interestingly, this machinery mostly consists of RNA which is assembled into a large molecular complex, the ribosome. Unlike DNA, RNA can thus readily process itself. Ribosomal RNA (rRNA) forms the ribosomal core, which then uses transfer RNA (tRNA) to probe the mRNA sequence in sets of three (codons), and to assemble polypeptide chains of amino acids. These polypeptides then assemble into what we call proteins, including polymerases and their accessory units. Proteins are responsible for accurate performance, regulation and catalysis of most cellular processes enabling life as we know it. Until the discovery and understanding of DNA by Watson and Crick, proteins were believed to be the cell defining molecules. Today we know that the three major species of intra-cellular macromolecules, DNA, RNA, and proteins are tightly interlinked and connected through feedback loops. Nevertheless, the basic workflow for a cell to do anything is to transcribe its DNA into RNA, and then translate the RNA into the cellular workforce in form of proteins. As a whole, this process is called gene expression, and a particular location on DNA which encodes for a particular protein or functional RNA is called a gene.

Metabolism

Human cells depend on many fundamental building blocks, which are freed when we digest our food consisting of other organisms and their cells. In cellular metabolism, metabolites are disassembled into their basic units for recycling by energy-releasing catabolic reactions. Anabolism uses energy to reassemble these building blocks into functional cellular protagonists. Some metabolites including nine amino acids are

essential, and need to be imported by our cells and across the PM. Others, including the 12 other amino acids can be produced through anabolism. While plants can harvest energy from sunlight to build organic molecules, we gain our energy from the oxidation and fermentation of the organic molecules that we eat. In our cells, the chemical energy that is stored in the atomic bonds of sugars and fats is converted to Adenosine triphosphate (ATP). The third phosphate group added onto Adenosine diphosphate (ADP) to make ATP, can readily be detached by proteins and other catalysts to use the high energy stored in its bond and fuel a plethora of cellular processes. ATP is therefore seen as the cellular currency for energy. It is produced in vast amounts by the central bank of the cell, our mitochondria.
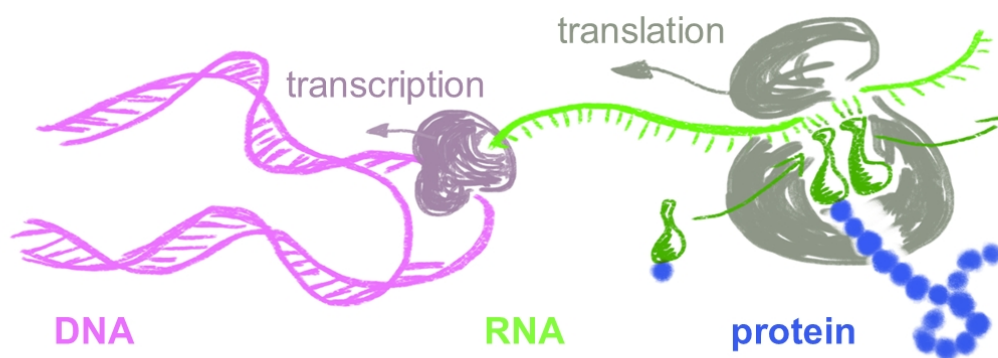
Figure 2: Central dogma in molecular biology: gene expression from DNA to RNA to protein. Double-stranded DNA (magenta) is transcribed into RNA (green) by a Polymerase. Charged tRNA (dark-green) then deliver amino acids (blue) for translation of RNA into proteins by a ribosome.

1.1) Mitochondria

The origin of mitochondria

Today's dominant view is that the mitochondrial origin lies in the engulfment of an α-proteobacterium by our archaeic ancestor ((Ryan *et al*, 2021)). Over time and through evolution, these two originally separate organisms then developed an intricate interdependency, and now form a single unit, or cell. Some argue that only through this symbiotic collaboration, and thus only by overcoming the principle of competition the marvels of multicellular cellular life have become possible (Alberts, 2015).

While there are many homologies between mitochondria of different species, there has also been a fair amount of divergence in eukaryotic evolution. This may at least in parts be due to the high mutation rate of mitochondrial DNA (Wallace & Chalkia, 2013). Therefore, yeast mitochondria and the regulation of their behaviour is very different from that of human cells. Throughout this thesis I will focus on our understanding of mammalian systems, mostly human, mouse or monkey cells unless stated otherwise.

Mitochondrial functions

After engulfment, the endosymbiont mitochondria now fulfil several vital functions inside eukaryotic cells. Their most prominent role is the efficient production of ATP through oxidative phosphorylation (OXPHOS) of

sugars and fats. Mitochondria also scavenge electrons off dangerous reactive oxygen species (ROS) in the cytosol. ROS are produced during sugar-catabolism (glycolysis) and other processes, and play an important role in undesired ageing processes. Mitochondria can also shunt intermediates of the tricarboxylic acid cycle (TCA) to and from the cytosol. Thereby, they buffer metabolite concentrations required for cell growth. Biosynthesis of heme-groups and Iron-sulfur clusters also take place inside mitochondria, and are important for the mitochondrial electron transport chain as well as other cellular pathways. Furthermore, mitochondria can buffer Calcium and synthesise lipids to build their own and other cellular membranes (Alberts, 2015). Additionally, the surface of mitochondria as well as the intermembrane space serve as an important hub for cellular signalling, and cell death (apoptosis) is regulated via mitochondria. Mitochondria have thus evolved to play a versatile and essential role at the centre of cellular metabolism.

Mitochondrial compartments

In addition to their functional importance, mitochondria are peculiar because they are encircled by two, an inner (IMM) and an outer mitochondrial membrane (OMM). The OMM contains large pores and is rather permeable. The intermembrane space is therefore sometimes considered as continuous with the cytosol. The IMM on the other hand has a peculiar lipid composition and is nearly impermeable to cellular components, including many metabolites. Within cells, lipid vesicles are often used to transport proteins or metabolites between cellular organelles, as well as the PM. However, the OMM obstructs vesicle fusion with the IMM and molecules destined to the mitochondrial matrix require regulated import via specialised complexes. The import-machinery for mitochondrial proteins consists of multimeric transmembrane complexes in the inner (TIM) and outer (TOM) membranes (Wiedemann & Pfanner, 2017). The TOM-complexes are spread throughout the OMM, where unhindered lateral diffusion allows their even distribution (Dieteren *et al*, 2011). Interestingly, the atomic structure of the TOM-complex has only recently been solved (Araiso *et al*, 2019; Tucker & Park, 2019).

The IMM on the other hand is subdivided into two functionally and molecularly distinct domains, the inner boundary membrane (IBM) and the cristae membrane. The IBM lies parallel to the OMM, and marks the interface to the intermembrane space. The IMM is impermeable to metabolites, and the IBM harbours selective transmembrane transport complexes to import both proteins and metabolites. Here, the TIM23 complex takes over emerging peptides destined for the IMM or the matrix directly from TOM. An example of a metabolite transporter is the mitochondrial pyruvate carrier (Herzig *et al*, 2012). It allows mitochondria to import the sugar-derivative from glycolysis for its combustion through the TCA and OXPHOS.

Cristae are membrane invaginations perpendicular and connected to the IBM at so called cristae junctions (CJs). They normally form flat, lamellar cisternae which stack in close proximity to each other and often occupy a large amount of the mitochondrial volume. At CJs, the mitochondrial contact and cristae organising system (MICOS) connects the IMM with the OMM (McArthur & Ryan, 2020). MICOS consist of two complexes (Stephan *et al*, 2020) (Mic10 and Mic60) with seven subunits. Mic60 appears to be responsible for the connection between cristae and the IBM at CJs, whereas Mic10 regulates cristae

morphology together with Opa1. Cristae-lamellae are about ~20nm wide (Dlasková *et al*, 2018), and are crucial for ATP-production through OXPHOS. The respiratory chains of the OXPHOS are confined to the large planes of cristae (Wilkens *et al*, 2013) whereas ATP-synthase dimers decorate the cristae rims (Davies *et al*, 2011). This assembly allows to generate the electrochemical gradients of protons (H^+), necessary to drive ATP synthesis (Alberts, 2015). Besides energy production, integral cristae morphology also has an important regulatory aspect in apoptosis. Cytochrome c escape from the cristae-lumen can trigger cell death.
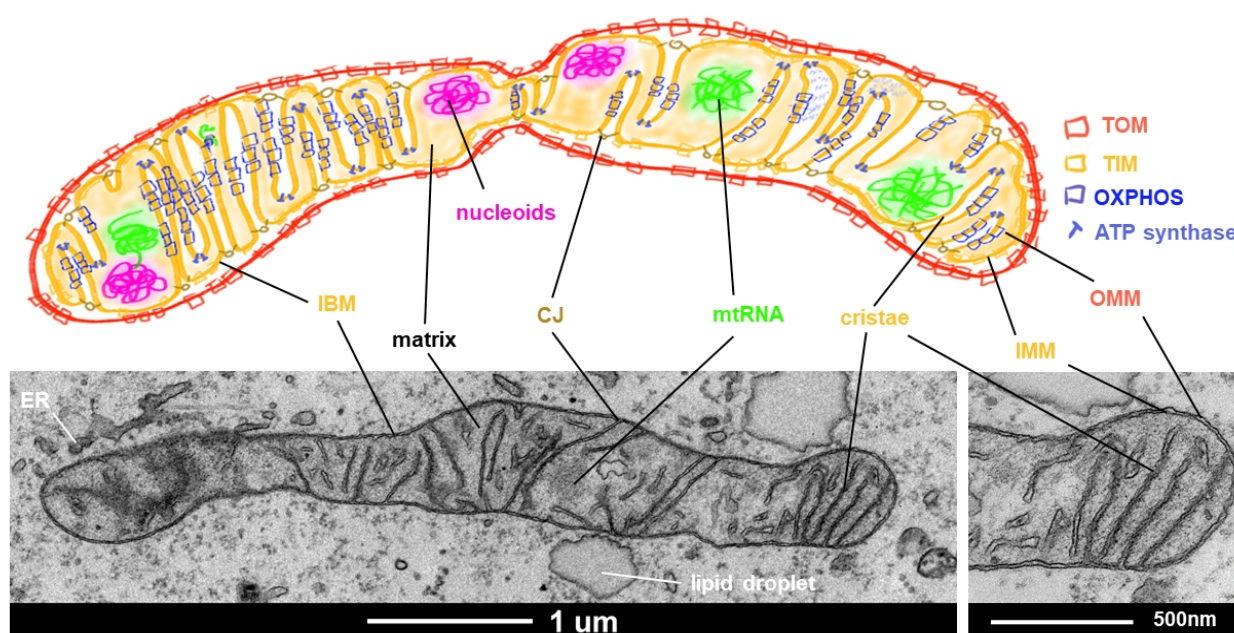
Figure 3: A Mitochondrion. Top, schematic of a typical mitochondrion with labelled features. Bottom, electron micrograph of a mitochondrion from COS7 cells at high magnification. Abbreviations: IBM = inner boundary membrane; CJ = cristae junction; IMM = inner mitochondrial membrane; OMM = outer mitochondrial membrane; TIM = translocase of the inner membrane; TOM = translocase of the outer membrane; OXPHOS = oxidative phosphorylation complex; ER = endoplasmic reticulon

Once passed the IMM, imported proteins and metabolites find themselves in the lumen of mitochondria, which is called the matrix. Many of the important processes take place in the matrix, such as iron-sulfur cluster biosynthesis, β-oxidation, and the TCA. Unlike in the cytosol, there is no skeleton or motor-proteins to allow for directed and fast transport inside the mitochondrial network. Furthermore, diffusion in the mitochondrial matrix is hindered by the obstructive stacks of cristae (Dieteren *et al*, 2011). Larger matrix-components are thus likely to be entrapped by steric hindrance, although the size and shape-dependence of this phenomenon has never been quantitatively assessed. It remains to be determined whether there is a size cut-off, and how fast mitochondrial ribosomes with a diameter of ~30nm disperse throughout the mitochondrial matrix could be compared to tRNAs with a diameter of ~7nm or mRNAs of unknown size and shape. The mitochondrial matrix is also home to mitochondrial gene expression from mtDNA, which will be elaborated in further detail throughout this thesis, and in chapter 4 and 5 in particular.

Mitochondrial DNA

In humans, mtDNA consists of 16'569 base-pairs, and encodes 37 genes. The two complementary strands of mtDNA can be distinguished by their molecular weight, as the four bases do not occur in equal proportion, and one strand comprises a significantly higher number of purines. This is called the *heavy* strand, and the other the *light* strand. Together, the two form a continuous circle of double-stranded mtDNA with a thickness of ~2nm. In theory this circle would have a circumference of around 5.6µm (5.6/1000mm) and thus a diameter of ~1.55µm. Inside living mitochondria however, mtDNA is compacted into nucleoids by a protein called mitochondrial transcription factor A (TFAM). Under normal conditions, TFAM can form dimers and bind mtDNA. Thereby it introduces bends and interconnections in linear stretches of DNA which ultimately compacts mtDNA in a concentration dependent manner (Kukat *et al*, 2015). Nucleoids have been found to be roundish granules of about 100nm in diameter (Kukat *et al*, 2011; Brown *et al*, 2011; Alán *et al*, 2016). The number of mtDNA-copies inside individual nucleoids had been a matter of debate for a long time (Kukat & Larsson, 2013). Despite that nucleoids are much shorter than the 5600nm one would expect from its sequence, their volume could fit more than 20 volumes of 16kb-mtDNA. Only through correct counting by superresolution microscopy, this conundrum could be solved. We now know, that there are only one to two mtDNA-molecules within single nucleoids in normal mammalian cells (Kukat *et al*, 2011). The principle and advantages of superresolution will be discussed in in the next chapter.

On each molecule of mtDNA, the 37 coding regions comprise two rRNAs (12S and 16S), 22 tRNAs and 13 mRNAs, which encode for different subunits of four of the five OXPHOS-complexes. The expression of mtDNA is therefore essential for the assembly of the OXPHOS-machinery, and thus for many mitochondrial functions. All steps, from transcription, until translation take place inside mitochondria, where the nascent proteins are directly inserted into the cristae membranes (Itoh *et al*, 2021). While the polymerases and many other transcription-related protein factors are imported, all RNA-components of the mitochondrial gene expression machinery are encoded on mtDNA. Interestingly, so-called rho-zero cells that lack or loose their mtDNA can be grown in tissue-culture conditions. To produce such cells it is sufficient to inhibit mitochondrial replication for around two weeks (Chandel & Schumacker, 1999).

Mitochondrial replication

In order to proliferate and meet the cellular energy demand mitochondria need to replicate their DNA. For this, a minimal set of proteins allows the sound replication of mtDNA. A single mitochondrial DNA-polymerase catalytic unit (POLG) associates with two regulatory subunits p55 (POLG2) (Young *et al*, 2015). This complex is recruited to origins of replication on each strand of mtDNA, with OriH for the heavy and OriL for the light strand. In addition to POLG and POLG2 a mitochondrial helicase (TWINKLE) is required to unwind the double-stranded mtDNA in front of the replication fork (Milenkovic *et al*, 2013). A peculiarity of mitochondrial replication in comparison to nuclear replication is it is unidirectionality from each of the two origins. Additionally, the two origins lie on near opposite sites of the mtDNA circle, and thus do not fire simultaneously. For protection of the lagging strand behind the replication complexes, mitochondrial single stranded DNA binding protein 1 (SSBP1) binds to single stranded mtDNA (Ruhanen *et al*, 2010).

Non-canonical roles of mtDNA in immune response and inflammation

In addition to the canonical function to encode essential RNAs and proteins for OXPHOS, mtDNA has also been linked to innate immune responses and inflammation. Being recognised as 'foreign', non-nuclear DNA, mtDNA can act as a damage associated molecular pattern (DAMP), which activates host pattern recognition receptors (PRR) to trigger an immune response (West & Shadel, 2017). Under normal conditions, mtDNA and PPRs are physically separated by the mitochondrial double-membrane, and no response is triggered. However, under particular circumstances, mtDNA can leak out of the mitochondrial matrix, and its non-nuclear features such as unique methylation patterns, oxidative damage patterns, or TFAM-packaging may be recognised as DAMPs (West & Shadel, 2017). Several pathways have been identified to specifically detect particular mtDNA-pathologies and trigger an immune and inflammatory response. The DNA-sensing cGAS and STING pathway for example, is activated and induces the expression of a broad range of interferon stimulated genes (ISGs) upon heterozygous deletion of TFAM (West *et al*, 2015; Riley & Tait, 2020). A recent discovery showed that corroborated pyrimidine synthesis or uptake into mitochondria perturbs mtDNA-homeostasis and also leads to ISG up-regulation via cGAS/STING (Sprenger *et al*, 2021). Interestingly, the immune reaction to mtDNA double-strand breaks on the other hand were found to not depend on the detection of DNA via cGAS/STING, but on the MAVS/RIG-1 system triggered by cytosolic mtRNA (Tigano *et al*, 2021). Together, this highlights the importance and intricacy of the precise regulation of mtDNA and its transcripts.

Studying mitochondria

At the beginning of the last century the development of new techniques and methods allowed to study the processes of life at unprecedented detail, and the field of molecular biology was born. Mitochondria themselves were first observed as long strings inside cells, in the 1890's (Ernster & Schatz, 1981). Electron micrographs of mitochondria then became famous from 1952, and highlighted the distinct double-membrane, as well as the cristae invaginations (Ernster & Schatz, 1981). Apart from these initial observations, the focus of many molecular biologists lied to biochemical work. Mitochondrial elements, and functional mitochondria can be isolated from cells and studied in a test tube (Liao *et al*, 2020). Through biochemical *in vitro* assays, sequencing, flux analyses with mass spectrometry, and atomic structure resolving electron microscopy much of the detailed biochemical composition, metabolic pathways and their interdependencies in mitochondria have become well understood. We know the hypothetical path the energy stored in each of the Carbon-Carbon bonds of a Pyruvate takes, to produce ATP, water and CO_2. However, a main limitation of biochemical assays are the often indirect interpretation of results. One cannot *see* the molecules and what they are doing, but must infer their activity on the premise that the chemistry in a test tube or cell sample works exactly as predicted. To obtain statistically significant quantities, sample-species of interest must often be enriched either by collective sampling of millions of cells or through several amplification steps. To harvest, original cells are first killed and besides the potential side-effects of killing and then processing this means that the identical cells cannot be sampled repeatedly. Furthermore, biochemical sampling and *in vitro* assays lose spatial information and thus cellular or molecular context-effects are often neglected.

In recent years, microscopy-based studies of cellular processes are regaining traction. In particular, the superresolution revolution in microscopy over the last decade allowed to better access the processes inside and around mitochondria of intact cells (Jakobs *et al*, 2020). While typical mammalian cells are between 5 to 50µm wide, mitochondria retained the size constrictions of their bacterial ancestors. They are mostly tubular with a diametre of around 500nm. In contrast, the physical limit to resolve any two points by standard light microscopy lies at around 200nm (see limit of resolution in chapter 1.2). Resolving sub-mitochondrial processes has thus remained at the virtue of feasibility. Superresolution microscopy now allows to resolve processes at the nanometre scale, and thus at the scale of typical cellular molecules such as proteins. Novel insights from the study of cell-to-cell, intracellular, inter organellar and even intra mitochondrial variability have therefore only started to emerge (Zhuang, 2021; Larsson *et al*, 2021). An interesting example of this, is the discovery that not all cristae inside a single mitochondrion are the same and that they can differ in their metabolic state (Wolf *et al*, 2019).

Throughout the work towards this thesis, I focused on using optimal imaging techniques to study the sub-cellular processes of mitochondria, and in the nucleus. In the next chapter I will highlight some of the major advantages of these methods to answer questions in molecular biology, as well as their limitations.
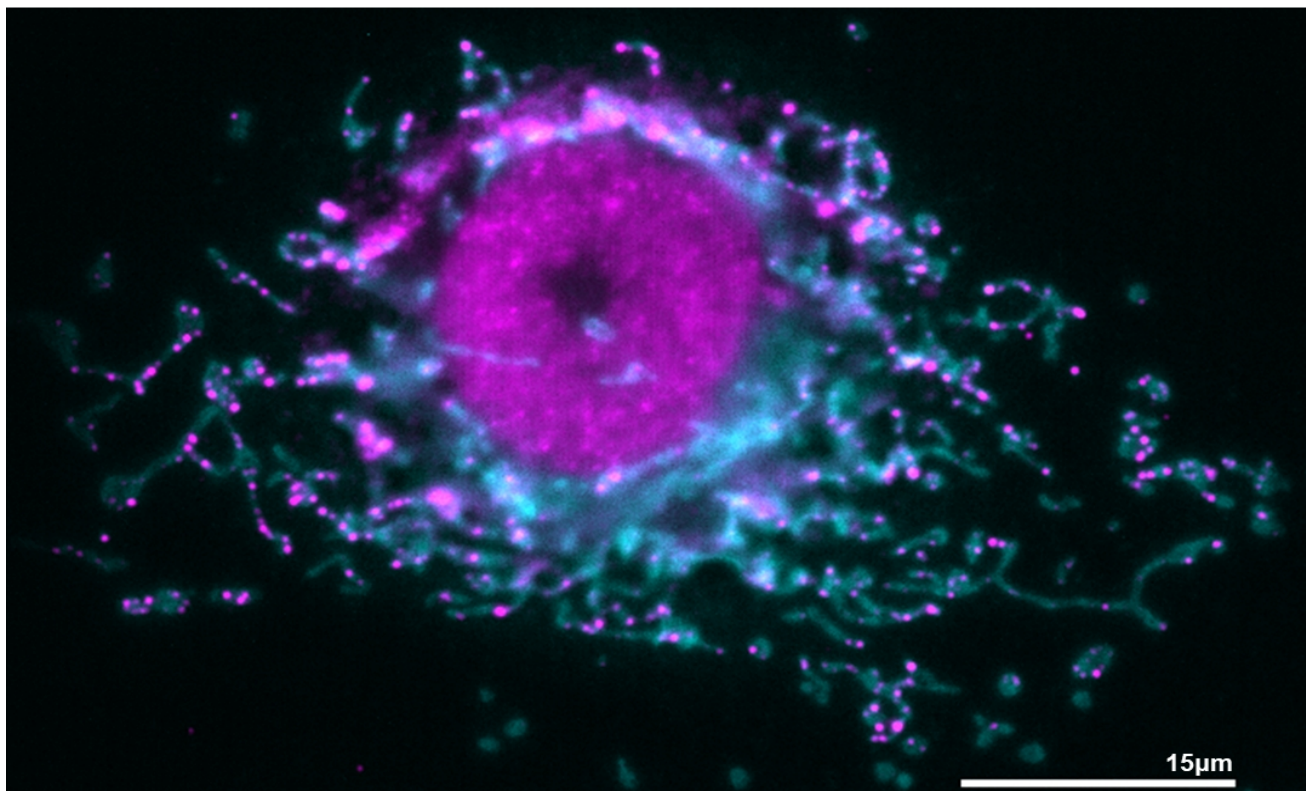

Figure 4: Widefield immunofluorescence microscopy image of a COS7 cell with mitochondria in cyan (anti-tom20) and nucleoids in magenta (anti-mtDNA).

1.2) When seeing is believing: Microscopy for cell biology

Light

Light travels as discrete portions of energy called photons, and this energy can be described as $E = h*v$ where h is a constant and v represents a variable frequency (of travelling photons). When photons reach our retina behind the lenses of our eyes, their energy excites particular molecules inside our photoreceptive cells. These cells collect and integrate this information and pass it on to our nervous system and the brain for processing and reconstruction into image-concepts for analysis. At the same time, the energy of light can also travel space as a wave expanding in all directions from an original point-source. The wavelength of light, or distance between the peaks of two consecutive wavefronts is inversely proportional to its frequency so that high energy, or high frequency corresponds to low wavelengths.

At the scale of human life we can regard light to form images instantaneously. Therefore, one of the most direct ways to study biology empirically is to observe ones subject. Over time, temporal information of its behaviour can be obtained, and simultaneous observation of several objects yields spatial and contextual information. For better analysis, and to share ones observations, capturing images on camera has become a gold standard.
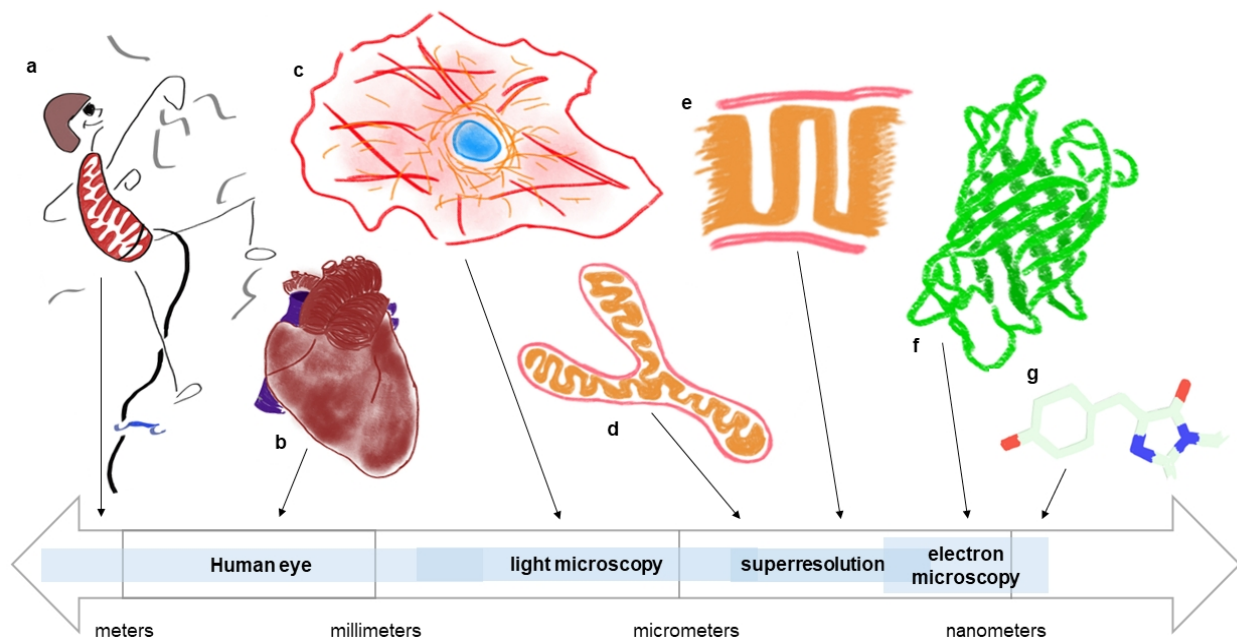
Figure 5: Biology at different length scales. From left to right: Human life (**a**) takes place on the order of meters, whereas our organs, such as the heart (**b**) operate in the range of tens of centimetres. Every organ consists of millions of cells (**c**), which are typically between 5 to 50 micrometer (μm) in diameter, just beyond the resolving power of our eyes. Mitochondria (**d**) inside our cells are typically several microns long and ~500nm wide, and can be observed using conventional light microscopy. To resolve cristae (**e**), which are separated by mere 10s of nanometres, and to monitor single proteins like GFP (**f**) on the order of single nanometres, the use of superresolution microscopy methods is required. Electron microscopes are ideally suited to investigate single molecules and macromolecular complexes with Angström resolution, which is on the order of atomic bond-lengths within amino (**g**).

Length scales

Biology takes place on a vast range of length scales. While animal behaviour occurs on metres to kilometres, mammalian cells have diameters of only five to 50μm. Cellular organelles often occur as small entities in the hundred-nanometre range, and molecular complexes such as ribosomes can be over 30nm whereas individual proteins or RNA span a few nanometres. Finally, small metabolites or atomic bonds of down to ~0.1nm (100pm) mark the lower boundary of length scales relevant for molecular cell biology (**Fig. 5**). Unfortunately, the resolving power of our eyes is limited to about the thickness of a human hair. Therefore, cell biologists typically use sets magnifying glasses and lenses to achieve the necessary magnification to observe subcellular behaviour. Complex assortments of lenses are often assembled into microscopes, for which the basic principles will be discussed below.

Microscopes

To locate an object that reflects or emits light (point source) on an image, it must span at least two pixels according to a sampling theorem proposed by Nyquist in 1928 and proven by Shannon in 1949. Lenses allow to focus, as well as to magnify the original image produced by an emitter to optimise its sampling (**Fig. 6**). However, the maximally attainable resolution of any microscope is physically linked to the wavelength of the signal. The limit of resolution is described by Airy's theory of diffraction from 1835, and Abbe's limit to resolve two distinct point sources, from 1873. Its lateral (xy) limit lies at approximately half the wavelength of the detected light, and in the third (z) dimension the limit is at ~1.5x of the wavelength. Another trade-off in microscopy comes from the fact that by magnifying the signal of interest one also magnifies the surrounding noise. In biological experiments one is often interested in the behaviour of a particular species. While contextual information can be crucial for correct conclusions, in today's prevailing reductionist approach this can lead to information overflow, and loss of interpretable results. Fluorescent labelling is one approach to improve the contrast of a specific target species of interest, and thereby increase its signal-to-noise ratio (SNR), allowing further magnification.

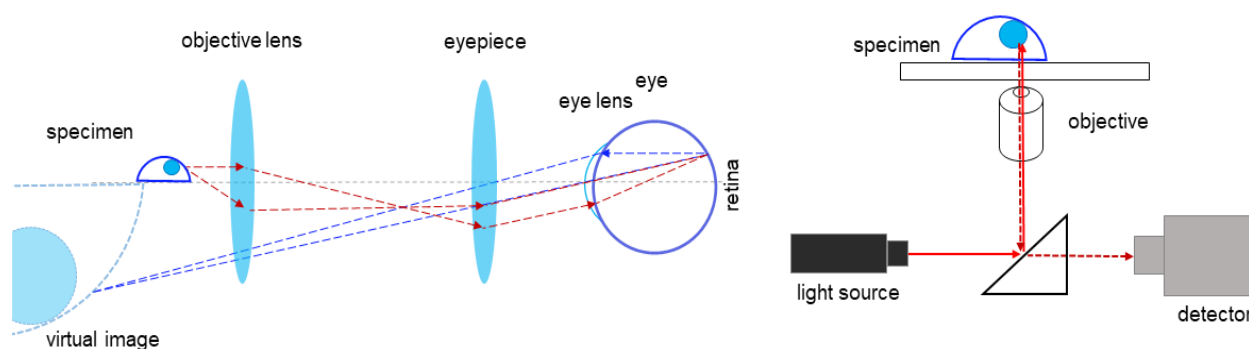**Figure 6**: Basic principles of microscopy. Left, principle of viewing a small object through an array of lenses. Right, principle of an epi-fluorescent microscope where a source sends the excitation light through an objective to the sample, and a detector registers the emitted fluorescent light. This set-up allows to reduce the background from additional excitation light, which passes through the sample.

1.2.1) Fluorescence Microscopy

Fluorescence

Brightfield transmission light microscopy is the simplest principle to observe a small specimen without contrast enhancement. Because of the densely packed nature of biological cells with billions of molecules of similar size and density, this often results in uninterpretable images. Marking particular molecules of interest can thus allow to distinguish them from a sea of unmarked molecules. Around the visible range of light (~400 to 750nm), fluorescent molecules can be distinguished from non-fluorescent molecules. Hereby, a fluorophore is first illuminated with light of a particular wavelength. Typical organic fluorophores comprise a pi-system with de-localised electrons which are excited by the energy of the incident light. This moves them from their ground-state (S_0) into a high-energy excited state (S_1). In the excited state, small amounts of energy are lost via molecular vibrations, rotations and other atomic processes, before the fluorophore spontaneously relaxes to its S_0. During the relaxation from S_1 to S_0, the remaining energy is then emitted as fluorescent light with slightly less energy, and thus higher wavelength. This difference between excitation and emission wavelengths, called stokes shift is what makes fluorophores particularly useful molecules in microscopy. It allows to separate the incident from the emitted light by using wave-length specific filters or mirrors to enhance contrast.

Labelling strategies

There are several types of fluorescent molecules and targeting strategies exploited in cell biology. A natural green fluorescent protein (GFP) was first discovered in deep sea jelly fish in the 1960s, and has since revolutionised live cell biological imaging (Lippincott-Schwartz *et al*, 2001). The responsible gene sequence was identified, and engineered versions of this protein are still heavily used in research today. The advantage of this system is that DNA-sequences encoding proteins of interest can be directly fused to DNA-sequences of the fluorescent protein (FP). Upon expression of this engineered DNA, a chimeric protein covalently bound to a FP will be produced by a transfected or genome-engineered cell. Today, many versions of FPs with different photophysical properties, and alternative emission and excitation spectra are available. This also allows to tag and distinguish multiple targets simultaneously. However, one major limitation of FPs is their potential effect on the functionality and behaviour of the protein of interest. An experimental problem comprises that the modified DNA needs to be delivered into the cell. Once introduced, for instance by genome engineering, the FP can no longer be exchanged and rational design is important to allow multiplexing of different labels.

Paralog systems to tag and track RNA inside living cells now also exist (You & Jaffrey, 2015). However, most metabolites are too small to be reasonably taggable. Therefore, FPs and RNA-aptamers have been selectively engineered to depend on binding of particular metabolites to fluoresce in live cells. The mito-R-GECO construct for instance, reports on Ca^{2+} levels inside mitochondria (Wu *et al*, 2013). Alternatively, environment-dependent organic dyes allow to infer molecular detail in specific regions of a cell. To use organic dyes on proteins, non-fluorescent SNAP or Halo-tag can be genetically attached like FPs. These

tags will then covalently bind organic dyes (Keppler *et al*, 2003; Los *et al*, 2008). This allows to harness the often superior photophysics of dyes compared to FPs. Another version of this principle is the use of inorganic quantum dots (QDs). QDs are very photostable and thereby allow for prolonged imaging (Yang *et al*, 2016).

As mentioned above, appending a relatively large fluorescent molecule to a protein of interest can directly affect its functionality and behaviour. Furthermore, protein-levels inside a cell are often tightly regulated and ectopic expression of additional quantities can perturb cell-physiology. To directly stain endogenous protein populations the principle of immunolabelling is often exploited for fluorescent microscopy. This principle has been around for decades, as it can also be used with density-tags for electron microscopy images. In brief, antibodies against a particular protein of interest are raised and produced in animals, which are then killed to allow harvest. These primary antibodies can either be directly labelled with a fluorophore, or targeted with a secondary antibody. The secondary-antibody approach allows for cost-economisation as well as signal amplification. However, it also doubles the size, which begins to play a role in today's superresolution microscopy (see chapter 1.2.3). Besides the specificity-problem (Voskuil *et al*, 2020), one major limitation of immunofluorescence is its reliance on cell-permeabilisation to target intra-cellular structures. This requires killing and fixing the specimen before analysis and thus only allows to retrieve spatial, but no temporal information.

Advantages and limitations

The main advantage of fluorescent labelling for scientific microscopy is its inherent signal-specificity, which allows to achieve the necessary contrast. However, fluorescent light is still limited by Abbe's principles and therefore the absolute limit of resolution for fluorescence microscopy lies around 200nm. Other limitations inherent to microscopy such as signal-scattering due to imperfect lenses of course also apply to fluorescence microscopy and thus affect the SNR. Furthermore, many biological molecules also absorb energy in the visible spectrum. Albeit at much lower efficiency than canonical fluorophores, this can generate relevant background fluorescence, hampering SNR. Fluorescent signal intensity typically increases with increased excitation irradiance because multiple rounds of S_0-S_1-S_0 cycles are possible. This can alleviate specific signals above the stochastic background. However, the additional energy also increases the risk of photobleaching. In photobleaching, the fluorophore-molecule suffers irreversible damage in the high-energy states attained, whereafter it no longer emits any fluorescence. Additionally, the excitation energy is also absorbed by the biological and sometimes living specimen, and is damaged in the process. Together, this limits both spatial and temporal sampling and resolution. In turn, the principle of photobleaching can also be exploited experimentally, and one such technique will be explained in the next chapter.

1.2.2) Special fluorescence microscopy techniques

Fluorescence recovery after photobleaching (FRAP)

FRAP was first developed to study protein-diffusion in cellular membranes in the 1970s (Peters *et al*, 1974; Schlessinger *et al*, 1976). The basic principle is simple, and has also been implemented to monitor protein diffusion in three dimensional cellular spaces, apart from the PM (Lippincott-Schwartz *et al*, 2001). For this method, the irreversibility of photobleaching is exploited to distinguish subpopulations of fluorescently tagged molecules in live cells. First, a particular region of a cell or cellular compartment is chosen for pulsed illumination with extremely strong excitation light. This high energy bleaches the fluorophores in the region through irreversible molecular damage. Then, the recovery of the fluorescent signal in the bleached region is monitored over time. Because all molecules within the region were bleached at time zero (t_0), the recovery of signal is proportional to the exchange of those molecules with new molecules from adjacent, non-bleached regions (**Fig. 7**). By determining the exchange rate, descriptors such as the apparent diffusion constant or the mobile fraction can be calculated for the tagged molecule.

Confocal

Confocal laser scanning microscopy is a particular microscopy method which has become the go-to standard for most cell-biological applications, and is commercially available. As discussed above, contrast is fundamental to see ones structure of interest. Because of the diffraction limit of light, the smallest possible focus-volume for the excitation light is around half the wavelength in xy, and due to imperfect lenses about 2-3 times more in z. In addition, the light also travels through the sample below and above the focal point. Together, a noisy signal is produced with contributions from both, fluorophores and auto-fluorescing molecules throughout the deep focal point, as well as from excited molecules around the focal point. In confocal microscopy, the emission-light is filtered through a narrow pinhole which rejects out of focus light. This allows to reduce the noise and thereby greatly increases contrast and SNR. The clean light from a small sampling-spot is then amplified and recorded in a single photon-receptor, which increases the sensitivity. To image a larger structure such as a cell, each point of the cell must be imaged individually, and the entire sample area has to be scanned point-by-point. While allowing for high contrast, point-scanning confocal microscopes are therefore relatively slow. Additionally, because the noise-rejecting pinhole also filters out some of the main signal, higher excitation laser-intensities are often used. The slow acquisition spee and the increased risk of photodamage therefore represent the major limiting factors for this type of microscopy.

Correlative light and electron microscopy (CLEM)

The combination of optical and electron microscopy (EM) allows to harness advantages of both types of analysis methods. EM allows for ultrastructural detail, for example of precise membrane arrangements. It allows for supreme resolution and complete information on electron-densities corresponding to biological molecules. In return, specific molecules can hardly be distinguished from each other and their environment due to the dense packing of molecules inside cells. Fluorescence microscopy on the other hand allows to introduce contrast and highlight particular molecules of interest through fluorescence tagging. Its resolution is

limited by the diffraction limit of light, which lies far above the size of individual molecules. Additionally, many cellular components, and in particular lipid membranes are difficult to tag and visualise using fluorescent strategies. In combination, the two allow to first identify the location of particular molecules or molecular assemblies through fluorescence microscopy. Subsequently, ultrastructural detail of these structures as well as their environment can be gained using EM. The major limitation in this procedure is to align the two resulting images. For this it is necessary to fix, and thereby kill the specimen. Additionally, the fixation procedure required for EM do not allow for optimal conditions of standard fluorescence staining procedures.
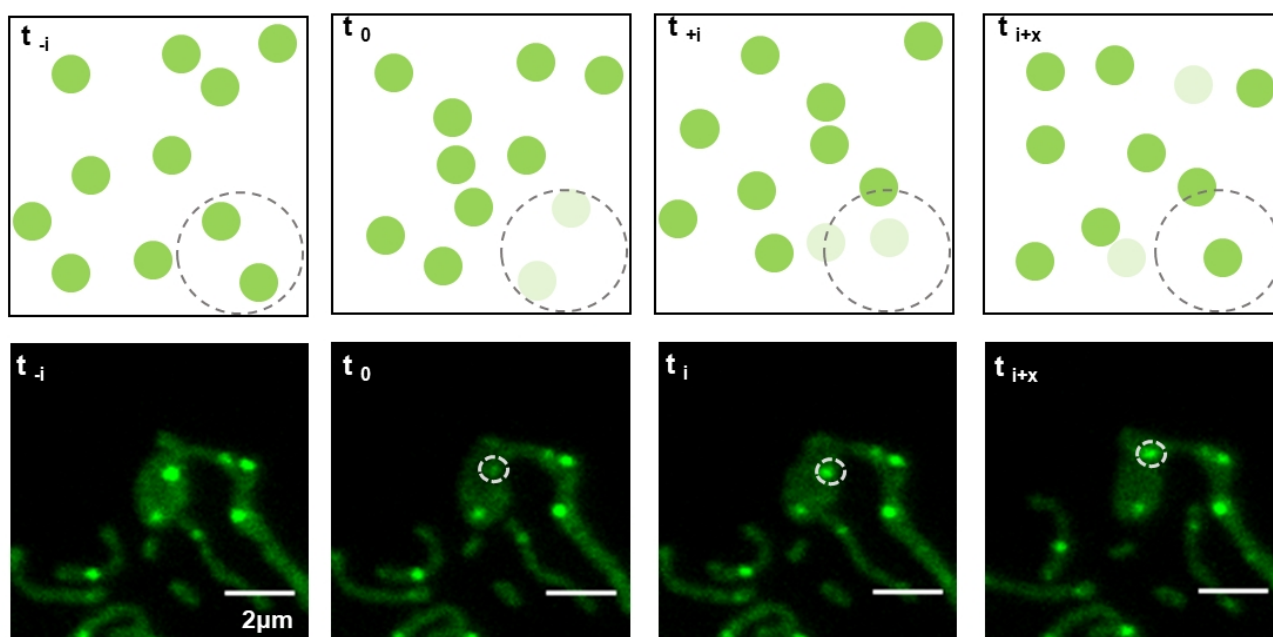
Figure 7: Principle of FRAP. Top row, scheme of fluorescent particle distribution during a FRAP-experiment. The particles (green dots) are randomly dispersed, and move around (t_{-i}). At time 0 (t_0), a defined area (indicated by grey circle) of the sample is photobleached, and molecules in this area will no longer fluoresce (indicated by faint colour). The dark molecules will continue to move around, as will non-bleached, bright molecules (t_{+i}). Depending on the properties of the system, and the monitored molecule, the fluorescence will eventually re-equilibrate (t_{i+x}). By monitoring the evolution of the fluorescent signal in the bleached area, one can deduce the speed of re-equilibration, and thereby the motion of the tagged molecules. Fast recovery indicates fast exchange between the bleached area and its surrounding, whereas slow recovery mean little exchange. Bottom row, example of FASTKD2-eGFP signal evolution in a FRAP experiment in COS7 cells. at t_0, nearly all fluorescent molecules inside the focus indicated with a white circle are bleached. Over time, (i = 3sec, x=17sec), the molecules are exchanged between the bulk and the granule phase, and the fluorescent signal is re-equilibrated.

1.2.3) Superresolution Microscopy

In recent decades, scientists achieved to surpass the limit of resolution in light-microscopy without decrease of the wavelength, and thus within the realm of fluorescence microscopy. There has been a wide range of developments of specific methods over the last decade, and these techniques have been termed superresolution microscopy or nanoscopy, as they shift the observable spectrum into the nanometre range (Nobel Prize, 2014). The fundamental principle inherent to all far-field superresolution microscopy methods is the redistribution of spatial information over time. Two different principles and their main implementation will be described below. It is interesting to note that there are also many computational methods including the use of deep learning and neuronal networks to improve signal quality such as CARE (Weigert *et al*, 2018). These methods however will not be discussed in further detail, as they were not used for the work collected in this thesis.

Structured illumination

Structured illumination microscopy (SIM) uses diffraction-limited interference to achieve a doubling of the resolution in 2D (Gustafsson, 2000) or 3D wide-field fluorescence microscopy (Gustafsson *et al*, 2008). As such, it is not limited by the nature of the fluorophore or excitation laser, but merely depends on the structuring element used to structure the excitation light. In brief, the structured illumination of the sample allows to trade low-frequency information for detailed information stored in high frequencies which would normally be lost. By acquiring multiple images with shifted illumination patterns, computational reconstruction then allows to connect the high with low-frequency information and create a new image with improved resolution. One main limitation of SIM comes from the importance of precise alignment of optical features of the microscope, as well as the complex computational reconstruction (Schermelleh *et al*, 2019). This makes SIM particularly artefact prone (Demmerle *et al*, 2017). A practical limitation for live-cell acquisition can be the dependence on multiple image acquisitions (typically 15 images for optimal 2D or 3D resolution). Especially for multicolour experiments of fast moving objects physical elements of the microscope, such as filter-wheels can represent major limiting factors in acquisition speed. On the current Nikon N-SIM system at the Bio Imaging Platform at EPFL, and which was used for the experiments presented in this thesis a two-colour acquisition would take at least ~5 seconds, despite short exposure times.

Another famous and commercially available method for structured illumination superresolution microscopy is stimulated emission and depletion microscopy (STED) (Hell & Wichmann, 1994). Instead of a patterning grid, STED uses a second illumination beam to shape the excitation light. This allows to decrease the sampling to a nanometre-sized area. Only fluorescent molecules within this area will be excited and emit fluorescence, whereas neighbouring molecules do not emit fluorescent light. As in a confocal, to obtain a full image the beam needs to be scanned across the sample and the emitted light is recorded one step at a time, with single-pixel photon detectors. Both, the scan-time as well as the extreme energies required to shape the excitation beam limit the applicability of STED for large fields of view and live cell microscopy experiments, despite its resolution in the range of ~60nm.

Single molecule localisation microscopy (SMLM)

Similar to STED, SMLM-approaches allow for diffraction unlimited superresolution fluorescence microscopy. However, SMLM typically do not depend on special optical elements, and can be performed on regular wide-field microscopes. Instead of structuring the excitation in space, in SMLM the fluorescence emission from the entire field of view (FOV) is spread over time. For this, only sparsely distributed fluorophores emit light, which can be imaged with a camera. The centre of these single emitters is then computed by fitting a Gaussian distribution to their image. This allows to individually image each emitter without interference from its neighbour. Over time, all potential emitters are switched on and off stochastically, and their positions can be used to reconstruct a superresolved image.

In photoactivation light microscopy (PALM) special photo-activatable or -convertable fluorescent proteins are fused to a protein of interest. Activation or conversion is achieved with high-energy light which induces a conformation change in the FPs (Betzig *et al*, 2006). Upon excitation, only previously activated FPs emit light, and the density of activated FPs can be controlled by fine-tuning the conversion light.

Stochastic optical resconstruction microscopy (STORM) harnesses fluorophore-*blinking*. This photophysical phenomenon is based on reversible photobleaching of fluorescent molecules, whereby the fluorophore remains in a long-lived dark-state before returning to its S_0 from which it can be excited again. A handful of particular dyes are especially suitable for this approach and their dark-state can be prolonged using thiol-based buffers (Rust *et al*, 2006; Heilemann *et al*, 2008, 2009). Other approaches such as PAINT achieve single-molecule emission distribution by fluorophore-species independent means (Sharonov & Hochstrasser, 2006).

In practice, SMLM methods have been shown to achieve supreme lateral resolution of ~20nm. Additionally, the acquisition speed in SMLM does not depend on the image size, but is proportional to signal-density. However, to achieve optimal sampling of a structure of interest this often includes 10s of thousands of images, and acquisition time is one of the major limiting factors in SMLM. One way to improve the throughput of SMLM experiments is the increase of the FOV. While this approach does not improve the minimal time to adequately sample a specific structure, it vastly increases the number of structures sampled in parallel, and thereby the throughput. High-throughput STORM (htSTORM) using flat-fielding for increased FOV has been established in our group (Douglass *et al*, 2016), and an example for its application is given in the following chapter 2.

Objective and aims

By combining a range of microscopy methods, and applying each to their advantage, the overarching aim of the research presented in this PhD thesis is to better understand the underlying principles of subcellular organisation. Particular attention is paid to newly discovered biophysical principles within mitochondria, at the resolution limit of light microscopy, and for which appropriate use of imaging modalities was essential. The gained insights allow to better understand the organisation of and within mitochondria, and open up new avenues for investigations in mitochondrial gene expression.

Aim 1: Use of superresolution microscopy to study the organisation of DNA domains.

Traditionally, genomic studies depend on vast amount of sample material from millions of cells, in order to obtain high-resolution information. However, emerging concepts from single-cell biology highlight both, the confounding effects as well as the biological importance of cell-to-cell variability. The use of advanced imaging techniques to study features of genome organisation allow to obtain single-cell information without loss of resolution. For this, I applied superresolution htSTORM to monitor the spatial organisation of TADs in single nuclei, and in parallel to Hi-C bulk-sample analysis.

Aim 2: Decipher differences in the organisation of mitochondrial fission.

Increasing molecular and physiological detail on the mitochondrial fission machinery has become clear over last decade, and the importance of fission for mitochondrial maintenance and thus human health is undisputed. Nevertheless, a clear picture of the distinct processes which converge at mitochondrial fission is still missing, and different research groups often found seemingly conflicting evidence. Using live and fixed cell microscopy, I assess the differences between different types of fission, and integrate the thereby gained insights into a holistic model of mitochondrial dynamics.

Aim 3: Elucidate the principles governing the organisation of mitochondrial RNA granules.

Upon transcription, mtRNA condenses into small foci, together with particular mitochondrial proteins. However, besides their existence and some of their components, not much is known about these so called mitochondrial RNA granules (MRGs). By surpassing the limit of resolution of light microscopy, I discover the spatial organisation of these foci, and determine whether they are indeed granule like. Further, I explore how MRGs form, and what processes they are capable of regulating. For this, challenges in analysis of highly mobile organelles had to be overcome. Finally, I will also discuss how MRGs and mtRNA distribution is organised within the mitochondrial network.

Aim 4: Understand the organisation of mitochondrial transcription.

Many of the molecular mechanisms involved in mitochondrial transcription are understood at atomic scale. But the spatial and temporal organisation of onset and completion of mitochondrial transcription events are largely elusive. To better understand the interplay of regulatory processes for mitochondrial

transcription, I propose live and fixed cell imaging assays, and begin to shed light on some of the organisational aspects of this initial step in mitochondrial gene expression.

Together, the work presented in this thesis provides novel insights into organisational aspects of mitochondrial biology through single-cell and single-organelle microscopy.

Chapter 2: Superresolved organisation of DNA in cancer

2.1) Organisation of nuclear DNA

DNA in the nucleus

The human genome comprises two copies of more than three billion base pairs in every single cell (GRCh38.p13, 2019). When laid out, all this DNA would span several meters. With cellular diameters on the micron-scale, it thus seems obvious that DNA must be packed as much as possible to fit into a normal nucleus. For this, there are many layers of compaction whereby nuclear DNA is first wrapped around histones, which are then assembled into chromatin. For expression, chromatin opens up to allow access for the transcription machinery (euchromatin). However, not all parts of DNA are equally important inside every single cell and at all times during a human life. Silent chromatin can therefore be further compressed for long-term storage (heterochromatin). Compression and decompression is highly regulated by specific proteins which read and write particular marks on chromatin. These proteins modulate molecular modifications such as methylation, acetylation or ubiquitination on histones. This additional layer to the DNA-sequence code allows for epigenetic regulation of gene expression. It was found that particular subdomains of DNA comprising several genes are often co-regulated in terms of their epigenetic state and thus their expression profile. Interestingly, these domains often associate in three dimensional space within the nucleus, and are called topologically associated domains (TADs) (Dixon *et al*, 2016). TADs are often conserved across cell-types and species (Dixon *et al*, 2012) and can be studied to monitor the epigenetic effect of mutations or drug treatments.

Methods to study DNA

A traditional method to study epigenetic marks is chromatin immunoprecipitation followed by next generation sequencing (ChIP-seq). In this approach, DNA fragments are cross-linked to their interacting proteins, which are then pulled down by Co-immunoprecipitation. The fragments are thereby sorted by their interaction partners, such as nucleosomes with particular histone marks. Sequencing and annotation then allows to identify the regions of a genome, enriched in particular epigenetic marks (Park, 2009).

Measuring the physical interaction between specific genetic loci inside cells was first made possible by Chromatin Conformation Capture (3C) (Dekker *et al*, 2002). For this, chromatin organisation in 3D-space is frozen at a given time-point and neighbouring DNA-stretches are cross-linked by formaldehyde treatment. The nuclear DNA is then fragmented by digestion with restriction enzymes. The small, formerly neighbouring and thus cross-linked DNA stretches are then linked and sequenced jointly, which reveals the spatial genetic interactome. This basic principle inspired a plethora of further developments. Highthroughput chromatin conformation capture (Hi-C) finally allows to infer genome wide topological association maps, even within single cells (Nagano *et al*, 2015).

DNA can also be studied more directly, through microscopy. Particular chromosomes occupy specific domains inside the nucleus, and heterochromatin preferentially associates with the nuclear periphery

(Cremer & Cremer, 2010). To study the location of particular DNA loci inside the nucleus, fluorescent in situ hybridisation (FISH) can be used to target specific DNA sequences (DNA-FISH). FISH readily allows for single-cell data, and thus to account for or study cell-to-cell heterogeneity. However, the limitations of fluorescent microscopy discussed in chapter 1.2 also apply here. For instance, the signal of a single bound fluorophore may not yield sufficient SNR to reliably identify the location of a specific locus. Additionally, hybridisation approaches are inherently noisy as recurrence of short DNA-sequences across the genome are probable, and some hybridisation mismatches can be tolerated. Therefore, aptamer-libraries against entire genes or larger loci are often used, and new techniques allow to further amplify the signal (Battich *et al*, 2013). Another limitation of fluorescence based methods is the restraint degree of simultaneously observable features due to the overlap and physical limitations of fluorescent emission spectra. Intricate techniques have been developed to expand the abilities of multiplexing in recent years, and single-cell genomics and transcriptomics now allow visualisation of up to 200 target-species in parallel (Zhuang, 2021). Methods to visualise DNA-loci in live cells are also emerging (Sato *et al*, 2020). However, these often rely on SNR-amplification through targeting of large repetitive sequences. Although, the use of quantum dots together with targeting TALEs allowed to track a single, non-repetitive nuclear locus in live cells, and holds promising potential (Ma *et al*, 2017). In addition to these limitations in SNR, and multiplexing, the resolution barrier poses another obstacle to analyse genomic loci inside cells. Here, superresolution microscopy allows to study the dimensions and shape of structures below the diffraction limit, includig TADs. Due to its supreme resolution, STORM was shown to be a suitable method in fixed cells (Boettiger *et al*, 2016). Therefore, we aimed to use htSTORM to elucidate the effect of a particular cancer mutation, and its drug-treatment on the dimensions of a human DNA TAD in lymphocytes, as described below.

2.2) EZH2 oncogenic mutations drive epigenetic, transcriptional, and structural changes within chromatin domains

The article under the title of this chapter was first published in *Nature Genetics*:

Maria C. Donaldson-Collier*, Stephanie Sungalee*, Marie Zufferey*, Daniele Tavernari*, Natalya Katanayeva, Elena Battistello, Marco Mina Kyle M. Douglass, **Timo Rey**, Franck Raynaud, Suliana Manley, Giovanni Ciriello[#], Elisa Oricchio[#] *Nature Genetics*, 2019, Vol. 51, pages 517-528, https://doi.org/10.1038/s41588-018-0338-y
*These people contributed equally to this work, [#]Corresponding author(s)

The aim of this study was to elucidate the nature of the epigenetic effects and chromatin modifications induced by a cancer associated gain-of-function mutation in the EZH2 gene. As part of the Polycomb repressor complex 2, EZH2 is the methyltransferase responsible to increase Histone 3 Lysine 27 3-methyl marks (H3K27me3) (Comet *et al*, 2016). H3K27me3 is associated with transcriptional repression, and its levels have been found to be globally increased in EZH2 Tyrosine 646 mutation bearing lymphoma cells. Therefore, several lymphoma and non-cancerous cells, with and without EZH2-mutation were analysed by

Hi-C with a resolution below 50kb. The results showed that genes within particular TADs are jointly regulated by EZH2 and thus concordantly affected by its mutation. Furthermore, an anti-cancer drug undergoing clinical trials (GSK126) could revert the effects of EZH2^{T646X}. In accordance with the biochemical data, small but statistically significant shape-changes were also found through microscopic assessment of a particular TAD spanning the genomic region between the FOXO3 and SESN1 genes. A library of DNA-FISH probes against this domain was used for htSTORM, and we found that eccentricity of this TAD was increased by GSK126 treatment (see article-figure 7i,j and article-supplementary figure 8).

Contribution

My contribution to this work comprised of devising and testing appropriate htSTORM image-acquisition conditions and protocols, image acquisition, data processing, data analysis, and data visualisation, under the supervision of K. M. Douglass.

2.3) Discussion

As discussed in chapter 1.2, achieving a high SNR for the structure of interest is crucial for quantitative microscopy. Therefore, STORM is often performed under total internal reflection (TIRF) conditions, whereby only a thin section of the sample within ~200nm of the coverslip is illuminated. This allows to increase the SNR by preventing fluorescent noise from outside of this zone. However, the nucleus of mammalian cells extends far beyond this zone. To observe TADs located anywhere in the nucleus the widefield-modality of our htSTORM set-up was essential, yet brought along increased noise and thus impractically low SNR. We reached a major breakthrough in our approach to visualise DNA-FISH stained FOXO3-TADs, when off-target signals could be reduced by the addition of salmon sperm DNA to increase the hybridisation-specificity during sample production. Another issue relevant for long image-acquisition with nanometre precision is sample-drift. We chose to rely on fiducial tracking to correct for lateral (xy) drift over the course of acquisition. However, as the focal plane to image TADs often lied far above the coverslip, finding gold fiducials stuck to nuclei on the same plane often proved difficult. Here, the large FOV of our htSTORM set-up was crucial to increase the chances to find a fiducial, and thus significantly increased our throughput.

The underlying principle of superresolution microscopy, and SMLM in particular is to separate visually inseparable fluorescent signals over time. We used visual inspection to determine good imaging conditions within the trade-off between single emitters and acquisition time. 405nm laser power was increased manually and in function of the signal observed by the experimenter. This somewhat arbitrary choice of parameters bears the risk of sub-optimal acquisition and thus raw-data quality. Today, a software-tool developed in our lab, ALICA allows for automated optimisation of signal-density via 405nm-laser increase (Štefko *et al*, 2018). However, while adaptive automation allows to optimise the quality of each acquisition independently, it hampers statistical comparison, as the sampling can no longer be considered identical. Simulations with known ground truths are also often used to determine optimal sampling. However, this requires both, good

prior knowledge of the subject, as well as a good simulation model taking into account sample-preparation, microscope specific details, and photophysics. In the future, it would be ideal if the community could devise a uniform and unbiased approach to determine ideal sampling parameters for SMLM.

Upon acquisition of large image-stacks with single-emitters, this raw-data requires heavy computational data processing to yield a final set of localisations for analysis and comparison. We used a customised MATLAB pipeline for single emitter fitting adapted to the specifics of our microscope's camera (Huang *et al*, 2013). Here, four free parameters allow to adapt the fitting-algorithm. Again, we chose parameter-values upon visual inspection of their effects. A rigorous assessment of the fluorophore-signal under given acquisition parameters could potentially yield a more reliable choice of localisation-parameters. Next, the large sets of localisations were computationally processed to produce reduced sets of drift-corrected and clustered data-points. For this, there exists a wide range of statistical or Bayesian clustering principles. While there still does not seem to be a clear consensus in the field of SMLM, DBSCAN is one of the most widely used algorithms (Khater *et al*, 2020). DBSCAN relies on only two parameters, the neighbourhood radius (h) and the number of required neighbours (Eps) (Ester *et al*, 1996). We performed a parameter-sweep to monitor the effect of varying values on the visual appearance of the clusters as well as the final cluster-descriptors (see below). We decided that a neighbourhood radius of 30, 40 or 50nm would be adequate for the EZH2-data. Again, there are no hard and unbiased criteria which allow to choose the correct set of parameters without extensive prior knowledge of the analysed object. Finally, clustered data-points were analysed to compare their shape under varying conditions. Again, there are many ways to describe the spatial dimensions of a cluster of points. We chose to use the radius of gyration (Rg) and eccentricity (Ecc), which both take the variance of the point clouds into account in multiple dimensions. Another popular descriptor of clusters is the convex hull, which however is sensitive to outlier localisations. We found no significant difference between the samples for Rg. A significant difference in comparison of GSK-treated cells with untreated cells became apparent when outlier clusters with low or very high number of localisations were removed, and with h = 30nm (see Article Figure 7j).

The difficulties of analysing subtle differences between the three-dimensional re-arrangement of TADs by STORM may have several reasons. An inherent challenge in the study of shape- and size-changes of three dimensional objects is the dimensionality itself. While TADs are three dimensional objects, we used 2D-microscopy to infer their shape. This induces a large variability of the shape-descriptors owed to the dimensionality-reduction. Extremely large changes in object-volumes would be required to produce a small difference in two-dimensional projections. Therefore, if I were to design a SMLM project to investigate the dimensions of a 3D-object in the future, I would aim to use one of the many 3D-imaging approaches. Together, the results presented in this chapter highlight the power, as well as the limitations and challenges in SMLM and htSTORM to study the three dimensional shape and size of DNA *in situ*.

Interlude: What is organised?

Organisation describes the intrinsic purpose of a process or object. Randomness is without aim. To classify behaviour and objects as either organised or random, one can assess their predictability. Organised processes are anticipatable as opposed to arbitrary behaviour, which is considered random. Organised objects have recurrent, and thus anticipatable features, shapes or behaviour. These attributes cannot be anticipated for random objects. As an example, mitochondrial inner membranes are organised as cristae, but the exact size of an isolated cristae cannot be predicted, and thus appears to be random. Natural scientists are obsessed with the search for patterns, and after measuring the size of many cristae it is likely one could devise a statistical model to associate probabilities to predict the observation of particular sizes. Patterns can then be viewed as indicators of organisation, and of the purpose of ones subject of study, which for biologists is life. In a deterministic view there is no randomness, only unidentified sources of errors.

Dynamics describes the behaviour of a particular object over time. For an object to be considered dynamic, it needs to change during a relevant interval of time. It is also important to specify the spatial frame of reference within which one assesses its behaviour. For example, a mitochondrion can dynamically change its position within a cell over the course of seconds to minutes. But if the entire cell moves with the mitochondrion inside, this motion should not be accounted to the mitochondrion. An object is stable when it does not change its velocity or speed, it is static when it does not move. In the context of molecular biology and biophysics, stable or directed motion, and static behaviour are often considered indicative of organisation, as opposed to random diffusion.

3) Organisation & dynamics of mitochondria

3.1) Mitochondrial dynamics

Mitochondrial morphology

Mitochondria occur in various shapes and sizes, ranging from small and round to very long and branched tubules, depending on the cellular context (Giacomello *et al*, 2020). The variable length and number of branches of individual mitochondria, as well as the varying degree of interconnections of mitochondria to form large networks have triggered much scientific interest. To compare mitochondrial networks, these are often classified as tubular, fragmented, or hyperfused, and network morphologies have been associated with disease ((Nunnari & Suomalainen, 2012; Chan, 2020; Zahedi *et al*, 2018)), cellular metabolism (Wai & Langer, 2016; Mishra & Chan, 2016), cell cycle (Kanfer & Kornmann, 2016; Horbay & Bilyy, 2016), and cell types (Kuznetsov *et al*, 2009). However, a clear understanding of the direct and causal links between mitochondrial morphology and mitochondrial function is often missing.

Mitochondrial dynamics

To adapt the mitochondrial network topology, individual mitochondria can undergo fusion and fission. Together, these two counteracting behaviours are referred to as mitochondrial dynamics, and tuning of their respective frequency defines the overall network morphology (Tilokani *et al*, 2018). Additionally, mitochondria are motile within cells, and they can even be transferred between neighbouring cells (Levoux *et al*, 2021). However, much of the current knowledge has been established in cell culture experiments and the relevance of mitochondrial dynamics *in vivo* and in differentiated cell-types is a matter of contemplation. Yet, many of the key molecular players involved in mitochondrial dynamics are essential for human health and embryonic development(Tilokani *et al*, 2018). Thus, to elucidate the cellular mechanisms and regulatory pathways behind mitochondrial organisation and dynamics will help to better understand these diseases and to find new avenues for their treatment.

Molecular mechanism of mitochondrial fission

The detailed molecular machinery necessary for mitochondrial fission as well as parts of the regulatory pathway have become well understood. To induce fission, dynamin related protein 1 (Drp1) assembles at prospective fission sites on the outer membrane of mitochondria (Smirnova *et al*, 2001). The multimerisation into constricting helices then drives the division of mitochondria in a GTP-dependent manner (Fröhlich *et al*, 2013; Ingerman *et al*, 2005; Mears *et al*, 2011; Kalia *et al*, 2018). For this, the fission machinery needs to overcome an energy barrier, which can be defined by membrane tension and bending energy (Mahecic *et al*, 2020a). Finally, dynamin 2 has been proposed to be involved in the ultimate step of OMM scission (Lee *et al*, 2016), albeit it appears to not be required (Fonseca *et al*, 2019; Kamerkar *et al*, 2018). Drp1 clusters on the OMM are curvature sensitive, and pre-constriction of mitochondria leads to their accumulation at prospective fission sites (Ji *et al*, 2015). Upstream of Drp1 recruitment, the ER has been found to mark prospective

fission sites (Friedman *et al*, 2011), and actin has been suggested as an essential driving force for mitochondrial fission (Ji *et al*, 2015). Interestingly, cycling actin wave-fronts were found to correlate with probability of fission (Moore *et al*, 2016), as well as to propel small mitochondria across the cell (Moore *et al*, 2021). It thus comes with little surprise that several actin interacting and organising proteins have been associated with ER-dependent mitochondrial fission, and some of these propose a connection between Calcium signalling and mitochondrial fission (Korobova *et al*, 2013; Manor *et al*, 2015; Korobova *et al*, 2014; Rehklau *et al*, 2017; Chakrabarti *et al*, 2018; Fung *et al*, 2019; Yang & Svitkina, 2019). Unfortunately, many of the conclusions are based on assessment of overall mitochondrial morphology, and upon physiological perturbations, such that direct observations of the interplay between actin, ER, calcium and mitochondrial fission in unperturbed live cells are often missing. In addition to the ER and actin, Drp1 also interacts with protein co-factors on the OMM. These are involved in specific Drp1-recruitment, and in mammalian cells comprise of Mff (Otera *et al*, 2010), Mid49/51 (Palmer *et al*, 2011) and Fis1 (Mozdy *et al*, 2000). However, conflicting evidence has been hampering the identification of the exact role and mechanism of each of these adaptors under physiological conditions (Osellame *et al*, 2016). Particularly, whether Fis1 is truly involved in the regulation of mitochondrial fission is under debate, and its absence has been shown to not affect mitochondrial network morphology (Otera *et al*, 2016).

Proposed purpose of mitochondrial fission

Two major functional roles for mitochondrial fission have been proposed. On one hand, mitochondria are believed to not be able to form *de novo* but to depend on expansion of existing organelle populations. Mitochondrial fission is thus required to create offspring mitochondria from existing parents. Indeed, it has recently been shown that replication of mtDNA spatially correlates with ER-associated mitochondrial division (Lewis *et al*, 2016). This distributes the replicated DNA into the two sibling mitochondria, and newly replicated mtDNA remains associated with mitochondrial tips for up to two days (Lewis *et al*, 2016). On the other hand, turnover of mitochondria and their content requires degradation and recycling in autophagosomes. This process has been termed mitophagy, and can be mediated by the Pink1/Parkin pathway (Pickles *et al*, 2018). Fission is necessary but not sufficient for mitophagy, as fissioned mitochondria need to be depolarised to prevent escape from degradation through re-fusion to the network (Twig *et al*, 2008; Burman *et al*, 2017). Both, proliferation as well as degradation depend on Drp1. The overlapping molecular machinery, and which regulatory mechanism could distinguish the two opposing outcomes of fission, has created much speculation. In the work described in this chapter, we establish a framework to decipher the individual roles and regulatory pathways which govern mitochondrial turnover. We also resolve particular conundrums and disentangle the overlapping mechanisms which allows to explain the seemingly contradictory nature of previous experiments and observations.

3.2) Distinct fission signatures predict mitochondrial degradation or biogenesis.

The manuscript under the title of this chapter was first published in *Nature*:

The aim of this study was to comprehend how opposing lines of evidence for the importance of fission in mitochondrial proliferation, and degradation can be integrated into a holistic model. Accurate regulation of mitochondrial fission is important to prevent human disease including cancer (Ma *et al*, 2019), and Parkinson's (Wang *et al*, 2016), and an understanding of the underlying regulatory mechanisms will provide grounds for improved treatment of such diseases in the future. For this, several thousands of mitochondrial fission events were analysed in multiple mammalian and human cell types. This led to the discovery that mitochondrial fissions can be classified into two distinct groups: *peripheral fissions*, which take place near the mitochondrial tips, within the first 25% of a particular mitochondrion's length; and *midzone fissions*, which occur around the centre of a mitochondrion. This geometric classification of mitochondrial fission sites provided us with a framework to disentangle the different molecular and functional pathways associated with mitochondrial fission.

In agreement with our expectation from Drp1 as a universal hallmark for mitochondrial fission, we found it to accumulate on both types of mitochondrial fission. However, altered mitochondrial physiology marked by a drop in membrane potential or a significant rise in calcium preceded peripheral but not midzone fission. On the contrary, previously described ER and actin association with mitochondrial fission sites could only be confirmed for midzone, but not peripheral fissions. We then used the geometric classification to disentangle the opposing outcomes, downstream of mitochondrial fission. We found, small mitochondria shed from peripheral fissions do not refuse with the rest of the mitochondrial network and are destined for mitophagy via Parkin and LC3 association. These small peripheral mitochondria often contain no genetic material and particularly few replicating nucleoids. Only upon UV-damage, mtDNA accumulated in these small parts destined for degradation. Midzone fission rates on the other hand was increased by promotion of cellular proliferation, further supporting their functional role in mitochondrial biogenesis. Finally, we resolved the long-standing conundrum around disputed compensatory effects of different adaptor proteins. We found that Mff is important for midzone, and thus replication associated fission. Fis1 on the other hand was previously reported to have little effect on overall mitochondrial morphology (Koirala *et al*, 2013). We show that Fis1 is involved in regulation of peripheral fission, and to be functionally important under stressful conditions.

Contribution

My main contributions to this study comprised of image acquisition, and image analysis including the design of experimental procedures, protocols, and analysis pipelines (MitoSox, mitoQ, TMRE-picoGreen,

FASTKD2-eGFP, TWINKLE-eGFP, BrU-foci count, actin, Inf2), and in close collaboration and constant exchange with T. Kleele and other members of our laboratory.

3.3) Discussion and outlook

The work presented in this chapter represents a breakthrough in our understanding of the regulatory pathways and different functions of mitochondrial fission. It provides a framework to integrate existing knowledge as well as future studies, and to decipher single-organelle behaviour. Much of the current knowledge is based on whole-cell analysis, network-states, and perturbations such as knock-downs or drug treatments. However, imperfect differences and statistics are often ignored or attributed to experimental errors in bulk-analysis. Thanks to recent advances in superresolution imaging techniques (Jakobs *et al*, 2020) we were able to investigate organelle biology at the level of single organelles. This is important to foster our understanding of the mitochondrial network as a dynamic system of individual, and only partially dependent units, similar to the ongoing paradigm shift in single cell and systems biology. I will highlight our advancements by discussing our updated view of a specific aspect of the fission-machinery, the role of ER and actin.

Role of actin and ER

In 2005, mitochondrial fragmentation upon drug treatment was found to depend on Drp1 and F-actin (De Vos *et al*, 2005). Later, 75% of Drp1-puncta on mitochondria were found to stably associate with ER over the course of two minutes (Friedman *et al*, 2011). A connection between ER and actin was proposed upon the identification of the ER-associated form of an F-actin interacting formin, INF2 (INF2-CAAX) through knock-down and rescue experiments (Korobova *et al*, 2013). A mitochondria-associated formin, Spire1C was then identified to recruit actin in over-expression and knockdown studies (Manor *et al*, 2015). However, mitochondrial fission and Drp1 accumulation still occurred without Spire1C, or INF2 (Manor *et al*, 2015; Korobova *et al*, 2013). A recent report suggests that two different populations of actin may be recruited to mitochondria, of which one depends on INF2 and thus ER, whereas the other is proposed to depend on mitochondrial depolarisation, and Arp2/3 (Fung *et al*, 2019). The same group also found that drug-induced actin polymerisation leads to an INF2-dependent mitochondrial calcium spike, and suggested that Ca^{2+} ions may act as a messenger molecule between ER and mitochondria during fission (Chakrabarti *et al*, 2018). Controversially, a recent electron microscopy study could not find Arp2/3 complexes at mitochondrial constriction sites, albeit a morphologically distinct and tip-associated actin population was observed apart from INF2-associated actin (Yang & Svitkina, 2019). Our results confirm that both, ER and F-actin accumulate at midzone fission sites in unperturbed cells. However, we did not find F-actin or ER particularly enriched at peripheral fissions, which provides a biological explanation for why mitochondrial fission and Drp1-foci could still be observed in knock-down experiments. Furthermore, to test whether INF2 is also preferentially associated with midzone fission, and thereby likely regulates the F-actin accumulation, we overexpressed different fluorescently tagged INF2-constructs. Unfortunately, we could not establish a

suitable transfection protocol (see **Fig. 8**). However, the observed reduction of midzone fission in siINF2-treated cells is supportive of distinct roles for INF2 in different types of mitochondrial fission. In the future, our geometrical framework could also allow to test whether Arp2/3, and a different type of actin assembly is associated with peripheral fission and thus mitophagy. Another explanation for the accumulation of actin at mitochondrial poles could be the recently discovered propelling function of actin (Moore *et al*, 2021). The investigation of actin-recruiting drug effects on midzone and peripheral fissions respectively could help to better comprehend the role of calcium as a signalling molecule. Furthermore, the role of mysoin II in either proliferative or mitophagic mitochondrial fission could be investigated using our geometrical framework.
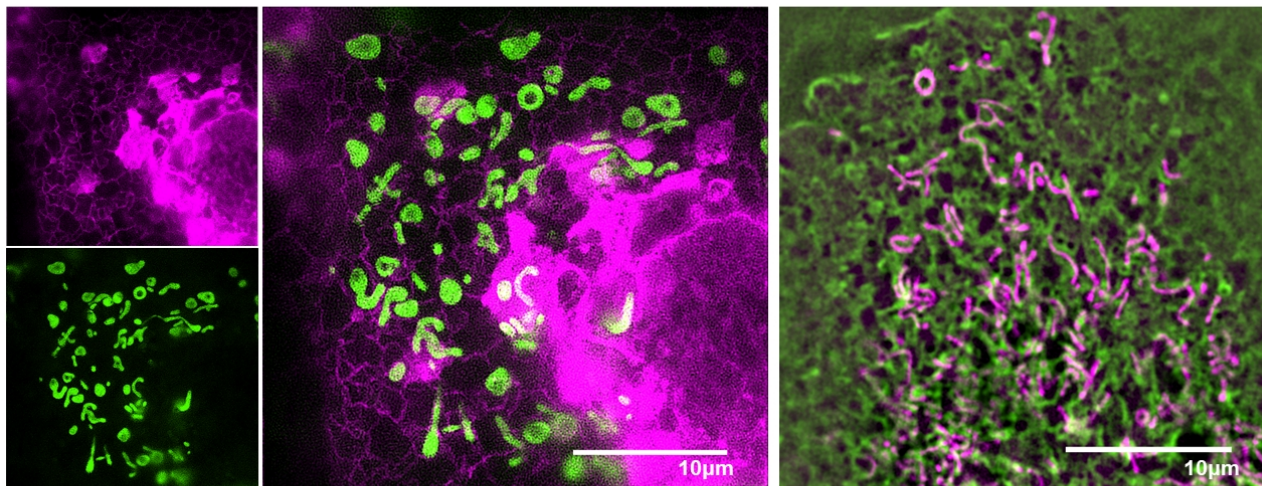

Figure 8: Exemplary SIM images from INF2 over-expression experiments. Left, COS7 cell transfected with mito-GFP (green) and INF2-mApple (magenta) constructs. Large aggregates of INF2, particularly in the perinuclear region indicate over-expression artefacts. Right, COS7 cells transfected with mito-Scarlet (magenta) and INF2-eGFP (green) shows faint INF2 signal everywhere in the cell, which makes it difficult to quantitatively assess ER-mitochondria overlaps based on the INF2 and mito signals.

Conclusion

Together, our results allow to draw an improved and holistic model for the interconnected pathways of mitochondrial fission and its machinery (see **Fig. 9**). Originally, a major limitation of our study was the use of siRNA knock-down technique. Knock-downs are often incomplete, and the degree of the effect in a particular cell which is analysed, is unknown. In further experiments, we replicated our siRNA-based experiments to investigate the different roles of adaptor-proteins using CRSPR/Cas9 knock-out cells. These experiments showed the same effects as previously observed in knock-downs, and therefore provide further evidence for our below proposed model (see **Fig.9**). Another limitation stems from the natural arrangement of mitochondria. Within mammalian tissue-culture cells, most of the mitochondria lie around the nucleus (perinuclear region). Here, individual mitochondria are often difficult to segment, even in superresolution microscopy, because they are often stacked above and below each-other. Therefore, typical single-organelle analysis is biased towards uniplanar, and well resolvable mitochondria, which often lie in the cellular periphery. Whether there are biological differences between perinuclear, and peripheral mitochondria regular

tissue-culture cells is currently unknown, though examples from polarised cells indicate that distinct populations exist in these cell types (Porat-Shliom *et al*, 2019).

One major draw-back of fluorescence microscopy is the loss of non-explicit context. While the exact relationship between mitochondrial behaviour and the cell cycle is still elusive, mitochondrial fragmentation via Drp1 at entry to mitosis is a well established phenomenon (Taguchi *et al*, 2007). In our experiments, we are agnostic to the cell cycle. In the future, it could be interesting to further investigate the relationship between mitochondrial turnover in different cell cycle phases. For instance, mitochondrial replication has been found to predominantly occur during S-phase (Sasaki *et al*, 2017). It would be interesting to determine whether midzone fission is augmented in S-phase as well, and whether this is already part of the fragmentation procedure towards mitosis, or if it is counteracted by augmented mitochondrial fusion. Whether mitochondrial quality control through peripheral fission is confined to a specific cell-cycle phase such as G1 could be another hypothesis to test.
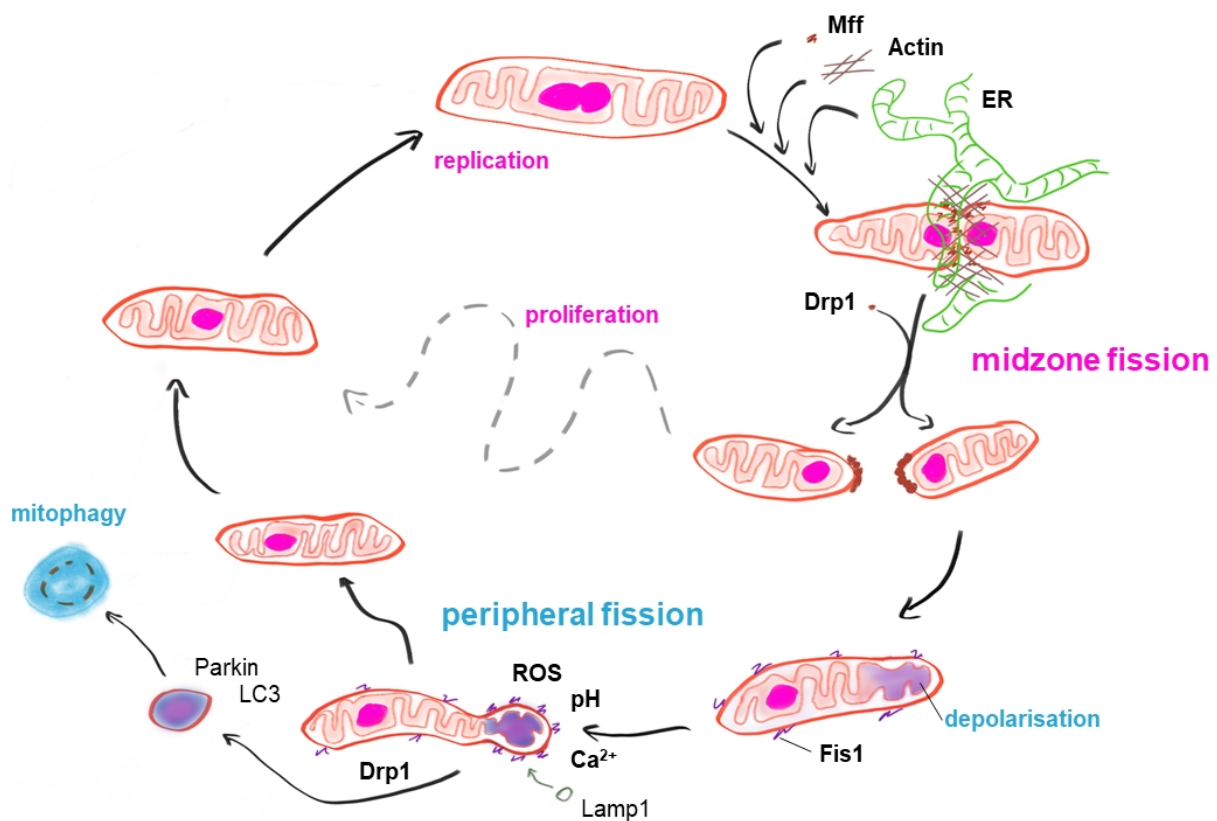

Figure 9: Holistic model for mitochondrial fission. Upon replication of mtDNA (magenta), Mff, actin and ER are recruited. These mark prospective fission sites by pre-constriction of the mitochondrial tubule, and recruit Drp1 for midzone fission. Midzone fission allows for proliferation of mitochondria, which can undergo further cycles of fusion and replication. Fis1 accumulation at depolarised mitochondrial poles on the other hand, is accompanied by a drop in pH, rise of Calcium and inccreased ROS, and leads to peripheral fission by Drp1. Peripheral fission is supported by lysosome contacts (Lamp1), and leads to degradation via Parkin-mediated mitophagy.

Outlook and open questions

While this work sets the framework to understand many of the molecular steps in mitochondrial fission, the upstream signalling and mechanic triggers remain unclear. In particular, the temporal relationship between events is not well investigated. For midzone, and proliferative fissions it is unknown whether mtDNA replication is the trigger to recruit ER or actin or vice-versa. Furthermore, whether actin accumulates before ER-mitochondrial overlap stabilisation, or after has not been assessed in unperturbed live cells. Given the theoretical duration of more than 60min for one mitochondrial replication cycle, it is likely that either replicated mtDNA or the replication machinery triggers the recruitment of the fission-machinery. However, how this internal event could be communicated to the mitochondrial environment remains elusive. Here, investigations of perturbation-effects on midzone-fission frequency instead of binary assessment of fission-occurrence, or network topology could allow fruitful insights. When and how mtDNA-replication is induced, and whether this is selective or stochastic represents yet another avenue to investigate, upstream of mitochondrial fission. Furthermore, whether there are other sub-types of mitochondrial fission could be investigated, and whether all midzone fissions are preceded or followed by mtDNA replication could be a good starting point. Alternatively, the effect of cellular stress on fission-routes could be further elucidated in the future. Similarly, whether and how mitochondria selectively target defective material including mutant mtDNA for mitophagy still poses a major conundrum in the field. To focus on peripheral fission could help to better disentangle these events. In our observations, we found Drp1, Ca^{2+}, Lamp1, and LC3 were all recruited or altered within the last one to two minutes prior to peripheral fission. Only TMRE indicated that membrane potential is already decreased prior to these late-stage fission events. Long-term imaging should be performed to better understand the sequence of upstream events preceding mitochondrial fission. To find a better way to directly monitor the defective material such as mutated mtDNA in live cells will be crucial to test the hypothesis of selective degradation in the future. Finally, the interplay between mitochondrial quality control and cellular states (Kimura *et al*, 2014), as well as organelle-cell communication pathways (Mottis *et al*, 2019) are important to understand, for a better approach to treat human disease. Additionally, particularities of *in vivo* and cell-type specific processes should be investigated. For this, neurons provide an excellent experimental system with slow mitochondrial turnover, and very clear delivery routes to allow holistic single-organelle tracking.

4) Organisation & dynamics of mitochondrial RNA

4.1.1) Mitochondrial RNA

Definition of mtRNA

Mitochondrial RNA (mtRNA) comprises all RNA found inside the matrix of mitochondria. Whether RNA is efficiently transported into and out of mitochondria in humans is still subject to controversial debate. For a recent review arguing for nuclear transcript (nRNA) relocation to mitochondria, see (Jeandard *et al*, 2019). To my knowledge however, no IMM RNA-import system has been identified in humans, and evidence for biologically relevant mitochondrial matrix localisation of nRNA is inconclusive. Therefore, I will use the term "mtRNA" to describe the transcripts of mtDNA throughout this thesis, albeit the key conclusions of this chapter do not depend on the presence or absence of nRNA in the mitochondrial matrix.

Production of mtRNA

RNA-transcription inside mitochondria occurs in both senses, from the heavy as well as the light template-strand of mtDNA. Unlike in the nucleus, mitochondrial genes are transcribed as long, polycistronic RNA. A single light strand promoter (LSP) lies just upstream of OriH and produces one long transcript comprising eight tRNAs and one mRNA, which encodes the ND6-protein. The other mtDNA genes comprising two rRNAs, 12 mRNAs and 14 tRNAs are transcribed from a heavy strand promoter (HSP) in the opposite direction, and just upstream of the LSP. The biological relevance of a second heavy strand promoter (HSP2) is still under debate (Bouda *et al*, 2019). The two-promoter model suggests that 12S and 16S could be transcribed independently from the rest of the heavy-strand genes. This is in good accordance with the 15-60x higher steady-state levels of mitochondrial rRNAs compared to mRNAs. However, old evidence suggests that augmented steady-state levels are reflective of the higher stability of rRNAs, and does not necessarily require increased production (Bouda *et al*, 2019).

Processing of mtRNA

Mitochondrial transcripts contain no introns, and thus no splicing is required before translation. However, individual mRNAs, rRNAs and tRNAs must first be separated before they can fulfil their respective functions. Interestingly, mRNAs and rRNAs on the polycistronic transcripts are typically flanked by two tRNAs at the 5'- and the 3'-end respectively. The folding of tRNAs is thought to then allow enzyme-assisted nucleolytic cleavage at their 3'- and 5'-ends. This so called 'tRNA punctuation model' involves the RNaseP protein complex for 5'- and RNaseZ for 3'-excision of rRNAs and mRNAs (Barchiesi & Vascotto, 2019). Nevertheless, there remain a few exceptions to this rule. COXI-mRNA for instance is flanked with non-coding RNA (ncRNA) at its 5'-end, as is ND6-mRNA at its 3'-end. ND5, CytB and COXIII also lack a punctuating tRNA, and the detailed mechanism for the non-canonical mtRNA-separation is still unknown today.

Modification of mtRNA

Maturation of mtRNA allows to further modify and regulate the different RNA-molecules upon transcription. The attachment of polyA-tails by the mitochondrial adenosine polymerase (mtPAP) is the only common modification for mRNAs, and can lead to either stabilisation (COXI-III) or destabilisation (ND1&2) of these. Both rRNAs and tRNAs undergo various base-modifications including pseudouridinylation, and methylation, which confer their structure and functionality (Pearce *et al*, 2017; Rebelo-Guiomar *et al*, 2019).

Purpose of mtRNA

After processing and modification, fully matured mitochondrial rRNA, tRNA and mRNA are used to translate some of the core subunits of the OXPHOS protein-complexes. 16S and 12S rRNA are assembled into the large and the small subunit of the mitochondrial ribosome, together with 82 proteins (Greber & Ban, 2016). It is notable that all proteins involved need to be imported into the matrix first. A unique feature of the mitochondrial ribosome is the incorporation of a specific, mitochondrially encoded tRNA (tRNA^{Val} in humans) instead of a small 5S rRNA, as common for other known ribosomes (Amunts *et al*, 2015). This tRNA fulfils the structural role within the central protuberance, and thereby mediates the association between the large and the small ribosomal subunits (Greber *et al*, 2014; Amunts *et al*, 2015). A large pool of readily available, mature and charged tRNAs is then required for efficient translation of a single mRNA, being read by a fully assembled ribosome. It is interesting to note that a potential role and function of non-coding light or heavy strand transcripts inside mitochondria is still under-explored (Kotrys & Szczesny, 2019).

Degradation of mtRNA

To allow quality-control and turnover, mtRNA is regularly degraded, and has an average half-life of about 45min (Iborra *et al*, 2004). The hSUV3-helicase and the PNPase have been found to cooperatively regulate mtRNA degradation (Borowski *et al*, 2013). For this, they assemble into protein-protein-association dependent foci and form degradosomes (D-foci). Interestingly, at the beginning of its life, mtRNA has also been found to assemble into distinct, and small foci (Iborra *et al*, 2004). Only about 18% of D-foci co-localise with nascent-RNA foci, and ~24% of D-foci associate with nucleoids directly, and almost 50% of the degradosomes are dispersed throughout the matrix, apart from mtRNA- and mtDNA accumulations. To counteract PNPase mediated degradation a RNA-binding pentatricopeptide repeat (PPR) protein, LRPPRC stabilises mitochondrial mRNA in a complex with a protein called SLIRP (Chujo *et al*, 2012). Additionally, many other factors have been found to impact the stability of mtRNA with varying specificity for particular RNAs (Rebelo-Guiomar *et al*, 2019). While LRPPRC shows a rather uniform distribution within the mitochondrial matrix, others accumulate at mtRNA-foci, which have now been termed mitochondrial RNA granules (MRGs), and will be discussed in more detail in the next chapter.

4.1.2) Mitochondrial RNA granules

History of MRGs

Newly transcribed RNA can be visualised by immunostaining against incorporated bromo-labelled Uridine (BrU), and was first applied in the nucleus (Jackson *et al*, 1998; Iborra *et al*, 1998). In 2004, the distribution of Br-decorated nascent transcripts was assessed in mitochondria for the first time. Iborra and his colleagues found that mtRNA forms distinct foci inside mitochondria upon short (20min) pulses of BrU-incubation, and in contrast to a model where nascent mtRNA would diffuse freely in the mitochondrial matrix immediately upon transcription (Iborra *et al*, 2004). BrU-foci lie adjacent to nucleoids initially, but become randomly spaced in the cell after longer pulses (60min). However, neither Iborra nor his colleagues followed up on the nature of mitochondrial RNA-foci. While accumulation of mitochondrial proteins into peculiar foci was observed, it took nine years to connect intra-mitochondrial foci of an RNA-binding protein, with mtRNA-foci (Jourdain *et al*, 2013; Antonicka *et al*, 2013). Since then, many additional mitochondrial proteins were assessed, and sometimes found to form co-localising foci. The term Mitochondrial RNA Granules, or MRGs was coined to describe these RNA-protein (RNP) accumulations inside mitochondria (Jourdain *et al*, 2016).

Components of MRGs

The original criterion of an MRG-component was to show observable accumulation at BrU-foci, though the BrU-pulse varied between experiments (Iborra *et al*, 2004; Jourdain *et al*, 2013; Antonicka *et al*, 2013). The first protein identified as a MRG-protein was GRSF1. 88% of BrU-foci were found to co-localise with overexpressed GRSF1-HA using immunofluorescence microscopy, though endogenous GRSF1 also forms foci (Jourdain *et al*, 2013). Another mitochondrial protein, FASTKD2 shows similarly high enrichment. Co-localisation of endogenous FASTKD2 was reported with >80% of BrU-foci, as well as with GRSF1 (Antonicka & Shoubridge, 2015). GRSF1 and FASTKD2 have since become established as *bona fide* markers for MRGs, and are often used in microscopy-based co-localisation assays, or as baits in pull-down experiments.

Today, the list of microscopically confirmed MRG-proteins has grown to 28 (see Table 1). Not surprisingly, all of these proteins are involved in mitochondrial gene expression. Nevertheless, they fulfil diverse functions, and while most interact with mtRNA directly, some structural ribosomal proteins are also associated with MRGs. The association of D-foci with MRGs is not very clear, and PNPase and hSUV3 are usually not counted as MRG-components (Pearce *et al*, 2017). For ELAC2 conflicting reports and inconclusive evidence make its accumulation in MRGs disputable (Brzezniak *et al*, 2011; Bogenhagen *et al*, 2014). Other examples show distinct accumulation in foci but were not tested for co-localisation with MRG-components (Bogenhagen *et al*, 2014). Unfortunately, published work often omits evidence for non-accumulating proteins. Additionally, exclusion of mitochondrial matrix-components from MRG-volumes has not been tested thus far, and to draw a complete picture of MRG-association remains difficult.

protein name(s)	described in
DDX28	(Antonicka & Shoubridge, 2015; Zaganelli *et al*, 2017; Tu & Barrientos, 2015)
DHX30	(Antonicka & Shoubridge, 2015)
ERAL1	(Zaganelli *et al*, 2017)
FASTK (mito)	(Jourdain *et al*, 2015; Zaganelli *et al*, 2017)
FASTKD1	(Zaganelli *et al*, 2017)
FASTKD2	(Jourdain *et al*, 2015; Antonicka & Shoubridge, 2015; Zaganelli *et al*, 2017)
FASTKD5	(Antonicka & Shoubridge, 2015; Zaganelli *et al*, 2017)
GRSF1 (iso1)	(Jourdain *et al*, 2015; Antonicka & Shoubridge, 2015; Zaganelli *et al*, 2017)
METTL15	(Antonicka *et al*, 2017)
MRPL47	(Zaganelli *et al*, 2017)
MRPP1	(Jourdain *et al*, 2013; Rackham *et al*, 2016)
MRPP2	(Jourdain *et al*, 2013; Rackham *et al*, 2016)
MRPP3 (KIAA0391)	(Jourdain *et al*, 2013; Rackham *et al*, 2016; Zaganelli *et al*, 2017)
MRPS7	(Zaganelli *et al*, 2017)
MRPS9	(Zaganelli *et al*, 2017)
MTERFD1	(Antonicka *et al*, 2017)
MTPAP	(Wilson *et al*, 2014)
NGRN	(Antonicka *et al*, 2017)
NLRX1	(Singh *et al*, 2018)
NOA1 (c4orf14)	(Zaganelli *et al*, 2017)
PTCD1	(Zaganelli *et al*, 2017)
PTCD2	(Zaganelli *et al*, 2017)
RPUSD3	(Antonicka *et al*, 2017; Zaganelli *et al*, 2017)
RPUSD4	(Antonicka *et al*, 2017; Zaganelli *et al*, 2017)
TFB1M	(Zaganelli *et al*, 2017)
TRUB2	(Antonicka *et al*, 2017; Zaganelli *et al*, 2017)
TWINKLE	(Hensen *et al*, 2019)
WBSCR16	(Antonicka *et al*, 2017)

D-foci:

PNPase (PNPT1)	(Borowski *et al*, 2013; Zaganelli *et al*, 2017)
hSUV3 (SUPV3L1)	(Borowski *et al*, 2013; Zaganelli *et al*, 2017)

Mitochondrial foci:

ELAC 2	(Bogenhagen *et al*, 2014; Zaganelli *et al*, 2017)
MRPL13	(Bogenhagen *et al*, 2014)
MRPS17	(Bogenhagen *et al*, 2014)
MRPS15	(Bogenhagen *et al*, 2014)
MRM1	(Zaganelli *et al*, 2017)
MRM2 (FTSJ2)	(Zaganelli *et al*, 2017)
MRM3 (RNMTL1)	(Lee *et al*, 2013; Zaganelli *et al*, 2017)

No foci:

AFG3L2	(Zaganelli *et al*, 2017)
CH60 (HSPD1)	(Zaganelli *et al*, 2017)
CHCHD3 (MIC19)	(Zaganelli *et al*, 2017)
CHCHD7 (COX23)	(Zaganelli *et al*, 2017)
GFM1	(Zaganelli *et al*, 2017)
MRPL10	(Bogenhagen *et al*, 2014)
MRPL12	(Antonicka *et al*, 2013)
MRPL45	(Zaganelli *et al*, 2017)
MRPS16	(Zaganelli *et al*, 2017)
MTERF2	(Zaganelli *et al*, 2017)
mtIF3	(Zaganelli *et al*, 2017)
NSUN4	(Zaganelli *et al*, 2017)
OXA1L	(Zaganelli *et al*, 2017)
PARK7	(Zaganelli *et al*, 2017)
PDE12	(Zaganelli *et al*, 2017)

PTCD3	(Zaganelli *et al*, 2017)
PUS1	(Zaganelli *et al*, 2017)
PUSL1	(Zaganelli *et al*, 2017)
REXO2	(Zaganelli *et al*, 2017)
SND1	(Zaganelli *et al*, 2017)
TACO1	(Zaganelli *et al*, 2017)
YARS2	(Zaganelli *et al*, 2017)
YBEY	(Zaganelli *et al*, 2017)
YMEL1 (OPA11)	(Zaganelli *et al*, 2017)

Table 1: List of currently known protein-components of MRGs, verified by microscopy, and published in peer-reviewed scientific articles. The lower part of the table lists proteins where accumulation in foci was observed but not assessed for co-localisation with known MRG-components followed by candidate proteins where no accumulation was found.

Dynamics of MRGs

Apart from their molecular components not much is known about MRGs as individual entities. MRG-association with nucleoids upon transcription, and randomisation of the spacing to nucleoids over time was first described by F. Iborra (Iborra *et al*, 2004) and later confirmed (Jourdain *et al*, 2013). However, whether MRGs move inside mitochondria, or whether they are re-distributed through mitochondrial dynamics has not been assessed. Also, the life-time of MRGs and whether a single granule could repeatedly take up new rounds of synthesized RNA has not been investigated. It is thus unknown when, and where MRGs disassemble. The BrU-signal in ECV304 (or T24) cells decays exponentially during non-labelled Uridine chases, and with a half-life ($t_{1/2}$) of 45min (Iborra *et al*, 2004), and in 143B cells BrU-foci disassemble with a $t_{1/2}$ of 50min (Jourdain *et al*, 2013). Interestingly, BrU-foci longevity can be enhanced by knockdown of GRSF1, while GRSF1-accumulation depends on continuous mitochondrial transcription (Jourdain *et al*, 2013). Unfortunately, other MRG-components have not been analysed with respect to their interdependency.

Proposed functions for MRGs

In accordance with the known roles of MRG-proteins in mitochondrial gene expression, diverse processes have been proposed to take place inside MRGs (Antonicka & Shoubridge, 2015; Jourdain *et al*, 2016). In analogy to the nucleus where the nucleolus forms a membraneless compartment at rRNA genes essential for ribosome-biogenesis a view of MRGs as "mitochondrioli" has been suggested (Barrientos, 2015). However, in mitochondria all genes are transcribed from the same locus, and it is difficult to imagine MRGs as pure ribosome assembly factories. Furthermore, not all ribosomal proteins accumulate in MRGs (Zaganelli *et al*, 2017). Another hypothesis suggests that only mtRNA processing, maturation and initial steps of mitoribosome assembly take place inside MRGs. In support of this hypothesis, a recent report has found mitochondrial translation to occur apart from MRGs (Zorkau *et al*, 2020). It also provides an explanation for how OXPHOS-complexes can be distributed throughout the mitochondrial network despite their confinement to particular cristae upon translation (Wilkens *et al*, 2013). However, what does happen within MRGs is still not answered, and it remains unclear what functionality the accumulation of mtRNA, and a subset of mitochondrial proteins into MRGs may serve.

Mysteries and peculiarities of MRGs

A large variety of RNA-protein (RNP) foci have been observed outside of mitochondria, throughout the cytosol and inside the nucleus. These granules range from small stress granules (SGs) which sequester and protect cytosolic mRNA during cellular stress (Buchan & Parker, 2009), to large nucleoli which structure the stages of ribosome production (Lafontaine *et al*, 2021). It is tempting to draw parallels between such cellular RNP-granules and MRGs, albeit there are a number of peculiarities about granules that are trapped inside a narrow organelle. Cytosolic granules typically reach micron sized diameters, and draw their components from a vast pool of protein and RNA. MRGs on the other hand, reside within mitochondria, and are limited to the proteome and nascent transcripts available within their host. Furthermore, diffusion inside mitochondria is obstructed by cristae (Dieteren *et al*, 2011), and it is currently unknown to how fast and to what size MRGs can grow. Depending on their size and shape, it would further be questionable whether MRGs could move freely between cristae, or whether they would be confined to cristae-devoid spaces, as has recently been observed for nucleoids in live cells (Stephan *et al*, 2019). Therefore, it would be interesting to know size and shape of MRGs, which could also help to understand whether they are really granule-like structures. In the contrary, cytosolic RNPs can themselves be rapidly transported along the cytoskeleton to reach their destination (Kiebler & Bassell, 2006). The hindered diffusion inside mitochondria also affects imported proteins in their search of specific targets, which for mtRNA can be a single copy anywhere inside the matrix. Depending on their size, and material properties, MRGs could be hypothesised as a net to catch enzymes, and decrease their search-radius to the granule-interior.

Mature mtRNA remain stable for up to several hours (Chrzanowska-Lightowlers *et al*, 1994). This is in stark contrast to the rapid turnover of BrU-foci with half-lives below one hour (Jourdain *et al*, 2013). Whether MRGs could exchange their RNA and persist for longer, has not been assessed. Similarly, while RNA-FISH against ND6-mRNA and 12S-rRNA showed the presence of these sequences inside foci that co-localise with GRSF1 (Antonicka *et al*, 2013), it is currently not known which mtRNA-species reside within MRGs, and for how long. In particular, whether precursor, processed, or matured mtRNA reside in MRGs could not be distinguished in these FISH experiments. Besides the temporal organisation of MRG-components, whether these are organised in space or uniformly distributed inside the MRGs has also not been investigated.

To better understand the purpose of MRG, it remains pertinent to answer the question of how they are formed. For this, when and where foci assemble inside mitochondria should be assessed. Whether MRGs are organised in distinct patterns or occur randomly along the mitochondrial network will then help to understand the regulatory importance of their formation. Finally, whether dynamic or active processes inside MRGs are even possible, has never been addressed. Biochemical reactions take place in solution, as reactants must be able to interact and change. Therefore, the interior of MRGs would need to be organised in a fluid manner to allow the required dynamics for their components to react. An alternative hypothesis could be, that MRGs assemble mtRNA and proteins into insoluble aggregates, and only allow reactions to take place on their surface, the boundary to the mitochondrial matrix. In recent years, a new concept for

membraneless compartmentalisation of reactants inside the cell has become apparent. Indeed, many RNP-granules have now been shown to be organised as so-called liquid droplets or biomolecular condensates (Banani *et al*, 2017). The next chapter introduces further detail of this framework, which, if applicable would help to better understand MRG function and purpose.

4.1.3) Fluid condensates in the cell

Biomolecular condensates

Mammalian cells are highly compartmentalised, including several membrane-encircled organelles. This allows to segregate and regulate many biochemical reactions. For example, enzymes required for the TCA-cycle are localised in the mitochondrial matrix, and controlled metabolite and protein import can regulate metabolic fluxes through the cycle. Additionally, cytosolic and nuclear accumulations of protein and RNA have been observed, and it was discovered that these can often form functional compartments as well, despite their lack of membrane boundaries. Recently, such membraneless compartments were termed biomolecular condensates (BC), which accounts for their unifying features to 1) comprise biological molecules and 2) concentrate molecules (Banani *et al*, 2017). Three criteria have been proposed for BCs: They must represent functional units, form easily and spontaneously, yet are resilient to random fluctuations (Jacobs & Frenkel, 2017). Many BCs have been found to not only concentrate but also rapidly exchange components with their environment. This is reminiscent of a liquid state of matter within many BCs. No exchange on the other hand indicates stable interactions, more closely resembling solid aggregates. The accumulation of material in distinct sites prompted researchers to hypothesize that phase separation could underlie the formation of BC-granules (Iborra, 2007), and in 2009 an experimental study found key indicatives for liquid-liquid phase separation (LLPS) to underlie P-body formation in worms (Brangwynne *et al*, 2009). This marked the beginning of a large number of studies over the last decade, leading to the development of LLPS as a conceptual framework to understand BCs and membraneless cellular compartments (Banani *et al*, 2017).

Principles of fluid condensation

Many fluid BCs consist of multiple protein and RNA species. A prevalent feature of these components is their multivalency, whereby individual molecules harbour multiple domains allowing inter- and intra-molecular interactions. Individual interactions of these domains are often weak, and thereby allow constant rearrangement of molecular conformation and transient association between molecules, which ultimately leads to the liquid nature of their such condensates (Hyman *et al*, 2014). It was found that condensing proteins often harbour low complexity (LCDs) or intrinsically disordered domains (IDDs), which promote multivalency (Kato *et al*, 2012). Lysine and Arginine residues in LCDs can mediate weak interactions through electrostatics (Wang *et al*, 2018). Other cellular mechanisms and conditions such as post translational modification, salt concentration or pH also affect protein-protein, protein-RNA and RNA-RNA interactions, including weak interactions, and thus provide common principles to regulate BC-formation. Finally, entropy

driven LLPS in multi-component systems such as a cell occur when molecular concentrations exceed a system and component-specific critical concentration (Banani *et al*, 2017).

Example of fluid condensates

A prominent example of a fluid BC is the nucleolus. The existence of this dense region inside the nucleus has been known since the early 19th century, but insights into its fluid nature has only started to unravel. Nucleoli comprise the genomic regions for rRNA transcription, rRNA itself, rRNA-processing enzymes, as well as ribosome assembly-factors and ribosomal proteins (Lafontaine *et al*, 2021). Interestingly, individual steps along this pathway from transcription to full ribosome assembly are sub-compartmentalised into immiscible liquid phases inside the nucleolus (Feric *et al*, 2016). Furthermore, rDNA transcription is essential to nucleate nucleolus formation via LLPS (Falahati *et al*, 2016). Together, these studies highlight the importance and intricacy of LLPS for ribosome assembly in the nucleus and it remains to be determined whether similar principles apply to ribosome production inside mitochondria.

There are a plethora of examples for other BCs inside mammalian cytoplasms, and nuclei. For many of these, fluid condensation or LLPS has been found or proposed as the underlying principle of their formation.

Proposed function for fluid condensation

Entropy driven BC-formation allows for energetically cheap and fast sub-cellular compartmentalisation, particularly in comparison to membrane biogenesis dependent organelles (Banani *et al*, 2017). At the same time, BCs offer a similar set of functions as organelles (Lyon *et al*, 2021). For instance, biochemical reaction kinetics can be tuned by managing internal concentration of reaction-partners. Compartments also allow to switch on or off reactions altogether by exclusion or inclusion of key regulatory molecules. Furthermore, BC-assembly allows for long-distance transport of sets of molecules for instance via motor-proteins and the cytoskeleton (Liao *et al*, 2019). Other interesting aspects of self-assembling BCs is their potential for noise-buffering (Stoeger *et al*, 2016; Riback & Brangwynne, 2020; Lyon *et al*, 2021). Furthermore, RNA-sequence dependent LLPS has recently been proposed to drive viral assembly in a concentration dependent manner (Iserman *et al*, 2020). Interestingly, experiments with optogenetic-tools to artificially induce LLPS showed that liquid phases can also affect cellular organisation mechanically (Shin *et al*, 2018). Together, the diversity of these functional principles highlights the importance to better understand the specific role of LLPS and fluid BCs inside living cells, and key experimental procedures to allow elucidative investigations are described below.

Experimental assessment of fluid condensation

To test whether the principles of fluid condensation or LLPS governs the formation of a particular BC, two key lines of evidence can be explored (Brangwynne *et al*, 2009). By FRAP, the diffusive behaviour of droplet components can be assessed. Hereby, rapid recovery in the order of seconds to minutes is generally considered indicative of a fluid-like state. The second key observation allowing to consider LLPS as an underlying principle, is droplet fusion. If two granules of equal composition retain their separate integrity even though they are in physical contact, it is likely they are solid-like entities. On the other hand, when two

droplets undergo fusion and relaxation into a single droplet this is indicative of their liquid-like state (Hyman *et al*, 2014). FRAP and fusion experiments can both be performed in living cells as well as *in vitro* (Alberti *et al*, 2019). Furthermore, mutational studies allow to investigate the exact mechanism which promote particular components to phase separate. *In vitro*, environmental factors can be fine tuned to elucidate the detailed reaction conditions, as well as to determine molecular properties such as the critical concentration of a particular protein or RNA species. However, *in vitro* reconstitution of biochemical reactions bears the risk of oversimplification and limited relevance for real biological systems (Alberti *et al*, 2019).

Potential pitfalls and critical aspects of BC-theory

For LLPS, the direct translation of *in vitro* behaviour to its relevance in cell biology is particularly limited due to its inherent sensitivity to its environment including pH, molecular crowding, and concentration (McSwiggen *et al*, 2019). As an example, any component will phase-separate upon supersaturation, and it is crucial to verify LLPS properties deduced from *in vitro* studies *in vivo*, under physiological conditions (Alberti *et al*, 2019). Additionally, the recent gain in popularity of LLPS resulted in a neglect to consider alternative mechanisms such that a causal relationship or functional relevance of LLPS often remains elusive (McSwiggen *et al*, 2019). Finally, the size and dimensions of many cellular BCs lies at the limit of resolution of diffraction-limited, standard fluorescence microscopy. This poses additional challenges, as quantification of molecular properties can be hampered by inadequate choice of imaging technique (McSwiggen *et al*, 2019).

4.2) Mitochondrial RNA granules are fluid condensates positioned by membrane dynamics.

The article under the title of this chapter was first published in *Nature Cell Biology*:

Timo Rey[#][*], Sofia Zaganelli[*], Emilie Cuillery, Evangelia Vartholomaiou, Marie Croisier, Jean-Claude Martinou[#], Suliana Manley[#] *Nature Cell Biology*, 2020, Vol. 22, pages 1180-1186,
https://doi.org/10.1038/s41556-020-00584-8
[#]Corresponding author(s), [*]These people contributed equally to this work

The key aim of this study was to investigate the biophysical properties of MRGs. For this, we teamed up with the cell-biologists Prof. Jean-Claude Martinou, and Sofia Zaganelli from the University of Geneva. Our findings were accepted for publication in the peer-reviewed scientific journal *Nature Cell Biology* and a full version of the published article can be found in the appendix of this thesis, or online.

Motivation and questions

Even today, it has not become very clear why mtRNA accumulates into distinct foci and what purpose this spatial organisation may serve. To tackle this conundrum, and given the knowledge on MRG-composition and appearance that was published by 2017, the most pertinent questions in the field appeared to be falling into three categories:

I) Structure and internal organisation of MRGs: How big are MRGs, and what shape do they have? Is there an internal structure and organisation or are MRG-components uniformly dispersed within?

II) Principle of formation of MRGs and their material properties: How do MRGs form, and what state of matter do they have? Does this state allow for metabolic reactions within MRGs?

III) Organisation and distribution of MRGs within mitochondria: Where do MRGs occur, and is this random or organised? What cellular mechanisms and structures are important for MRG-distribution?

Key findings

We found that MRGs are comprised of a near spheric FASTKD2 and GRSF1 protein-cloud with a diameter of ~140nm and ~120nm respectively. After 60min of BrU incorporation, mtRNA-foci showed a smaller diameter of around 90nm, and we found the RNA-component of MRGs to lie inside the protein-cloud in two-colour htSTORM experiments. We used mtDNA as a positive control for our analysis pipeline and found nucleoid size and shape in good accordance with previously published literature. Next, we assessed the dynamics of MRGs through live-cell microscopy. We found, albeit on rare occasions, MRGs can fuse in both, COS7 and U2OS cells. In FRAP experiments we observed fast exchange of MRG proteins with the mitochondrial matrix on the order of seconds. Together, these results indicate that the material properties of MRGs are liquid-like, and do not resemble those of solid aggregation. As a reference, we also assessed the exchange of Twinkle, the mitochondrial DNA-helicase, due to its MRG-independent accumulation in mitochondrial foci. Twinkle-foci did not recover over the course of 1 minute, which is in accordance with a tight association of the helicase and mtDNA. We then determined the ultrastructure of MRGs and assessed their distribution within the mitochondrial network. We found MRGs in close apposition to mitochondrial inner membrane and to retain their membrane-association even in swollen mitochondria. In comparison to simulated random data, we found no significant difference for MRG-positions along the mitochondrial network. This indicates MRGs are relatively evenly distributed, which is in accordance with the observed correlation between mitochondrial number and mitochondrial size. Finally, we investigated the mechanism of MRG-distribution and found that, similarly to nucleoids mitochondrial network-dynamics are required for a uniform distribution of MRGs. Interestingly, despite their close apposition when mitochondrial fission is inhibited, individual MRGs retain their integrity as well as their dynamic properties.

Additional data

Some additional experiments remained unpublished, but will be exemplified here. In addition to ERAL1 and DDX28, and based on plasmids obtained from Sofia Zaganelli, the human coding sequences for GRSF1, MRPL47 and RPUSD4 were also fused to eGFP, together with Hélène Perreten. I overexpressed MRPL47-eGFP, GRSF1-eGFP, as well as GRSF1-mCherry (from SZ) in COS7 cells. However, in these primate cells it was difficult to find good, and reproducible cell-culture, transfection, sample-preparation, and imaging conditions to obtain clean images of intra-mitochondrial foci with these constructs (**Fig. 10**). Therefore, FRAP-data from these exploratory experiments were not quantified.

To investigate the relationship between MRG material properties and mitochondrial state, we again used FRAP as a read-out for MRG-fluidity. To shift cellular metabolism towards oxidative phosphorylation, we used
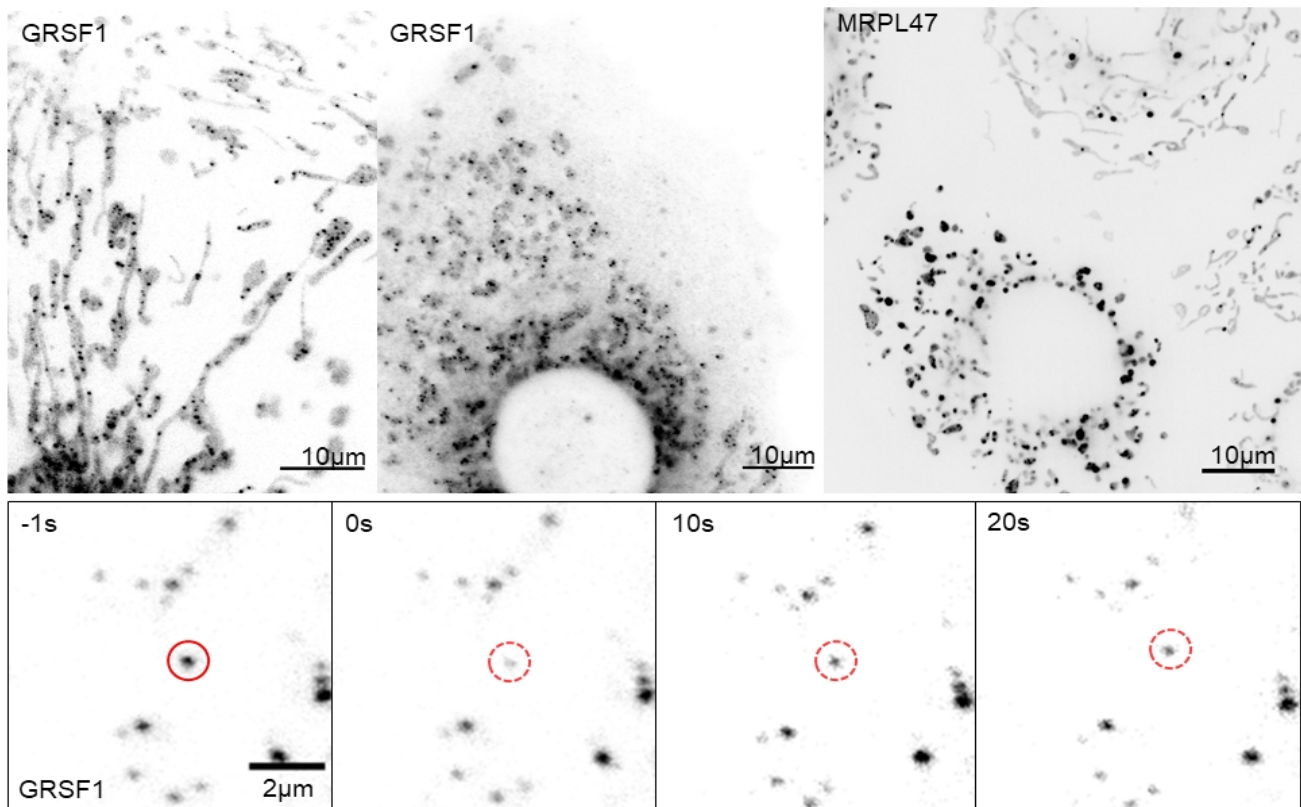
Figure 10: Fluorescence microscopy of COS7 cells expressing MRPL47-eGFP (top right) or GRSF1-eGFP (top left & bottom) respectively. GRSF1-eGFP was imaged by confocal microscopy and exemplary images from a FRAP-experiment are shown (time-points as indicated). MRPL47-eGFP was imaged using a flat-fielded instant SIM (Mahecic *et al*, 2020b).
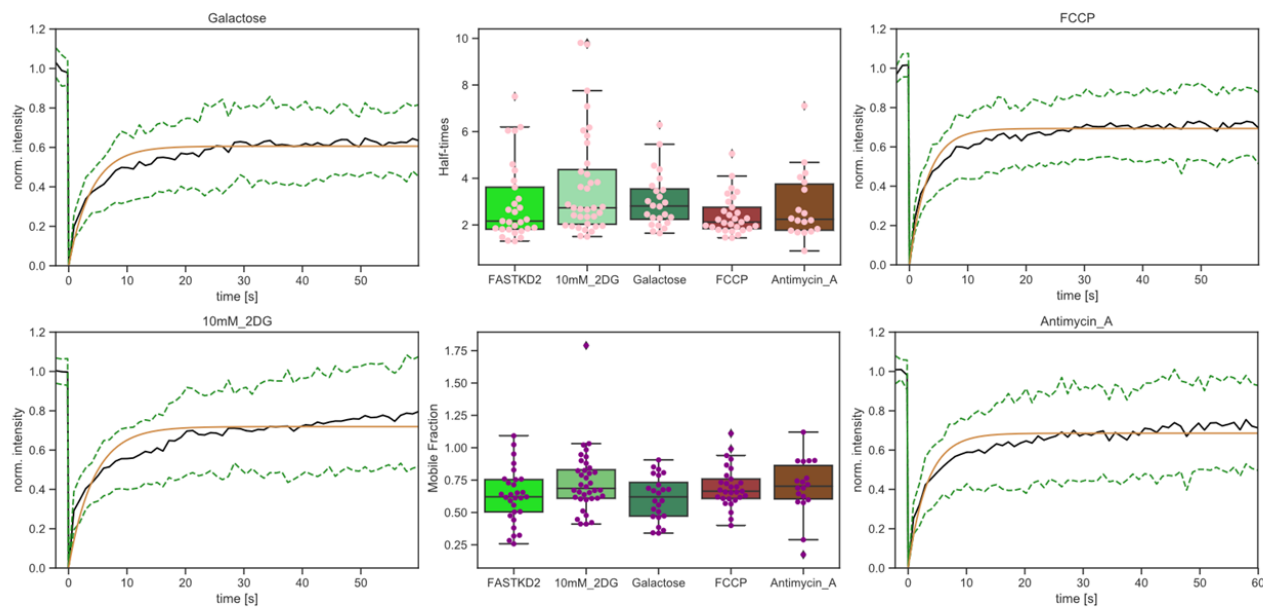

Figure 11: Recovery curves from FRAP experiments under different growth conditions as indicated. Half-times and mobile fraction are also indicated, including those of a control group grown with 10mM Glucose (labelled FASTKD2).

glucose-free medium supplemented with galactose or 2-deoxy glucose. Alternatively, we perturbed mitochondrial respiration with uncoupling (FCCP) and blocking (Antimycin A) agents. However, we found no difference in the FRAP-recovery for any of the assessed growth- or drug-conditions (**Fig. 11**). Additionally, the effect of galactose-dependent growth on the size of MRGs was assessed by htSTORM, but again no difference was observed (data not shown). Therefore, we did not follow up in this direction, and these results thus remain preliminary and qualitative, given the low number replications.

Contribution

My main contributions to this study comprised of devising the project ideas, experimental approaches and protocols, as well as project management, supervision, image acquisition and analysis, coding, manuscript writing, and data curation, in collaboration and exchange with Sofia Zaganelli, Jean-Claude Martinou and Suliana Manley.

4.3) Discussion and outlook

MRG dimensions

MRGs were described as "small foci" based on confocal microscopy (Iborra *et al*, 2004; Jourdain *et al*, 2013). However, because of the diffraction limit these images did not allow to conclude how small MRGs truly are, and whether they indeed resemble granules. Nucleoid dimensions had previously been investigated in several studies and by different means of superresolution microscopy, and were found to resemble roundish granules with a mean diameter of ~100nm (Kukat *et al*, 2011; Brown *et al*, 2011; Alán *et al*, 2016). In our work, we found MRGs are similar in size and shape to nucleoids. However, the distribution of MRG-size shows a larger variability than previously reported for nucleoids. Particularly the RNA-component of MRGs occurred in a wide range of sizes. One explanation for this heterogeneity of mtRNA-foci shape and size is inherent to our experimental procedure, as we did not distinguish between BrU-foci of different age. After 60 minutes of BrU-incubation, MRGs which had for instance started BrU-incorporation 30 minutes before fixation could not be distinguished from others, which had stopped transcription after the first 30 minutes of incubation time. In addition, nucleoids are normally comprise a single copy of mtDNA. For MRGs on the other hand, it is unknown whether they comprise a single, full transcript or any number of processed mtRNA. With lifetimes of about 90 minutes for MRGs (Iborra *et al*, 2004; Jourdain *et al*, 2013) compared to weeks for nucleoids (Poovathingal *et al*, 2012), and opposed by estimated ~60 minutes for full transcript-synthesis or replication, turnover rates are expected to be very different for the two. More heterogeneous populations of MRGs are thus expected to co-exist. In the future, foci-intensity, as well as their distance to the nearest nucleoid could be taken into account to better distinguish between different populations of MRGs, and to investigate the effect of MRG maturation on their size. Interestingly, the size of FASTKD2 and GRSF1 protein-clouds is more homogenous, albeit significantly different from each other. This may indicate that nascent mtRNA is still hidden from FASTKD2 or GRSF1 at first, and while being transcribed inside the nucleoid. Only upon reaching a certain stage of transcription or mtRNA-size, proteins

start to condense and rapidly mature into stable protein-clouds. This hypothesis could be investigated by assessing the emergence and condensation of MRG components from nucleoids in multicolour superresolution imaging of nucleoids, BrU, and MRG proteins together. Alternatively, the molecular shape of long polymers of mtRNA compared to smaller and spherical proteins are much smaller may also explain the dimensional differences we observed between these species. An explanation for the difference in foci-size between GRSF1- and FASTKD2-clouds could be that MRGs may undergo different developmental stages during the processing and maturation of mtRNA, which may be associated with different sets of proteins and granule size. In the future it will be interesting to further investigate the distinct steps of MRG-formation and component recruitment. In multicolour live-cell acquisitions, differences between MRGs associated with particular proteins could be tracked. Long-term imaging of MRGs would allow test whether their formation and dissipation are spatially or temporally organised. It is interesting to note that in the hundreds of movies I analysed, I could never identify an MRG-formation or -dissipation event. Monitoring the relationship between MRGs and nucleoids in dual-colour live-cell microscopy could provide a useful platform to study these events.

Together, our structural observations showed that MRGs are similar in size and shape to nucleoids, and that regular or SIM fluorescence microscopy methods provide sufficient resolution to study their behaviour in live cells. Our findings also contribute towards a comprehension of MRGs as fluid condensates of mtRNA-interacting proteins dispersed throughout a protein cloud, and around nucleating mtRNA polymers.

MRG state of matter

Gaining a clear understanding of *why* mitochondrial RNA and mtRNA-interacting proteins are organised into MRGs, or in other words: "Why do MRGs exist?", still poses the main conundrum in this field. We aimed to elucidate the material properties which underlie MRG formation in order to gain further insight into the possible functions of MRGs. It has previously been hypothesized that processing and maturation steps of mtRNA in mitochondrial gene expression could take place within MRGs (Jourdain *et al*, 2016). However, this hypothesis has never been tested. Alternatively, MRGs could be precipitates of oversaturated mitochondrial components, destined for degradation. In chapter 3, we show that MRGs are not predominantly destined for degradation, but that small mitochondria from peripheral division often contained no MRGs at all. Next, we tested whether MRGs are solid-like precipitates or whether the recently proposed mechanism of LLPS could underlie MRG formation. We observed that MRG proteins exchange rapidly between the dilute phase in the mitochondrial matrix and the condensed phase of MRGs. This shows that MRG protein behaviour cannot be considered as static, as would be expected upon solid aggregation, and provides a first indication that MRG-proteins can indeed participate in dynamic biochemical reactions within MRGs. To further assess LLPS as a model, it is important to test whether the dynamically accumulated RNPs in MRGs form a distinct phase. In addition to the structural measurements by htSTORM, our micrographs show clearly distinguishable electron-dense granules, reminiscent of electron micrographs of stress granules (Souquere *et al*, 2009). Together, these nanoscopic and ultrastructural details provide our first evidence that MRGs are indeed granule like entities of relatively uniform density. Next, we also monitored the behaviour of MRGs in live cells. As fusion is indicative of liquid-like states, whereas solid-like granules would be expected to retain their

integrity, we used SIM to attain the necessary resolution to distinguish fusions from apposition of MRGs. We observed several, albeit rare MRG fusion events in two cell lines. These fusions further substantiate a model where MRGs comprising FASTKD2-eGFP are made of a miscible yet distinct fluid phase. Together, our results thus prompted us to suggest a model where fluid condensation underlies MRG-formation. This has functional implications, as MRGs could act as regulators of reaction kinetics for mtRNA processing and maturation inside mitochondria. Our findings provide a starting ground for future investigations to better understand the exact sequence and kinetics of the processes of MRG assembly and mitochondrial gene expression. Additionally, our findings provide the first evidence that even small, membrane-bound cellular organelles can be further sub-compartmentalised by membrane-less biomolecular condensates.

One main limitation of our live-cell experiments to investigate the phase-properties of MRGs is the use of protein over-expression systems. As mentioned above, upon surpassing a critical solubility concentration, *any* protein or biomolecule will precipitate. Our measurements of granule properties may therefore not reflect exact values under physiological conditions. However, in our htSTORM experiments, both FASTKD2 and GRSF1 accumulate in MRGs when stained with endogenous-protein targeting antibodies, and without perturbation of protein concentrations. Furthermore, oversaturation from augmented expression would be expected to increase density and thus decelerate dynamics. True dynamics may therefore be even faster, and thus substantiate a model of liquid-like MRGs. The variability from overexpression and severity of its effect depending on the protein and construct used may further explain some of the differences between the recovery rates of individual MRG proteins. Another potential experimental bias stems from the use of non-human COS7 cells, together with human cDNA derived protein constructs for most of our experiments. Therefore, it was important to verify our findings in human cells, and we repeated most of our live-cell experiments in U2OS, or HeLa cells.

In the future, it will be interesting to elucidate the mode of recruitment of MRG components. Emerging theory on biomolecular condensates, and LLPS may guide such investigations. Very preliminary experimental results show that the predicted unstructured N-terminal domain of FASTKD2 tagged with GFP can suffice to accumulate in MRGs (data not shown). Next, it will be interesting to test whether the RNA-binding domain alone can also contribute to the recruitment of FASTKD2 to MRGs, and to test the effect on exchange-rates by FRAP. Interestingly, mtRNA remains the only component to be required for condensate formation (Jourdain *et al*, 2013). In line with our additional data whereby MRGs are metabolically robust (**Fig. 11**), this further promotes a model whereby mtRNA acts as a seed for MRG protein condensation. Recent evidence proposes nucleoids also form by phase separation (Feric *et al*, 2021). In contrast to our approach, Feric and colleagues make use of many *in vitro* experiments to determine key descriptors of the nucleoid phase. In the future, it will be interesting to further investigate both types of mitochondrial granules using endogenous protein tags, and thus without perturbing protein homeostasis. This may also help to overcome our limitations in monitoring MRPL47 or GRSF1 in live cells (**Fig. 11**). To then track both, nucleoids and MRGs simultaneously will surely further our understanding of their functional relationship.

MRG distribution and dynamics

Apart from the molecular composition of MRGs (**Tab. 1**), little was known about their distribution or behaviour inside mitochondria and within the cell. We investigated whether MRGs occur randomly or in an organised manner along the mitochondrial network, and determined the cellular mechanism responsible for MRG distribution. We found the number of MRGs to correlate with mitochondrial length, which proposes a level of organisation of MRG-concentration along the mitochondrial network. Nucleoid-distribution has previously been noticed to depend on mitochondrial dynamics (Ban-Ishihara *et al*, 2013; Ishihara *et al*, 2015), and we wondered whether this could be true for MRGs. Interestingly, we found that MRGs also accumulate in clusters, together with nucleoids when mitochondrial fission or fusion are perturbed. It is still under debate whether nucleoids accumulate due to unopposed fusion or due to absent fission upon replication. In the future, live-cell experiments to monitor the emergence of aberrant-distribution of mitochondrial granules will shed light on the precise connection between mitochondrial replication, transcription, fission and fusion. It is notable that, by qualitative assessment MRGs show little movement along their parent mitochondrion. This is sensible in light of their size, and the steric hindrance by cristae, and ties with our observations by CLEM and STED, as well as a recent study (Stephan *et al*, 2019) where MRGs and nucleoids occupy cristae devoid spaces. In the future, it will be interesting to quantitatively assess MRG and nucleoid movement, and to investigate the relevance of their confinement by cristae.

Remaining questions and outlook

An interesting hypothesis for the role of MRGs could be that their local concentration of proteins could outcompete RNA-degradation enzymes and thereby prevent premature turnover of mtRNA within them. To test this hypothesis, the concentration dependence of individual proteins for catalytic performance and binding competition could be studied *in vitro* or *in silico*. In parallel, a better understanding of the effect of concentration could also be gained by determining the concentrations of mitochondrial proteins in cells and single organelles. For this, existing mass spectrometry data could be mined to extract and compare concentrations of MRG-proteins with respect to non-MRG proteins. They could be normalised with respect to TFAM or FASTKD2-concentrations, and questions on whether correlation between the abundance of TFAM and other mitochondrial proteins exist, could be investigated.

Alternatively, MRGs can be hypothesised to buffer and integrate different pathways, relevant for regulation of mitochondrial gene expression. For example, nuclear transcription has been found to occur in stochastic bursts, which can be buffered by nuclear compartmentalisation (Stoeger *et al*, 2016). Whether mitochondrial transcription initiation is uniform, regulated or stochastic within single cells, and single organelles is currently unknown, but MRGs could potentially act as a transcriptional buffer for regulated translation. Similarly, MRGs could allow to buffer noise in cellular ATP-demand. Indicative for this hypothesis are the divergent orders of magnitude between timescales relevant for cellular ATP production and depletion (seconds to minutes), mitochondrial transcription (~1hour), and ribosome, and OXPHOS assembly (many hours)(Bogenhagen *et al*, 2018; Bogenhagen & Haley, 2020). Furthermore, MRGs may also help to buffer the time during mtDNA replication, during which transcription may be inhibited. A similar role of MRGs may

be relevant in mitochondria which lack nucleoids altogether, and to allow their survival until reintegration into the mitochondrial network through fusion.

Ultimately, to allow more comprehensive models of MRG-related processes in the future, it will be important to compile both "positive" as well as "negative" and "uninteresting" experimental results. We are currently lacking a complete list of mitochondrial proteins which have been tested to be included or excluded from MRGs, which would be important to both deduce ontological roles of MRGs in mitochondrial gene expression, as well as to efficiently design future studies.

5) Outlook on organisation of mitochondrial transcription

5.1) Mitochondrial transcription

Transcription of mtDNA is the first regulatory step in the process of mitochondrial gene expression, and thus in the production of new OXPHOS-complexes to meet cellular ATP-demands. Besides mtDNA, a set of three proteins are required to assemble a transcription initiation complex at heavy and light strand promoters: mitochondrial transcription factor A (TFAM), mitochondrial transcription factor B2 (TFB2M), and the mitochondrial RNA polymerase (POLRMT) (Basu *et al*, 2020). Recent atomic structures provide insight into the exact molecular arrangement of these proteins, and highlight the importance of transcription factors in humans (Hillen *et al*, 2017a). An additional layer or regulation is stems from post translational modifications of these proteins, albeit their exact functional roles are only starting to unravel (Bostwick *et al*, 2020). Upon transcription initiation and promoter escape, TFB2M is then released, and subsequently replaced by the mitochondrial transcription elongation factor (TEFM) (Hillen *et al*, 2017b). TEFM is an essential component of the transcription elongation complex and increases its processivity to ~4nt/sec (Yu *et al*, 2018). Altered mitochondrial transcription is associated with severe disease, including cancer, where inhibition of POLRMT may help to reduce aberrant proliferation (Bonekamp *et al*, 2020). However, apart from the detailed mechanistic understanding down to specific conserved nucleotides, nothing is known about when and where mitochondrial transcription takes place (Basu *et al*, 2020). Nuclear genes, particularly encoding rRNA are often transcribed in multiple sequential rounds (Trendelenburg, 1983). However, how often a specific nucleoid is transcribed, and whether both strands always transcribe in parallel, is currently not known. Furthermore, whether transcription and replication can take place in the same mitochondrion, or the same nucleoid, has never been assessed, and it remains speculative whether there may be different populations of nucleoids inside single cells, or whether mitochondria follow a specific cycle of replication and transcription. Together, this highlights our extensive mechanistic knowledge on *how* mtDNA is transcribed, but absence of data on *when* and *where* this occurs. To better understand the overall organisation of mitochondrial transcription in single cells, the spatial and temporal organisation of mtDNA transcription needs to be assessed in single organelles, and for individual nucleoids. These insights will provide a basis to better understand nucleus-mitochondria coordination, and decision making processes, and ultimately allow novel avenues to improve human health.

5.2) Observations on the organisation of mitochondrial transcription

This section provides preliminary data towards a better understanding of where mitochondrial transcription takes place inside human cells. Furthermore, test results, as well as planned experiments to shed light on the temporal and biophysical organisation of mitochondrial transcription, will be discussed. Potential future directions and implications will be highlighted in the final sub-chapter.

Mitochondrial transcription is spatially confined

   To monitor mitochondrial transcription, incorporation of BrU into newly synthesised mtRNA can be visualised in fixed cells (Iborra *et al*, 2004). As discussed in the previous chapters, accumulated mtRNA in MRGs dissociate from nucleoids over time. To highlight nucleoids with ongoing transcription, it is thus important to use a short pulse of BrU-supplementation, immediately before fixation. I incubated U2OS cells with 5mM of BrU for 20 minutes before fixation in line with the recently published protocol (Xavier & Martinou, 2021). I then acquired images of immunolabelled samples by confocal microscpy (**Fig. 12**). A major challenge in image analysis however, is the reproducible identification of labelled foci. While automated pipelines start to replace traditional hand-annotation, recent instructions for high-throughput BrU-foci quantification depend on microscope specific, commercial software (Kotrys *et al*, 2021). Therefore, I created a prototype for an open source Fiji-macro, which will allow to standardise reproducible mitochondrial-foci analysis across different experiments, as well as different laboratories (**Fig 12**). With this tool, I identified BrU-foci and manually determined their distance to mitochondrial tips. For simplification, I only retain foci within straight (two poled) mitochondria for subsequent analysis. I find transcribing nucleoids appear to follow a bimodal distribution with a peripheral population and a midzone population (**Fig. 12d**). Upon longer incubation of BrU for 60 minutes, the foci follow a uniform distribution along the mitochondrial network (**Fig.12e**), which is in line with our finding of randomly distributed MRGs (see chapter 4). Similarly, analysis of live COS7 with TMRE-stained mitochondria shows that nucleoids (picoGreen) generally follow a uniform distribution (**Fig.12f**).

Figure 12: Automated foci-quantification shows mitochondrial transcription is spatially confined. **a** & **b**, Immunofluorescence confocal image of U2OS cells incubated with 5mM BrU for 60 minutes, BrU stained with Alex647 (green) and mitochondria (black) stained with ATP5i primary and Alexa488 secondary antibodies, exemplifies the variability of BrU-foci, and imminent difficulties for manual counting. **c** Number of foci from automated foci-detection with varying prominence-settings for 0 minutes control (light blue), 20 minutes (orange) and 60 minutes (green) BrU-incubation samples. Distribution of transcribing nucleoids (n= 177) after 20 minutes of BrU incubation from 2 U2OS cells (**d**), of MRGs (n = 280) after 60 minutes of BrU incubation from 3 U2OS cells (**e**), and of nucleoids (n=77) stained by picoGreen from 3 COS7 cells.

Mitochondrial nucleoids are licensed for transcription

Our current knowledge of mitochondrial transcription is based on fixed or harvested cell and molecular samples, which represent a mosaic of snapshots of this dynamic process. To monitor ongoing mitochondrial transcription in live cells, Hélène Perreten cloned a eGFP-tagged human POLRMT, and a tRFP-tagged human TEFM, based on cDNA used for in vitro studies (Posse *et al*, 2015). We decided to fuse the tRFP to the N-terminus considering the recently published structural model of the elongation complex, whereby hTEFM C-termini are involved in functional dimerisation (Hillen *et al*, 2018). In accordance with original studies of C-terminally HA-tagged hTEFM (Minczuk *et al*, 2011), I observe tRFP-hTEFM to accumulate in mitochondrial foci in both, transfected U2OS and COS7 cells (**Fig 13**). As TEFM is involved in both, full-length mtDNA transcription, as well as short mtDNA replication primer synthesis, one could expect to find two populations of TEFM-foci, a long and a short-lived one. In several 20 minute long time-lapse experiments using live-cell 2D-SIM microscopy, I never observed a TEFM-focus formation or dissipation event. To test whether tRFP-TEFM foci associate with mitochondrial nucleoids as expected, I co-stained nucleoids with picoGreen. In live-cell confocal microscopy I found every nucleoid stained by picoGreen was also stained by tRFP-TEFM (**Fig. 13**).

Figure 13: Overexpressed tRFP-TEFM foci co-localise with nucleoids stained by picoGreen in live COS7 cells. Left, green channel; centre, red channel; right, overlay.

Given the relatively bright signal, and high photostability of the tRFP-TEFM foci, I suspect more than the minimal set of four TEFM molecules, essential for bi-directional transcription, accumulate within each

nucleoid. To test whether TEFM solely recruited to nucleoids in stable active transcription elongation complexes, or else forms a dynamic protein pool, I aim to assess protein exchange by FRAP. Initial qualitative tests show a relatively rapid recovery of TEFM-foci intensity upon photobleaching (**Fig. 14**), indicative of dynamic exchange between nucleoid associated and free tRFP-TEFM protein pools.

5.3) Discussion and outlook

Together, our preliminary data suggest a model where all nucleoids are licensed to efficiently transcribe mtDNA, yet actual transcription only takes place at distinct sites within the mitochondria. The apparent spatial confinement of actively transcribing nucleoids to mitochondrial midzones and poles is surprisingly reminiscent of the distribution of mitochondrial fission sites (see chapter 3). Replication of mtDNA depends on primer synthesis by the transcription machinery (Kühl *et al*, 2016; Jiang *et al*, 2019), and is likely followed by midzone fission (Lewis *et al*, 2016; Kleele *et al*, 2021). A hypothetical model could therefore involve midzone transcription preceding midzone replication. Tip-associated transcription on the other hand, may allow mitochondria to assess the quality and integrity of individual mtDNA, and subsequent isolation for targeted degradation via peripheral fission. Alternatively, tip-association may also be speculated to reflect licensing of replicated nucleoids for transcription, as newly replicated nucleoids retain their affiliation with mitochondrial poles for up to two days (Lewis *et al*, 2016). To better understand these processes, additional data is necessary to allow quantitative and statistical evaluation of the proposed distribution patterns. Further shortening the BrU incubation time could increase the time-resolution to capture truly actively transcribing nucleoids. As a positive control, co-staining against mtDNA could allow to distinguish transcribing nucleoids from newly formed MRGs. Next, the spatial distribution of mtDNA replication could also be investigated using short BrdU, or EdU pulses. This would allow to test the proposed hypothesis that actively replicating nucleoids are preferentially located at the centre of mitochondria, prior to midzone fission. Finally, to improve data-analysis the robustness and userfriendliness of the macro-code may be enhanced, and a gui allow for wide-spread application by other users. An additional feature to automatically measure the integrated intensity of detected foci was already developed in chapter 4, and could be integrated to the foci-localiser. This could for instance be useful to distinguish 'young' granules in long pulses of BrU, as well as to estimate *in cellulo* mitochondrial transcription and replication times. In the future, it will be interesting to investigate the molecular and regulatory mechanisms which define the distinct distribution patterns within mitochondria.

To confirm the percentage of TEFM positive nucleoids in mammalian cells, it would be ideal to label the endogenous protein population. This can be achieved by genome engineering through CRSPR knock-in strategies, or immunolabelling of hTEFM. Additionally, potential side-effects of tagging-strategies at the N- or C-terminus of the coding sequence could be compared, for instance by mtRNA or mtDNA quantification by qPCR. Additionally, co-localisation with active mitochondrial transcription by short BrU pulse labelling will provide further insight into what extent TEFM-foci are associated with ongoing transcription. To then further elucidate the biophysical properties of nucleoids, it will be interesting to perform quantitative FRAP

measurements of tRFP-TEFM foci. A phase separation model has recently been proposed to underlie the recruitment of TFAM to nucleoids (Feric *et al*, 2021). Thus far, I have not found tRFP-TEFM overexpression to result in any apparent morphological changes to mitochondria, even two days after transfection. My test results, indicating a fast recovery of TEFM-foci thus indicate that tRFP-TEFM constructs may provide a useful tool to further investigate the phase properties of nucleoids *in vivo*. Additionally, other transcription associated proteins including POLRMT and TFB2M could be tagged and monitored in live cells in the future. Albeit, our first approach to overexpress tagged POLRMT resulted in large protein aggregates, and directly labelling of this low copy number protein in the genome may be necessary. Ultimately, interplay between mitochondrial replication and transcription could be examined both in fixed and live cells. By combining tRFP-TEFM, FASTKD2-eGFP and the established POLG2-eGFP (Young *et al*, 2015), as well as BrU and BrdU, the hypothesis of a mitochondrial cycle could be investigated.
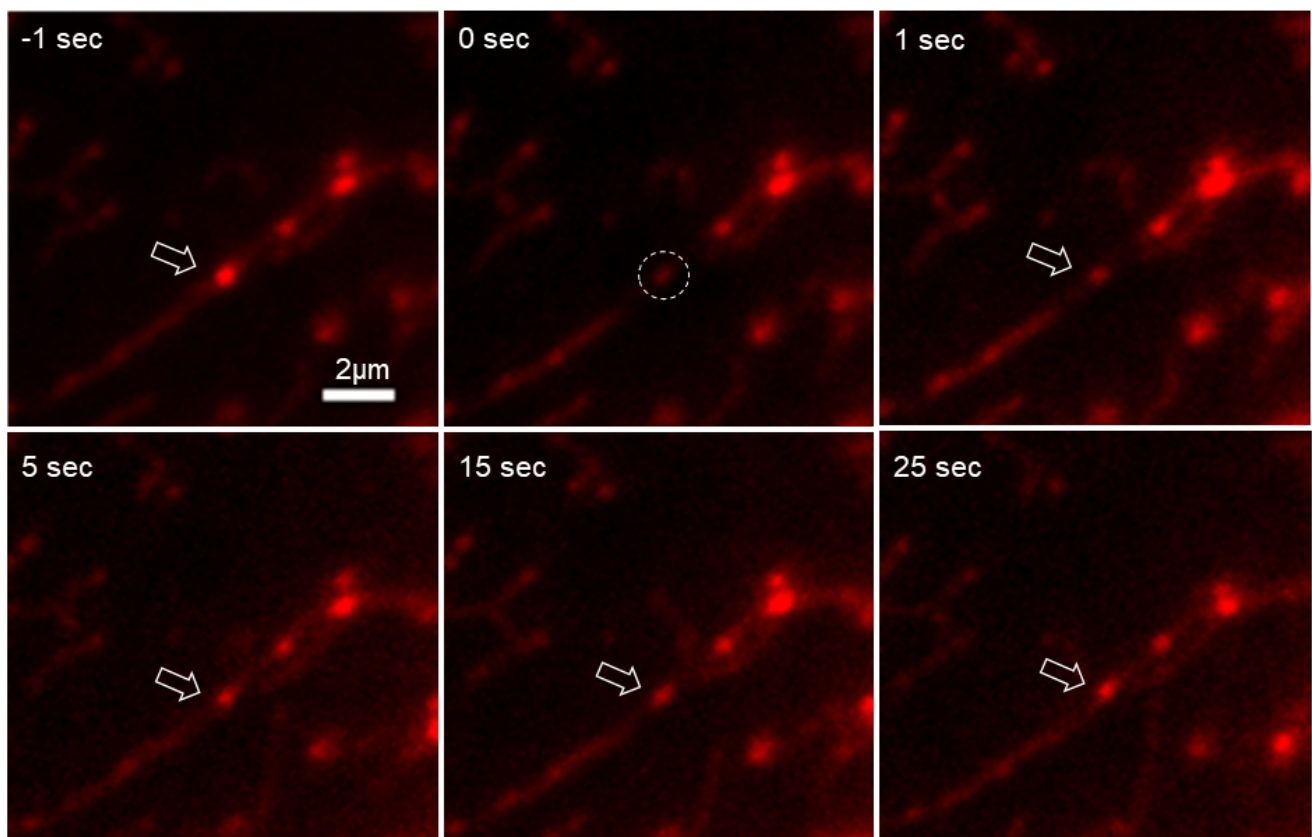
Figure 14: Exemplary FRAP time-series. tRFP-TEFM was expressed COS7 cells and photobleached at t0 (white circle). Fluorescence recovery was monitored over the course of 30 seconds. To account for general photobleaching, contrast was adjusted manually in the images shown, adjacent foci act as visual reference points for fluorescence intensity.

6) Conclusion and final remarks

Summary

The organisation and dynamics of intracellular processes have fascinated cell biologists for over a century. Technological advances continue to allow gaining evermore detailed insights into the underlying structures and mechanisms which allow our cells to collaborate, grow and thrive, and thereby enable human life. With this doctoral thesis I hope to have contributed to our collective understanding of human cell biology, and mitochondrial dynamics and organisation in particular. For this, I applied advanced and superresolved microscopic imaging techniques to investigate the molecular mechanism and biophysical principles of mitochondrial gene expression. I demonstrate the applicability and limitations of htSTORM to study structural dimensions in both the nucleus and mitochondria, and find that MRGs are nanometric granular condensates. I also present a new framework which enables to better comprehend mitochondrial fission, and show how mitochondrial proliferation and turnover can both be linked to mitochondrial dynamics in distinct, though overlapping pathways. We discover that the spatial organisation of MRG is interlinked with mitochondrial dynamics, and I show that MRGs themselves are dynamic structures. This is the first evidence that fluid biomolecular condensation or LLPS can take place within membrane bound organelles outside the nucleus, and thereby further subcompartmentalise these cellular subcompartments at the nanometre scale. It also allows to form new hypotheses about an active role of MRGs in mtRNA processing. Finally, I discover that mitochondrial transcription may be spatially confined, and provide further indications that mitochondrial nucleoids also form fluid compartments, licensed for transcription. Together, my observations and the results from my research harnessing state-of-the-art biotechnology help to shed light on the intricate and complex dynamic organisation of mitochondria and their RNA.

Remaining challenges in microscopy for molecular cell biology

The development of superresolution microscopy in the last decades led to a surge of interest in these methods to study subcellular and molecular biology. While the main hardware-engineering problems appear to be solved, automation of acquisition parameter optimisation could help to lower the entry-barrier for cell biologists even more. Albeit, shifting the focus from biochemistry to microscopy methods in undergraduate teaching could be a more efficient route. Especially because oversimplification may lead to a loss of methodological control, and ultimately to biased and reduced scopes of results. A more fundamental problem to fluorescence microscopy is the limited photon budget. Emerging technology including AiryScan, re-scan confocal, and MINFLUX may be key to overcome these issues to improve live-cell imaging in the near future (Zeiss; De Luca *et al*, 2013; Balzarotti *et al*, 2017). Alternatively, computational methods such as CARE, Noise2Noise or Noise2Void can also help to improve image quality for long imaging (Krull *et al*, 2020; Lehtinen *et al*, 2018; Weigert *et al*, 2018).

However, throughout my thesis I have come to realise that the main challenges today often lie in the correct and reproducible analysis of images. Promising developments, particularly in the use of machine learning and neuronal networks for computer vision, which can be used for segmentation, classification, contrast, and even resolution enhancement add on top of increasingly large open source communities

providing software and analysis pipelines (Christiansen *et al*, 2018; Berg *et al*, 2019; Belthangady & Royer, 2019; Wang *et al*, 2019; Nehme *et al*, 2020; Schindelin *et al*, 2012; McQuin *et al*, 2018). Increasing automation of image analysis, together with open source and open data sharing are finally starting to overcome some long overdue aspects of prevailing issues with reproducibility in cell biological research. Automation also allows to increase the throughput, and can be accompanied by more standardised, or at least machine-friendlier output. Increasingly large data-sets with molecular resolution will become available and it will be interesting to see how the imaging community will organise this wealth of information to gain unprecedented insight into sub-single-cell biology, potentially analogous to other -omics fields. A first step in the direction of harnessing fluorescence big data could be to shift structural biology from artificial *in vitro* systems to *in cellulo* studies of molecular assemblies, building on approaches developed in our group (Sieben *et al*, 2018; Mahecic *et al*, 2020b).

Challenges and outlook in mitochondrial biology

Genetic and biochemical methods have been instrumental to establish a catalogue of molecules and pathways, including theoretical reaction kinetics, which can take place inside mitochondria of living human cells. Furthermore, novel single-cell technology, such as single-cell mitochondrial and ATAC sequencing promise to increase our understanding of cell-to-cell, and cell-type specific variation of mitochondrial composition (Lareau *et al*, 2020; Walker *et al*, 2020). In addition, I believe that the future breakthrough in mitochondrial biology will lie in deciphering the interplay of dynamic processes not only in single cells, but in single organelles, and thereby shed light on mitochondrial and cellular decision making. Studies using live cell microscopy to track *when* and *where* particular events and reaction take place, and will allow a dynamic model to account for the dynamic organisation of cellular life. Similar to using mitochondrial fission as a reference point for mitochondrial birth, the life of a nucleoid could be tracked beginning from its replication. Personally, I would be fascinated to learn to what extent two mtDNA twins live the same life, whether there are organisational patterns that determine differential outcomes, or if the events following a mtDNA replication are completely unpredictable and random. Using mtDNA as a reference would provide a framework to enable disentangling the plethora of known molecular pathways which possibly take place inside a mitochondrion. Finally, this would allow a more complete and holistic picture of mitochondrial biology, at the heart of cellular metabolism.

Final remarks

All in all, my personal discovery of mitochondrial biology and microscopic imaging methods over the past four years has been a fantastic adventure. I became intrigued by their complexity, and am fascinated by their limited but intricate genetics. Mitochondria are mesmerising organelles, at the heart of human metabolism. While the molecular pathways have become relatively well known, their decision making processes has remained completely unexplained. It will be revealing to unravel the temporal and spatial relationships between molecules and behaviour at this organellar scale over the next years of research, and I believe that live and single-cell microscopy will play a vital role therein. I also hope to be able to continue to contribute to these investigations over the next decades.

Acknowledgments

Asking questions and trying to understand how life works for over four years in a row has been extremely fun, rewarding, challenging, tough, interesting, stimulating, disappointing, puzzling, and much more. Nearly nothing turned out the way I imagined, and that has been the most exciting of all.

First and foremost, I would like to thank Suliana, for giving me the opportunity to work in her laboratory and within her interdisciplinary group of researchers from all over the world. It has been a steep learning curve with the least possible flat stretches up until these last days. I believe the extraordinary amount of trust and freedom to explore that you provide were instrumental for my development. While challenging at times, it was extremely rewarding to have the space to develop my own questions and attempt to tackle them in your group, together with everyone, and with your support.

Then, I would like to express my gratitude to all members of the LEB-lab, but in particular to the first generation of LEBbers who welcomed me when I started in February 2017. I found the group in a fantastically open-minded and well-hearted spirit, and truly enjoyed to chat with and learn from each member and their diverse interests and backgrounds. In particular, I would like to thank Kyle, who patiently responded to my endless number of questions on optics, microscopes and everything else. I profited tremendously from your calm, and well structured working style. Dora, you had only just started your PhD a few months before me, yet you were another invaluable resource of knowledge and wisdom on almost any topic that I encountered in my research. It has truly been great fun to work alongside, exchange ideas, complaints, and insights, and your way of working has been a fantastic inspiration. A special thank you goes to Tatjana, for letting me contribute to the fantastic endeavour on elucidating the molecular signatures of distinct types of mtFission. To Christian, Anna and all other LEBbers, from masters students and summer interns to fellow PhDs (Aster, Quentin, Khalid, Chen, Julius, Jenny & Sheda) and PostDocs (Lina, Charlotte, Ambroise, Kyle, Sofia, Juliette, Sofia, Davide & Willi), your enthusiasm and drive to do research have kept me motivated throughout my thesis. Another great thank you clearly goes to Hélène, who has been keeping the lab running and providing massive help in cloning and other lab-chores without hesitation!

A particular thank you goes to the people I was lucky enough to be able to collaborate with, and without whom the work presented in this thesis would not have been possible. Thank you Maria for making me discover that "TADs are rad!". Then, I would like to thank Sofia and Jean-Claude for your open-mindedness and willingness to share your expertise and to think about MRGs together. It was truly great fun to exchange ideas and I very much enjoyed visiting Geneva on several of these occasions. Thank you for this fantastic team-spirit! In addition, I would like to highlight the fantastic work and enthusiasm to help at the various facilities at EPFL, including the BIOP (thank you Arne, Thierry, Luigi, José, Nicolas, Olivier, and Romain), the FACS & the BioEM centres.

For this thesis, I would like to thank my committee, Jean-Claude Martinou, Johan Auwerx, Lothar Schermelleh, and Andy Oates for taking the time to evaluate my work. A specific thank you also goes to

those who's feedback was greatly appreciated in the writing of this thesis: thank you Erik, Claudia, Jenny, and Tatjana.

Beyond the lab, there have been numerous other people at EPFL from ADSV-board members to lunch-companions, and co-skiers. I learned a lot from you, and am grateful to have met so many different people from all over the place. Thank you Zeno & Franck for being great coffee-mates (and more importantly, climbing-, skiing-, brewing-, and organising-friends), as well as to the other 4th-floor cafeteria users for lunch company and chats.

Finally, I would like to thank the people, family and friends beyond EPFL, and who were absolutely fundamental to make these past four years a blast. "Work hard, play hard", is what I proclaimed during my first interview at EPFL, and that's what you helped me strive for. Thank you, thank you, thank you, for climbing adventures in Finale and the Alps, for skiing adventures on snow, on ice, on grass, on dirt, under the rain, between massive seracs, in the sun, in the forest, on glaciers, and through freshest powder, for building snow bars, for raclette, for raving, for dancing our hinds off, for celebrating my birthday at 3'500m - with cake, on skis!, for trusting me, blindly, for running marathons, for drinking beer, and wine, for Abenufe, for ups and downs, for highs, for bearing with me, for pulling pulkas, for family dinners, for apéro, for Tichu, for feeling home, for entrusting me as Götti, for exploring, for enjoying, and for having fun.

Thank you Christine, Philippe, Hans, and Luca for our joint adventures and for teaching me to ask. Thank you Claudia for joining me in all of this, for bearing with me, for enjoying together, and for envisioning with me. Your support has been fundamental throughout these years, and I am really looking forward to what lies ahead, and what we will be discovering together!

7) References

7.1) Softwares used

To write this thesis, the following software was used: LibreOffice Writer, Zotero, Fiji, Microsoft PowerPoint, Adobe Acrobate.

7.2) Bibliography

Alán L, Špaček T & Ježek P (2016) Delaunay algorithm and principal component analysis for 3D visualization of mitochondrial DNA nucleoids by Biplane FPALM/dSTORM. *Eur Biophys J* 45: 443–461

Alberti S, Gladfelter A & Mittag T (2019) Considerations and Challenges in Studying Liquid-Liquid Phase Separation and Biomolecular Condensates. *Cell* 176: 419–434

Alberts B (2015) Molecular biology of the cell. New York, NY: Garland Science

Alberts Bruce (2008) Molecular biology of the cell New York: Garland Science

Amunts A, Brown A, Toots J, Scheres SHW & Ramakrishnan V (2015) The structure of the human mitochondrial ribosome. *Science* 348: 95–98

Antonicka H, Choquet K, Lin Z, Gingras A, Kleinman CL & Shoubridge EA (2017) A pseudouridine synthase module is essential for mitochondrial protein synthesis and cell viability. *EMBO Rep* 18: 28–38

Antonicka H, Sasarman F, Nishimura T, Paupe V & Shoubridge EA (2013) The Mitochondrial RNA-Binding Protein GRSF1 Localizes to RNA Granules and Is Required for Posttranscriptional Mitochondrial Gene Expression. *Cell Metabolism* 17: 386–398

Antonicka H & Shoubridge EA (2015) Mitochondrial RNA Granules Are Centers for Posttranscriptional RNA Processing and Ribosome Biogenesis. *Cell Reports* 10: 920–932

Araiso Y, Tsutsumi A, Qiu J, Imai K, Shiota T, Song J, Lindau C, Wenz L-S, Sakaue H, Yunoki K, *et al* (2019) Structure of the mitochondrial import gate reveals distinct preprotein paths. *Nature* 575: 395–401

Balzarotti F, Eilers Y, Gwosch KC, Gynnå AH, Westphal V, Stefani FD, Elf J & Hell SW (2017) Nanometer resolution imaging and tracking of fluorescent molecules with minimal photon fluxes. *Science* 355: 606–612

Banani SF, Lee HO, Hyman AA & Rosen MK (2017) Biomolecular condensates: organizers of cellular biochemistry. *Nat Rev Mol Cell Biol* 18: 285–298

Ban-Ishihara R, Ishihara T, Sasaki N, Mihara K & Ishihara N (2013) Dynamics of nucleoid structure regulated by mitochondrial fission contributes to cristae reformation and release of cytochrome c. *Proceedings of the National Academy of Sciences* 110: 11863–11868

Barchiesi A & Vascotto C (2019) Transcription, Processing, and Decay of Mitochondrial RNA in Health and Disease. *IJMS* 20: 2221

Barrientos A (2015) Mitochondriolus: assembling mitoribosomes. *Oncotarget* 6: 16800–16801

Basu U, Bostwick AM, Das K, Dittenhafer-Reed KE & Patel SS (2020) Structure, mechanism, and regulation of mitochondrial DNA transcription initiation. *Journal of Biological Chemistry* 295: 18406–18425

Battich N, Stoeger T & Pelkmans L (2013) Image-based transcriptomics in thousands of single human cells at single-molecule resolution. *Nat Methods* 10: 1127–1133

Belthangady C & Royer LA (2019) Applications, promises, and pitfalls of deep learning for fluorescence image reconstruction. *Nat Methods* 16: 1215–1225

Berg S, Kutra D, Kroeger T, Straehle CN, Kausler BX, Haubold C, Schiegg M, Ales J, Beier T, Rudy M, *et al* (2019) ilastik: interactive machine learning for (bio)image analysis. *Nat Methods* 16: 1226–1232

Betzig E, Patterson GH, Sougrat R, Lindwasser OW, Olenych S, Bonifacino JS, Davidson MW, Lippincott-Schwartz J & Hess HF (2006) Imaging Intracellular Fluorescent Proteins at Nanometer Resolution. *Science* 313: 1642–1645

Boettiger AN, Bintu B, Moffitt JR, Wang S, Beliveau BJ, Fudenberg G, Imakaev M, Mirny LA, Wu C & Zhuang X (2016) Super-resolution imaging reveals distinct chromatin folding for different epigenetic states. *Nature* 529: 418–422

Bogenhagen DF & Haley JD (2020) Pulse-chase SILAC–based analyses reveal selective oversynthesis and rapid turnover of mitochondrial protein components of respiratory complexes. *Journal of Biological Chemistry* 295: 2544–2554

Bogenhagen DF, Martin DW & Koller A (2014) Initial Steps in RNA Processing and Ribosome Assembly Occur at Mitochondrial DNA Nucleoids. *Cell Metabolism* 19: 618–629

Bogenhagen DF, Ostermeyer-Fay AG, Haley JD & Garcia-Diaz M (2018) Kinetics and Mechanism of Mammalian Mitochondrial Ribosome Assembly. *Cell Reports* 22: 1935–1944

Bonekamp NA, Peter B, Hillen HS, Felser A, Bergbrede T, Choidas A, Horn M, Unger A, Di Lucrezia R, Atanassov I, *et al* (2020) Small-molecule inhibitors of human mitochondrial DNA transcription. *Nature* 588: 712–716

Borowski LS, Dziembowski A, Hejnowicz MS, Stepien PP & Szczesny RJ (2013) Human mitochondrial RNA decay mediated by PNPase–hSuv3 complex takes place in distinct foci. *Nucleic Acids Research* 41: 1223–1240

Bostwick AM, Moya GE, Senti ML, Basu U, Shen J, Patel SS & Dittenhafer-Reed KE (2020) Phosphorylation of mitochondrial transcription factor B2 controls mitochondrial DNA binding and transcription. *Biochemical and Biophysical Research Communications* 528: 580–585

Bouda E, Stapon A & Garcia-Diaz M (2019) Mechanisms of mammalian mitochondrial transcription. *Protein Science* 28: 1594–1605

Brangwynne CP, Eckmann CR, Courson DS, Rybarska A, Hoege C, Gharakhani J, Julicher F & Hyman AA (2009) Germline P Granules Are Liquid Droplets That Localize by Controlled Dissolution/Condensation. *Science* 324: 1729–1732

Brown TA, Tkachuk AN, Shtengel G, Kopek BG, Bogenhagen DF, Hess HF & Clayton DA (2011) Superresolution Fluorescence Imaging of Mitochondrial Nucleoids Reveals Their Spatial Range, Limits, and Membrane Interaction. *Molecular and Cellular Biology* 31: 4994–5010

Brzezniak LK, Bijata M, Szczesny RJ & Stepien PP (2011) Involvement of human ELAC2 gene product in 3' end processing of mitochondrial tRNAs. *RNA Biology* 8: 616–626

Buchan JR & Parker R (2009) Eukaryotic Stress Granules: The Ins and Outs of Translation. *Molecular Cell* 36: 932–941

Burman JL, Pickles S, Wang C, Sekine S, Vargas JNS, Zhang Z, Youle AM, Nezich CL, Wu X, Hammer JA, *et al* (2017) Mitochondrial fission facilitates the selective mitophagy of protein aggregates. *Journal of Cell Biology* 216: 3231–3247

Chakrabarti R, Ji W-K, Stan RV, de Juan Sanz J, Ryan TA & Higgs HN (2018) INF2-mediated actin polymerization at the ER stimulates mitochondrial calcium uptake, inner membrane constriction, and division. *Journal of Cell Biology* 217: 251–268

Chan DC (2020) Mitochondrial Dynamics and Its Involvement in Disease. *Annu Rev Pathol Mech Dis* 15: 235–259

Chandel N & Schumacker P (1999) Cells depleted of mitochondrial DNA (p0) yield insight into physiological mechanisms. *FEBS Letters* 454: 173–176

Christiansen EM, Yang SJ, Ando DM, Javaherian A, Skibinski G, Lipnick S, Mount E, O'Neil A, Shah K, Lee AK, *et al* (2018) In Silico Labeling: Predicting Fluorescent Labels in Unlabeled Images. *Cell* 173: 792-803.e19

Chrzanowska-Lightowlers ZM, Preiss T & Lightowlers RN (1994) Inhibition of mitochondrial protein synthesis promotes increased stability of nuclear-encoded respiratory gene transcripts. *Journal of Biological Chemistry* 269: 27322–27328

Chujo T, Ohira T, Sakaguchi Y, Goshima N, Nomura N, Nagao A & Suzuki T (2012) LRPPRC/SLIRP suppresses PNPase-mediated mRNA decay and promotes polyadenylation in human mitochondria. *Nucleic Acids Research* 40: 8033–8047

Comet I, Riising EM, Leblanc B & Helin K (2016) Maintaining cell identity: PRC2-mediated regulation of transcription and cancer. *Nat Rev Cancer* 16: 803–810

Cremer T & Cremer M (2010) Chromosome Territories. *Cold Spring Harbor Perspectives in Biology* 2: a003889–a003889

Davies KM, Strauss M, Daum B, Kief JH, Osiewacz HD, Rycovska A, Zickermann V & Kuhlbrandt W (2011) Macromolecular organization of ATP synthase and complex I in whole mitochondria. *Proceedings of the National Academy of Sciences* 108: 14121–14126

De Luca GMR, Breedijk RMP, Brandt RAJ, Zeelenberg CHC, de Jong BE, Timmermans W, Azar LN, Hoebe RA, Stallinga S & Manders EMM (2013) Re-scan confocal microscopy: scanning twice for better resolution. *Biomed Opt Express* 4: 2644

De Vos KJ, Allan VJ, Grierson AJ & Sheetz MP (2005) Mitochondrial Function and Actin Regulate Dynamin-Related Protein 1-Dependent Mitochondrial Fission. *Current Biology* 15: 678–683

Dekker J, Rippe K, Dekker M & Kleckner N (2002) Capturing Chromosome Conformation. *Science* 295: 1306–1311

Demmerle J, Innocent C, North AJ, Ball G, Müller M, Miron E, Matsuda A, Dobbie IM, Markaki Y & Schermelleh L (2017) Strategic and practical guidelines for successful structured illumination microscopy. *Nat Protoc* 12: 988–1010

Dieteren CEJ, Gielen SCAM, Nijtmans LGJ, Smeitink JAM, Swarts HG, Brock R, Willems PHGM & Koopman WJH (2011) Solute diffusion is hindered in the mitochondrial matrix. *Proceedings of the National Academy of Sciences* 108: 8657–8662

Dixon JR, Gorkin DU & Ren B (2016) Chromatin Domains: The Unit of Chromosome Organization. *Molecular Cell* 62: 668–680

Dixon JR, Selvaraj S, Yue F, Kim A, Li Y, Shen Y, Hu M, Liu JS & Ren B (2012) Topological domains in mammalian genomes identified by analysis of chromatin interactions. *Nature* 485: 376–380

Dlasková A, Engstová H, Špaček T, Kahancová A, Pavluch V, Smolková K, Špačková J, Bartoš M, Hlavatá LP & Ježek P (2018) 3D super-resolution microscopy reflects mitochondrial cristae alternations and mtDNA nucleoid size and distribution. *Biochimica et Biophysica Acta (BBA) - Bioenergetics* 1859: 829–844

Douglass KM, Sieben C, Archetti A, Lambert A & Manley S (2016) Super-resolution imaging of multiple cells by optimized flat-field epi-illumination. *Nature Photon* 10: 705–708

Ernster L & Schatz G (1981) Mitochondria: a historical review. *Journal of Cell Biology* 91: 227s–255s

Ester M, Kriegel H-P & Xu X (1996) A Density-Based Algorithm for Discovering Clusters in Large Spatial Databases with Noise. *KDD-96 Proceedings*

Falahati H, Pelham-Webb B, Blythe S & Wieschaus E (2016) Nucleation by rRNA Dictates the Precision of Nucleolus Assembly. *Current Biology* 26: 277–285

Feric M, Demarest TG, Tian J, Croteau DL, Bohr VA & Misteli T (2021) Self-assembly of multi-component mitochondrial nucleoids via phase separation. *EMBO J* 40

Feric M, Vaidya N, Harmon TS, Mitrea DM, Zhu L, Richardson TM, Kriwacki RW, Pappu RV & Brangwynne CP (2016) Coexisting Liquid Phases Underlie Nucleolar Subcompartments. *Cell* 165: 1686–1697

Fonseca TB, Sánchez-Guerrero Á, Milosevic I & Raimundo N (2019) Mitochondrial fission requires DRP1 but not dynamins. *Nature* 570: E34–E42

Friedman JR, Lackner LL, West M, DiBenedetto JR, Nunnari J & Voeltz GK (2011) ER Tubules Mark Sites of Mitochondrial Division. *Science* 334: 358–362

Fröhlich C, Grabiger S, Schwefel D, Faelber K, Rosenbaum E, Mears J, Rocks O & Daumke O (2013) Structural insights into oligomerization and mitochondrial remodelling of dynamin 1-like protein. *EMBO J* 32: 1280–1292

Fung TS, Ji W-K, Higgs HN & Chakrabarti R (2019) Two distinct actin filament populations have effects on mitochondria, with differences in stimuli and assembly factors. *J Cell Sci* 132: jcs234435

Giacomello M, Pyakurel A, Glytsou C & Scorrano L (2020) The cell biology of mitochondrial membrane dynamics. *Nat Rev Mol Cell Biol* 21: 204–224

GRCh38.p13 (2019) Genome Reference Consortium Human Build 38 patch release 13 (GRCh38.p13). *https://www.ncbi.nlm.nih.gov/assembly/GCF_00000140539*

Greber BJ & Ban N (2016) Structure and Function of the Mitochondrial Ribosome. *Annu Rev Biochem* 85: 103–132

Greber BJ, Boehringer D, Leibundgut M, Bieri P, Leitner A, Schmitz N, Aebersold R & Ban N (2014) The complete structure of the large subunit of the mammalian mitochondrial ribosome. *Nature* 515: 283–286

Gustafsson MGL (2000) Surpassing the lateral resolution limit by a factor of two using structured illumination microscopy. *J Microsc* 198: 82–87

Gustafsson MGL, Shao L, Carlton PM, Wang CJR, Golubovskaya IN, Cande WZ, Agard DA & Sedat JW (2008) Three-Dimensional Resolution Doubling in Wide-Field Fluorescence Microscopy by Structured Illumination. *Biophysical Journal* 94: 4957–4970

Heilemann M, van de Linde S, Mukherjee A & Sauer M (2009) Super-Resolution Imaging with Small Organic Fluorophores. *Angew Chem Int Ed* 48: 6903–6908

Heilemann M, van de Linde S, Schüttpelz M, Kasper R, Seefeldt B, Mukherjee A, Tinnefeld P & Sauer M (2008) Subdiffraction-Resolution Fluorescence Imaging with Conventional Fluorescent Probes. *Angew Chem Int Ed* 47: 6172–6176

Hell SW & Wichmann J (1994) Breaking the diffraction resolution limit by stimulated emission: stimulated-emission-depletion fluorescence microscopy. *Opt Lett* 19: 780

Hensen F, Potter A, van Esveld SL, Tarrés-Solé A, Chakraborty A, Solà M & Spelbrink JN (2019) Mitochondrial RNA granules are critically dependent on mtDNA replication factors Twinkle and mtSSB. *Nucleic Acids Research* 47: 3680–3698

Herzig S, Raemy E, Montessuit S, Veuthey J-L, Zamboni N, Westermann B, Kunji ERS & Martinou J-C (2012) Identification and Functional Expression of the Mitochondrial Pyruvate Carrier. *Science* 337: 93–96

Hillen HS, Morozov YI, Sarfallah A, Temiakov D & Cramer P (2017a) Structural Basis of Mitochondrial Transcription Initiation. *Cell* 171: 1072-1081.e10

Hillen HS, Parshin AV, Agaronyan K, Morozov YI, Graber JJ, Chernev A, Schwinghammer K, Urlaub H, Anikin M, Cramer P, *et al* (2017b) Mechanism of Transcription Anti-termination in Human Mitochondria. *Cell* 171: 1082-1093.e13

Hillen HS, Temiakov D & Cramer P (2018) Structural basis of mitochondrial transcription. *Nat Struct Mol Biol* 25: 754–765

Horbay R & Bilyy R (2016) Mitochondrial dynamics during cell cycling. *Apoptosis* 21: 1327–1335

Huang F, Hartwich TMP, Rivera-Molina FE, Lin Y, Duim WC, Long JJ, Uchil PD, Myers JR, Baird MA, Mothes W, *et al* (2013) Video-rate nanoscopy using sCMOS camera–specific single-molecule localization algorithms. *Nat Methods* 10: 653–658

Hyman AA, Weber CA & Jülicher F (2014) Liquid-Liquid Phase Separation in Biology. *Annu Rev Cell Dev Biol* 30: 39–58

Iborra FJ (2007) Can visco-elastic phase separation, macromolecular crowding and colloidal physics explain nuclear organisation? *Theor Biol Med Model* 4: 15

Iborra FJ, Jackson DA & Cook PR (1998) The path of transcripts from extra-nucleolar synthetic sites to nuclear pores: transcripts in transit are concentrated in discrete structures containing SR proteins. *Journal of Cell Science* 111: 2269–2282

Iborra FJ, Kimura H & Cook PR (2004) The functional organization of mitochondrial genomes in human cells. *BMC Biology* 2

Ingerman E, Perkins EM, Marino M, Mears JA, McCaffery JM, Hinshaw JE & Nunnari J (2005) Dnm1 forms spirals that are structurally tailored to fit mitochondria. *Journal of Cell Biology* 170: 1021–1027

Iserman C, Roden CA, Boerneke MA, Sealfon RSG, McLaughlin GA, Jungreis I, Fritch EJ, Hou YJ, Ekena J, Weidmann CA, *et al* (2020) Genomic RNA Elements Drive Phase Separation of the SARS-CoV-2 Nucleocapsid. *Molecular Cell* 80: 1078-1091.e6

Ishihara T, Ban-Ishihara R, Maeda M, Matsunaga Y, Ichimura A, Kyogoku S, Aoki H, Katada S, Nakada K, Nomura M, *et al* (2015) Dynamics of Mitochondrial DNA Nucleoids Regulated by Mitochondrial Fission Is Essential for Maintenance of Homogeneously Active Mitochondria during Neonatal Heart Development. *Mol Cell Biol* 35: 211–223

Itoh Y, Andréll J, Choi A, Richter U, Maiti P, Best RB, Barrientos A, Battersby BJ & Amunts A (2021) Mechanism of membrane-tethered mitochondrial protein synthesis. *Science* 371: 846–849

Jackson DA, Iborra FJ, Manders EMM & Cook PR (1998) Numbers and Organization of RNA Polymerases, Nascent Transcripts, and Transcription Units in HeLa Nuclei. *MBoC* 9: 1523–1536

Jacobs WM & Frenkel D (2017) Phase Transitions in Biological Systems with Many Components. *Biophysical Journal* 112: 683–691

Jakobs S, Stephan T, Ilgen P & Brüser C (2020) Light Microscopy of Mitochondria at the Nanoscale. *Annu Rev Biophys* 49: 289–308

Jeandard D, Smirnova A, Tarassov I, Barrey E, Smirnov A & Entelis N (2019) Import of Non-Coding RNAs into Human Mitochondria: A Critical Review and Emerging Approaches. *Cells* 8: 286

Ji W, Hatch AL, Merrill RA, Strack S & Higgs HN (2015) Actin filaments target the oligomeric maturation of the dynamin GTPase Drp1 to mitochondrial fission sites. *eLife* 4: e11553

Jiang S, Koolmeister C, Misic J, Siira S, Kühl I, Silva Ramos E, Miranda M, Jiang M, Posse V, Lytovchenko O, *et al* (2019) TEFM regulates both transcription elongation and RNA processing in mitochondria. *EMBO Rep* 20: e48101

Jourdain AA, Boehm E, Maundrell K & Martinou J (2016) Mitochondrial RNA granules: Compartmentalizing mitochondrial gene expression. *J Cell Biol* 212: 611–614

Jourdain AA, Koppen M, Rodley CD, Maundrell K, Gueguen N, Reynier P, Guaras AM, Enriquez JA, Anderson P, Simarro M, *et al* (2015) A Mitochondria-Specific Isoform of FASTK Is Present In Mitochondrial RNA Granules and Regulates Gene Expression and Function. *Cell Reports* 10: 1110–1121

Jourdain AA, Koppen M, Wydro M, Rodley CD, Lightowlers RN, Chrzanowska-Lightowlers ZM & Martinou J-C (2013) GRSF1 Regulates RNA Processing in Mitochondrial RNA Granules. *Cell Metabolism* 17: 399–410

Kalia R, Wang RY-R, Yusuf A, Thomas PV, Agard DA, Shaw JM & Frost A (2018) Structural basis of mitochondrial receptor binding and constriction by DRP1. *Nature* 558: 401–405

Kamerkar SC, Kraus F, Sharpe AJ, Pucadyil TJ & Ryan MT (2018) Dynamin-related protein 1 has membrane constricting and severing abilities sufficient for mitochondrial and peroxisomal fission. *Nat Commun* 9: 5239

Kanfer G & Kornmann B (2016) Dynamics of the mitochondrial network during mitosis. *Biochemical Society Transactions* 44: 510–516

Kato M, Han TW, Xie S, Shi K, Du X, Wu LC, Mirzaei H, Goldsmith EJ, Longgood J, Pei J, *et al* (2012) Cell-free Formation of RNA Granules: Low Complexity Sequence Domains Form Dynamic Fibers within Hydrogels. *Cell* 149: 753–767

Keppler A, Gendreizig S, Gronemeyer T, Pick H, Vogel H & Johnsson K (2003) A general method for the covalent labeling of fusion proteins with small molecules in vivo. *Nat Biotechnol* 21: 86–89

Khater IM, Nabi IR & Hamarneh G (2020) A Review of Super-Resolution Single-Molecule Localization Microscopy Cluster Analysis and Quantification Methods. *Patterns* 1: 100038

Kiebler MA & Bassell GJ (2006) Neuronal RNA Granules: Movers and Makers. *Neuron* 51: 685–690

Kimura W, Muralidhar S, Canseco DC, Puente B, Zhang CC, Xiao F, Abderrahman YH & Sadek HA (2014) Redox Signaling in Cardiac Renewal. *Antioxidants & Redox Signaling* 21: 1660–1673

Kleele T, Rey T, Winter J, Zaganelli S, Mahecic D, Perreten Lambert H, Ruberto FP, Nemir M, Wai T, Pedrazzini T, *et al* (2021) Distinct fission signatures predict mitochondrial degradation or biogenesis. *Nature* 593: 435–439

Koirala S, Guo Q, Kalia R, Bui HT, Eckert DM, Frost A & Shaw JM (2013) Interchangeable adaptors regulate mitochondrial dynamin assembly for membrane scission. *Proceedings of the National Academy of Sciences* 110: E1342–E1351

Korobova F, Gauvin TJ & Higgs HN (2014) A Role for Myosin II in Mammalian Mitochondrial Fission. *Current Biology* 24: 409–414

Korobova F, Ramabhadran V & Higgs HN (2013) An Actin-Dependent Step in Mitochondrial Fission Mediated by the ER-Associated Formin INF2. *Science* 339: 464–467

Kotrys AV, Borowski LS & Szczesny RJ (2021) High-Throughput Measurement of Mitochondrial RNA Turnover in Human Cultured Cells. *Methods Mol Biol* 2192: 133–146

Kotrys AV & Szczesny RJ (2019) Mitochondrial Gene Expression and Beyond—Novel Aspects of Cellular Physiology. *Cells* 9: 17

Krull A, Vičar T, Prakash M, Lalit M & Jug F (2020) Probabilistic Noise2Void: Unsupervised Content-Aware Denoising. *Front Comput Sci* 2: 5

Kühl I, Miranda M, Posse V, Milenkovic D, Mourier A, Siira SJ, Bonekamp NA, Neumann U, Filipovska A, Polosa PL, *et al* (2016) POLRMT regulates the switch between replication primer formation and gene expression of mammalian mtDNA. *Sci Adv* 2: e1600963

Kukat C, Davies KM, Wurm CA, Spåhr H, Bonekamp NA, Kühl I, Joos F, Polosa PL, Park CB, Posse V, *et al* (2015) Cross-strand binding of TFAM to a single mtDNA molecule forms the mitochondrial nucleoid. *Proc Natl Acad Sci USA* 112: 11288–11293

Kukat C & Larsson N-G (2013) mtDNA makes a U-turn for the mitochondrial nucleoid. *Trends in Cell Biology* 23: 457–463

Kukat C, Wurm CA, Spahr H, Falkenberg M, Larsson N-G & Jakobs S (2011) Super-resolution microscopy reveals that mammalian mitochondrial nucleoids have a uniform size and frequently contain a single copy of mtDNA. *Proceedings of the National Academy of Sciences* 108: 13534–13539

Kuznetsov AV, Hermann M, Saks V, Hengster P & Margreiter R (2009) The cell-type specificity of mitochondrial dynamics. *The International Journal of Biochemistry & Cell Biology* 41: 1928–1939

Lafontaine DLJ, Riback JA, Bascetin R & Brangwynne CP (2021) The nucleolus as a multiphase liquid condensate. *Nat Rev Mol Cell Biol* 22: 165–182

Lareau CA, Ludwig LS, Muus C, Gohil SH, Zhao T, Chiang Z, Pelka K, Verboon JM, Luo W, Christian E, *et al* (2020) Massively parallel single-cell mitochondrial DNA genotyping and chromatin profiling. *Nat Biotechnol*

Larsson L, Frisén J & Lundeberg J (2021) Spatially resolved transcriptomics adds a new dimension to genomics. *Nat Methods* 18: 15–18

Lee JE, Westrate LM, Wu H, Page C & Voeltz GK (2016) Multiple dynamin family members collaborate to drive mitochondrial division. *Nature* 540: 139–143

Lee S-J, Zhang J, Choi AMK & Kim HP (2013) Mitochondrial Dysfunction Induces Formation of Lipid Droplets as a Generalized Response to Stress. *Oxidative Medicine and Cellular Longevity* 2013: 1–10

Lehtinen J, Munkberg J, Hasselgren J, Laine S, Karras T, Aittala M & Aila T (2018) Noise2Noise: Learning Image Restoration without Clean Data. *arXiv*

Levoux J, Prola A, Lafuste P, Gervais M, Chevallier N, Koumaiha Z, Kefi K, Braud L, Schmitt A, Yacia A, *et al* (2021) Platelets Facilitate the Wound-Healing Capability of Mesenchymal Stem Cells by Mitochondrial Transfer and Metabolic Reprogramming. *Cell Metabolism* 33: 283-299.e9

Lewis SC, Uchiyama LF & Nunnari J (2016) ER-mitochondria contacts couple mtDNA synthesis with mitochondrial division in human cells. *Science* 353: aaf5549

Liao P-C, Bergamini C, Fato R, Pon LA & Pallotti F (2020) Isolation of mitochondria from cells and tissues. In *Methods in Cell Biology* pp 3–31. Elsevier

Liao Y-C, Fernandopulle MS, Wang G, Choi H, Hao L, Drerup CM, Patel R, Qamar S, Nixon-Abell J, Shen Y, *et al* (2019) RNA Granules Hitchhike on Lysosomes for Long-Distance Transport, Using Annexin A11 as a Molecular Tether. *Cell* 179: 147-164.e20

Lippincott-Schwartz J, Snapp E & Kenworthy A (2001) Studying protein dynamics in living cells. *Nat Rev Mol Cell Biol* 2: 444–456

Los GV, Encell LP, McDougall MG, Hartzell DD, Karassina N, Zimprich C, Wood MG, Learish R, Ohana RF, Urh M, *et al* (2008) HaloTag: A Novel Protein Labeling Technology for Cell Imaging and Protein Analysis. *ACS Chem Biol* 3: 373–382

Lyon AS, Peeples WB & Rosen MK (2021) A framework for understanding the functions of biomolecular condensates across scales. *Nat Rev Mol Cell Biol* 22: 215–235

Ma J-T, Zhang X-Y, Cao R, Sun L, Jing W, Zhao J-Z, Zhang S-L, Huang L-T & Han C-B (2019) Effects of Dynamin-related Protein 1 Regulated Mitochondrial Dynamic Changes on Invasion and Metastasis of Lung Cancer Cells. *J Cancer* 10: 4045–4053

Ma Y, Wang M, Li W, Zhang Z, Zhang X, Tan T, Zhang X-E & Cui Z (2017) Live cell imaging of single genomic loci with quantum dot-labeled TALEs. *Nat Commun* 8: 15318

Mahecic D, Carlini L, Kleele T, Colom A, Goujon A, Matile S, Roux A & Manley S (2020a) Mitochondrial membrane tension governs fission. *BioRxiv*

Mahecic D, Gambarotto D, Douglass KM, Fortun D, Banterle N, Ibrahim KA, Le Guennec M, Gönczy P, Hamel V, Guichard P, *et al* (2020b) Homogeneous multifocal excitation for high-throughput super-resolution imaging. *Nat Methods* 17: 726–733

Manor U, Bartholomew S, Golani G, Christenson E, Kozlov M, Higgs H, Spudich J & Lippincott-Schwartz J (2015) A mitochondria-anchored isoform of the actin-nucleating spire protein regulates mitochondrial division. *eLife* 4: e08828

McArthur K & Ryan MT (2020) Resolving mitochondrial cristae: introducing a new model into the fold. *EMBO J* 39

McQuin C, Goodman A, Chernyshev V, Kamentsky L, Cimini BA, Karhohs KW, Doan M, Ding L, Rafelski SM, Thirstrup D, *et al* (2018) CellProfiler 3.0: Next-generation image processing for biology. *PLoS Biol* 16: e2005970

McSwiggen DT, Mir M, Darzacq X & Tjian R (2019) Evaluating phase separation in live cells: diagnosis, caveats, and functional consequences. *Genes Dev* 33: 1619–1634

Mears JA, Lackner LL, Fang S, Ingerman E, Nunnari J & Hinshaw JE (2011) Conformational changes in Dnm1 support a contractile mechanism for mitochondrial fission. *Nat Struct Mol Biol* 18: 20–26

Milenkovic D, Matic S, Kuhl I, Ruzzenente B, Freyer C, Jemt E, Park CB, Falkenberg M & Larsson N-G (2013) TWINKLE is an essential mitochondrial helicase required for synthesis of nascent D-loop strands and complete mtDNA replication. *Human Molecular Genetics* 22: 1983–1993

Minczuk M, He J, Duch AM, Ettema TJ, Chlebowski A, Dzionek K, Nijtmans LGJ, Huynen MA & Holt IJ (2011) TEFM (c17orf42) is necessary for transcription of human mtDNA. *Nucleic Acids Research* 39: 4284–4299

Mishra P & Chan DC (2016) Metabolic regulation of mitochondrial dynamics. *Journal of Cell Biology* 212: 379–387

Moore AS, Coscia SM, Simpson CL, Ortega FE, Wait EC, Heddleston JM, Nirschl JJ, Obara CJ, Guedes-Dias P, Boecker CA, *et al* (2021) Actin cables and comet tails organize mitochondrial networks in mitosis. *Nature* published online

Moore AS, Wong YC, Simpson CL & Holzbaur ELF (2016) Dynamic actin cycling through mitochondrial subpopulations locally regulates the fission–fusion balance within mitochondrial networks. *Nat Commun* 7: 12886

Mottis A, Herzig S & Auwerx J (2019) Mitocellular communication: Shaping health and disease. *Science* 366: 827–832

Mozdy AD, McCaffery JM & Shaw JM (2000) Dnm1p Gtpase-Mediated Mitochondrial Fission Is a Multi-Step Process Requiring the Novel Integral Membrane Component Fis1p. *Journal of Cell Biology* 151: 367–380

Nagano T, Lubling Y, Yaffe E, Wingett SW, Dean W, Tanay A & Fraser P (2015) Single-cell Hi-C for genome-wide detection of chromatin interactions that occur simultaneously in a single cell. *Nat Protoc* 10: 1986–2003

Nehme E, Freedman D, Gordon R, Ferdman B, Weiss LE, Alalouf O, Naor T, Orange R, Michaeli T & Shechtman Y (2020) DeepSTORM3D: dense 3D localization microscopy and PSF design by deep learning. *Nat Methods* 17: 734–740

Nobel Prize (2014) Press release Nobel Prize in Chemistry 2014. *https://www.nobelprize.org/prizes/chemistry/2014/press-release/*

Nunnari J & Suomalainen A (2012) Mitochondria: In Sickness and in Health. *Cell* 148: 1145–1159

Osellame LD, Singh AP, Stroud DA, Palmer CS, Stojanovski D, Ramachandran R & Ryan MT (2016) Cooperative and independent roles of the Drp1 adaptors Mff, MiD49 and MiD51 in mitochondrial fission. *J Cell Sci* 129: 2170–2181

Otera H, Miyata N, Kuge O & Mihara K (2016) Drp1-dependent mitochondrial fission via MiD49/51 is essential for apoptotic cristae remodeling. *Journal of Cell Biology* 212: 531–544

Otera H, Wang C, Cleland MM, Setoguchi K, Yokota S, Youle RJ & Mihara K (2010) Mff is an essential factor for mitochondrial recruitment of Drp1 during mitochondrial fission in mammalian cells. *Journal of Cell Biology* 191: 1141–1158

Palmer CS, Osellame LD, Laine D, Koutsopoulos OS, Frazier AE & Ryan MT (2011) MiD49 and MiD51, new components of the mitochondrial fission machinery. *EMBO Rep* 12: 565–573

Park PJ (2009) ChIP–seq: advantages and challenges of a maturing technology. *Nat Rev Genet* 10: 669–680

Pearce SF, Rebelo-Guiomar P, D'Souza AR, Powell CA, Van Haute L & Minczuk M (2017) Regulation of Mammalian Mitochondrial Gene Expression: Recent Advances. *Trends in Biochemical Sciences* 42: 625–639

Peters R, Peters J, Tews KH & Bähr W (1974) A microfluorimetric study of translational diffusion in erythrocyte membranes. *Biochimica et Biophysica Acta (BBA) - Biomembranes* 367: 282–294

Pickles S, Vigié P & Youle RJ (2018) Mitophagy and Quality Control Mechanisms in Mitochondrial Maintenance. *Current Biology* 28: R170–R185

Poovathingal SK, Gruber J, Lakshmanan L, Halliwell B & Gunawan R (2012) Is mitochondrial DNA turnover slower than commonly assumed? *Biogerontology* 13: 557–564

Porat-Shliom N, Harding OJ, Malec L, Narayan K & Weigert R (2019) Mitochondrial Populations Exhibit Differential Dynamic Responses to Increased Energy Demand during Exocytosis In Vivo. *iScience* 11: 440–449

Posse V, Shahzad S, Falkenberg M, Hällberg BM & Gustafsson CM (2015) TEFM is a potent stimulator of mitochondrial transcription elongation in vitro. *Nucleic Acids Research* 43: 2615–2624

Rackham O, Busch JD, Matic S, Siira SJ, Kuznetsova I, Atanassov I, Ermer JA, Shearwood A-MJ, Richman TR, Stewart JB, *et al* (2016) Hierarchical RNA Processing Is Required for Mitochondrial Ribosome Assembly. *Cell Reports* 16: 1874–1890

Rebelo-Guiomar P, Powell CA, Van Haute L & Minczuk M (2019) The mammalian mitochondrial epitranscriptome. *Biochimica et Biophysica Acta (BBA) - Gene Regulatory Mechanisms* 1862: 429–446

Rehklau K, Hoffmann L, Gurniak CB, Ott M, Witke W, Scorrano L, Culmsee C & Rust MB (2017) Cofilin1-dependent actin dynamics control DRP1-mediated mitochondrial fission. *Cell Death Dis* 8: e3063–e3063

Riback JA & Brangwynne CP (2020) Can phase separation buffer cellular noise? *Science* 367: 364–365

Riley JS & Tait SW (2020) Mitochondrial DNA in inflammation and immunity. *EMBO Rep* 21

Ruhanen H, Borrie S, Szabadkai G, Tyynismaa H, Jones AWE, Kang D, Taanman J-W & Yasukawa T (2010) Mitochondrial single-stranded DNA binding protein is required for maintenance of mitochondrial DNA and 7S DNA but is not required for mitochondrial nucleoid organisation. *Biochimica et Biophysica Acta (BBA) - Molecular Cell Research* 1803: 931–939

Rust MJ, Bates M & Zhuang X (2006) Sub-diffraction-limit imaging by stochastic optical reconstruction microscopy (STORM). *Nat Methods* 3: 793–796

Ryan DG, Frezza C & O'Neill LA (2021) TCA cycle signalling and the evolution of eukaryotes. *Current Opinion in Biotechnology* 68: 72–88

Sasaki T, Sato Y, Higashiyama T & Sasaki N (2017) Live imaging reveals the dynamics and regulation of mitochondrial nucleoids during the cell cycle in Fucci2-HeLa cells. *Sci Rep* 7: 11257

Sato H, Das S, Singer RH & Vera M (2020) Imaging of DNA and RNA in Living Eukaryotic Cells to Reveal Spatiotemporal Dynamics of Gene Expression. *Annu Rev Biochem* 89: 159–187

Schermelleh L, Ferrand A, Huser T, Eggeling C, Sauer M, Biehlmaier O & Drummen GPC (2019) Super-resolution microscopy demystified. *Nat Cell Biol* 21: 72–84

Schindelin J, Arganda-Carreras I, Frise E, Kaynig V, Longair M, Pietzsch T, Preibisch S, Rueden C, Saalfeld S, Schmid B, *et al* (2012) Fiji: an open-source platform for biological-image analysis. *Nat Methods* 9: 676–682

Schlessinger J, Koppel DE, Axelrod D, Jacobson K, Webb WW & Elson EL (1976) Lateral transport on cell membranes: mobility of concanavalin A receptors on myoblasts. *Proceedings of the National Academy of Sciences* 73: 2409–2413

Sharonov A & Hochstrasser RM (2006) Wide-field subdiffraction imaging by accumulated binding of diffusing probes. *Proceedings of the National Academy of Sciences* 103: 18911–18916

Shin Y, Chang Y-C, Lee DSW, Berry J, Sanders DW, Ronceray P, Wingreen NS, Haataja M & Brangwynne CP (2018) Liquid Nuclear Condensates Mechanically Sense and Restructure the Genome. *Cell* 175: 1481-1491.e13

Sieben C, Banterle N, Douglass KM, Gönczy P & Manley S (2018) Multicolor single-particle reconstruction of protein complexes. *Nat Methods* 15: 777–780

Singh K, Sripada L, Lipatova A, Roy M, Prajapati P, Gohel D, Bhatelia K, Chumakov PM & Singh R (2018) NLRX1 resides in mitochondrial RNA granules and regulates mitochondrial RNA processing and bioenergetic adaptation. *Biochimica et Biophysica Acta (BBA) - Molecular Cell Research* 1865: 1260–1276

Smirnova E, Griparic L, Shurland D-L & van der Bliek AM (2001) Dynamin-related Protein Drp1 Is Required for Mitochondrial Division in Mammalian Cells. *MBoC* 12: 2245–2256

Souquere S, Mollet S, Kress M, Dautry F, Pierron G & Weil D (2009) Unravelling the ultrastructure of stress granules and associated P-bodies in human cells. *Journal of Cell Science* 122: 3619–3626

Sprenger H-G, MacVicar T, Bahat A, Fiedler KU, Hermans S, Ehrentraut D, Ried K, Milenkovic D, Bonekamp N, Larsson N-G, *et al* (2021) Cellular pyrimidine imbalance triggers mitochondrial DNA–dependent innate immunity. *Nat Metab*

Štefko M, Ottino B, Douglass KM & Manley S (2018) Autonomous illumination control for localization microscopy. *Opt Express* 26: 30882

Stephan T, Brüser C, Deckers M, Steyer AM, Balzarotti F, Barbot M, Behr TS, Heim G, Hübner W, Ilgen P, *et al* (2020) MICOS assembly controls mitochondrial inner membrane remodeling and crista junction redistribution to mediate cristae formation. *EMBO J* 39

Stephan T, Roesch A, Riedel D & Jakobs S (2019) Live-cell STED nanoscopy of mitochondrial cristae. *Sci Rep* 9: 12419

Stoeger T, Battich N & Pelkmans L (2016) Passive Noise Filtering by Cellular Compartmentalization. *Cell* 164: 1151–1161

Taguchi N, Ishihara N, Jofuku A, Oka T & Mihara K (2007) Mitotic Phosphorylation of Dynamin-related GTPase Drp1 Participates in Mitochondrial Fission. *Journal of Biological Chemistry* 282: 11521–11529

Tigano M, Vargas DC, Tremblay-Belzile S, Fu Y & Sfeir A (2021) Nuclear sensing of breaks in mitochondrial DNA enhances immune surveillance. *Nature* 591: 477–481

Tilokani L, Nagashima S, Paupe V & Prudent J (2018) Mitochondrial dynamics: overview of molecular mechanisms. *Essays in Biochemistry* 62: 341–360

Trendelenburg MF (1983) Progress in visualization of eukaryotic gene transcription. *Hum Genet* 63

Tu Y-T & Barrientos A (2015) The Human Mitochondrial DEAD-Box Protein DDX28 Resides in RNA Granules and Functions in Mitoribosome Assembly. *Cell Reports* 10: 854–864

Tucker K & Park E (2019) Cryo-EM structure of the mitochondrial protein-import channel TOM complex at near-atomic resolution. *Nat Struct Mol Biol* 26: 1158–1166

Twig G, Elorza A, Molina AJA, Mohamed H, Wikstrom JD, Walzer G, Stiles L, Haigh SE, Katz S, Las G, *et al* (2008) Fission and selective fusion govern mitochondrial segregation and elimination by autophagy. *EMBO J* 27: 433–446

Voskuil JLA, Bandrowski A, Begley CG, Bradbury ARM, Chalmers AD, Gomes AV, Hardcastle T, Lund-Johansen F, Plückthun A, Roncador G, *et al* (2020) The Antibody Society's antibody validation webinar series. *mAbs* 12: 1794421

Wai T & Langer T (2016) Mitochondrial Dynamics and Metabolic Regulation. *Trends in Endocrinology & Metabolism* 27: 105–117

Walker MA, Lareau CA, Ludwig LS, Karaa A, Sankaran VG, Regev A & Mootha VK (2020) Purifying Selection against Pathogenic Mitochondrial DNA in Human T Cells. *N Engl J Med* 383: 1556–1563

Wallace DC & Chalkia D (2013) Mitochondrial DNA Genetics and the Heteroplasmy Conundrum in Evolution and Disease. *Cold Spring Harbor Perspectives in Biology* 5: a021220–a021220

Wang H, Rivenson Y, Jin Y, Wei Z, Gao R, Günaydın H, Bentolila LA, Kural C & Ozcan A (2019) Deep learning enables cross-modality super-resolution in fluorescence microscopy. *Nat Methods* 16: 103–110

Wang J, Choi J-M, Holehouse AS, Lee HO, Zhang X, Jahnel M, Maharana S, Lemaitre R, Pozniakovsky A, Drechsel D, *et al* (2018) A Molecular Grammar Governing the Driving Forces for Phase Separation of Prion-like RNA Binding Proteins. *Cell* 174: 688-699.e16

Wang W, Wang X, Fujioka H, Hoppel C, Whone AL, Caldwell MA, Cullen PJ, Liu J & Zhu X (2016) Parkinson's disease–associated mutant VPS35 causes mitochondrial dysfunction by recycling DLP1 complexes. *Nat Med* 22: 54–63

WATSON JD & CRICK FHC (1953) Molecular Structure of Nucleic Acids: A Structure for Deoxyribose Nucleic Acid. *Nature* 171: 737–738

Weigert M, Schmidt U, Boothe T, Müller A, Dibrov A, Jain A, Wilhelm B, Schmidt D, Broaddus C, Culley S, *et al* (2018) Content-aware image restoration: pushing the limits of fluorescence microscopy. *Nat Methods* 15: 1090–1097

West AP, Khoury-Hanold W, Staron M, Tal MC, Pineda CM, Lang SM, Bestwick M, Duguay BA, Raimundo N, MacDuff DA, *et al* (2015) Mitochondrial DNA stress primes the antiviral innate immune response. *Nature* 520: 553–557

West AP & Shadel GS (2017) Mitochondrial DNA in innate immune responses and inflammatory pathology. *Nat Rev Immunol* 17: 363–375

Wiedemann N & Pfanner N (2017) Mitochondrial Machineries for Protein Import and Assembly. *Annu Rev Biochem* 86: 685–714

Wilkens V, Kohl W & Busch K (2013) Restricted diffusion of OXPHOS complexes in dynamic mitochondria delays their exchange between cristae and engenders a transitory mosaic distribution. *J Cell Sci* 126: 103–116

Wilson WC, Hornig-Do H-T, Bruni F, Chang JH, Jourdain AA, Martinou J-C, Falkenberg M, Spåhr H, Larsson N-G, Lewis RJ, *et al* (2014) A human mitochondrial poly(A) polymerase mutation reveals the complexities of post-transcriptional mitochondrial gene expression. *Human Molecular Genetics* 23: 6345–6355

Wolf DM, Segawa M, Kondadi AK, Anand R, Bailey ST, Reichert AS, Bliek AM, Shackelford DB, Liesa M & Shirihai OS (2019) Individual cristae within the same mitochondrion display different membrane potentials and are functionally independent. *EMBO J* 38

Wu J, Liu L, Matsuda T, Zhao Y, Rebane A, Drobizhev M, Chang Y-F, Araki S, Arai Y, March K, *et al* (2013) Improved Orange and Red Ca 2+ Indicators and Photophysical Considerations for Optogenetic Applications. *ACS Chem Neurosci* 4: 963–972

Xavier VJ & Martinou J-C (2021) Visualization of Mitochondrial RNA Granules in Cultured Cells Using 5-Bromouridine Labeling. *Methods Mol Biol* 2192: 69–73

Yang C & Svitkina TM (2019) Ultrastructure and dynamics of the actin−myosin II cytoskeleton during mitochondrial fission. *Nat Cell Biol* 21: 603–613

Yang X, Zhanghao K, Wang H, Liu Y, Wang F, Zhang X, Shi K, Gao J, Jin D & Xi P (2016) Versatile Application of Fluorescent Quantum Dot Labels in Super-resolution Fluorescence Microscopy. *ACS Photonics* 3: 1611–1618

You M & Jaffrey SR (2015) Structure and Mechanism of RNA Mimics of Green Fluorescent Protein. *Annu Rev Biophys* 44: 187–206

Young MJ, Humble MM, DeBalsi KL, Sun KY & Copeland WC (2015) POLG2 disease variants: analyses reveal a dominant negative heterodimer, altered mitochondrial localization and impaired respiratory capacity. *Hum Mol Genet* 24: 5184–5197

Yu H, Xue C, Long M, Jia H, Xue G, Du S, Coello Y & Ishibashi T (2018) TEFM Enhances Transcription Elongation by Modifying mtRNAP Pausing Dynamics. *Biophysical Journal* 115: 2295–2300

Zaganelli S, Rebelo-Guiomar P, Maundrell K, Rozanska A, Pierredon S, Powell CA, Jourdain AA, Hulo N, Lightowlers RN, Chrzanowska-Lightowlers ZM, *et al* (2017) The Pseudouridine Synthase RPUSD4 Is an Essential Component of Mitochondrial RNA Granules. *Journal of Biological Chemistry* 292: 4519–4532

Zahedi A, On V, Phandthong R, Chaili A, Remark G, Bhanu B & Talbot P (2018) Deep Analysis of Mitochondria and Cell Health Using Machine Learning. *Sci Rep* 8: 16354

Zeiss Airiscan Zeiss, https://www.zeiss.de/mikroskopie/produkte/confocal-microscopes/lsm-980-mit-airyscan-
2.html.

Zhuang X (2021) Spatially resolved single-cell genomics and transcriptomics by imaging. *Nat Methods* 18:
18–25

Zorkau M, Albus CA, Berlinguer-Palmini R, Chrzanowska-Lightowlers ZM & Lightowlers RN (2020) High
resolution imaging of nascent mitochondrial protein synthesis in cultured human cells *Cell Biology*

8) Curriculum Vitae - Timo Rey

Curious about life at any scale, from mountains to molecules.

Personal details

Birth-name: Timo Rey

Address: Kanonenweg 18, 3012 Bern

E-mail (private): timorey@hotmail.com

E-mail (work): timo.rey@epfl.ch; timo.rey@unifr.ch

Born: 2nd of April 1989

Nationality: Swiss

Fluency: German, English, French

OrcID: https://orcid.org/0000-0002-2124-937X

GitHub: https://github.com/TimoHenry/

Education & Degrees

2020 - tbd **M.Sc. in Bioinformatics and Computational Biology**

University of Fribourg (UniFR) - Fribourg, Switzerland

2017 - 21 **Ph.D. program in Biotechnology and Bioengineering** (EDBB)

4-year program Swiss Federal Institute of Technology Lausanne (EPFL) - Lausanne, Switzerland

2014 - 16 **M.Sc. in Biology**, Structural Biology and Biophysics

Swiss Federal Institute of Technology Zurich (ETHZ) - Zurich, Switzerland

2013 - 14 Part II Zoology

University of Cambridge - Cambridge, United Kingdom

2011 - 14 **B.Sc. in Biology**

University of Zurich (UZH) - Zurich, Switzerland

2005 - 10 Bilingual **Matura** (German/English)

Kantonsschule Wettingen - Argovia, Switzerland

2007 - 08 Newtown High School - Connecticut, USA

AFS-exchange year

Research experience

Feb. 2017 - May 2021: **Ph. D. candidate**

Swiss Federal Institute of Technology Lausanne (EPFL), Institute of Physics

Advisor: Prof. Dr. Suliana Manley

Studies on the organisation and dynamics of mitochondria & their RNA

- Project & experimental design: finding and determining a subject to study

- Live & fixed cell superresolution microscopy: STORM, STED, SIM, & iSIM

- Fluorescence microscopy: FRAP, confocal, live cell, immuno fluorescence

- Image analysis: Custom pipelines, scripts & programming (Python, MATLAB, Fiji)

 - Other: Project management, data analysis, cell culture, cloning, optogenetics

May 2016 - Sept 16: **Research assistant**

Swiss Federal Institute of Technology Zurich (ETHZ), Institute of Microbiology

Advisor: Prof. Dr. Julia Vorholt

Analysis of metabolites from single cells by Mass Spectrometry using FluidFM:

- Project & experimental design: find & test application of newly developed protocol

Sept 2015 - Apr. 16: **Master Thesis**

Swiss Federal Institute of Technology Zurich (ETHZ), Institute of Microbiology

Advisor: Prof. Dr. Julia Vorholt

Analysing metabolites from single cells by Mass Spectrometry using FluidFM:

- Experimental design: Develop a protocol to analyse metabolites from single cells

- FluidFM: learn to use the instrument and devise a workflow to extract metabolites

- Mass Spectrometry: MALDI-ToF sample preparation, acquisition & analysis

Feb. 2015 - Jun. 15: **Research project II**

Swiss Federal Institute of Technology Zurich (ETHZ), Institute of Molecular Biology

Advisor: Prof. Dr. Frédéric Allain

Structural rearrangement of the pRN1 Prim/Pol domain upon cofactor association:

- Assessment of binding position & affinity of nucleotides to protein subdomain.

 - HPLC protein purif.; ITC; NMR experiments & data evaluation (Sparky, Pymol), Linux

Oct. 2014 - Jan. 15: **Research project I**

Swiss Federal Institute of Technology Zurich (ETHZ), Institute of Molecular Health

Advisor: Prof. Dr. Anton Wutz

Validation of candidate targets of the lnRNA, Xist by modification of a mouse:

- Test candidate-genes via targeted knockout.

 - mES-cell culture; CRISPR/Cas knockout design and conduction; Cloning

Oct. 2013 - Mar. 14: **Part II project**

University of Cambridge, Cancer Research UK Gurdon Institute

Advisor: Dr. Philipp Zegerman

Screening for novel interactions of SLD3 in C. elegans:

- Cloning; Yeast-two-hybrid library screening; β-Gal assay; Yeast growth assay

Jul. 2012 - Aug. 12: **Research Intern**

University of Zurich, Institute of Evolutionary Biology and Ecology

Advisor: Prof. Dr. Carsten Schradin

Correlative study on the behaviour of the four-striped mouse in a field experiment and under standardised conditions in regard of boldness:

- Field & laboratory behavioural experiments; field station maintenance

Publications

Distinct fission signatures predict mitochondrial degradation or biogenesis

Kleele T[§] , **Rey T**, Winter, J, Zaganelli S, Mahecic D, Perreten Lambert H, Ruberto F, Nemir M, Wai T, Pedrazzini T, and Manley S[§]

Nature; Vol. 593, 435-439, 2021 https://doi.org/10.1038/s41586-021-03510-6

Mitochondrial RNA Granules are fluid condensates positioned by membrane dynamics

Rey T *[§] , Zaganelli S*, Cuillery E, Vartholomaiou E, Croisier M, Martinou JC[§] , Manley S[§]

Nature Cell Biology Vol. 22, 1180-1186, 2020 https://doi.org/10.1038/s41556-020-00584-8

EZH2 oncogenic mutations drive epigenetic transcriptional and structural changes within chromatin domains

Donaldson-Collier M*, Sungalee S*, Zufferey M*, Tavernari D*, Katanayeva N, Battistello E, Mina M, Douglass KM, **Rey T**, Raynaud F, Manley S, Ciriello G[§], Oricchio E[§]

Nature Genetics Vol. 51, 517-528, 2019 https://doi.org/10.1038/s41588-018-0338-y

Single-Cell Mass Spectrometry of Metabolites Extracted from Live Cells by Fluidic Force Microscopy

Guillaume-Gentil O*[§], **Rey T***, Kiefer P, Ibanez AJ, Steinhoff R, Brönnimann R, Dorwling-Carter L, Zambelli T, Zenobi R, Vorholt J[§]

Anal Chem 89 (9), 5017-5023, 2017 https://doi.org/10.1021/acs.analchem.7b00367

* authors contributed equally

[§] corresponding authors

Awards

2021:   Zeiss poster prize, LS^2-meeting in Zurich, Switzerland (500chf)

2019:   FEBS poster prize, LS^2-meeting in Zurich, Switzerland (300chf)

2015:   BCI best presentation award, ETHZ (class II laser pointer)

Conferences & presentations

2021:   LS^2 meeting, Virtual conference - poster (with prize) & selected oral presentations

2020:   ASCB Cell Bio, Virtual conference, e-presentation

2020:   LS^2 meeting, Zurich - poster & 2 selected oral presentations

2019:   Physics of living systems, Lausanne - oral presentation

2019:   Mitochondria in Life death and disease, Montenegro - poster presentation

2019:   Cell symposium: Regulatory RNA, Berlin - poster presentation

2019:   EDBB-Minisympsium, Lausanne - oral presentation

2019:   LS^2 meeting, Zurich - poster (with prize) & selected oral presentation

2019:   LEB-retreat, Crans Montana - oral presentation

2018:   Faculty presentations, Université Genève - oral introduction

2018:   Cellular mechanisms driven by phase separation, EMBO/EMBL Heidelberg - poster presentation

2018:   LS^2 meeting, Lausanne - poster presentation

Supervision and mentoring

01.2020 **Yassine Zouaghi**, M.Sc. in Life Sciences, EPFL

   09.2019   Master Thesis: Applied machine learning for long-term imaging of mitochondria

02.2019 **Eliana Renzo**, M.Sc. in Physics, EPFL

   06.2019   Semester project: Simulation of hindered particle diffusion

07.2019 **Céline Le**, B.Sc. in Life Sciences, EPFL

   06.2019   Summer project: MRG-size in U2OS cells using STORM

07.2019 **Mariona Colomer**, B.Sc. in Physics, Barcelona

   06.2019   Summer internship: Development of various analysis pipelines

07.2019 **Marian Martinez**, B.Sc. in Mathematics & Physics, Barcelona

   06.2019   Summer internship: Simulation of random distributions

11.2018 **Emilie Cuillery**, M.Sc. in Life Sciences, EPFL

   02.2018   Semester project + internship: Development of TrackFRAP & FRAPtrackAnalyser

06.2018 **Armin Soushtarizadeh**, M.Sc. in Physics, École Normale Supérieur Paris

   09.2017   Co-supervised: Encoding a Neuronal Network to segment & track mitochondria

07.2017 **Etienne Chenais**, B.Sc. in Life Sciences, EPFL

   06.2017   Semester project: Cloning of optogenetic probes

04.2017 **Cordelia Berz**, B.Sc. in Physics, Technical University Berlin

   04.2017   3-week internship: Cloning of optogenetic probes

Teaching

09-12.2019 Biophysics I, EPFL [2 weekly hours + exam corrections]

09-12.2018 Biophysics I, EPFL [2 weekly hours + exam corrections]

09-12.2018 Cell Biology II, EPFL [2 weekly hours + exam corrections]

09-12.2017 Biophysics I, EPFL [2 weekly hours + exam corrections]

02-07.2017 Trigonometry & matrix calculus (MAN), EPFL [4 weekly hours + exam corrections]

Work experience

2016 - 2017 Tansa Backpacking AG, Zurich (Sales, 20-100%)

2011 - 2016 Rolf Beeler, Maître Fromager, Nesselnbach AG (Sales & Hosting, 5-25%)

2008 - 2015 Galerie Römerapotheke, Zurich (Curation, Sales & Hosting, 20%)

2015   STAFF Finder, Zurich (Catering, on-demand)

2011   Restaurant Blaue Ente, Zurich (Catering & waiter, 30%)

2011   Phontom GmbH, Dättwil (telemarketing, 100%)

2010   Fantoche International animation film festival, Baden (Assistant location manager, 100%)

2009 - 2010 BTC Badener Tanzcentrum AG, Baden (Bartending, 30%)

2008 - 2009 Energy Video AG, Baden (DVD-rental, 30%)

Extracurricular engagements

2018 - 20:   *Representative intermediary corps* - School Assembly (AE), EPFL (elected)

2018 - 20:   *Treasurer* - ADSV, EPFL (2x elected; working group on PhD-well being)

2017 - 20:   *Co-founder* - MARDI PARDI & Abenufe-Festival (concert & festival label)

2018 - 19:   *Moderator* - IBI-Grad student minisymposium, Lausanne

2018 - 19:   *Co-organiser* - first LEB-retreat in Crans-Montana

2015 - 17:   *Founder & President* - Student Wine Association Zurich: swaz.vseth.ethz.ch

2015:   *Student Representative* - Structural Biology and Biophysics master advertisement, ETHZ

2014:   *Festival staff* - various May balls, Cambridge UK

2013 - 14:   *Student Representative* - Part II Zoology, University of Cambridge UK

2011 - 14:   *Student Representative* - Fokusgruppe BSc Biologie, teaching commission biology, promotion committee, faculty meeting MNF, UZH

Personal competences & interests

Programming: Python, MATLAB (beginner), bash (beginner), R (beginner), Fiji-macro

Computer skills: Unix, Libre-Office, Fiji (ImageJ), microscope steering software

Language fluency in German, English (TOEFL score: 115), and French; Rudimentary skills: Italian

Additional certificates: Chainsaw handling (degree Wald Schweiz, 2021); viticulture (degree ZHAW, 2018)

Personal interests: Mountaineering, Rock-climbing, Bouldering, Skitouring, Running (2017-21: several half-Marathons & two Marathons), Rowing (2003 -2007 & 2013/14)

9) Appendix

9.1) EZH2 oncogenic mutations drive epigenetic, transcriptional, and structural
 changes within chromatin domains
as published by *Nature Genetics*
https://doi.org/10.1038/s41588-018-0338-y

9.2) Distinct fission signatures predict mitochondrial degradation or biogenesis
as published by *Nature*
https://doi.org/10.1038/s41586-021-03510-6

9.3) Mitochondrial RNA granules are fluid condensates positioned by membrane
 dynamics
as published by *Nature Cell Biology*
https://doi.org/10.1038/s41556-020-00584-8

EZH2 oncogenic mutations drive epigenetic, transcriptional, and structural changes within chromatin domains

Maria C. Donaldson-Collier[1,5], Stephanie Sungalee [1,5], Marie Zufferey[2,3,5], Daniele Tavernari [2,3,5], Natalya Katanayeva [1], Elena Battistello[1,2,3], Marco Mina[2,3], Kyle M. Douglass[4], Timo Rey[4], Franck Raynaud[2,3], Suliana Manley [4], Giovanni Ciriello [2,3]* and Elisa Oricchio [1]*

Chromatin is organized into topologically associating domains (TADs) enriched in distinct histone marks. In cancer, gain-of-function mutations in the gene encoding the enhancer of zeste homolog 2 protein (EZH2) lead to a genome-wide increase in histone-3 Lys27 trimethylation (H3K27me3) associated with transcriptional repression. However, the effects of these epigenetic changes on the structure and function of chromatin domains have not been explored. Here, we found a functional interplay between TADs and epigenetic and transcriptional changes mediated by mutated *EZH2*. Altered EZH2 (p.Tyr646* (EZH2[Y646X])) led to silencing of entire domains, synergistically inactivating multiple tumor suppressors. Intra-TAD gene silencing was coupled with changes of interactions between gene promoter regions. Notably, gene expression and chromatin interactions were restored by pharmacological inhibition of EZH2[Y646X]. Our results indicate that EZH2[Y646X] alters the topology and function of chromatin domains to promote synergistic oncogenic programs.

n eukaryotic cells, chromatin progressively folds into a hierarchical structure including loops made of relatively short sequences (~1–10 kb), medium-sized domains (100–1,000 kb), also known as topologically associating domains (TADs), and large chromatin compartments (>1 Mb)[1–3]. In particular, TADs are highly conserved among species and cell types[4]. They are preferentially decorated by either active (H3K36me3) or inactive (H3K27me3) epigenetic marks, which can affect the transcriptional activity within the domains[5–7], and have thus been proposed as functional units regulating gene expression in development and differentiation[8,9]. Interestingly, cancer cells can hijack these chromatin domains to drive oncogenic transformation, either through chromosomal aberrations[10,11] or as a consequence of selected mutations affecting the cancer epigenome[12,13].

Mutations of epigenetic modifiers have been detected in several tumor types[14], and alterations in these proteins vary the global epigenetic status of tumor cells. However, their effects on chromatin organization remain unclear. Among recurrent alterations of chromatin remodeling factors, *EZH2* gain-of-function mutations affecting Tyr646 (RefSeq isoform: NM_004456) are common in non-Hodgkin lymphoma[15] and other tumor types[16,17]. EZH2 is the histone lysine methyltransferase regulating H3K27 methylation, and it is part of the Polycomb repressor complex 2 (ref. [18]). EZH2[Y646X] aberrantly increases H3K27me3, promoting transcriptional repression[19,20]. This process has been implicated in stalling B-cell differentiation[21] and epigenetic silencing of tumor suppressors[22]. Given the associations among H3K27me3, chromatin subcompartments, and TADs[23], we wondered whether oncogenic *EZH2* mutations might lead to chromatin structural and/or functional modifications. Here, we show that epigenetic and transcriptional changes induced by

EZH2 mutations are more concordant within TADs than expected and modulate intra-TAD interactions proximal to gene promoters. Intra-TAD structural changes are associated with transcriptional inactivation of entire domains. Our results illustrate how cancer-associated epigenetic alterations can act beyond single genes and modify the activity of entire chromatin domains.

Results

Hi-C chromatin maps of EZH2[WT] and EZH2[Y646X] lymphomas. EZH2 p.Tyr646* gain-of-function alterations lead to a genome-wide increase in H3K27me3 (Supplementary Fig. 1a). To establish whether this global accumulation of H3K27me3 modifies the genome topology on a similarly broad scale, we performed high-throughput chromatin conformation capture (Hi-C) in two lymphoma cell lines (Karpas422 and WSU-DLCL2) expressing the mutant form of EZH2 (EZH2[Y646X]) and a lymphoma cell line (OCI-Ly19) expressing the wild-type EZH2 (EZH2[WT]) protein (Supplementary Table 1 and Supplementary Note). Contact maps of EZH2[Y646X] and EZH2[WT] cells were binned in regions of 50 kb and compared with multiple metrics (Fig. 1). For each pair of maps, we compared the overall distribution of chromosomal contacts by using the stratum-adjusted correlation coefficient (SCC)[24] (Fig. 1a); the fraction of 1-Mb regions assigned to the same compartment (A or B)[3] (Fig. 1b); the similarity among TADs[25–27] (Fig. 1c); and the fraction of bin interactions that were significant in both maps, also known as the cell interactome[28,29] (Fig. 1d). To build a reference scale of values for each metric, we compared Hi-C maps of EZH2[Y646X] lymphoma cell lines with Hi-C maps of endothelial cells (HUVEC), fetal fibroblasts (IMR90), and normal lymphoblastoid cells (GM12878). Moreover, we used randomized contact maps or

[1]Swiss Institute for Experimental Cancer Research (ISREC), School of Life Science, École Polytechnique Fédérale de Lausanne (EPFL), Lausanne, Switzerland. [2]Department of Computational Biology, University of Lausanne (UNIL), Lausanne, Switzerland. [3]Swiss Institute of Bioinformatics (SIB), Lausanne, Switzerland. [4]Institute of Physics, École Polytechnique Fédérale de Lausanne (EPFL), Lausanne, Switzerland. [5]These authors contributed equally: Maria C. Donaldson-Collier, Stephanie Sungalee, Marie Zufferey, Daniele Tavernari. *e-mail: giovanni.ciriello@unil.ch; elisa.oricchio@epfl.ch
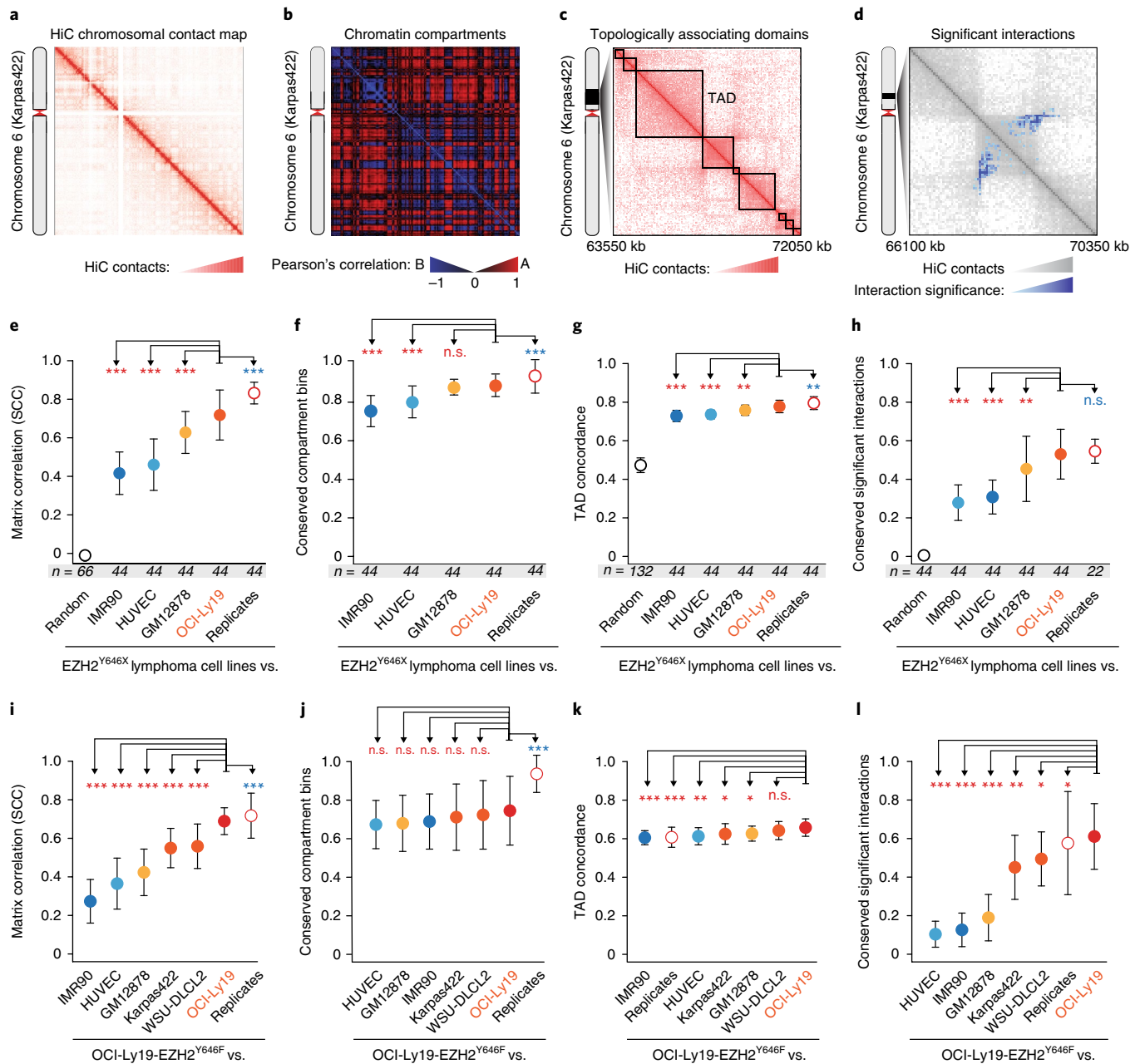
Fig. 1 | Comparison of the genome 3D organization in EZH2^WT and EZH2^Y646X cells. a–d, Chromatin structural elements identifiable by Hi-C; representative images for Chr.6 of the GM12878 cell line: intrachromosomal contact map (**a**); correlation of observed/expected contact ratios for each pair of 1-Mb bins, with the plaid (blue/red) pattern showing chromatin compartments A or B (**b**); TADs (**c**); significant interactions determined by using HiC-DC, with all pairs of 50-kb bins within a 2-Mb window tested (**d**). **e–h**, Comparison between the intrachromosomal contact maps of EZH2^Y646X cell lines (Karpas422 and WSU-DLCL2) and of the indicated cell lines, based on the overall Hi-C matrix correlation using the SCC (**e**); fraction of 1-Mb bins assigned to the same compartment (**f**); TAD similarity measured by measure of concordance (MoC) (**g**); and fraction of shared significant interactions between 50-kb bins determined by HiC-DC (**h**). **i–l**, Comparison between intrachromosomal contact maps of OCI-Ly19-EZH2^Y646F and of the indicated cell lines as described above, that is, based on SCC (**i**), compartment conservation (**j**), TAD similarity (**k**), and the fraction of shared significant interactions (**l**). For all comparisons, the number of compared intrachromosomal maps is indicated below the graphs (*n*), when not indicated *n* = 22; the dotd represent the mean values, and error bars are ±1 standard deviation. *P* values were computed with two-tailed Wilcoxon test (Supplementary Table 1). *$P < 0.05$, **$P < 0.01$, ***$P < 0.001$; n.s., not significant.

TADs and independent experimental replicates of EZH2^Y646X lymphoma cell lines to provide the lowest and highest expected values for each metric, respectively. The similarity ranks obtained with all metrics were highly concordant and invariably showed that the contact maps from EZH2^Y646X lymphoma were on average more similar to those from EZH2^WT cell lines than to any other cell model that

we tested, except for their replicates (Fig. 1e–h and Supplementary Fig. 1b–e).

To validate this observation and allay nonspecific effects due to heterogeneity among samples, we generated a syngeneic lymphoma cell line (OCI-Ly19) expressing the altered protein EZH2^Y646F (c.1937A>T, p.Tyr646Phe). We confirmed that expression of

EZH2[Y646F] increased H3K27me3 across the genome, as compared with both the parental cell line and OCI-Ly19 transduced with an empty vector, whereas expression of EZH2 remained similar in the three conditions (Supplementary Fig. 1f,g). Hi-C contact maps derived for OCI-Ly19-EZH2[Y646F] and OCI-Ly19 cells were as similar to or more similar than maps derived from independent replicates of the same cell line (Fig. 1i–l and Supplementary Fig. 1h). We conclude that although a certain diversity exists for a limited number of specific contacts and contact domains, on average, the genome topology of *EZH2*-mutated and wild-type lymphoma cells is highly similar.

EZH2[Y646X] inactivates selected TADs. Given the observed consistency between the chromatin structures of EZH2[Y646X] and EZH2[WT] cell lines, we asked whether an association might exist between chromatin structural elements and the epigenetic and transcriptional changes induced by *EZH2* gain-of-function mutations. In particular, we focused on chromatin subcompartments and TADs, given that both have been associated with H3K27me3 (ref. [23]).

To assess changes in H3K27me3 specifically induced by *EZH2* mutations, we analyzed H3K27me3 levels in OCI-Ly19 cells expressing either EZH2[Y646F] or EZH2[WT]. The distribution of H3K27me3 in chromatin subcompartments confirmed the previously reported enrichment in H3K27me3 within the B1 compartment[23] (Supplementary Fig. 2a). However, in OCI-Ly19-EZH2[Y646F], we observed a significant but similar increase in H3K27me3 across all subcompartments (Supplementary Fig. 2a,b), thus suggesting that EZH2[Y646X] does not induce epigenetic changes specifically within one subcompartment.

Next, we tested whether differences in H3K27me3 and gene expression were more concordant within TADs than expected and whether this association might lead to the activation or inactivation of specific domains (Fig. 2a). First, we extracted a consensus list of 2,038 TADs that comprised at least three expressed genes and were conserved among three EZH2[Y646X] cell lines (Karpas422, WSU-DLCL2, and OCI-Ly19-EZH2[Y646F]) and one EZH2[WT] cell line (OCI-Ly19) (Supplementary Table 2). H3K27me3 chromatin immunoprecipitation and high-throughput sequencing (ChIP-seq) data were compared both between OCI-Ly19-EZH2[WT] and OCI-Ly19-EZH2[Y646F] and between OCI-Ly19-EZH2[WT] and two cell lines (Karpas422 and WSU-DLCL2) with endogenous *EZH2* mutations. The TAD mean H3K27me3 values in OCI-Ly19-EZH2[Y646F] were highly correlated with those observed in Karpas422 and WSU-DLCL2 (Supplementary Fig. 2c); thus, we decided to focus on the OCI-Ly19-EZH2[WT] and OCI-Ly19-EZH2[Y646F] ChIP-seq datasets, because they reflected H3K27me3 changes directly associated with the *EZH2* mutation. The distribution of TAD mean H3K27me3 values exhibited a positive shift in EZH2[Y646X] compared with EZH2[WT]

cells (Fig. 2b). H3K27me3 profiles of loci within the same TAD were more correlated than profiles of loci belonging to distinct adjacent domains in both cell lines (Supplementary Fig. 2d,e). Moreover, H3K27me3 fold changes between OCI-Ly19 mutated cells and wild-type cells were also more correlated within the same TAD than between adjacent TADs (Fig. 2c), and this trend was independent of the distance between the genomic loci (Fig. 2d). Overall, these results indicate that the EZH2-mediated increase in H3K27me3 is associated with the compartmentalization of the chromatin in TADs.

Interestingly, the distribution of H3K27me3 fold changes (EZH2[Y646X] versus EZH2[WT]) within TADs exhibited a greater number of high fold changes than random distributions obtained by permuting 50-kb or 100-kb intervals of H3K27me3 ChIP-seq reads (Fig. 2e). This trend was independent of the subcompartment to which each TAD was assigned (Supplementary Fig. 2f) and of the interval size used in the permutations (Supplementary Fig. 2g). Moreover, by comparing matched TAD mean H3K27me3 values in EZH2[WT] and EZH2[Y646F] OCI-Ly19 cells, we found that H3K27me3 did not proportionally increase in all domains, but fold changes were greater in domains that had low histone methylation in EZH2[WT] cells than in domains that were already enriched in H3K27me3 (Fig. 2f). Therefore, the increase in H3K27me3 mediated by EZH2 alterations within specific domains was not randomly distributed but were dependent on the initial level of H3K27me3 (Fig. 2g).

Next, we assessed the effects of H3K27me3 changes on transcription, in OCI-Ly19-EZH2[Y646F] and OCI-Ly19-EZH2[WT] cell lines. In particular, we wondered whether the observed correlation between H3K27me3 changes within TADs might be reflected in concordant mRNA expression changes in genes within the same TAD. For this purpose, we scored each TAD on the basis of the number and magnitude of concordant gene fold changes within the domain (mRNA fold-change concordance (FCC) scores; Supplementary Fig. 3a). For this analysis, we selected only TADs for which at least three genes had detectable mRNA expression in either OCI-Ly19-EZH2[Y646F] or OCI-Ly19-EZH2[WT]. The observed FCC scores were compared with those obtained after randomly permuting gene-to-TAD assignments. The observed FCC scores were higher than expected on the basis of random permutations, thus indicating that changes in gene expression in OCI-Ly19-EZH2[Y646F] compared with OCI-Ly19-EZH2[WT] were significantly concordant within TADs (Supplementary Fig. 3b).

To validate this finding in larger cohorts of B-cell lymphoma samples, we collected independent mRNA expression data for diffuse large B-cell lymphoma (DLBCL) cell lines[30] including Karpas422 and WSU-DLCL2 (EZH2[WT] $n = 2$, EZH2[Y646X] $n = 6$; each sample was analyzed in duplicate, GSE40792), and primary samples from germinal center (GC) patients with DLBCL[21] (EZH2[WT] $n = 30$,

Fig. 2 | Epigenetic and transcriptional changes in EZH2[Y646X] cells occur within TADs. a, Study design: H3K27me3 ChIP-seq, mRNA expression, and Hi-C data in EZH2[Y646X] and EZH2[WT] lymphomas were integrated to identify epigenetically and transcriptionally inactive, neutral, and active TADs. **b**, Distribution of mean H3K27me3 signal within TADs in OCI-Ly19-EZH2[WT] and OCI-Ly19-EZH2[Y646F] cells. **c**, Correlation across $n = 2,038$ TADs of H3K27me3 fold changes in loci within the same TAD and loci separated by one TAD boundary. **d**, Correlation (y axis) of H3K27me3 fold changes between all 25-kb bin pairs within the same TADs and bin pairs separated by one TAD boundary as a function of their distance (x axis). **e**, Distributions of mean H3K27me3 fold changes for $n = 2,038$ TADs and of fold changes obtained by permuting H3K27me3 bins (50 kb and 100 kb). **f**, Correlation between TAD mean H3K27me3 ($n = 2,038$ TADs) in OCI-Ly19-EZH2[WT] (x axis) and OCI-Ly19-EZH2[Y646F] (y axis). **g**, TAD mean H3K27me3 fold changes ($n = 2,038$ TADs) between OCI-Ly19-EZH2[Y646F] and OCI-Ly19-EZH2[WT]; H3K27me3 values in OCI-Ly19-EZH2[WT] were binned (bin$_i = (i - 1, i)$), and TAD mean H3K27me3 fold changes in each bin are reported. Expected values were determined by TAD permutation. **h–j**, Cumulative sum curves of mRNA FCC for EZH2[Y646X] ($n = 12$) versus EZH2[WT] cells ($n = 4$) in 2,038 TADs (**h**), GC-DLBCL EZH2[Y646X] ($n = 7$) versus EZH2[WT] ($n = 30$) patient samples in 2,038 TADs (**i**), and FL EZH2[Y646X] ($n = 6$) versus EZH2[WT] ($n = 17$) patient samples in 1,908 TADs (**j**). Observed curves are compared with random curves obtained after 10,000 gene-to-TAD assignment permutations (gray area delimits minimum and maximum values; dark line is the mean). **k,l**, TAD mean H3K27me3 fold changes between OCI-Ly19-EZH2[Y646F] and OCI-Ly19-EZH2[WT] cells (x axis) versus the TAD mRNA-expression fold changes in EZH2[Y646X] versus EZH2[WT] cell lines (y axis) for $n = 2,038$ TADs; in **l**, inactive TADs ($\log_2(\text{FC}_{\text{H3K27me3}}) > 1$ and $\log_2(\text{FC}_{\text{mRNA}}) < -1$) are highlighted. **m**, Gene-set enrichment analysis for $n = 283$ genes within inactive TADs according to Gene Ontology categories ($n = 5,337$) and experimentally derived gene sets ($n = 3,409$). Gene-set enrichment was tested by hypergeometric test (one-sided) and adjusted by false discovery rate.

EZH2^{Y646X} $n = 7$, GSE23501) and patients with follicular lymphoma (FL)[31] (EZH2^{WT} $n = 17$, EZH2^{Y646X} $n = 6$, PRJNA278311). Across all datasets, we verified that mRNA expression was more correlated between genes in the same TAD than between genes in different TADs, independently of their genomic distance (Supplementary Fig. 3c–e). Furthermore, the FCC scores obtained by comparing EZH2^{Y646X} and EZH2^{WT} cases were always greater than random,

with an overall increase ranging between 15% and 33% (increase in area under the curve; Fig. 2h–j and Supplementary Fig. 3b). Across all the expression datasets that we analyzed, expression changes associated with *EZH2* mutations were more concordant within TADs than expected.

Next, we compared matched mean H3K27me3 and mRNA expression changes within TADs in OCI-Ly19-EZH2^{Y646F} and
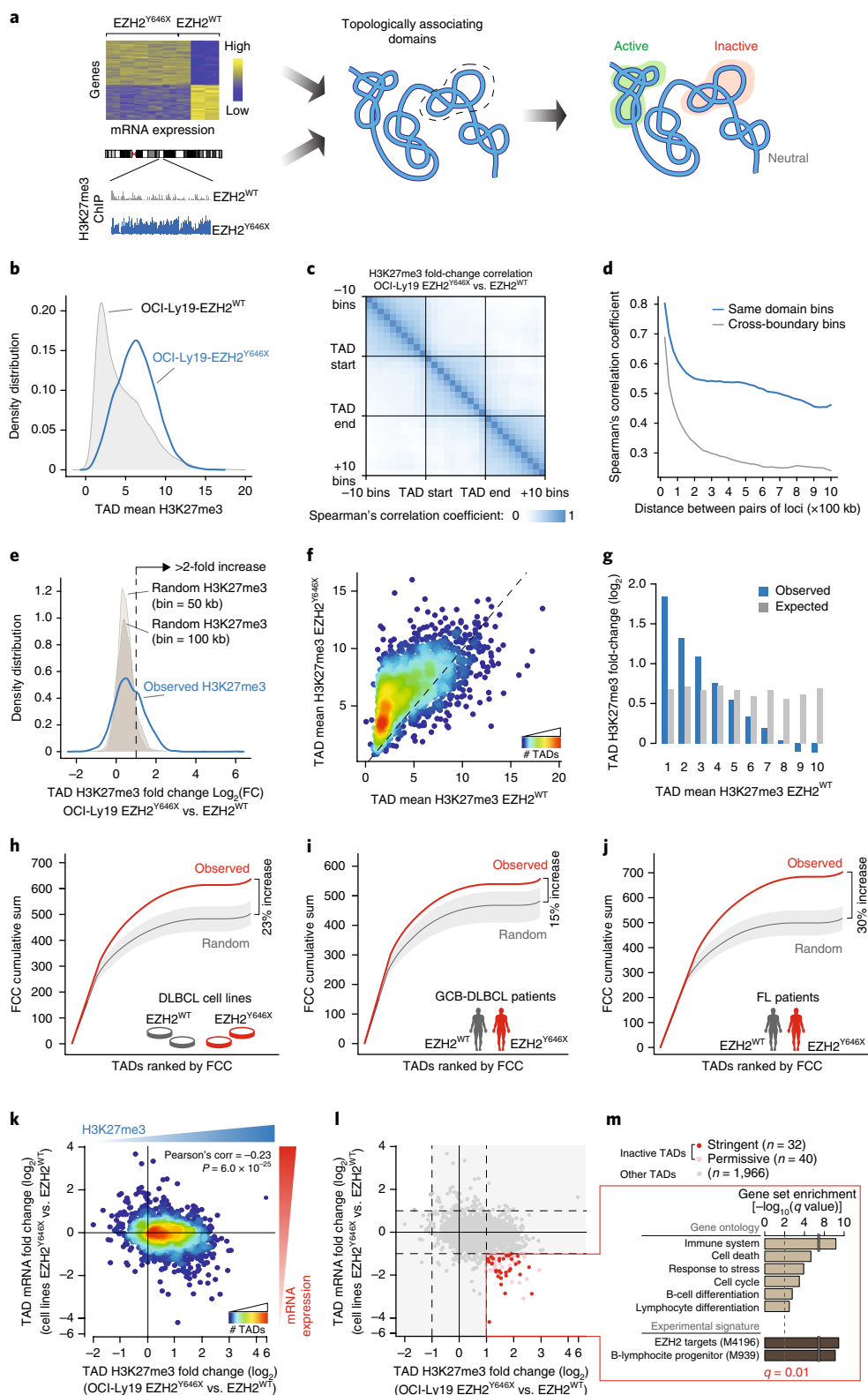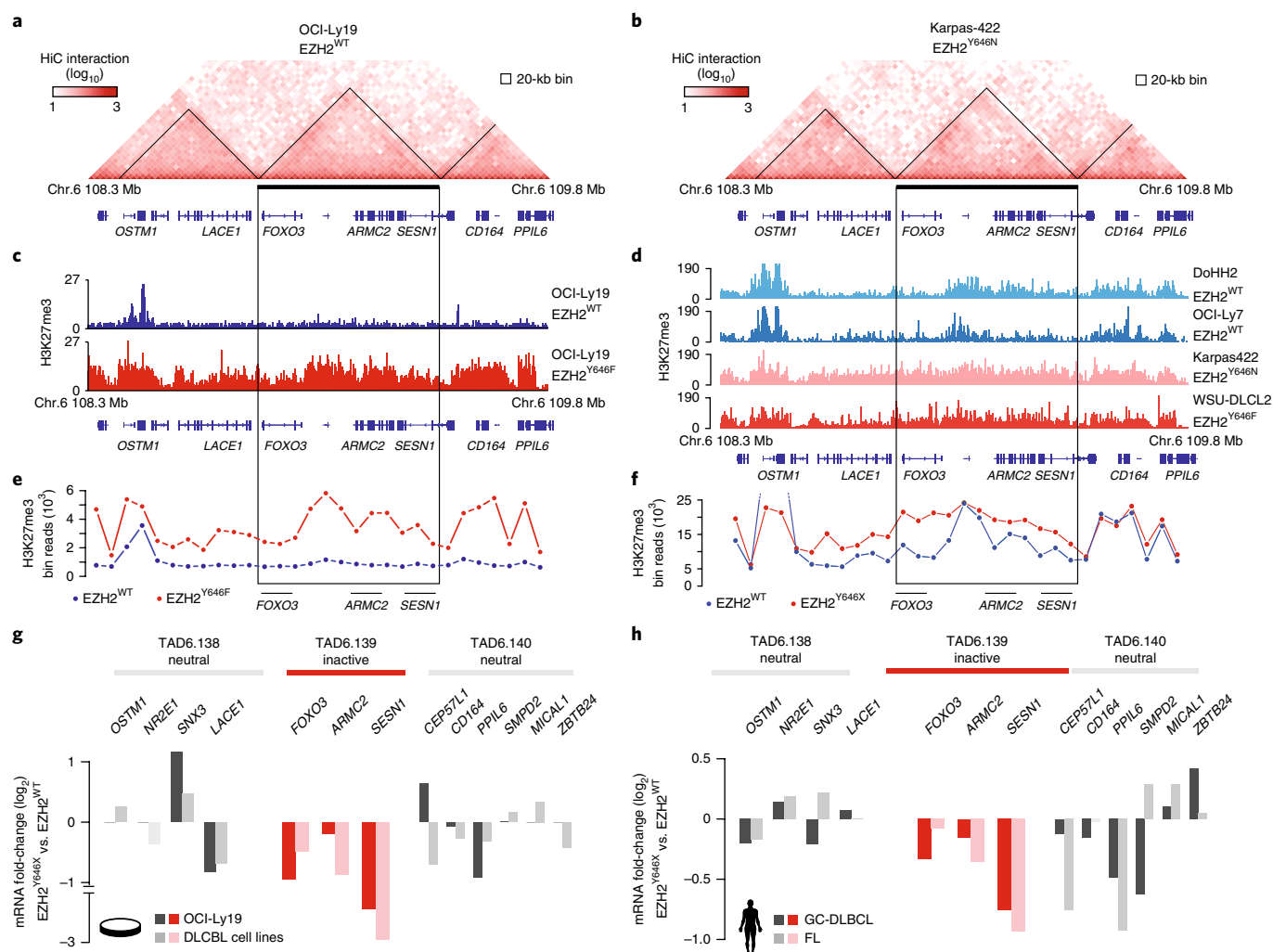
Fig. 3 | Inactivation of the tumor-suppressive TAD comprising *FOXO3* and *SESN1*. a,b, Hi-C contact maps at 20-kb resolution of the genomic region Chr.6 108.3–109.8 Mb in OCI-Ly19-EZH2^{WT} (**a**) and Karpas422-EZH2^{Y646N} (**b**). TADs are contoured in black, and representative genes within the TADs are shown. **c,d**, H3K27me3 ChIP-seq tracks on Chr.6 108.3–109.8 Mb for OCI-Ly19-EZH2^{WT} and OCI-Ly19-EZH2^{Y646F} ($n=3$ experiments per cell line) (**c**) and for the indicated EZH2^{WT} (DoHH2 and OCI-Ly7) and EZH2^{Y646X} (Karpas422 and WSU-DLCL2) cell lines ($n=2$ experiments per cell lines, except WSU-DLCL2 for which $n=1$) (**d**). **e,f**, Superimposition of H3K27me3 number of reads within 50-kb bins in Chr.6 108.3–109.8 Mb for OCI-Ly19-EZH2^{WT} and OCI-Ly19 EZH2^{Y646F} (**e**) and EZH2^{WT} and EZH2^{Y646X} (**f**) cells. **g**, mRNA expression fold changes of genes in Chr.6 108.3–109.8 Mb obtained by comparing OCI-Ly19-EZH2^{Y646F} and OCI-Ly19-EZH2^{WT} cell lines and EZH2^{Y646X} ($n=12$ samples) and EZH2^{WT} ($n=4$ samples) cell lines. **h**, mRNA expression fold changes of the genes in Chr.6 108.3–109.8 Mb obtained by comparing EZH2^{Y646X} ($n=7$) versus EZH2^{WT} ($n=30$) GC-DLBCL patient samples and EZH2^{Y646X} ($n=6$) versus EZH2^{WT} ($n=17$) FL patient samples. Fold changes corresponding to the inactive TAD are highlighted in red.

OCI-Ly19-EZH2^{WT} cells. TAD expression fold changes were moderately yet significantly anticorrelated with TAD H3K27me3 fold changes (Pearson's correlation $= -0.31$, $P = 3.2 \times 10^{-21}$, Supplementary Fig. 3f). Moreover, TADs exhibiting an H3K27me3 fold change greater than two and an mRNA expression fold change less than negative two represented the majority (77%) of TADs exhibiting at least a twofold difference in both molecular features (Supplementary Fig. 3f), a result consistent with *EZH2* mutations increasing H3K27me3 and repressing transcription. Within the cell-line cohort including Karpas422 and WSU-DLCL2 (GSE40792), we confirmed a significant anticorrelation between TAD mRNA and H3K27me3 fold changes (Pearson's correlation $= -0.23$, $P = 6 \times 10^{-25}$, Fig. 2k), and TADs exhibiting H3K27me3 fold changes greater than two and mRNA expression fold changes less than negative two represented 86% of the TADs exhibiting at least a twofold difference in both molecular features. This anticorrelation was even more pronounced when only TADs comprising the

most differentially expressed genes were considered (Supplementary Fig. 3g,h). Overall, EZH2^{Y646X}-driven epigenetic and transcriptional changes within TADs were found to be significantly anticorrelated.

The interdependency between gene regulation and TAD structure prompted us to investigate TADs that exhibited a strong increase in H3K27me3 and a strong decrease in gene expression. Within the full set of conserved TADs, we identified 72 'inactive' TADs characterized by a greater than twofold increase in H3K27me3 and a greater-than-twofold decrease in mRNA expression (Fig. 2l). Notably, largely overlapping results were obtained when we considered OCI-Ly19 expression differences (EZH2^{Y646F} versus EZH2^{WT}) or Karpas422 and WSU-DLCL2 H3K27me3 profiles (Supplementary Fig. 3i). Inactive TADs were enriched in genes that were significantly downregulated in EZH2^{Y646X} cell lines (Fisher's exact test $P = 2.8 \times 10^{-37}$, odds ratio (OR) $= 12.4$). Moreover, in 32 of these 72 domains, more than 80% of the genes within the domain exhibited concordant negative fold changes.

We defined these TADs as 'stringent inactive' (Fig. 2l) and the remaining 40 TADs as 'permissive inactive' (Fig. 2l). In primary patient samples, the mRNA fold changes in inactive TADs were significantly lower than those in other TADs (GC–DLBCL, two-tailed t test $P = 2.3 \times 10^{-5}$ and FL, two-tailed t test $P = 1.7 \times 10^{-8}$), and inactive TADs were enriched among TADs with concordant negative fold changes in more than 80% of the genes within their boundaries (Fisher's exact test: $P_{GC-DLBCL} = 0.0006$, $OR_{GC-DLBCL} = 3.2$, and P_{FL} 2.9×10^{-5}, $OR_{FL} = 3.6$).

To explore the functional relevance of inactive TADs, we performed a gene-set enrichment analysis on all genes within these domains. Multiple Gene Ontology categories scored as significant (Supplementary Table 3), including cancer and lymphoma-specific categories (Fig. 2m). Notably, most significantly enriched gene sets contained EZH2 targets previously identified in prostate cancer[32] and genes differentially expressed in B-lymphocyte progenitors (Fig. 2m and Supplementary Table 3). These findings are consistent with EZH2[Y646X] locking in an inactive state genes that are transiently repressed in the GC during B-cell differentiation[21]. To determine whether inactive TADs are also repressed in normal GC cells, we compared the mRNA expression of their genes in normal centroblasts and centrocytes versus differentiated memory B cells[33]. Across all 72 inactive TADs, we identified seven domains that exhibited significant downregulation in centrocytes and centroblasts compared with memory B cells (Supplementary Fig. 3j). Transcriptionally repressed domains included genes regulating B-cell proliferation (for example SESN1)[22], DNA repair (DTX3L and PARP9)[34], and lymphocyte migration and trafficking (for example S1PR1)[35] (Supplementary Fig. 3k).

Overall, these results suggest that genes within inactive TADs are bona fide targets of EZH2 and that inactivation of TADs containing genes involved in B-cell differentiation and proliferation is potentially selected in EZH2-mutated tumors.

Silencing multiple tumor suppressors in inactive TADs. One of the top stringent inactive TADs included the genes *SESN1, FOXO3,* and *ARMC2* (TAD6.139 at chromosome (Chr.) 6 108850−109450 kb; Fig. 3a,b). Recently, we reported that *SESN1* is a direct target of mutated EZH2 and that it acts as a tumor suppressor in FL[22]. *FOXO3* has been described as bona fide tumor-suppressor gene controlling multiple signalings[36]. Moreover, genes within this locus are frequently co-deleted in non-Hodgkin lymphoma, and these deletions are largely mutually exclusive with *EZH2* mutations[22,37,38]. The inactive TAD6.139 exhibited a significant increase in H3K27me3 encompassing the entire domain in OCI-Ly19 cells overexpressing EZH2[Y646F], whereas H3K27me3 was detected only in specific regions in OCI-Ly19-EZH2[WT] cells (Fig. 3c,e). Similarly, an independent comparison of H3K27me3 levels in EZH2-mutated and wild-type cells confirmed a clear increase in H3K27me3 within the entire inactive TAD (Fig. 3d,f). Consistently, all genes within TAD6.139 exhibited lower mRNA expression in OCI-Ly19-EZH2[Y646F]

and in EZH2-mutated lymphoma cells (Fig. 3g), as well as in GC-DLBCL and FL patient samples with EZH2[Y646X] mutations (Fig. 3h) compared with EZH2[WT] lymphomas. Enrichment in H3K27me3 was confirmed by targeted ChIP (Supplementary Fig. 4a), and changes in expression in OCI-Ly19-EZH2[Y646F] cells were confirmed by quantitative PCR (Supplementary Fig. 4b). Notably, additional genes with previously described tumor-suppressive function were found within inactive TADs (Supplementary Table 2). For example, similar patterns of H3K27me3 and gene downregulation were confirmed in TAD3.47 (Chr.3 33150−33450 kb), encompassing the tumor-suppressor gene *FBXL2* (refs. [39,40]) and silenced targets in lymphoma, *CRTAP*[41], and *SUSD5*[42] (Supplementary Fig. 4c−e). In particular, FBXL2 mediates degradation of cyclin-D3, which is the most expressed and mutated cyclin-D protein in B-cell lymphoma[43].

Together, these results indicate that mutated *EZH2* promotes concordant downregulation of multiple tumor suppressors within the same TAD, thus suggesting that these domains may function as tumor-suppressive units.

TAD inactivation accelerates lymphomagenesis. To assess the functional consequences of simultaneous downregulation of multiple tumor-suppressor genes within the same chromatin domain, we knocked down, alone and in combination, the expression of *FOXO3, ARMC2,* and *SESN1,* which are included in the candidate tumor-suppressive TAD6.139. We used IL3-dependent pro-B FL5-12 cells as a surrogate model to measure the effects of gene downregulation on B-cell proliferation[38,44]. We knocked down *Foxo3, Sesn1,* and *Armc2* by using short hairpin RNAs (shRNAs, denoted by 'sh'prefix) coupled with a fluorescent marker[22,44] (Supplementary Fig. 5a−c). The number of cells expressing either sh*Foxo3* or sh*Sesn1* increased two to threefold after four cycles of IL3 withdrawal (12 days). Notably, in the same time frame, cells with the dual knockdown of *Foxo3* and *Sesn1* increased 7- to 12-fold (Fig. 4a,b, Supplementary Fig. 5d, and Supplementary Table 4). We observed a similar enrichment in double-positive cells in normal growth conditions (Supplementary Table 4), whereas a synergistic effect was not observed with concurrent knockdown of *Armc2* and either *Foxo3* or *Sesn1* (Supplementary Fig. 5e,f), thus suggesting a specific functional synergy between loss of *Foxo3* and *Sesn1* to enhance pro-B cell proliferation.

Next, to test the oncogenic potential of the dual loss of *Foxo3* and *Sesn1* in tumor development and progression, we transduced hematopoietic progenitor cells (HPCs) isolated from an Eµ-myc mouse model[45,46] with shRNAs targeting *Foxo3, Sesn1,* or both (Fig. 4c). Animals harboring tumors expressing sh*Foxo3* ($n = 16$), sh*Sesn1* ($n = 17$), or both ($n = 21$) had shorter overall survival than those expressing vector ($n = 14$, sh*Foxo3* versus vector $P = 0.04$, sh*Sesn1* versus vector $P = 0.03$, and sh*Foxo3* and sh*Sesn1* versus vector $P = 0.02$) (Supplementary Fig. 5g). Tumors that originated from HPCs transduced with single shRNAs were enriched in either

Fig. 4 | Concurrent downregulation of genes within tumor-suppressive TADs accelerates B-cell proliferation and lymphoma progression. a, Representative flow cytometry analysis of FL5-12 cells expressing empty vectors coupled with dsRed or GFP, or the sh1-*Foxo3*-dsRed and the sh2-*Sesn1*-GFP at days 0 and 12. Numbers indicate the percentages of cells in each subpopulation ($n = 3$ independent experiments). **b**, Percentages of cells in each subpopulation at days 4, 8, and 12, relative to day 0. Bars indicate mean values, and error bars correspond to one standard deviation over three independent experiments. P values were calculated by two-way analysis of variance (independent variables are shRNA and day of measurement). **c**, Study design of in vivo experiments: HPCs were isolated from Eµ-myc embryos, retrovirally modified with the indicated plasmids, and transplanted into recipient animals. **d**, Representative flow cytometry analysis of HPC before transplantation (left column) and of isolated tumor cells (right column). Numbers indicate the percentages of cells in each subpopulation (sh2-*Sesn1* $n = 3$, sh1-*Foxo3* $n = 4$, sh2-*Sesn1* + sh1-*Foxo3* $n = 4$, independent animals). **e**, Quantitative expression analysis of tumors expressing vector ($n = 4$ independent animals and two technical replicates), sh2-*Sesn1* ($n = 5$ independent animals), sh1-*Foxo3* ($n = 4$ independent animals), and sh2-*Sesn1* and sh1-*Foxo3* ($n = 6$ independent animals). Bars indicate mean values, and error bars correspond to one standard deviation. P values were calculated with two-tailed t test. **f**, Hematoxylin and eosin (H&E) cellular staining and Ki-67 immunohistochemistry of tumor and liver tissue biopsies of Eµ-myc mice expressing the indicated shRNAs or vector ($n = 2$ independent experiments). Scale bar, 200 µm. **g**, Overall survival of secondary recipient animals transplanted with Eµ-myc tumor cells expressing vector ($n = 5$), sh1-*Foxo3* ($n = 5$), sh2-*Sesn1* ($n = 5$) or sh2-*Sesn1* and sh1-*Foxo3* ($n = 5$). P value was calculated with log-rank test.

GFP-positive (sh*Sesn1*) or dsRed-positive (sh*Foxo3*) cells (Fig. 4d). Notably, even though HPCs transduced with both shRNAs showed a low percentage of double-positive cells in the initial population (5–8%), tumors originating from these HPCs were almost exclusively composed of double-positive cells (Fig. 4d), thus suggesting that cells expressing both shRNAs expanded more rapidly than cells with a single shRNA. We confirmed that tumors expressing single or double shRNAs efficiently downregulated the expression of

targeted genes (Fig. 4e), and all of the animals exhibited characteristic features of aggressive lymphoma (Fig. 4f and Supplementary Fig. 5h,i). To determine whether dual loss of *Foxo3* and *Sesn1* boosts tumor aggressiveness, we transplanted purified tumor cells with single and double knockdown into secondary recipient animals. Here, we observed a significant acceleration of tumor development (*P* = 0.001) (Fig. 4g) in animals receiving cells with double knockdown compared with those with a single shRNA. These results
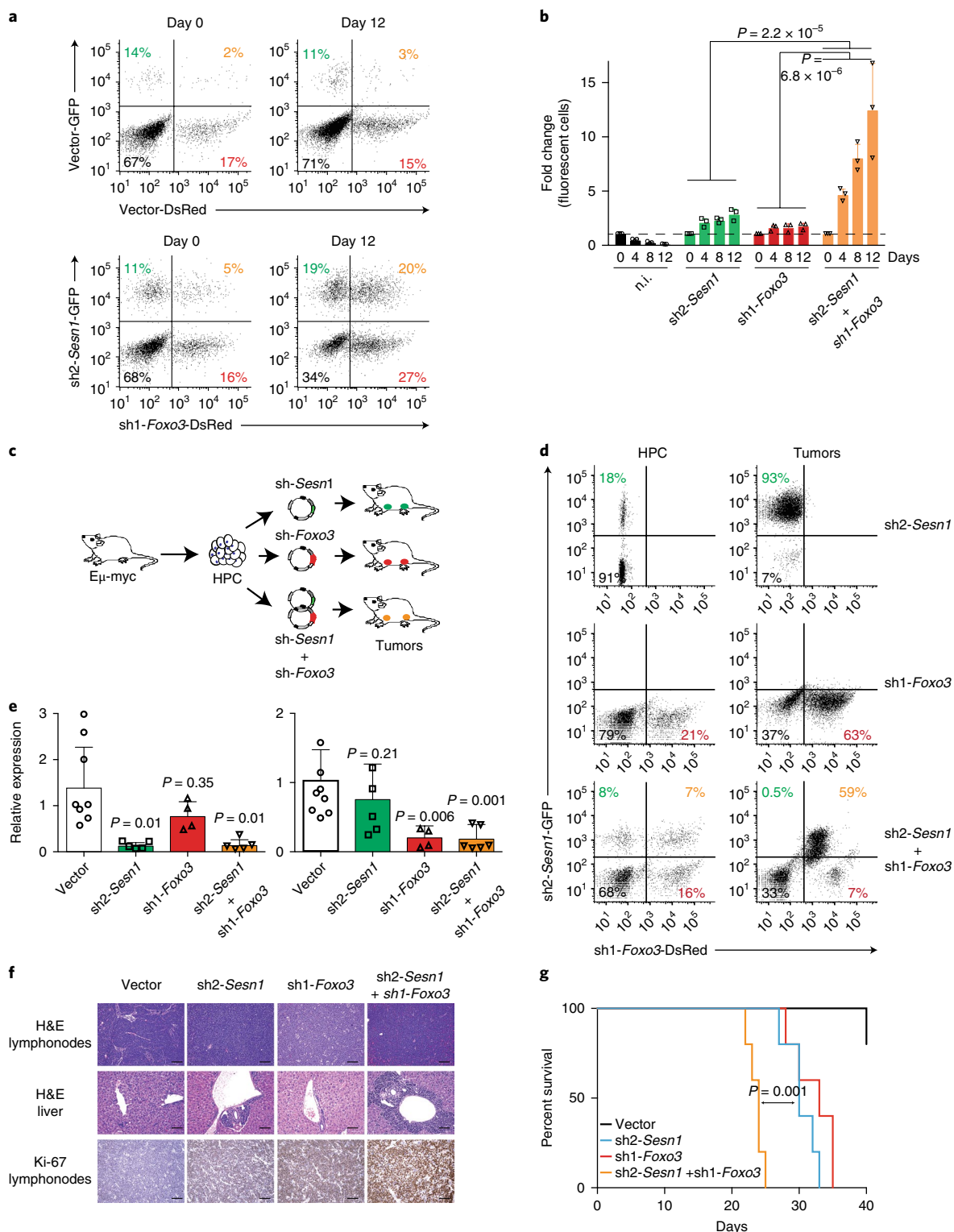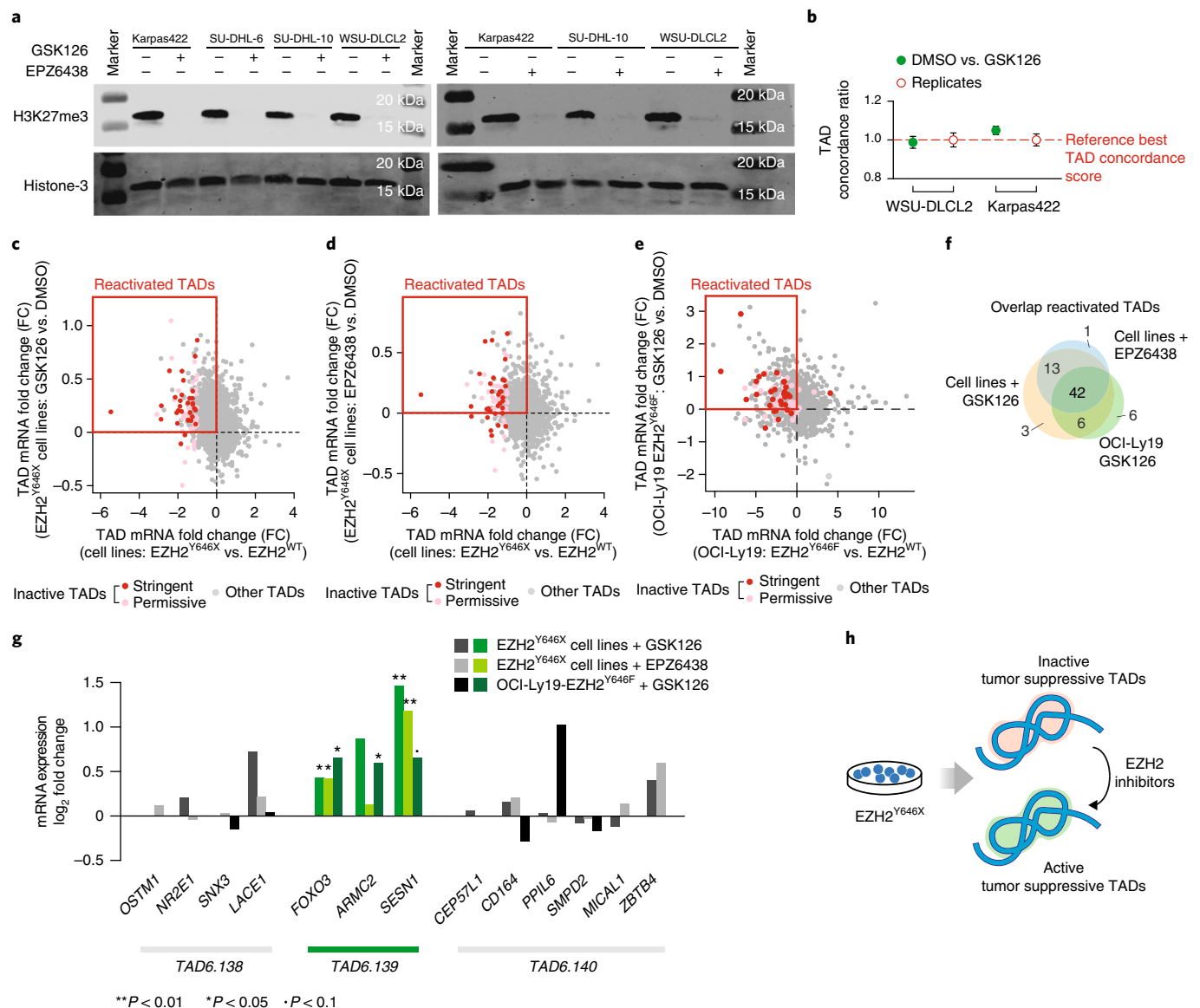
Fig. 5 | Inhibition of EZH2 abrogates H3K27me3 and reactivates inactive TADs. a, Immunoblot for H3K27me3 in EZH2[Y646X] cell lines treated with 2 μM of GSK126 or 1 μM of EPZ6438 or vehicle (DMSO) for 72 h. Total histone H3 was used as a loading control, and the experiment was repeated twice. **b**, Ratio of TAD concordance (MoC) between WSU-DLCL2 and Karpas422 treated with DMSO or GSK126 and TAD concordance between independent replicates of each cell line (DMSO). Dots indicate the means of 22 intrachromosomal-map comparisons, and error bars are ±1 standard deviation. **c,d**, TAD mRNA expression fold changes in EZH2[Y646X] ($n=12$) versus EZH2[WT] ($n=4$) cell lines (x axis) versus TAD mRNA expression fold changes in EZH2[Y646X] cells treated with GSK126 ($n=12$) versus DMSO ($n=12$) (**c**) or treated with EPZ6438 ($n=12$) versus DMSO ($n=12$) (y axis) (**d**). **e**, TAD mRNA expression fold changes of OCI-Ly19-EZH2[Y646F] versus OCI-Ly19-EZH2[WT] (x axis) and in OCI-Ly19-EZH2[Y646F] treated with GSK126 versus DMSO (y axis). **f**, Intersection of inactive TADs obtaining a $\log_2(FC_{mRNA}) > 0$ (reactivated) in EZH2[Y646X] cell lines treated with GSK126 or EPZ6438, or OCI-Ly19-EZH2[Y646F] cells treated with GSK126. **g**, mRNA expression fold changes of individual genes in Chr.6 108.3–109.8 Mb obtained by comparing EZH2[Y646X] cell lines treated with GSK126 ($n=12$) or EPZ6438 ($n=12$) versus DMSO ($n=12$) and OCI-Ly19-EZH2[Y646F] treated with GSK126 ($n=3$) versus vehicle ($n=3$). Fold changes corresponding to the inactive TAD are highlighted in green; P values were computed with limma two-sided t test. **h**, Graphical summary of the results: treatment with EZH2 inhibitors act as a switch turning tumor-suppressive TADs from transcriptionally inactive to active domains. *$P < 0.05$, **$P < 0.01$, ●$P < 0.1$.

demonstrate that the inactivation of the tumor-suppressive TAD6.139 by mutated *EZH2* synergistically downregulates multiple tumor suppressors to drive tumor development and progression.

EZH2[Y646X] inhibition reactivates transcription within TAD. Next, we explored the potential of blocking EZH2 methyltransferase activity by using two pharmacological inhibitors (GSK126 and EPZ6438) to reactivate inactive TADs. Pharmacological inhibition of EZH2 with either GSK126 or EPZ6438 efficiently

depleted H3K27me3 in lymphoma cells (Fig. 5a). However, loss of H3K27me3 did not significantly modify the chromatin compartmentalization into TADs. Indeed, TADs derived from intrachromosomal maps of treated and untreated cells exhibited conservation scores similar to those observed for independent replicates of the same cell line (Fig. 5b). Nevertheless, EZH2[Y646X] cell lines treated with the EZH2 inhibitors GSK126 and EPZ6438 ($n=12$ treated and $n=12$ DMSO) exhibited multiple transcriptional changes, although not as extreme as those observed between EZH2[Y646X] and EZH2[WT]

cells (Supplementary Fig. 6a,b). By mapping differentially expressed genes to our list of conserved TADs, we found that the TAD mRNA expression changes induced by the two inhibitors were positively correlated (Supplementary Fig. 6c) and mostly corresponded to upregulation (positive fold changes) of TADs that were downregulated (negative fold changes) in EZH2^{Y646X} compared with EZH2^{WT} cells (Supplementary Fig. 6d,e). Importantly, most inactive TADs (64/72 with GSK126 and 56/72 with EPZ6438) exhibited positive fold changes, and these reactivated TADs were enriched in significantly upregulated genes (adjusted P value < 0.01) from both experiments (Fig. 5c,d) (DMSO versus GSK126: Fisher's exact test $P = 10^{-4}$, OR = 2.74, DMSO versus EPZ6438: Fisher's exact test $P = 6.8 \times 10^{-8}$, OR = 3.17). A similar reactivation (54/72 inactive TADs) was verified in OCI-Ly19-EZH2^{Y646F} cells treated with the GSK126 inhibitor (Fig. 5e and Supplementary Fig. 6f). Reactivated TADs had a high degree of overlap among the three experiments (Fig. 5f). In particular, after treatment with both EZH2 inhibitors, genes within the tumor-suppressive TAD6.139 exhibited positive fold changes in all three models, results consistent with a stringent inactive-to-active switch of the domain, in which all genes are concordantly regulated (Fig. 5g). Conversely, TADs flanking TAD6.139 showed no pattern of co-regulation. These results were validated through quantitative PCR (Supplementary Fig. 6g). Notably, treatment with EZH2 inhibitors increased *FOXO3*, *SESN1*, and *ARMC2* expression exclusively in OCI-Ly19-EZH2^{Y646F} cells, whereas no significant expression changes were observed in the OCI-Ly19-EZH2^{WT} cells (Supplementary Fig. 6h). Reactivation of the tumor-suppressive TAD6.139 is thus a direct effect of inhibiting the mutated form of EZH2. Together, these results indicate that pharmacological depletion of H3K27me3 is sufficient to restore the transcriptional activity in previously silenced tumor-suppressive chromatin domains (Fig. 5h).

EZH2^{Y646X} modulates intra-TAD chromatin interactions. Changes in transcriptional activity are frequently associated with novel or missing interactions among regulatory elements[10,12,47]. Although TADs in EZH2^{Y646X}, untreated or treated with EZH2 inhibitors, and EZH2^{WT} cells were highly conserved (Supplementary Fig. 7a), we asked whether transcriptional changes in tumor-suppressive TADs were associated with rewiring of specific interactions within the domains.

To address this question within the TAD6.139, we compared 20-kb-resolution Hi-C maps for Karpas422 treated with vehicle (Karpas422-DMSO, Fig. 6a) and with GSK126 (Karpas422-GSK126, Fig. 6a). Significant interactions between the 5' ends of the domain (Chr.6 108860–108880 kb) and a region spanning ~100 kb in the middle part of the TAD (Chr.6 109100–109220 kb) were detected in treated and untreated cells (Supplementary Table 5). However, only Karpas422 treated with GSK126 exhibited a highly significant

interaction between genomic regions near the 5' and 3' ends of the domain (Chr.6 108860–108880 kb and 109380–109400 kb) (Fig. 6b). Next, we systematically compared significant interactions in Karpas422-DMSO and/or Karpas422-GSK126 to identify significant differences between these conditions (empirical q value < 0.1) (Fig. 6c). Notably, top-scoring differential interactions (empirical q value = 0.025) highlighted a stronger interaction between the 5' end and the middle region of the domain in Karpas422-DMSO than Karpas422-GSK126, whereas Karpas422-GSK126 exhibited a significantly stronger interaction between the 5' and 3' ends of the domain than Karpas422-DMSO (Fig. 6c,d and Supplementary Table 5). This observation was confirmed by quantification of the number of normalized reads between the 20-kb regions Chr.6 108860–108880 kb and Chr.6 109380–109400 kb ($P = 0.02$) (Supplementary Fig. 7b), and the same significantly different interactions were found in WSU-DLCL2 cells treated with vehicle or GSK126 (Supplementary Fig. 7c–e). To corroborate the observed changes in interaction frequency at higher resolution, we performed UMI-4C in Karpas422, either untreated or treated with GSK126, by using two independent sets of primers (Supplementary Table 6). We observed an enrichment in interactions between the Chr.6 108861–108863 kb and Chr.6 109370–109400 kb regions in cells treated with GSK126 compared with untreated cells (DMSO) with both primers (Fig. 6e,f and Supplementary Fig. 7f,g).

By mapping significantly differential interactions to functionally annotated regions in the genome, we found that these interactions linked genomic regions proximal to gene promoters that are recognizable by H3K4me3 peaks (Fig. 6g and Supplementary Fig. 7h). Notably, chromatin contacts were stronger between genomic regions proximal to *FOXO3* and *SESN1* promoters in EZH2^{Y646X} cells treated with GSK126 than in untreated cells (Fig. 6g). Concordant with the inactive status of TAD6.139 in EZH2^{Y646X} cells, the promoters of *FOXO3*, *ARMC2*, and *SESN1* exhibited lower H3K4me3 and higher H3K27me3 in EZH2^{Y646X} than in EZH2^{WT} cells (Fig. 6g and Supplementary Fig. 7h). Moreover, a peak of H3K27ac and H3K4me1 was detected at the *SESN1* promoter only in OCI-Ly7 EZH2^{WT} cells, thus suggesting that in these cells, this promoter might have distal enhancer function[48] (Supplementary Fig. 7h).

To determine whether treatment with EZH2 inhibitor restored intra-TAD interactions that were modified by the increase of H3K27me3 in EZH2 mutated tumors, we performed the same differential-interaction comparison between syngeneic EZH2^{Y646F} and EZH2^{WT} OCI-Ly19 cells as well as between Karpas422 (EZH2^{Y646N}) and OCI-Ly19 (EZH2^{WT}). OCI-Ly19-EZH2^{WT} showed stronger interactions between *FOXO3* and *SESN1* promoter regions than OCI-Ly19 cells expressing EZH2^{Y646F} (Fig. 6h). The same difference in interaction between these loci was detected between OCI-Ly19-EZH2^{WT} and Karpas422-EZH2^{Y646N} (Supplementary Fig. 7i). Conversely, both OCI-Ly19-EZH2^{Y646F} and Karpas422-EZH2^{Y646N}

Fig. 6 | Intra-TAD structural changes in EZH2^{WT} and EZH2^{Y646X} cells. a, Hi-C contact maps of TAD6.139 at 20-kb resolution (Chr.6 108.84–109.44 Mb) in Karpas422 treated with DMSO (top) or 2 μM GSK126 for 72 h (bottom). **b**, Significant interactions in Karpas422-DMSO (top) or Karpas422-GSK126 (bottom) determined by HiC-DC. Bin pairs within 2-Mb windows were tested. **c**, Significantly different interactions (q value < 0.1) between Karpas422-DMSO and Karpas422-GSK126 ($n = 435$ tested interactions). Empirical q values were determined as described in Methods. **d**, Most significantly different interactions between Karpas422-DMSO and Karpas422-GSK126. **e**, UMI-4C domainogram: mean number of contacts (percentage of the maximum) in the Chr.6 108.80–109.45 kb region. **f**, Normalized number of UMI-4C reads in Karpas422-DMSO and Karpas422-GSK126. **g**, Significantly stronger interaction (compare to **c**) in Karpas422-GSK126 than Karpas422-DMSO connecting Chr.6 108.85–108.81 Mb and Chr.6 109.39–109.45 Mb. H3K4me3 and H3K27me3 ChIP-seq tracks in Karpas422 and OCI-Ly7 ($n = 3$ experiments) within the same genomic coordinates. **h**, Left, Hi-C contact maps of TAD6.139 at 20-kb resolution in OCI-Ly19-EZH2^{Y646F} (top) and OCI-Ly19-EZH2^{WT} (bottom). Center, significant interactions in OCI-Ly19-EZH2^{Y646F} (top) or OCI-Ly19-EZH2^{WT} (bottom) determined by HiC-DC. Top right, significantly different interactions (q value < 0.1) between OCI-Ly19-EZH2^{Y646F} and OCI-Ly19-EZH2^{WT} ($n = 435$ tested interactions). Empirical q values were determined as described in Methods. Bottom right, most significantly different interactions between OCI-Ly19-EZH2^{Y646F} and OCI-Ly19-EZH2^{WT}. **i**, FISH library design for TAD6.139 and representative images acquired in wide field (left) and by STORM (right). **j**, Eccentricity of TAD6.139 (neighborhood radius = 40) in WSU-DLCL2 treated with 2 μM GSK126 or DMSO for 72 h ($n = 4$ experiments), and OCI-Ly19-EZH2^{WT} and OCI-Ly19-EZH2^{Y646F} ($n = 3$ experiments). Dots are means of multiple measurements of independent cells (Supplementary Table 7), and error bars are standard errors.

exhibited stronger interactions between promoter regions of *FOXO3* and *ARMC2* than OCI-Ly19-EZH2[WT] (Fig. 6h and Supplementary Fig. 7i). To verify whether changes in promoter proximity also occurred in other inactive TADs, we performed a differential interactome analysis within the complete set of 72 inactive TADs, as well as within 100 sets of 72 randomly sampled neutral TADs. By comparing Karpas422-EZH2[Y646N] and OCI-Ly19-EZH2[WT] cells,

we found 34 interactions that were significantly different within inactive TADs, but only 19 on average in neutral TADs ($P = 0.04$, Supplementary Fig. 7j). Furthermore, significant different interactions between EZH2[WT] and EZH2[Y646X] cells were highly overlapping with those observed between cells treated with the EZH2 inhibitor GSK126 and untreated cells (17 out of 34, Fisher's exact test $P = 6 \times 10^{-20}$, OR = 130) (Supplementary Fig. 7k). In summary, we
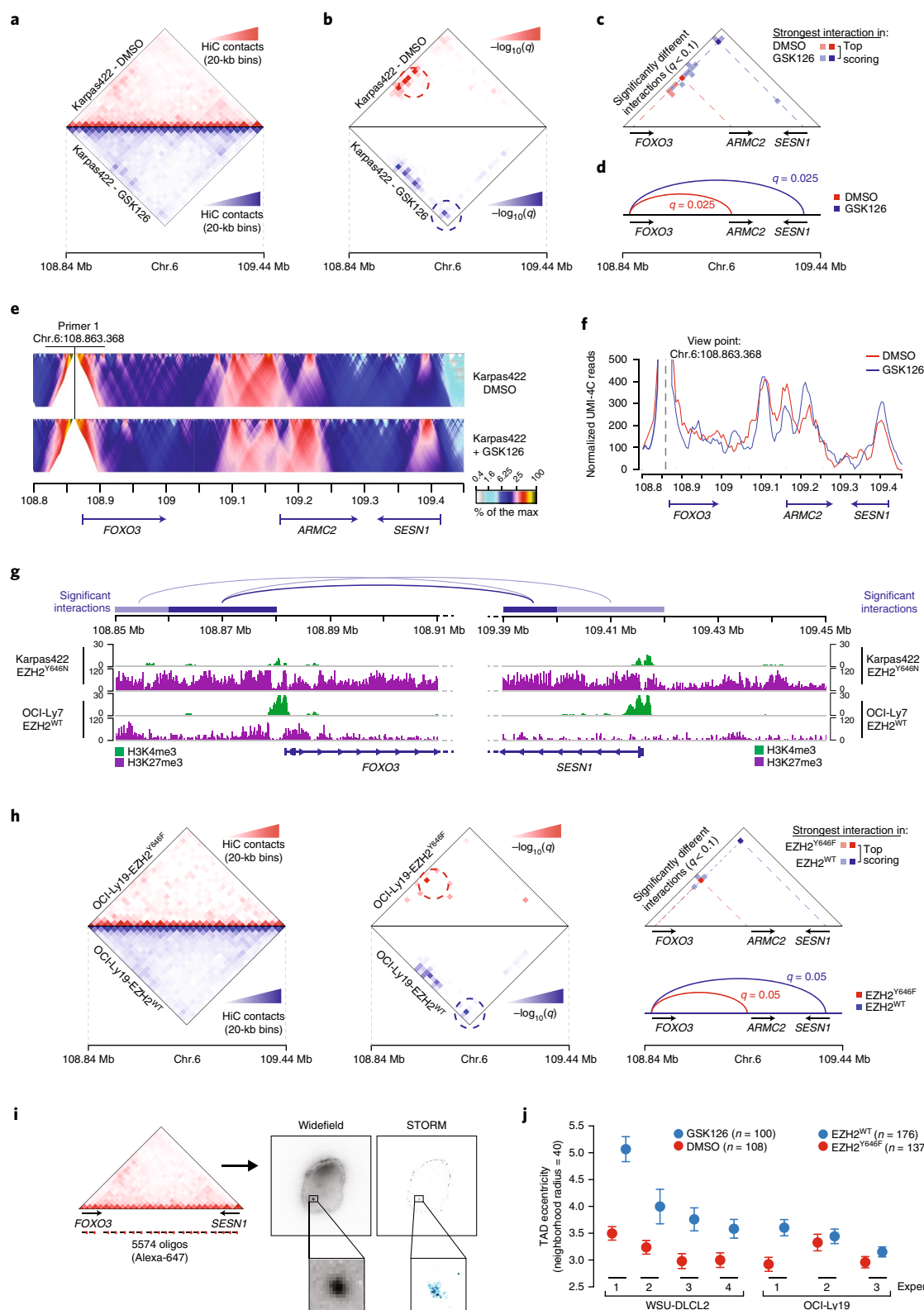
confirmed in multiple conditions, that the increase in H3K27me3 in *EZH2*-mutated tumors modulates promoter–promoter interactions within inactive TADs, which are coupled with silencing of gene transcription.

To investigate the degree of observable physical changes of the intra-TAD structure, we used a super-resolution imaging technique (stochastic optical reconstruction microscopy, or STORM)[49,50] and analyzed WSU-DLCL2 (DMSO versus GSK126, $n=4$ experiments) and OCI-Ly19 cells (EZH2^{Y646F} versus EZH2^{WT}, $n=3$ experiments). To image the TAD structure by STORM, we designed a fluorescence in situ hybridization (FISH) library painting the entire TAD6.139 (Fig. 6i, Supplementary Fig. 8a, and Supplementary Note). TAD6.139 did not change significantly in size (as estimated by radius of gyration, R_g) between the two conditions in all experiments (Supplementary Table 7). However, we observed consistent changes in shape, as evidenced by higher eccentricity values in EZH2^{WT} and EZH2^{Y646X}-GSK126 cells than in EZH2^{Y646X} cells (Fig. 6j and Supplementary Fig. 8b–e). This increase in eccentricity was not observed in a neutral TAD of similar size (TAD1.54, Chr.1: 28650–29100 kb), exhibiting neither transcriptional nor epigenetic changes (Supplementary Fig. 8f,g).

Overall, our results indicate that the increase in H3K27me3 associated with *EZH2* gain-of-function mutations can modify the architecture and transcriptional activity within TADs.

Discussion

The recent advent of chromatin-conformation-capture techniques provides new opportunities and perspectives to unravel the effects of chromatin remodeling in cancer. EZH2^{Y646X} increases H3K27me3 across the genome, thus leading to transcriptional repression. Here, we found that these epigenetic and transcriptional changes were not randomly distributed but were enriched and concordant within specific TADs, termed inactive TADs. Although future work will be needed to explore whether this specificity is predetermined or emerges through selection of oncogenic traits, inactive TADs were enriched in both EZH2 targets and B-cell differentiation programs, thus suggesting that both scenarios are likely and play a role in implementing EZH2^{Y646X} oncogenic potential.

H3K27me3 determines changes in nucleosome proximity and is a marker of closed chromatin. Using multiple models, we showed that H3K27me3 modulates the proximity of gene promoters in association with gene expression changes. In particular, concordant expression changes of *FOXO3* and *SESN1* suggest co-regulated transcription. Interestingly, both genes are direct transcriptional targets of p53 (refs. [51,52]), thus prompting the hypothesis that promoter proximity may favor coordinated transcription of genes controlled by the same transcription factor.

Coordinated epigenetic and transcriptional reprogramming within TADs led to the synergistic inactivation of multiple tumor suppressors, enhancing B-cell proliferation and tumor growth. On the basis of these results, we introduced the concept of tumor-suppressive TADs. Importantly, analysis of expression changes in individual genes, rather than TADs, would probably have missed this synergistic effect. Moreover, although relatively small mRNA expression changes for individual genes are typically dismissed as random variations, the unexpected concordance of these variations within TADs could identify functionally relevant gene modules.

Chromatin domains can therefore provide a new lens through which to study oncogenic alterations, especially in the context of cancer epigenetic reprogramming.

URLs. ENCODE, https://www.encodeproject.org/; GEO, https://www.ncbi.nlm.nih.gov/geo/; GitHub custom scripts, https://github.com/CSOgroup/Donaldson-et-al-scripts/; Zenodo, https://zenodo.org/; NCBI BioProject https://www.ncbi.nlm.nih.gov/bioproject/; Bioconductor, https://bioconductor.org/; R, https://www.r-project.

org/; Cufflinks, http://cole-trapnell-lab.github.io/cufflinks/; STAR, https://github.com/alexdobin/STAR/; Bowtie, http://bowtie-bio.sourceforge.net/bowtie2/manual.shtml; MACS2, https://github.com/taoliu/MACS/; Picard, http://broadinstitute.github.io/picard/; LIMMA, http://bioconductor.org/packages/release/bioc/html/limma.html; Bedtools, https://bedtools.readthedocs.io/en/latest/; HiC-DC, https://bitbucket.org/leslielab/hic-dc/; TopDom, http://zhoulab.usc.edu/TopDom/; mSIGdb, http://software.broadinstitute.org/gsea/msigdb/index.jsp; hg19 mappability file, http://hgdownload.soe.ucsc.edu/goldenPath/hg19/encodeDCC/wgEncodeMapability/wgEncodeCrgMapabilityAlign36mer.bigWig.

Online content

References

1. Bonev, B. & Cavalli, G. Organization and function of the 3D genome. *Nat. Rev. Genet.* **17**, 661–678 (2016).
2. Dixon, J. R., Gorkin, D. U. & Ren, B. Chromatin domains: the unit of chromosome organization. *Mol. Cell* **62**, 668–680 (2016).
3. Lieberman-Aiden, E. et al. Comprehensive mapping of long-range interactions reveals folding principles of the human genome. *Science* **326**, 289–293 (2009).
4. Dixon, J. R. et al. Topological domains in mammalian genomes identified by analysis of chromatin interactions. *Nature* **485**, 376–380 (2012).
5. Sexton, T. et al. Three-dimensional folding and functional organization principles of the Drosophila genome. *Cell* **148**, 458–472 (2012).
6. Nora, E. P. et al. Spatial partitioning of the regulatory landscape of the X-inactivation centre. *Nature* **485**, 381–385 (2012).
7. Le Dily, F. et al. Distinct structural transitions of chromatin topological domains correlate with coordinated hormone-induced gene regulation. *Genes Dev.* **28**, 2151–2162 (2014).
8. de Laat, W. & Duboule, D. Topology of mammalian developmental enhancers and their regulatory landscapes. *Nature* **502**, 499–506 (2013).
9. Fraser, J. et al. Hierarchical folding and reorganization of chromosomes are linked to transcriptional changes in cellular differentiation. *Mol. Syst. Biol.* **11**, 852 (2015).
10. Hnisz, D. et al. Activation of proto-oncogenes by disruption of chromosome neighborhoods.*Science* **351**, 1454–1458 (2016).
11. Weischenfeldt, J. et al. Pan-cancer analysis of somatic copy-number alterations implicates IRS4 and IGF2 in enhancer hijacking. *Nat. Genet.* **49**, 65–74 (2017).
12. Flavahan, W. A. et al. Insulator dysfunction and oncogene activation in IDH mutant gliomas. *Nature* **529**, 110–114 (2016).
13. Taberlay, P. C. et al. Three-dimensional disorganisation of the cancer genome occurs coincident with long range genetic and epigenetic alterations. *Genome Res.* **26**, 719–731 (2016).
14. Plass, C. et al. Mutations in regulators of the epigenome and their connections to global chromatin patterns in cancer. *Nat. Rev. Genet.* **14**, 765–780 (2013).
15. Morin, R. D. et al. Somatic mutations altering EZH2 (Tyr641) in follicular and diffuse large B-cell lymphomas of germinal-center origin. *Nat. Genet.* **42**, 181–185 (2010).
16. Souroullas, G. P. et al. An oncogenic Ezh2 mutation induces tumors through global redistribution of histone 3 lysine 27 trimethylation. *Nat. Med.* **22**, 632–640 (2016).
17. Tirode, F. et al. Genomic landscape of Ewing sarcoma defines an aggressive subtype with co-association of STAG2 and TP53 mutations. *Cancer Discov.* **4**, 1342–1353 (2014).
18. Comet, I., Riising, E. M., Leblanc, B. & Helin, K. Maintaining cell identity: PRC2-mediated regulation of transcription and cancer. *Nat. Rev. Cancer* **16**, 803–810 (2016).
19. Sneeringer, C. J. et al. Coordinated activities of wild-type plus mutant EZH2 drive tumor-associated hypertrimethylation of lysine 27 on histone H3 (H3K27) in human B-cell lymphomas. *Proc. Natl Acad. Sci. USA* **107**, 20980–20985 (2010).
20. Yap, D. B. et al. Somatic mutations at EZH2 Y641 act dominantly through a mechanism of selectively altered PRC2 catalytic activity, to increase H3K27 trimethylation. *Blood* **117**, 2451–2459 (2011).

21. Béguelin, W. et al. EZH2 is required for germinal center formation and somatic EZH2 mutations promote lymphoid transformation. *Cancer Cell* **23**, 677–692 (2013).

22. Oricchio, E. et al. Genetic and epigenetic inactivation of SESTRIN1 controls mTORC1 and response toEZH2 inhibition in follicular lymphoma. *Sci. Transl. Med.* **9**, eaak9969 (2017).

23. Rao, S. S. P. et al. A 3D map of the human genome at kilobase resolution reveals principles of chromatin looping. *Cell* **159**, 1665–1680 (2014).

24. Yang, T. et al. HiCRep: assessing the reproducibility of Hi-C data using a stratum-adjusted correlation coefficient. *Genome Res.* **27**, 1939–1949 (2017).

25. Pfitzner, D., Leibbrandt, R. & Powers, D. Characterization and evaluation of similarity measures for pairs of clusterings. *Knowl. Inf. Syst.* **19**, 361 (2009).

26. Shin, H. et al. TopDom: an efficient and deterministic method for identifying topological domains in genomes. *Nucleic Acids Res.* **44**, e70 (2016).

27. Zufferey, M., Tavernari, D., Oricchio, E. & Ciriello, G. Comparison of computational methods for the identification of topologically associating domains. *Genome. Biol.* **19**, 217 (2018).

28. Carty, M. et al. An integrated model for detecting significant chromatin interactions from high-resolution Hi-C data. *Nat. Commun.* **8**, 15454 (2017).

29. Jin, F. et al. A high-resolution map of the three-dimensional chromatin interactome in human cells. *Nature* **503**, 290–294 (2013).

30. McCabe, M. T. et al. EZH2 inhibition as a therapeutic strategy for lymphoma with EZH2-activating mutations. *Nature* **492**, 108–112 (2012).

31. Ortega-Molina, A. et al. The histone lysine methyltransferase KMT2D sustains a gene expression program that represses B cell lymphoma development. *Nat. Med.* **21**, 1199–1208 (2015).

32. Nuytten, M. et al. The transcriptional repressor NIPP1 is an essential player in EZH2-mediated gene silencing. *Oncogene* **27**, 1449–1460 (2008).

33. Klein, U. et al. Transcriptional analysis of the B cell germinal center reaction. *Proc. Natl Acad. Sci.* **100**, 2639–2644 (2003).

34. Yang, C.-S. et al. Ubiquitin modification by the E3 ligase/ADP-ribosyltransferase Dtx3L/Parp9. *Mol. Cell* **66**, 503–516.e5 (2017).

35. Matloubian, M. et al. Lymphocyte egress from thymus and peripheral lymphoid organs is dependent on S1P receptor 1. *Nature* **427**, 355–360 (2004).

36. Dansen, T. B. & Burgering, B. M. T. Unravelling the tumor-suppressive functions of FOXO proteins. *Trends. Cell Biol.* **18**, 421–429 (2008).

37. Okosun, J. et al. Integrated genomic analysis identifies recurrent mutations and evolution patterns driving the initiation and progression of follicular lymphoma. *Nat. Genet.* **46**, 176–181 (2014).

38. Oricchio, E. et al. The Eph-receptor A7 is a soluble tumor suppressor for follicular lymphoma. *Cell* **147**, 554–564 (2011).

39. Chen, B. B., Glasser, J. R., Coon, T. A. & Mallampalli, R. K. F-box protein FBXL2 exerts human lung tumor suppressor-like activity by ubiquitin-mediated degradation of cyclin D3 resulting in cell cycle arrest. *Oncogene* **31**, 2566–2579 (2012).

40. Li, L., Pan, D., Chen, H., Zhang, L. & Xie, W. F-box protein FBXL2 inhibits gastric cancer proliferation by ubiquitin-mediated degradation of forkhead box M1. *FEBS Lett.* **590**, 445–452 (2016).

41. Hatzimichael, E. et al. The collagen prolyl hydroxylases are novel transcriptionally silenced genes in lymphoma. *Br. J. Cancer* **107**, 1423–1432 (2012).

42. Chambwe, N. et al. Variability in DNA methylation defines novel epigenetic subgroups of DLBCL associated with different clinical outcomes. *Blood* **123**, 1699–1708 (2014).

43. Oricchio, E. et al. Frequent disruption of the RB pathway in indolent follicular lymphoma suggests a new combination therapy. *J. Exp. Med.* **211**, 1379–1391 (2014).

44. Mavrakis, K. J. et al. Genome-wide RNA-mediated interference screen identifies miR-19 targets in Notch-induced T-cell acute lymphoblastic leukaemia. *Nat. Cell Biol.* **12**, 372–379 (2010).

45. Scuoppo, C. et al. A tumour suppressor network relying on the polyamine-hypusine axis. *Nature* **487**, 244–248 (2012).

46. Schatz, J. H. et al. Targeting cap-dependent translation blocks converging survival signals by AKT and PIM kinases in lymphoma. *J. Exp. Med.* **208**, 1799–1807 (2011).

47. Lupiáñez, D. G. et al. Disruptions of topological chromatin domains cause pathogenic rewiring of gene-enhancer interactions. *Cell* **161**, 1012–1025 (2015).

48. Dao, L. T. M. et al. Genome-wide characterization of mammalian promoters with distal enhancer functions. *Nat. Genet.* **49**, 1073–1081 (2017).

49. Boettiger, A. N. et al. Super-resolution imaging reveals distinct chromatin folding for different epigenetic states. *Nature* **529**, 418–422 (2016).

50. Rust, M. J., Bates, M. & Zhuang, X. Sub-diffraction-limit imaging by stochastic optical reconstruction microscopy (STORM). *Nat. Methods* **3**, 793–796 (2006).

51. Budanov, A. V. & Karin, M. The p53-regulated Sestrin gene products inhibit mTOR signaling. *Cell* **134**, 451–460 (2008).

52. Renault, V. M. et al. The pro-longevity gene FoxO3 is a direct target of the p53 tumor suppressor. *Oncogene* **30**, 3207–3221 (2011).

Acknowledgements

Author contributions

M.C.D.-C. prepared Hi-C, UMI-4C, ChIP-seq and RNA-seq libraries and performed in vitro validation experiments and DNA FISH experiments. S.S. analyzed Hi-C, UMI-4C, and ChIP-seq data. M.Z. performed the comparison of Hi-C contact maps, TAD calling, and all analyses based on mRNA expression data. D.T. performed interactome analyses and all analyses based on ChIP-seq data. K.M.D. and T.R. acquired and analyzed STORM images. N.K. and E.B. performed in vitro and in vivo experiments. M.M. assisted in the analysis of Hi-C data. F.R. assisted in the analysis of STORM data. S.M. supervised in STORM acquisition and image analyses. G.C and E.O. designed the study and wrote the manuscript with comments from all authors.

Competing interests

The authors declare no competing interests.

Additional information

Supplementary information is available for this paper at https://doi.org/10.1038/s41588-018-0338-y.

Reprints and permissions information is available at www.nature.com/reprints.

Correspondence and requests for materials should be addressed to G.C. or E.O.

Publisher's note: Springer Nature remains neutral with regard to jurisdictional claims in published maps and institutional affiliations.

Methods

Data generation and models. Lymphoma cell lines used in this study (OCI-Ly19, DoHH2, SU-DHL-10, WSU-DLCL2, Toledo, SU-DHL-6, and Karpas422) were authenticated within the past year by short tandem repeat (STR) cell-line authentication analysis (MicroArray, Switzerland) and cultured as described in the Supplementary Note. OCI-Ly19 cells were transduced with lentiviral particles to express EZH2Y646F in tandem with GFP or the empty vector (OCI-Ly19-EZH2[Y646F]). After the initial transduction, 3–5% of the GFP-positive cells were sorted to obtain a pure population of GFP-positive cells. We confirmed by RNA-sequencing (RNA-seq) analysis that only one copy of mutated *EZH2* was integrated in the genome.

Hi-C experiments were performed on Karpas422, WSU-DLCL2, OCI-Ly19-EZH2[WT], and OCI-Ly19-EZH2[Y646F], treated with 2 µM GSK-126 or DMSO for 72 h. Data generation and analysis are detailed in the Supplementary Note. Targeted chromosome conformation capture using unique molecular identifiers (UMI-4C) was performed in Karpas-422 treated with 2 µM GSK126 or DMSO for 72 h, as described in ref. [53]. Hi-C and UMI-4C library preparation, contact-map generation, and data normalization were performed as described in the Supplementary Note. A list of the primers used in this study is provided in Supplementary Table 8.

mRNA expression was assessed by means of RNA-seq in OCI-LY19-EZH2[WT], OCI-Ly19-EZH2[Y646F], and OCI-Ly19-EZH2[Y646F] after treatment with the EZH2 inhibitor GSK126 for 72 h. ChIP-seq was performed in OCI-Ly19-EZH2[WT] and OCI-Ly19-EZH2[Y646F], Toledo, and WSU-DLCL2 cells by using a monoclonal antibody to H3K27me3 (Cell Signaling, 9733). H3K27me3 ChIP-seq data for OCI-Ly7, DOHH2, and Karpas422 were obtained from ENCODE, whereas for WSU-DLCL2, data were obtained from the GEO Database (GSE40792). Targeted ChIP validation was performed for *FOXO3* and *SESN1* on Toledo and WSU-DLCL2 cell lines. All data generation and analyses are detailed in the Supplementary Note.

STORM was used to compare the structure of TAD6.139 between WSU-DLCL2 treated with either 2 µM GSK126 or DMSO (four independent experiments), and between OCI-Ly19-EZH2[WT] and OCI-Ly19-EZH2[Y646X] (three independent experiments). The structure of the neutral TAD1.54 was compared between WSU-DLCL2 treated with either 2 µM GSK126 or DMSO (two independent experiments). STORM data were generated and analyzed as described in the Supplementary Note.

Mouse model. We isolated Eµ-myc transgenic fetal liver cells from embryos at embryonic day 13.5. The HPCs were grown for 4 d in a specially adapted growth medium (DMEM, IMDM, ʟ-glutamine, pen/strep, FBS, and SCS-stem cell supplement (Whei, IL3, IL6, SCF, and polybrene) and retrovirally transduced with either the vector MLS-GFP containing shRNA for *Sesn1* or *Foxo3* or the empty vectors. We inoculated genetically modified HPCs into lethally irradiated, syngeneic wild-type recipient animals. Disease onset was monitored by palpation and blood smears. Data were analyzed in Kaplan–Meier format by using the log-rank (Mantel–Cox) test for statistical significance. Transgenic animals were maintained in EPFL SPF animal facility, and all animal studies were approved by Swiss Cantonal authorities (animal license VD2932 and VD2932.1).

Comparison of intrachromosomal Hi-C contact maps. All pairwise comparisons between intrachromosomal contact maps (or matrices) were based on four different metrics: overall matrix correlation by SCC, fraction of corresponding bins assigned to the same compartment (A or B), conservation of TADs, and conservation of significant interactions between bins.

Matrix correlation (stratum-adjusted correlation coefficient). To compare the overall distribution of contacts across intrachromosomal Hi-C maps, we used the SCC, as implemented in the *hicrep* R package[24] in Bioconductor (*get.scc* function, after having trained the smoothing parameter with the *htrain* function for the range 0:20). After smoothing Hi-C matrices with a 2D mean filter to reduce noise and bias effects, we stratified chromatin contacts according to the genomic distance between interacting loci. The number of strata K is given by the maximal interaction distance divided by the bin size (for example $K = 3,840$, for a 192-Mb chromosome binned at 50 kb; here, we chose the chromosome size as the maximal interaction distance). The SCC was then computed as a weighted average of stratum-specific Pearson's correlation coefficients, and it can be interpreted as a classical correlation coefficient with values ranging from –1, for perfect anticorrelation, to +1, for perfect correlation.

Fraction of corresponding bins assigned to the same compartment. Compartments were calculated as previously described[3]: Hi-C contact matrices were binned at 1 Mb by using the *pca.hic* function from the *HiTC* R package in Bioconductor, and compartments A and B were defined according to the signs of the values of the first eigenvector retrieved from principal component analysis of the Pearson correlation matrix of the observed over expected Hi-C matrix (when the first eigenvector separated the two chromosome arms, the second eigenvector was used). To compare the compartments between two intrachromosomal matrices, we defined the sign (positive or negative) associated with a specific compartment (A or B) as the one achieving the highest correlation between the eigenvectors of the two

datasets. For each pair of 1,000-kb bins corresponding to the same genomic region in the two Hi-C contact matrices, we compared the sign of the corresponding eigenvalue: concordant signs corresponded to bins assigned to the same compartment, opposite signs corresponded to bins in different compartments. A similarity score for each pair of intrachromosomal maps was defined as the fraction of bins that were assigned to the same compartment.

Conservation of TADs. First, TADs were called at 50-kb resolution by using the TopDom[26] (*TopDom* function from the *TopDom* R package with a window size $w = 5$).

Next, we compared the set of TADs identified in two intrachromosomal matrices by computing the concordance of the two corresponding chromosome partitions. For this purpose, we used the measure of concordance (MoC) previously introduced to compare clustering assignments[25]. MoC is defined as follows:

$$MoC(\mathbf{P}, \mathbf{Q}) = \begin{cases} 1 & if \ N_P = N_Q = 1 \\ \dfrac{1}{(\sqrt{N_P N_Q} - 1)} \left(\displaystyle\sum_{i=1}^{N_P} \sum_{j=1}^{N_Q} \dfrac{\|F_{i,j}\|^2}{\|P_i\| \|Q_j\|} \right) & otherwise \end{cases}$$

where **P** and **Q** are the sets of TADs being compared, including N_P and N_Q numbers of TADs, respectively. P_i and Q_j are two individual TADs within **P** and **Q** having size $\|P_i\|$ and $\|Q_j\|$, respectively, measured in base pairs. Finally, $\|F_{ij}\|$ corresponds to the size (number of base pairs) of the overlap between the two TADs P_i and Q_j.

Conservation of significant interactions. The statistical significance of chromatin interactions at the bin level was estimated with HiC-DC[28] in 'fixed bin' mode. The bin size was set to 50 kb, with degrees of freedom (df) = 6 and size = 1.0. The hg19 mappability file was retrieved by following the link provided in the URLs section. Interactions were called significant if the HiC-DC q value was smaller than 0.05. Conservation of significant interactions between two given cell lines c1 and c2 was computed as the overlap between their set of significant interactions as follows:

$$overlap = \frac{\# \ of \ common \ s.i.}{\min\{(\# \ of \ s.i. \ in \ c1), (\# of \ s.i. \ in \ c2)\}}$$

Generation of Hi-C contact maps for replicates and randomized maps for comparison. To build a reference scale of values for the different metrics, we included comparisons between our Hi-C maps and randomized Hi-C maps, as well as comparisons between independent replicates of the same cell line.

In the comparisons based on the SCC measure and on the fraction of conserved significant interactions, we generated randomized Hi-C maps by shuffling count values within each diagonal of the Hi-C matrix, that is by permuting the number of contacts among bins located at the same genomic distance. For the comparison of TAD by MoC, random TAD partitions were generated by shuffling the original set of TADs in a way that preserved the number and the size of the TADs. The resulting random maps were used to estimate the expected similarity score between Hi-C experiments performed without any expected structural similarity.

Additionally, for each cell line, we selected and aggregated independent replicates in two groups with similar total number of reads and generated separate contact maps and the list of contacts (interactomes) for each group. The maps and the interactomes were used to estimate the expected similarity score between Hi-C experiments performed on the same cell line (that is, expected highest similarity).

Concordance analyses of H3K27me3 and transcriptional changes within TADs. A consensus list of TADs conserved among Karpas422, OCI-Ly19-EZH2[WT], OCI-Ly19-EZH2[Y646F], and WSU-DLCL2 cell lines was determined by using an approach based on weighted interval scheduling (WIS) efficiently solved with a dynamic programming (DP) approach[54]. Briefly, each interval/TAD received a weight according to how conserved it was across cell lines (allowing a tolerance radius of two bins or 100 kb), and the goal was to identify a set of nonoverlapping intervals of maximum total weight (details in Supplementary Note). Using this approach, we identified a total of $n = 3,773$ consensus TADs.

H3K27me3 comparison among subcompartments. Chromosome subcompartments derived in GM12878 were downloaded from the GEO database (GSE63525). Subcompartment calls were used to partition contact maps generated by our experiments, given the high concordance between A and B compartments derived in GM12878 and in our cell lines (Fig. 1c,d). Moreover, subcompartments have been called only in GM12878, given that the procedure requires an extremely high number of reads (documentation in GSE63525). To compare H3K27me3 across subcompartments, we considered the mean H3K27me3 levels within each continuous DNA sequence that was assigned to the same subcompartment (sc region) and compared the distribution of mean H3K27me3 values among sc regions annotated for the same compartment. Unannotated sc regions were excluded from this analysis. H3K27me3 fold changes were computed for each sc

region through comparing the mean H3K27me3 values in OCI-Ly19-EZH2[Y646F] versus OCI-Ly19-EZH[WT] cells.

Intra-TAD and inter-TAD correlation between H3K27me3 fold changes and levels. Correlations between normalized H3K27me3 profiles of OCI-Ly19-EZH2[Y646F] and OCI-Ly19-EZH2[WT] cells were investigated as previously described[23]. Briefly, each TAD was divided into ten equally spaced bins, as well as two flanking regions of the same size of the TAD. Mean H3K27me3 levels and the fold changes of mean H3K27me3 levels in mutated versus wild-type samples within each of these 30 bins were then stored as a row of an $N \times 30$ matrix, where N is the number of TADs. Finally, Spearman correlation coefficients were computed between each pair of columns of this matrix, thus constructing a 30×30 symmetric pairwise correlation matrix, whose columns 11–20 corresponded to bins within a TAD, whereas columns 1–10 and 21–30 corresponded to bins within upstream and downstream regions, respectively. The central 10×10 block represented intra-TAD correlations, whereas the 10×10 blocks above (or below) it and on its right (or left) corresponded to inter-TAD correlations. The correlation of H3K27me3 fold changes as a function of distance for intra-TAD and inter-TAD pairs of loci (Fig. 2d) was performed as follows:

1. Each TAD was divided into bins of 25 kb, as well as its two flanking regions (of the same size as the TAD) upstream and downstream; fold changes in each bin were computed as explained above.
2. A distance vector was constructed as a sequence of distances ranging from 25 kb to 1 Mb, each of them separated by 25 kb.
3. For each element i of the distance vector, we extracted all pairs of loci that were separated by a distance equal to i; next, we derived an $N \times 2$ matrix storing the N pairs for which both loci were in the same TAD, and we computed the Spearman correlation coefficient between the two columns, which represented the intra-TAD correlation at distance i; analogously, we derived an $M \times 2$ matrix storing the M pairs for which one locus was in the TAD, and the other was in one of the two flanking regions and computed the inter-TAD correlation for distance i in the same way.
4. Finally, we plotted the intra-TAD and inter-TAD correlation versus distance in two different lines.

Concordance between H3K27me3 changes and TADs. H3K27me3 ChIP-seq levels in OCI-Ly19-EZH2[Y646F] cells and in OCI-Ly19-EZH2[WT] were jointly normalized across the two cell lines, as described in the Supplementary Note. Normalized H3K27me3 levels were averaged within each conserved TAD, and the $\log_2$ fold change was computed between the two conditions (mutated versus wild type). Density distributions of $\log_2$ fold change values were visualized by using the 'density' R function.

Random distributions of H3K27me3 TAD fold changes were generated by permutation of intervals (bins) of H3K27me3 read counts. Specifically, for a given size S, each chromosome was partitioned into bins of S base pairs, and read counts within each bin were summed. Corresponding bins in EZH2[Y646F] and EZH2 wild-type OCI-Ly19 cells were permuted together to preserve the H3K27me3 ratio between the two conditions for each bin. Bins within each chromosome were permuted separately. TAD fold changes were recalculated as described above. Random distributions were generated with bin sizes ranging from 1 kb to 2 Mb. The number of TADs obtaining a fold change greater than two was compared when using the observed H3K27me3 distribution and distributions generated with bin size ranging from 50 kb to 2 Mb.

Concordance between transcriptional changes and TADs. For each mRNA expression dataset, genes with detectable expression were assigned to the TADs with the highest overlap, and genes nonoverlapping with a TAD were discarded. TADs containing fewer than three genes or more than the 0.99-quantile of the number of genes by TAD distribution were excluded. With these filters, we retained $n = 2,038$ TADs for the comparison between EZH2[Y646X] and EZH2[WT] DLBCL primary samples and cell lines, $n = 1,923$ TADs for the comparison of follicular lymphoma primary samples, and $n = 900$ TADs for the comparison of OCI-Ly19 EZH2[Y646F] and OCI-Ly19-EZH2[WT]. For the latter comparison, we retained considerably fewer TADs, a result consistent with the RNA-seq dataset including only three replicates for OCI-Ly19-EZH2[Y646F] and three replicates for OCI-Ly19-EZH2[WT]; thus, fewer genes had detectable expression in both conditions than in the other datasets.

To test whether the mRNA expression changes were more concordant within TADs than expected, we first defined TAD mRNA expression fold changes as the mean of the fold changes of each gene within the TAD. Gene fold changes were determined for both microarray and RNA-seq datasets as described above. Next, we defined a measure of concordance for fold changes within a TAD and compared the observed cumulative sum distribution of concordance values obtained by our set of conserved TADs with the expected cumulative sum distribution under random permutation of the gene-to-TAD assignments. Briefly, an FCC score was computed for each TAD as:

$$FCC = \left(2^{\frac{\#FC^-}{\#FC}} - 1\right) * \left(2^{\frac{\sum |FC^-|}{\sum |FC|}} - 1\right)$$

where #FC is the number of genes within the TAD, #FC⁻ is the number of genes with a negative fold change within the TAD, |FC| are absolute fold-change values, and |FC⁻| are absolute values of negative fold changes ($\log_2$ fold changes were used). TADs were ranked from highest to lowest FCC, and the cumulative sum curve was calculated. For each test, we compared the observed cumulative sum curve against curves obtained after random permutation of gene-to-TAD assignments. Intuitively, the more concordant the gene expression changes within TADs, the steeper the increase in the cumulative sum. We considered the observed concordance to be greater than expected when the observed curve was higher than all random curves. To permute gene-to-TAD assignments, we divided genes in five classes according to their overall levels of expression and shuffled TAD labels within each class. For each test, we performed 10,000 permutations and reported the range comprising all random curves.

Pearson's correlation of mRNA expression between genes located in the same TAD or different TADs were compared as a function of their genomic distance (maximum 500 Kb). Microarray data were normalized by using the median absolute deviation method, whereas RNA-seq data was transformed by using quantile normalization. Curves were fitted by using the R *loess* function (from the *stats* package, with default parameters).

Genes within inactive TADs were analyzed by gene-set enrichment analysis, and their expression was assessed in centrocytes, centroblasts, and memory B-cells, as described in the Supplementary Note.

Differential intra-TAD interactome analysis for TAD6.139. For each pair of cell lines/conditions, significantly different interactions between 20-kb bins within the TAD 6.139 were determined as follows:

1. HiC-DC was run on Hi-C read pairs of Chr.6 with a bin size of 20 kb, and the q values obtained for each pair of bins within the entire chromosome were retained;
2. For each pair of bins i and j (with $i_s > j_s$), the interaction difference d between condition A and condition B was computed as $d_{i,j}^{A-B} = -\log_{10}(q_{i,j}^A) + \log_{10}(q_{i,j}^B)$;
3. Distributions of $d_{i,j}^{A-B}$ values were determined for pairs of bins at the same genomic distance;
4. For each pair of bins i_s and j_s in TAD6.139, the significance of the corresponding interaction difference was tested by computing its empirical P value against the distribution of interaction differences computed between bins at the same distance, namely $\{d_{i,j}^{A-B}\}_{i,j | i-j = i_s - j_s}$;
5. Empirical P values obtained for all pairs of bins within TAD 6.139 were corrected for multiple testing by using the Benjamini–Hochberg procedure;
6. Finally, interactions were called significantly stronger in condition A than in condition B if they satisfied both the following conditions:

   a. The q value computed by HiC-DC was smaller than 0.1,
   b. The q value resulting from step (5) was smaller than 0.1.

Differential-interaction analysis for intra-TAD promoter-proximal regions. For each pair of cell lines/conditions A and B, significantly different interactions between 50-kb bins mapping to gene promoters located in a set of TADs were determined as follows:

1. HiC-DC was run on Hi-C read pairs of all chromosomes with a bin size of 50 kb, and the q values obtained for each pair of bins were retained;
2. Bin-level promoter-promoter interactions (PPIs) between genes x and y were identified as $PPI_{x,y} = -\log_{10}(q_{i,j})$, where i and j are 50-kb bins overlapping the transcription start sites of genes x and y, respectively. Only PPIs between genes in the same TAD and less than 2 Mb apart were retained;
3. Significantly different PPIs between conditions A and B were determined as described in steps 2–6 described in 'Differential intra-TAD interactome analysis', with a cutoff of 0.25 for q values computed in step 5

Random sets of neutral TADs were sampled from our consensus list of 2,038 TADs such that:

1. Only TADs with $|log_2$(H3K27me3 fold change$_{OCI-Ly19\ EZH2-Y646F\ vs\ EZH2-wt})| < 0.5$ and $|log_2$(mRNA fold change$_{Cell\ lines\ EZH2-Y646X\ vs\ EZH2-wt})| < 0.5$ were sampled;
2. The distributions of the numbers of genes per TAD in the random sets were the same as in the set of 72 inactive TADs

Reporting Summary. Further information on research design is available in the Nature Research Reporting Summary linked to this article.

Data availability

In this study, we used the following mRNA expression datasets: GSE23501 for wild-type and *EZH2*-mutated GCB-DLBCL primary human samples, PRJNA278311 (NCBI-BioProject) for wild-type and *EZH2*-mutated FL primary human samples, GSE40792 for wild-type and *EZH2*-mutated cell lines before and after treatment with GSK126, GSE49284 for *EZH2*-mutated cell lines before and after treatment

with EPZ6438, and GSE12195 for centrocytes, centroblasts, and memory B cells. ChIP-seq data for H3K27me3 in OCI-Ly7, DOHH-2, and Karpas-422 were downloaded from ENCODE; H3K27me3 in WSU-DLCL2 was downloaded from GSE40970; H3K4me3 in OCI-Ly7 and Karpas-422 were downloaded from ENCODE. ChIP-seq data for H3K27me3 and RNA-seq data for OCI-Ly19 and OCI-Ly19-EZH2^{Y646F} were generated as described in the manuscript and have been deposited at GSE114270. HiC matrices and UMI-4C data have been deposited at Zenodo: https://doi.org/10.5281/zenodo.1244182. Custom scripts are available

through a public GitHub repository at: https://github.com/CSOgroup/Donaldson-et-al-scripts/.

References

53. Schwartzman, O. et al. UMI-4C for quantitative and targeted chromosomal contact profiling. *Nat. Methods* **13**, 685–691 (2016).
54. Kleinberg, J. & Tardos, É. *Algorithm Design* (Pearson, Boston, 2005).

Article

Distinct fission signatures predict mitochondrial degradation or biogenesis

Check for updates

Tatjana Kleele[1✉], Timo Rey[1], Julius Winter[1], Sofia Zaganelli[1], Dora Mahecic[1], Hélène Perreten Lambert[1], Francesco Paolo Ruberto[2], Mohamed Nemir[2], Timothy Wai[3], Thierry Pedrazzini[2] & Suliana Manley[1✉]

Mitochondrial fission is a highly regulated process that, when disrupted, can alter metabolism, proliferation and apoptosis[1–3]. Dysregulation has been linked to neurodegeneration[3,4], cardiovascular disease[3] and cancer[5]. Key components of the fission machinery include the endoplasmic reticulum[6] and actin[7], which initiate constriction before dynamin-related protein 1 (DRP1)[8] binds to the outer mitochondrial membrane via adaptor proteins[9–11], to drive scission[12]. In the mitochondrial life cycle, fission enables both biogenesis of new mitochondria and clearance of dysfunctional mitochondria through mitophagy[1,13]. Current models of fission regulation cannot explain how those dual fates are decided. However, uncovering fate determinants is challenging, as fission is unpredictable, and mitochondrial morphology is heterogeneous, with ultrastructural features that are below the diffraction limit. Here, we used live-cell structured illumination microscopy to capture mitochondrial dynamics. By analysing hundreds of fissions in African green monkey Cos-7 cells and mouse cardiomyocytes, we discovered two functionally and mechanistically distinct types of fission. Division at the periphery enables damaged material to be shed into smaller mitochondria destined for mitophagy, whereas division at the midzone leads to the proliferation of mitochondria. Both types are mediated by DRP1, but endoplasmic reticulum- and actin-mediated pre-constriction and the adaptor MFF govern only midzone fission. Peripheral fission is preceded by lysosomal contact and is regulated by the mitochondrial outer membrane protein FIS1. These distinct molecular mechanisms explain how cells independently regulate fission, leading to distinct mitochondrial fates.

Qualitatively, fission appears to occur randomly along the length axis of mitochondria (Fig. 1a). We recorded spontaneous mitochondrial dynamics at high temporal and spatial resolution, without pharmacological induction. Structured illumination microscopy imaging of live Cos-7 cells enabled us to precisely determine the fission positions of mitochondria of various shapes and lengths (Fig. 1b, Supplementary Video 1). Analysis of hundreds of spontaneous fissions revealed a nonuniform probability distribution wherein fission locations are bimodally distributed along the relative length of a mitochondrion (Fig. 1c). We term these either 'peripheral' (less than 25% from a tip) or 'midzone' divisions (within the central 50%). Similar results were obtained by considering mitochondrial area instead of length (Extended Data Fig. 1a, b), as expected, as mitochondrial diameter is relatively constant. This distribution was independent of the length of the dividing mitochondria (Extended Data Fig. 1c, d). Because of this bimodality, smaller daughter mitochondria derived from peripheral divisions have a relatively narrow length distribution (1–2 μm) (Extended Data Fig. 1e). Mitochondria that were labelled with inner or outer membrane markers revealed similar bimodal distributions, confirming complete fission (Extended Data Fig. 1f). To test the generality of our observations, we measured fissions in postnatal mouse cardiomyocytes (Fig. 1d,

Supplementary Video 2). Again, we found a bimodal distribution with mitochondria dividing either in the midzone or peripherally (Fig. 1e).

Dysfunction precedes peripheral fission

We wondered whether geometrically distinct fission types reflected underlying physiological differences. Mitochondria are hubs for metabolic functions, that are characterized by distinct physiological and biochemical properties. The potential across the inner membrane drives oxidative phosphorylation, creating a pH difference between matrix and intermembrane spaces. Reactive oxygen species (ROS), a toxic by-product of oxidative phosphorylation, can lead to mitochondrial damage, often accompanied by loss of membrane potential and release of Ca^{2+} and cytochrome c (ref. [14]). We investigated the physiological states preceding mitochondrial fission with fluorescent sensors (Fig. 1f–i). We found that mitochondrial membrane potential as reported by the dye tetramethylrhodamine ethyl ester (TMRE) was reduced before fission in small peripheral daughter mitochondria (Fig. 1f, g, Supplementary Video 3) compared with corresponding large daughter mitochondria or non-dividing mitochondria. By contrast, no differences were observed between daughter mitochondria

[1]Institute of Physics, École Polytechnique Fédérale de Lausanne (EPFL), Lausanne, Switzerland. [2]Experimental Cardiology Unit, Department of Cardiovascular Medicine, University of Lausanne Medical School, Lausanne, Switzerland. [3]Mitochondrial Biology Group, Institut Pasteur, CNRS UMR 3691, Paris, France. ✉e-mail: tatjana.kleele@epfl.ch; suliana.manley@epfl.ch

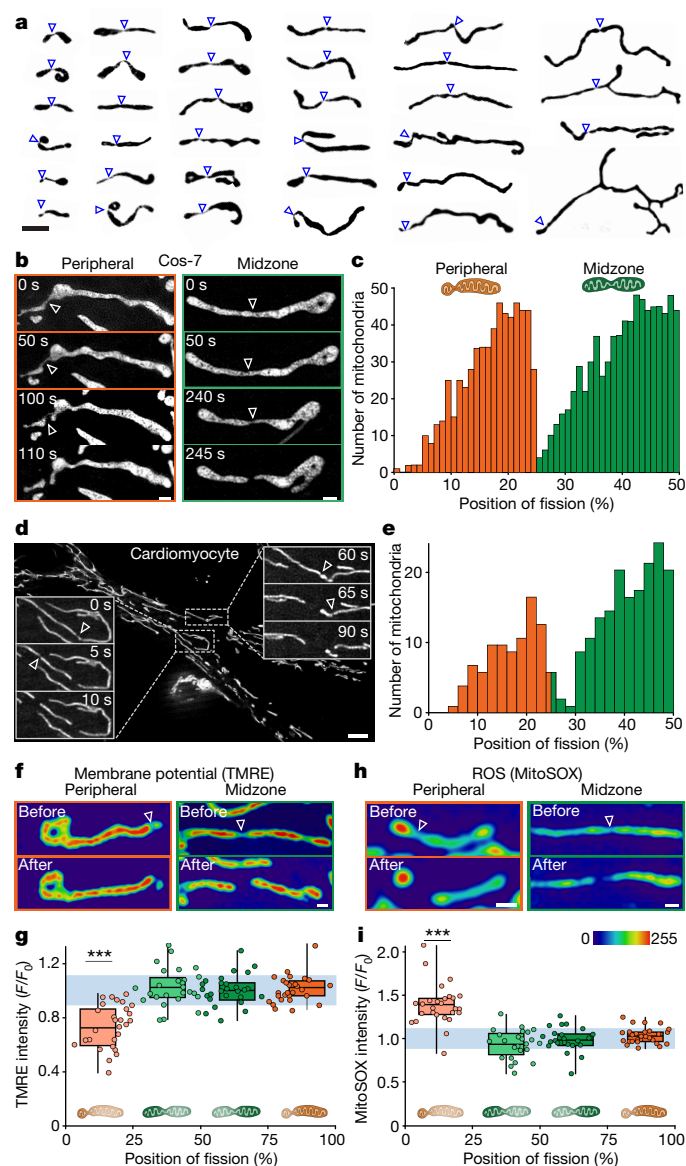**Fig. 1 | Mitochondrial fissions are bimodally positioned and linked to distinct physiologies. a**, Gallery of mitochondria one frame before division from structured illumination microscopy (SIM) movies, binarized. **b**, Time-lapse SIM sequence of a peripheral and a midzone fission of mitochondria (Mitotracker Green). **c**, Histogram of fission positions relative to the total mitochondrial length ($n = 1,393$ fissions pooled from multiple datasets). Fissions occurring near the tip (orange, 0–25%) are termed 'peripheral'; those near the centre (green, 25–50%) are termed 'midzone'. **d**, Instant SIM (iSIM) of mitochondria (Mitotracker Green) in primary mouse cardiomyocytes. Insets: time-lapse sequences from indicated boxes. **e**, Histogram of the relative position of fission in cardiomyocyte mitochondria ($n = 381$ fissions), as in **c**. **f**, Mitochondrial membrane potential before and after a peripheral or midzone fission from SIM movies of tetramethylrhodamine ethyl ester (TMRE)-stained mitochondria. **g**, Normalized TMRE intensity as a function of relative position of fission, measured immediately before fission ($n = 56$ fissions). **h**, MitoSOX labelling reveals ROS levels before and after a peripheral or midzone fission. **i**, Normalized MitoSOX intensity as a function of relative fission position, measured immediately before fission ($n = 52$ fissions). In **g** and **i**, circles indicate individual measurements; line, mean; bounds of box, 25th and 75th percentiles; whiskers, minimum and maximum values; light blue area indicates mean intensity in non-dividing mitochondria ($\pm$ s.d.). Scale bars, 0.5 μm in **b**, **f**, **h** and 10 μm in **d**. Arrows indicate fission sites. All panels excluding **d** and **e** show data from Cos-7 cells. ***$P < 0.001$. Number of experiments, statistical tests and exact P values are provided in Supplementary Table 1.

from midzone fissions. Similarly, the genetically encoded pH sensor SypHer reported a reduced matrix pH in small daughter mitochondria before fission (Extended Data Fig. 2, Supplementary Video 4). Small peripheral daughter mitochondria containing mito–GFP maintained their intensity; therefore, these results cannot be explained by their reduced volume (Extended Data Fig. 2). Furthermore, the smallest mitochondria derived from midzone fission are similar in size to those from peripheral fissions.

Another indication of mitochondrial dysfunction is ROS accumulation, usually eliminated by anti-oxidative enzymes[15]. ROS levels measured by MitoSOX (Fig. 1h, i) and genetically encoded mito–GRX1–roGFP (Extended Data Fig. 2) were elevated in peripheral daughter mitochondria compared with those in non-dividing mitochondria or daughters from midzone fissions. Cells treated with a 500 nM concentration of the ROS scavenger MitoQ exhibited reduced peripheral fission rates, whereas midzone fission rates were unaffected (Extended Data Fig. 2). Finally, we examined mitochondrial Ca^{2+} levels with the genetically encoded sensors mito–R-GECO1 (Extended Data Fig. 2, Supplementary Video 5) and CEPIA3–mt (Extended Data Fig. 2). Mitochondrial Ca^{2+} has a role in cell survival and death by buffering homeostasis[16]. Ca^{2+} levels increased significantly in small peripheral daughter mitochondria, and mildly in large peripheral daughter mitochondria, compared with midzone or non-dividing mitochondria. Thus, we found no differences in the physiological states of midzone fissions before or after fission, whereas peripheral fission is preceded by increased Ca^{2+} and ROS, and reduced membrane potential and pH.

Distinct positions and distinct fates

As individual mitochondria showed signs of stress and damage upstream of peripheral fission, we hypothesized that it could lead to degradation, whereas midzone fission could serve biogenesis. To test this, we analysed the distribution of mitochondrial DNA (mtDNA) in Cos-7 cells stained with PicoGreen (Fig. 2a, b, Extended Data Fig. 3a). On average, there was no significant difference in the total number of mtDNA foci (nucleoids) between peripherally and centrally dividing mitochondria. However, we observed that 32% of smaller daughter mitochondria from peripheral fissions contained no nucleoids, compared with 3% of those from midzone fissions. Mitochondria lacking mtDNA also had diminished membrane potential compared with those containing mtDNA (Extended Data Fig. 3b). We observed similar results for mitochondrial RNA granules (Extended Data Fig. 3c–e), which are composed of mtRNA and RNA-processing proteins[17]. Daughter mitochondria from midzone fissions contained an elevated number of replicating, TWINKLE-positive nucleoids compared with non-dividing mitochondria, consistent with a proliferative role (Fig. 2c, d, Extended Data Fig. 3f). By contrast, 75% of smaller peripheral daughter mitochondria contained no TWINKLE foci. We then induced mtDNA damage by exposure to ultraviolet (UV) light (Fig. 2e, f) and labelled newly synthesized RNA with bromouridine (BrU). We found that mitochondria had fewer BrU foci after UV treatment, indicating disruption of transcription (Extended Data Fig. 3g). Consistent with their putative degradative role, the prevalence of nucleoids was increased in small peripheral daughter mitochondria (82% compared with 68% without UV irradiation).

We followed daughter mitochondria resulting from peripheral fissions, to discern their fates. Previous studies reported lysosome–mitochondria contacts before fission[18], which we observed in 92% of peripheral fissions, compared with only 13% of midzone fissions (Fig. 2g, h, Supplementary Video 6). At peripheral fission sites, we also observed mitochondria-derived vesicles, which are known to be targeted to late endosomes for degradation[19] (Extended Data Fig. 6c, d). Mitochondria that were undergoing peripheral fission also accumulated YFP–Parkin (Fig. 2i, j). These signatures link peripheral fission with mitophagy, the turnover of mitochondria by PINK1 and Parkin-regulated autophagy[20]. In some cases, we observed the uptake of small daughter mitochondria
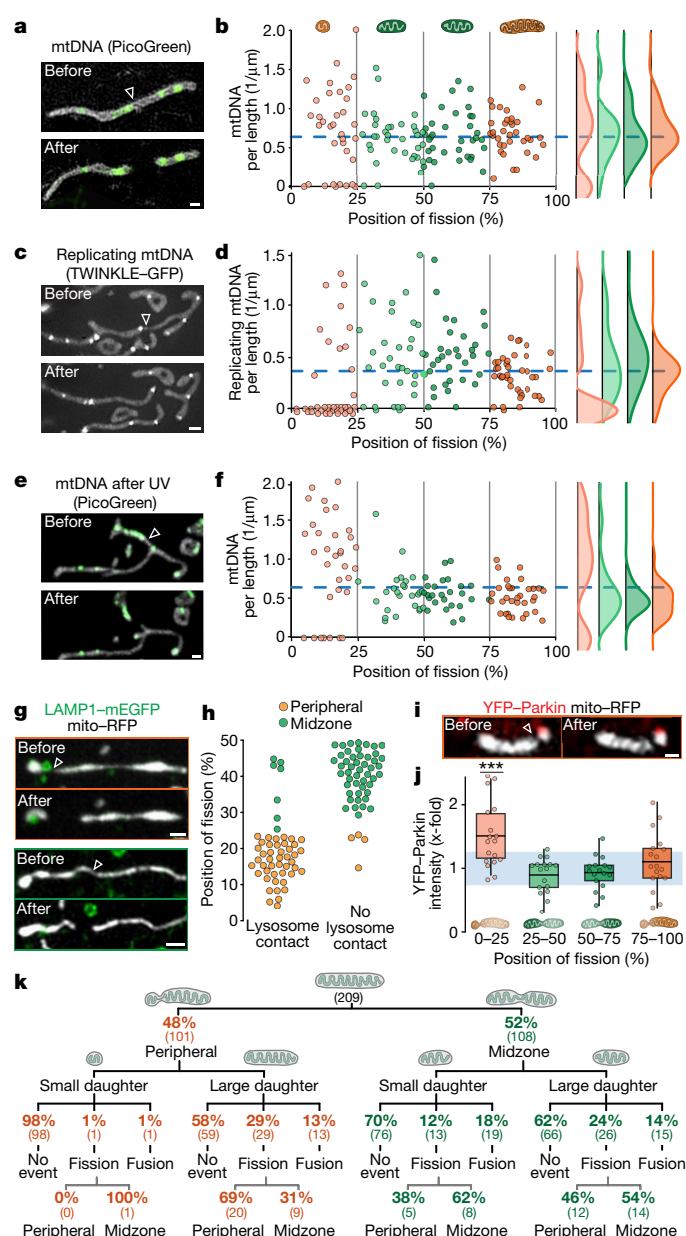
Fig. 2 | Midzone and peripheral fissions differ in mitochondrial DNA content and fates. a, Mitochondria (mito–RFP) and mitochondrial (mt)DNA (PicoGreen, green) before and after fission. **b,** Linear density of nucleoids as a function of fission position, individual data points (left) and violin plots (right) for binned groups (*n* = 78 fissions). **c, d,** Replicating nucleoids (TWINKLE–GFP) (**c**) and linear density (**d**), as in **b** (*n* = 74 fissions). **e, f,** mtDNA (**e**) and linear density (**f**) after UV irradiation, as in **b** (*n* = 62 fissions). **g,** Mitochondria (mito–RFP, greyscale) and lysosomes (LAMP1–mEGFP, green) before and after peripheral or midzone fission. **h,** Position of fission in divisions contacting lysosomes or not before fission (*n* = 104 fissions). **i,** Mitochondria (mito–RFP, greyscale) and pre-mitophagic marker (YFP–Parkin, red) before and after fission. **j,** Pre-fission YFP–Parkin fold-change in intensity as a function of fission position (*n* = 34). **k,** Schema depicting the fates of daughter mitochondria from peripheral and midzone fissions. Mitochondria tracked for >100 s after fission were included. Numbers in parentheses are total numbers of events. All panels show data from Cos-7 cells, and circles indicate individual measurements. In **b, d** and **f**, the blue line represents mean mitochondrial DNA density. In **j**, line, mean, bounds of box, 25th and 75th percentiles; whiskers, minimum and maximum values; light blue area indicates mean intensity in non-dividing mitochondria (± s.d.). Scale bars, 0.5 µm. White arrowheads indicate fission sites. ****P* < 0.001. Number of experiments, statistical tests and exact *P* values are provided in Supplementary Table 1.

derived from peripheral fissions by autophagosomes (Extended Data Fig. 3h, Supplementary Video 7). To determine the sequence of events leading to fission, we analysed the timing of changes in mitochondrial physiology (Extended Data Fig. 4) and recruitment of the fission and autophagic machinery. This revealed that a drop in membrane potential, a rise in Ca^{2+} and recruitment of the autophagic machinery all precede peripheral fission. Changes in membrane potential and Ca^{2+} occur even before the inner mitochondrial membrane is notably constricted (Extended Data Fig. 4c), suggesting that compartmentalization occurs before fission.

Previous studies established a paradigm whereby dividing mitochondria either re-fuse with the network or remain isolated and undergo mitophagy[1]. Therefore, we followed the fate of daughter mitochondria after division. We found that, in contrast to other mitochondria, small peripheral daughter mitochondria are excluded from further fusions or divisions in both Cos-7 cells (Fig. 2k) and primary mouse cardiomyocytes (Extended Data Fig. 5a).

Cell context-dependent modulation

To determine whether cells would be able to modulate each fission type independently, in a context-dependent manner (Fig. 3a, b), we subjected Cos-7 cells to metabolic stress by growing them in glucose-free, galactose-supplemented medium. We observed that the rate of peripheral fissions per cell increased, whereas the rate of centrally dividing mitochondria remained constant (Fig. 3a, Extended Data Fig. 5b). A similar trend emerged in response to mtDNA damage induced by UV light. We also tested the effects of increased energy demand and hence oxidative stress on primary mouse cardiomyocytes, by treatment with isoproterenol, a non-selective β-adrenergic receptor agonist that increases contractility and induces hypertrophy. We imaged cells after 48 h of stimulation and found increased rates of peripheral fission compared with non-treated cells, whereas the rate of midzone fission remained constant (Fig. 3b, Extended Data Fig. 5c). By contrast, when cells proliferate, our model predicts an upregulation of midzone fissions. To test this, we treated cardiomyocytes with a microRNA (miR)-199 mimic; we found increased rates of midzone fission, whereas peripheral fission rates remained unchanged (Fig. 3b, Extended Data Fig. 5d). Thus, cellular stress and high energy demands, associated with oxidative damage, increase the rate of peripheral fission, whereas cell proliferation, which requires the biogenesis of new mitochondria, increases the rate of midzone fission.

Distinct molecular machineries

The differences in physiology and fate between mitochondria that are derived from midzone fissions and those derived from peripheral fissions prompted us to investigate the molecular players involved. Previous studies reported that mitochondrial–endoplasmic reticulum (ER) contacts[6], in coordination with actin polymerization[21], define division sites and trigger mtDNA replication upstream of DRP1. All fissions we observed were spontaneous and mediated by DRP1 assembly (Extended Data Fig. 6a, b). We found that midzone fission sites consistently contacted the ER before fission, but most peripheral fission sites did not (Fig. 3c, d, Extended Data Fig. 6h, Supplementary Video 8). In accordance with that observation, immunostaining against PDZD8, a mitochondria–ER tethering protein[22], revealed a higher fluorescence signal at midzone fission sites (Extended Data Fig. 6e, f). This conditional involvement of ER contacts in midzone fissions lends insight to reports that not all fissions engage ER contacts (60–90%)[6,23] or include mtDNA replication (77%)[24]. Similarly, we found that actin consistently polymerized at midzone, but not peripheral fission sites (Fig. 3e, f). Small interfering RNA (siRNA) of INF2, a formin protein that accelerates actin polymerization at the ER[21], led to decreased rates of midzone fission, while having no effect on rates of peripheral fission (Extended Data Figs. 6g, 7a).
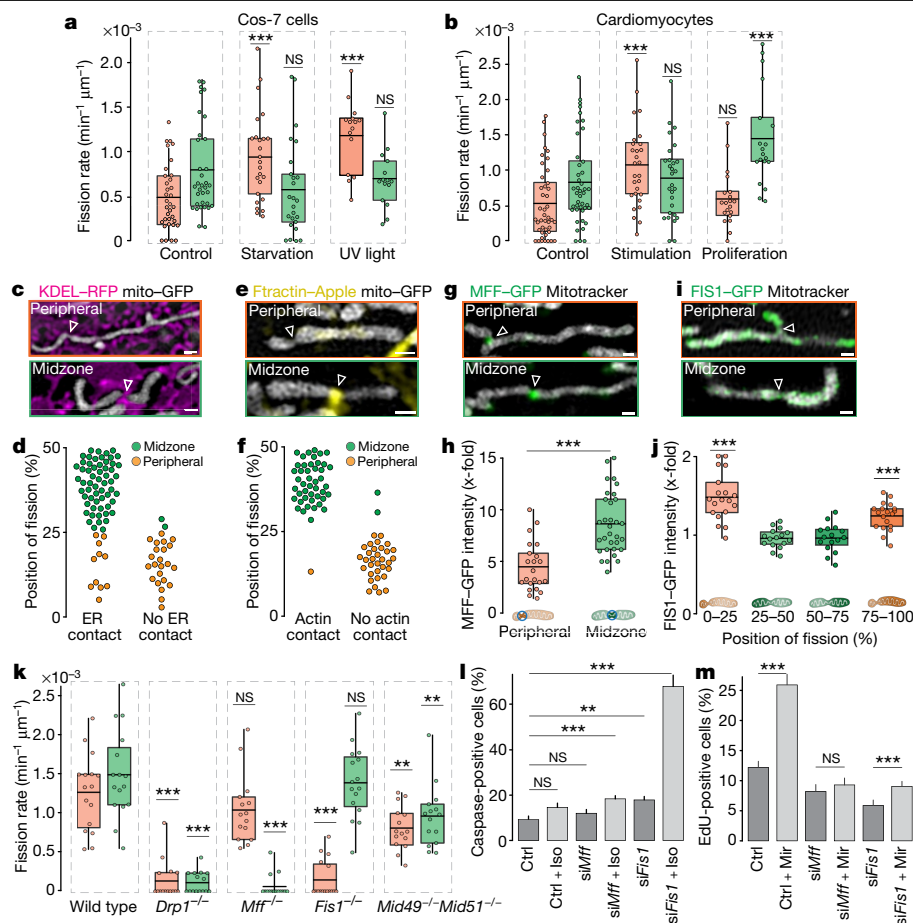
Fig. 3 | Midzone and peripheral fissions are independently regulated by distinct molecular machineries. a, Peripheral (orange) and midzone (green) fission rates in control, starved or UV-exposed Cos-7 cells ($n \geq 15$ fields of view (FOV) per group). **b**, Fission rates in postnatal mouse cardiomyocytes in control, stimulated or proliferation-induced cells ($n \geq 19$ FOV per group). **c**, SIM of mitochondria (mito–GFP, grey) and endoplasmic reticulum (ER) (KDEL–RFP, magenta) before a peripheral or midzone fission. **d**, Position of fission in mitochondria contacting the ER (left) or not (right) before fission ($n = 93$ fissions) in Cos-7 cells. **e**, SIM of mitochondria (mito–GFP, grey) and actin (Ftractin–Apple, yellow) before peripheral and midzone fissions. **f**, Fission position in mitochondria that accumulate actin (left) or not (right) before fission ($n = 80$ fissions). **g**, SIM of mitochondria (Mitotracker Red, grey) in U2OS cells endogenously expressing MFF–GFP for a peripheral and a midzone fission. **h**, MFF–GFP fold-change in intensity at the fission site of peripheral and midzone divisions ($n = 54$ fissions). **i**, SIM of mitochondria (Mitotracker Red, grey) in U2OS

cells endogenously expressing FIS1–GFP (green) for a peripheral and a midzone fission. **j**, FIS1–GFP fold-change in intensity over the surface of a daughter mitochondrion before fission ($n = 35$ fissions). **k**, Peripheral (orange) and midzone (green) fission rates in wild-type, $Drp1^{-/-}$, $Mff^{-/-}$, $Fis1^{-/-}$ and $Mid49^{-/-}$ $Mid51^{-/-}$ double-knockout mouse embryonic fibroblasts, stained with Mitotracker Green ($n \geq 15$ cells per group). **l**, Percentage of apoptotic (caspase 3/caspase 7-positive) cardiomyocytes ($\pm$ s.e.m.) in control, FIS1- and MFF-depleted cells with or without stimulation with isoproterenol ($n > 29$ FOV per group). **m**, Percentage of proliferating (EdU-positive) cardiomyocytes ($\pm$ s.e.m.) in control, FIS1- and MFF-depleted cells with or without treatment with miR-199 (Mir) ($n \geq 49$ FOV per group). In **a**, **b**, **h**, **j** and **k**, line, mean; bounds of box, 25th and 75th percentiles; whiskers, minimum and maximum values; circles, individual measurements. Number of experiments, statistical tests and exact P values are provided in Supplementary Table 1; NS $P > 0.05$, **$P < 0.01$, ***$P < 0.001$. Scale bars, 0.5 μm. Constriction sites are indicated by white arrowheads.

Several mitochondrial outer membrane proteins (MFF[9], MiD49 and MiD51 (hereafter MiD49/MiD51) (ref. [10]) and FIS1 (ref. [25])) regulate fission, but whether their roles are redundant or distinct remains unclear[11]. To investigate their roles in midzone versus peripheral fissions, we generated U2OS cell lines that express endogenously tagged MFF–GFP or FIS1–GFP. Live-cell structured illumination microscopy revealed stark differences in the distribution of MFF and FIS1. MFF forms bright foci at constrictions that lead to midzone fissions, and foci that were twofold dimmer at peripheral fissions (Fig. 3g, h). By contrast, FIS1 does not show a punctate accumulation, decorating the outer membrane more evenly. However, we observed a significant enrichment of FIS1–GFP on small daughter mitochondria from peripheral divisions (Fig. 3i–j, Extended Data Fig. 6o), consistent with its reported roles in mitophagy[26] and lysosome recruitment[18]. We observed similar distribution patterns of immunolabelled MFF and FIS1 in Cos-7 cells (Extended Data Fig. 6i–l) but did not find differences in accumulation of the DRP adaptors MiD49/MiD51 (Extended Data Fig. 6m, n). To quantify the

distinct roles of MFF, FIS1 and MiD49/MiD51, we measured peripheral and midzone fissions in wild-type and knockout mouse embryonic fibroblast (MEF) lines[11] ($Drp1^{-/-}$, $Mff^{-/-}$, $Fis1^{-/-}$, $Mid49^{-/-}Mid51^{-/-}$ double knockout and $Mff^{-/-}Mid49^{-/-}Mid51^{-/-}$ triple knockout (Fig. 3k, Extended Data Fig. 6p). Although $Drp1^{-/-}$ MEFs show a global inhibition of fission, Mff knockout reduces only midzone fission rates, and conversely, $Fis1$ knockout reduces only peripheral fission rates. We obtained similar results with siRNA-mediated knockdown of $FIS1$ and MFF (Extended Data Figs. 6q, 7b–d). By contrast, cells depleted of MiD49 and MiD51 exhibit a 35% decrease in both peripheral and midzone fission rates, compared with wild-type cells. Thus, MiD49 and MiD51 are engaged in but not required for both types of fission.

To examine the implications of adaptor depletions, we studied their effect on the response of cardiomyocytes to perturbations. We induced contraction for 48 h in cardiomyocytes and subsequently quantified apoptosis in control and FIS1-depleted cells (Fig. 3l, Extended Data Fig. 7e, f). We found that 68% of stimulated cardiomyocytes that lack

FIS1 underwent apoptosis (in contrast to 9–18% in control groups). FIS1 depletion also decreased proliferation rates, even in control conditions, perhaps owing to disrupted mitochondrial quality control, which is linked to cell cycle arrest in cardiomyocytes[27]. Finally, we knocked down *Mff* in cardiomyocytes that were stimulated to proliferate. Although miR-199 increased cell proliferation in the control group, MFF-depleted cell proliferation rates were significantly reduced (Fig. 3m, Extended Data Fig. 7e, f). This further highlights the importance of MFF-mediated midzone fissions for mitochondrial biogenesis during cell proliferation and FIS1-mediated peripheral fission for cell survival under stress conditions.

Discussion

Previous studies revealed that fission underlies both proliferation and degradation of mitochondria[1]. We discovered organelle-level regulation that reconciles this paradox, with the positioning of the fission site as a key morphological signature of the decision to proliferate or degrade. The formation of small daughter mitochondria to sequester damaged components has an advantage: such small mitochondria can be engulfed by autophagosomes and allow the mass of degraded material to be minimized. Our fine spatiotemporal analyses of mitochondrial physiology revealed that most peripheral divisions are preceded by a decrease in membrane potential and proton motive force, and an increase in ROS and Ca^{2+} levels, well before the constriction by DRP1. Although it is remarkable that a gradient forms within one mitochondrion, biological systems frequently use gradients to monitor their geometries[28], and even individual cristae can maintain different membrane potentials[29]. Thus, we speculate that peripheral fissions could use this gradient as a positioning cue, in the absence of extramitochondrial membrane contacts to define the location of the division site. This would explain how cells may regulate peripheral and midzone mitochondrial divisions independently, through intrinsic signals that reflect mitochondrial physiology.

Independent regulation is further supported by our observation that different adaptor proteins mediate peripheral and midzone fissions. Such a paradigm could account for the reported variability and seeming redundancy in the division machinery[30]. MFF accumulates at, and is only required for, midzone fissions, whereas FIS1 is important for regulation of peripheral fission. Weaker accumulation of MFF at poles and peripheral fission sites may be driven by curvature[6]. Initially, FIS1 was proposed to act as a DRP1 adaptor in yeast[31], but later studies in mammalian cells found no direct interactions with DRP1 (ref. [11]). Indeed, we observe a global enrichment of FIS1 on the outer membrane of small, peripherally dividing mitochondria, instead of foci. Therefore, we propose that FIS1 does not act as a DRP1 adaptor, but instead regulates peripheral fission through the recruitment of lysosomes, consistent with findings that FIS1 recruits the lysosome–mitochondria tethering molecule TBC1D15 (ref. [18]).

The existence of two mechanistically and functionally distinct types of fission has implications in the context of pathology. Excessive fission rates are a hallmark of diverse diseases[4,32], and pharmacological inhibition of fission has been proposed as a potential therapy[33]. Other therapeutic approaches have aimed to stimulate mitochondrial biogenesis[34]. However, our model suggests that if under pathological conditions only one type of fission is dysregulated, treatment with global inhibitors may further disrupt cell homeostasis. Therefore, our findings indicate the potential for more rational and specific therapeutic targets.

Online content

Any methods, additional references, Nature Research reporting summaries, source data, extended data, supplementary information, acknowledgements, peer review information; details of author contributions and competing interests; and statements of data and code availability are available at https://doi.org/10.1038/s41586-021-03510-6.

1. Twig, G. et al. Fission and selective fusion govern mitochondrial segregation and elimination by autophagy. *EMBO J.* **27**, 433–446 (2008).
2. Rambold, A. S., Kostelecky, B., Elia, N. & Lippincott-Schwartz, J. Tubular network formation protects mitochondria from autophagosomal degradation during nutrient starvation. *Proc. Natl Acad. Sci. USA* **108**, 10190–10195 (2011).
3. Song, M., Franco, A., Fleischer, J. A., Zhang, L. & Dorn, G. W., II. Abrogating mitochondrial dynamics in mouse hearts accelerates mitochondrial senescence. *Cell Metab.* **26**, 872–883 (2017).
4. Wang, W. et al. Parkinson's disease-associated mutant VPS35 causes mitochondrial dysfunction by recycling DLP1 complexes. *Nat. Med.* **22**, 54–63 (2016).
5. Ma, J.-T. et al. Effects of dynamin-related protein 1 regulated mitochondrial dynamic changes on invasion and metastasis of lung cancer cells. *J. Cancer* **10**, 4045–4053 (2019).
6. Friedman, J. R. et al. ER tubules mark sites of mitochondrial division. *Science* **334**, 358–362 (2011).
7. Ji, W. K., Hatch, A. L., Merrill, R. A., Strack, S. & Higgs, H. N. Actin filaments target the oligomeric maturation of the dynamin GTPase Drp1 to mitochondrial fission sites. *eLife* **4**, e11553 (2015).
8. Smirnova, E., Griparic, L., Shurland, D. L. & van der Bliek, A. M. Dynamin-related protein Drp1 is required for mitochondrial division in mammalian cells. *Mol. Biol. Cell* **12**, 2245–2256 (2001).
9. Gandre-Babbe, S. & van der Bliek, A. M. The novel tail-anchored membrane protein Mff controls mitochondrial and peroxisomal fission in mammalian cells. *Mol. Biol. Cell* **19**, 2402–2412 (2008).
10. Palmer, C. S. et al. MiD49 and MiD51, new components of the mitochondrial fission machinery. *EMBO Rep.* **12**, 565–573 (2011).
11. Osellame, L. D. et al. Cooperative and independent roles of the Drp1 adaptors Mff, MiD49 and MiD51 in mitochondrial fission. *J. Cell Sci.* **129**, 2170–2181 (2016).
12. Fröhlich, C. et al. Structural insights into oligomerization and mitochondrial remodelling of dynamin 1-like protein. *EMBO J.* **32**, 1280–1292 (2013).
13. Burman, J. L. et al. Mitochondrial fission facilitates the selective mitophagy of protein aggregates. *J. Cell Biol.* **216**, 3231–3247 (2017).
14. Ashrafi, G. & Schwarz, T. L. The pathways of mitophagy for quality control and clearance of mitochondria. *Cell Death Differ.* **20**, 31–42 (2013).
15. Sturtz, L. A., Diekert, K., Jensen, L. T., Lill, R. & Culotta, V. C. A fraction of yeast Cu,Zn-superoxide dismutase and its metallochaperone, CCS, localize to the intermembrane space of mitochondria. A physiological role for SOD1 in guarding against mitochondrial oxidative damage. *J. Biol. Chem.* **276**, 38084–38089 (2001).
16. Mallilankaraman, K. et al. MICU1 is an essential gatekeeper for MCU-mediated mitochondrial Ca^{2+} uptake that regulates cell survival. *Cell* **151**, 630–644 (2012).
17. Jourdain, A. A. et al. GRSF1 regulates RNA processing in mitochondrial RNA granules. *Cell Metab.* **17**, 399–410 (2013).
18. Wong, Y. C., Ysselstein, D. & Krainc, D. Mitochondria-lysosome contacts regulate mitochondrial fission via RAB7 GTP hydrolysis. *Nature* **554**, 382–386 (2018).
19. Soubannier, V., Rippstein, P., Kaufman, B. A., Shoubridge, E. A. & McBride, H. M. Reconstitution of mitochondria derived vesicle formation demonstrates selective enrichment of oxidized cargo. *PLoS One* **7**, e52830 (2012).
20. Pickles, S., Vigié, P. & Youle, R. J. Mitophagy and quality control mechanisms in mitochondrial maintenance. *Curr. Biol.* **28**, R170–R185 (2018).
21. Korobova, F., Ramabhadran, V. & Higgs, H. N. An actin-dependent step in mitochondrial fission mediated by the ER-associated formin INF2. *Science* **339**, 464–467 (2013).
22. Hirabayashi, Y. et al. ER-mitochondria tethering by PDZD8 regulates Ca^{2+} dynamics in mammalian neurons. *Science* **358**, 623–630 (2017).
23. Murley, A. et al. ER-associated mitochondrial division links the distribution of mitochondria and mitochondrial DNA in yeast. *eLife* **2**, e00422 (2013).
24. Lewis, S. C., Uchiyama, L. F. & Nunnari, J. ER-mitochondria contacts couple mtDNA synthesis with mitochondrial division in human cells. *Science* **353**, aaf5549 (2016).
25. Yu, R., Jin, S.-B., Lendahl, U., Nistér, M. & Zhao, J. Human Fis1 regulates mitochondrial dynamics through inhibition of the fusion machinery. *EMBO J.* **38**, e99748 (2019).
26. Xian, H., Yang, Q., Xiao, L., Shen, H.-M. & Liou, Y.-C. STX17 dynamically regulated by Fis1 induces mitophagy via hierarchical macroautophagic mechanism. *Nat. Commun.* **10**, 2059 (2019).
27. Kimura, W. et al. Redox signaling in cardiac renewal. *Antioxid. Redox Signal.* **21**, 1660–1673 (2014).
28. Chang, F. & Minc, N. Electrochemical control of cell and tissue polarity. *Annu. Rev. Cell Dev. Biol.* **30**, 317–336 (2014).
29. Wolf, D. M. et al. Individual cristae within the same mitochondrion display different membrane potentials and are functionally independent. *EMBO J.* **38**, e101056 (2019).
30. Koirala, S. et al. Interchangeable adaptors regulate mitochondrial dynamin assembly for membrane scission. *Proc. Natl Acad. Sci. USA* **110**, E1342–E1351 (2013).
31. Mozdy, A. D., McCaffery, J. M. & Shaw, J. M. Dnm1p GTPase-mediated mitochondrial fission is a multi-step process requiring the novel integral membrane component Fis1p. *J. Cell Biol.* **151**, 367–380 (2000).
32. Song, W. et al. Mutant huntingtin binds the mitochondrial fission GTPase dynamin-related protein-1 and increases its enzymatic activity. *Nat. Med.* **17**, 377–382 (2011).
33. Guo, X. et al. Inhibition of mitochondrial fragmentation diminishes Huntington's disease-associated neurodegeneration. *J. Clin. Invest.* **123**, 5371–5388 (2013).
34. Zamora, M., Pardo, R. & Villena, J. A. Pharmacological induction of mitochondrial biogenesis as a therapeutic strategy for the treatment of type 2 diabetes. *Biochem. Pharmacol.* **98**, 16–28 (2015).

Article

Methods

No statistical methods were used to predetermine sample size. For studies involving multiple experimental conditions, studies were performed on cells originated from the same cell line batch and randomly assigned to experimental conditions.

Plasmids and reagents

Mito–GFP (Cox-8 presequence) was a gift from H. Shroff (NIH, Bethesda), mCherry–DRP1 and BFP–KDEL were gifts from G. Voeltz (Addgene, plasmid no. 49152 and no. 49150)[6], SypHer mt was a gift from N. Demaurex (Addgene plasmid no. 48251)[35], pLPCX mito–GRX1–roGFP2 was a gift from T. Dick (Addgene plasmid no. 64977)[36], pCMV CEPIA3–mt was a gift from M. Iino (Addgene plasmid no. 58219)[37], LAMP1–mEGFP was a gift from R. Vale (Addgene plasmid no. 16290)[38], YFP–Parkin was a gift from R. Youle (Addgene plasmid no. 23955)[39] and EGFP–LC3 was a gift from K. Kirkegaard (Addgene plasmid no. 11546)[40], CMV-mito–R-GECO1 was a gift from R. Campbell (Addgene plasmid no. 46021)[41]. FASTKD2–EGFP and TWINKLE–EGFP[42] were gifts from J.-C. Martinou. Ftractin–Apple was a gift from H. N. Higgs (Dartmouth College, Hanover), mito–tagRFP was amplified from mito–GFP. Wild-type, $Drp1^{-/-}$, $Mff^{-/-}$, $Fis1^{-/-}$, $Mid49^{-/-}Mid51^{-/-}$ double knockout, $Mff^{-/-}Mid49^{-/-}Mid51^{-/-}$ triple knockout mouse embryonic fibroblasts were a gift from M. Ryan and have previously been described[11].

The stable FASTKD2–EGFP cell line was recently described[43]. In brief, co-transfection of human embryonic kidney 293T (HEK293T) cells (ATCC CRL-11268) with pWPT_FASTKD2–EGFP and packaging plasmids pMD2.G and psPAX2 was achieved using calcium phosphate precipitation. Medium containing virus was collected 48 h after transfection and filtered using membranes with a pore size of 0.45 μm. The viral supernatant and polybrene were added to 70% confluent recipient cells. Fluorescence-activated cell sorting (FACS) was performed to select for cells expressing GFP.

Oligonucleotides for siRNA were made by Microsynth to knock down *MFF* (sense strand 5′-CGC UGA CCU GGA ACA AGG A-dTdT-3′), *FIS1* (sense strand 5′-CGA GCU GGU GUC UGU GGA G-dTdT-3′) and *INF2* (sense strand 5′-GCA GUA CCG CUU CAG CAU UGU CAT T-3′ and 5′-GGA UCA ACC UGG AGA UCA UCC GCT T-3′). siRNA transfection was performed using Lipofectamine RNAi Max (Invitrogen) and cells were imaged 72 h after transfection.

The following reagents were also used: Mitotracker Green (ThermoFisher M7514), Mitotracker Red FM (ThermoFisher M22425), tetra-methylrhodamine ethyl ester perchlorate (Sigma, 87917), MitoSOX Red Mitochondrial Superoxide Indicator (Thermo Fisher M36008), Mitoquinol 98% (Adipogen SA CAY-89950-10), Quant-iT PicoGreen (Life Technologies P7581), CellEvent Caspase-3/7 (Life Technologies C10723), FIS1 polyclonal antibody (Proteintech 109561-AP), MFF (C2orf33) polyclonal antibody (Life Technologies PA567357), PDZD8 polyclonal antibody (Life Technologies PA553368), MiD49 (SMCR7) polyclonal antibody (Life Technologies, PA559950), TOM20 mouse monoclonal antibody (Santa Cruz sc-17764) and Alexa fluorophore-conjugated secondary antibodies from Life Technologies.

Generation of knock-in U2OS cells

CRISPR–Cas9-mediated knock-in of EGFP into the *MFF* locus directly upstream of the start codon was performed using a plasmid encoding EGFP2 flanked by 729 bp of upstream and 723 bp of downstream homologous DNA sequence cloned into pEX-A258 to create plasmid pTW344 (pEX-A258–EGFP_hMFF_Template KI). Two pairs of single guide DNA (sgDNA) targeting *MFF* (sgDNA1: forward 5′- aaacAGTGATG TGTCACTGCTTGTC-3′ and reverse 5′ CACCGACAAGCAG TGACACATCACT-3′, sgDNA2: forward 5′- CACCGCATTTAAATACAG-TAAATAC and reverse 5′- aaacGTATTTACTGTATTTAAATGC-3′) were cloned into pSpCas9n(BB)-2A-Puro (PX462) V2.0 (a gift from F. Zhang (Addgene plasmid no. 62987))[44].

CRISPR–Cas9-mediated knock-in of EGFP into the *FIS1* locus directly upstream of the start codon was performed using a plasmid encoding EGFP2 flanked by 721 bp of upstream and 624 bp of downstream homologous DNA sequence cloned into pEX-A258 to create plasmid pTW343 (pEX-A258–EGFP_hFIS1_Template KI). Two pairs of sgDNA targeting *FIS1* (sgDNA1: forward 5′- CACCGCTGAACGAGCTGGTGTCTG-3′ and reverse 5′ aaacCAGACACCAGCTCGTTCAGC-3′, sgDNA2: forward 5′- CACCGCTCGTTCAGCACGGCCTCCA and reverse 5′-aaacTGGAGGCCGTGCTGAACGAGC-3′) were cloned into pSpCas9n(BB)-2A-Puro (PX462) V2.0 (a gift from F. Zhang (Addgene plasmid no. 62987)). To knock in *EGFP* into either the *MFF* or the *FIS1* loci, U2OS cells were co-transfected with pSpCas9n(BB)-2A-Puro (PX462) V2.0 constructs carrying the appropriate sgDNA sequences and linearized template plasmids (pTW343 for hMFF and pTW344 for hFIS1) using Lipofectamine 2000. GFP-positive cells were individually isolated 24 h after transfection by FACS. Clones were expanded and were validated by PCR genotyping of genomic DNA and fluorescent imaging.

Cell culture and transfection

Cells were grown either in Dulbecco's modified Eagle's medium (DMEM) supplemented with 10% fetal bovine serum and maintained in culture for a maximum of 20 passages or in galactose-supplemented medium[45]. Cells were plated on 25-mm glass coverslips (Menzel, no. 1.5) 10–24 h before transfection at 1×10^5 cells ml^{-1}. Plasmid transfections were performed with 1.5 μl of Lipofectamine 2000 (Invitrogen) per 100 μl of Opti-MEM medium (Invitrogen). The following amounts of DNA were transfected per ml: 150 ng of mito–GFP, 250 ng of mito–tagRFP, 100 ng of mCherry–DRP1, 300 ng of TOM20–RFP, 400 ng of mito–SypHer, 400 ng of mito–GRX1–roGFP2, 150 ng of mito–R-GECO1, 400 ng of CEPIA3–mt, 350 ng of KDEL–RFP, 250 ng of LAMP1–mEGFP, 350 ng of EGFP–LC3, 400 ng of YFP–Parkin and 200 ng of TWINKLE–GFP. Cells were imaged the next day.

All cell lines were routinely tested for *Mycoplasma* contamination and discarded if positive. Cos-7 cells (ECACC 87021302) and U2OS cells (ECACC 92022711) were obtained from ECACC, and HEK293T cells (ATCC CRL-11268) were obtained from ATCC. ECACC and ATCC use STR profiling for authentication.

Primary mouse cardiomyocyte culture

Cardiac myocytes were prepared from ventricles of P1 neonatal mice using Pierce Cardiomyocyte Isolation Kit (Life Technologies 88281) following the manufacturer's instructions. After digestion, the adherent non-myocyte cells were removed by pre-plating in 10-cm tissue culture plates for 45 min. The non-adherent cardiomyocytes were seeded in complete cardiomyocyte plating medium supplemented with 10% fetal calf serum (FCS) and antibiotics at a density of $4–5 \times 10^5$ cells/well on poly-L-lysine (Sigma P-7890) and gelatin (Sigma G9891)-coated coverslips in six-well plates. To stimulate contraction, 24 h after plating the cardiomyocytes were fed with fresh medium supplemented with 2% FCS and with 10^{-5} M isoproterenol (Sigma I-2760). To induce proliferation, cardiomyocytes were transfected with 50 nM miR-199 mimic[46] (Pharmacon, miRIDIAN Mimic Has-miR-199a-3p; C300535-05) using Lipofectamine RNAi-Max following the manufacturer's instructions (Life Technologies, 13778). Cardiomyocytes were observed 48 h after treatment or transfection.

Western blotting

For immunoblots 48–72 h after siRNA transfection (Supplementary Fig. 1), Cos-7 cells were lysed in radioimmunoprecipitation (RIPA) buffer (Sigma) supplemented with fresh proteases inhibitors (Sigma Aldrich 11836170001) on ice for 30 min. A centrifugation at 16,000g for 10 min at 4 °C was performed to remove the insoluble material. Protein concentrations were determined using a Pierce BCA protein assay kit (Life Technologies, 23227) and equal amounts of protein were analysed by self-casted 7.5% or 15% SDS–PAGE (30–50 μg of protein

per lane). For immunoblotting, proteins were transferred to nitrocellulose membranes (BioRad) electrophoretically and incubated with the specified primary antibodies (see above), diluted in 5% non-fat dry milk in Tris-buffered saline with Tween 20 (TBST). The blots were further incubated with anti-rabbit or anti-mouse horseradish peroxidase (HRP)-conjugated secondary antibodies (GE Healthcare) and visualized using ECL (GE Healthcare). Where required, images of western blotting were treated for contrast enhancement, and densitometric analyses were performed using ImageJ.

Primary antibodies used for western blot
The following primary antibodies were used for western blots: anti-FIS1 (LuBioScience GmbH, 10956-1-AP, diluted 1:2,000), anti-MFF (Life Technologies, PA5-52765, diluted 1:500–1:1,000), anti-INF2 (Sigma-Aldrich HPA000724, diluted 1:2,000), anti-α-tubulin (Santa Cruz sc-5286, diluted 1:2,000).

RT–PCR
Total RNA was extracted from neonatal cardiomyocytes 48 h after transfection using the miRNeasy Mini Kit (Qiagen, no. 1038703). An optional step of DNase (Qiagen no. 79254) digestion was performed following the manufacturer's protocol. cDNA was synthesized from 1 µg of total RNA using the PrimeScript RT–PCR Kit (Takara no. RR014B) and Syber Green qRT–PCR was performed on QuantStudio 12K (Life Technologies) using the Power SYBR Green PCR Master Mix (Applied Biosystems, no. 4367659). For SYBR Green qRT–PCR, 4 µl of cDNA (25 ng µl^{-1}) were mixed with 5 µl of Power SYBR Green PCR Master Mix, 0.5 µl of forward primer (5 µM) and 0.5 µl of reverse primer (5 µM). The cDNA mix was incubated 2 min at 50 °C followed by a denaturation step of 2 min at 95 °C and an amplification step of 40 cycles at 95 °C for 15 s and at 60 °C for 45 s.

The following primers were used: *Fis1* forward primer 5′-CCGGC TCAAGGAATATGAAA-3′; *Fis1* reverse primer 5′-ACAGCCAGTCCAA TGAGTCC-3′; *Mff* forward primer 5′-AGTGTGATAATGCAAGTCCCAGA-3′; *Mff* reverse primer 5′-GAGTGGACTGGATAAGGTCAAGA-3′; *Gapdh* forward primer 5′-TGCACCACCAACTGCTTAGC-3′; and *Gapdh* reverse primer 5′-GGCATGGACTGTGGTCATGAG-3′.

Live-cell treatments
TMRE. Cells were incubated with 500 nM TMRE for 10 min followed by rinsing in phosphate-buffered saline (PBS).

Mitotracker. Cells were incubated in 500 nM Mitotracker for 5 min followed by rinsing in PBS.

PicoGreen. To image mtDNA, cells were stained with PicoGreen diluted 1:500 for 20 min.

MitoSOX. Cells were incubated with 5 µM MitoSOX for 2–4 h before imaging.

MitoQ. Cells were incubated with 500 nM MitoQ[47] for 30–45 min prior and during imaging following the manufacturer's instructions, and fresh aliquots were made every day.

BrU tagging of RNA
Cos-7 cells were incubated with 5 mM 5-bromouridine (BrU) in complete culture medium for 1 h before fixation, as described previously[43]. BrU was stored at −20 °C, and heated and vortexed before use. Samples were immunolabelled with anti-bromodeoxyuridine (BrdU) (Roche 11170376001; 1:250 to 1:500 dilution) to visualize BrU signal.

SIM imaging
Single and dual-colour SIM imaging was performed on a 3D NSIM Nikon inverted fluorescence microscope (Eclipse Ti; Nikon) equipped with an electron charge-coupled device camera (iXon3 897; Andor Technologies). The microscope was equipped with a 100× 1.49 NA oil immersion objective (CFI Apochromat TIRF 100×C Oil; Nikon). Live-cell imaging was performed at 37 °C using a 488-nm and a 561-nm laser. Acquisition settings were adapted to yield the best image quality with minimal photobleaching (laser power 0.5–15%, exposure time 30–100 ms). Images were captured using NIS elements software (Nikon) at temporal resolution of 1 s for single-colour and 6–8 s for dual-colour imaging. Imaging was performed at 37 °C in pre-warmed Leibovitz medium. Each sample was imaged for a maximum of 90 min.

Instant SIM
Single and dual colour iSIM imaging was performed on a custom-built microscope set-up as previously described[48,49]. Fluorescence was collected with a 1.49 NA oil immersion objective (APONXOTIRF; Olympus), with 488-nm and 561-nm excitation lasers and an sCMOS camera (PrimeBSI, 01-PRIME-BSI-R-M-16-C; Photometric). Images were captured at temporal resolution of 0.5–5 s for both channels. All imaging was performed at 37 °C in Leibovitz medium. Raw iSIM images were subsequently deconvolved using the Lucy-Richardson deconvolution algorithm[50] provided by Hari Shroff implemented in MATLAB and were run for 40 iterations.

Confocal imaging
Ratiometric imaging of mito–GRX1–roGFP was performed on an inverted microscope (DMI 6000; Leica) equipped with hybrid photon counting detectors (HyD; Leica). The sample was excited sequentially frame by frame at 408 nm and 488 nm with the detection set to 500–535 nm. Fluorescence was collected through a 63× 1.40 NA oil immersion objective (HC PL APO 63×/1.40 Oil CS2; Leica). Images were captured using the LAS X software (Leica). All imaging was performed at 37 °C in pre-warmed Leibovitz medium for maximum 90 min per sample.

For confocal microscopy of fixed BrU samples the imaging was performed using a Leica TCS SP8 inverted microscope equipped with 405-, 488-, 552- and 638-nm lasers and a Plan-Apochromat oil objective (×63, NA 1.4). The Lightning mode (Leica) was used to generate deconvolved images. Microscope acquisitions were controlled by LAS X (v. 3.5.2) software from Leica.

CLEM and caspase 3/caspase 7 samples were imaged on a Zeiss LSM 700 inverted confocal microscope equipped with a Plan-Apochromat oil objective (×63, NA 1.40) and 488-nm and 555-nm solid-state lasers and three photomultipliers. Acquisitions were controlled by the Zeiss Zen (v. 6.0.0) software.

Immunofluorescence
Cells were seeded on glass coverslips and grown to a confluence of ~80%. Fixation of cultured cells was performed in cold 4% paraformaldehyde (PFA) in PBS for 20 min, then cells were washed 3× in PBS. Subsequently, cells were incubated with 0.3% Triton X-100 and 1% pre-immune goat serum for 30 min. The same buffer was used to incubate cells with the specified primary antibody (see above) overnight at 4 °C. After washing in PBS, cells were incubated with the appropriate secondary antibody for 1 h and rinsed in PBS before imaging.

Immunohistochemistry on cardiomyocytes
Cardiomyocytes (CMs) (P1) were transfected with 25 nM si*Fis1* or si*Mff* for 6 h and then transfected with 50 nM miR-199 mimic for 48 h. EdU was added in fresh medium after 56 h and kept for the last 18 h. Cells were then fixed for 10 min in in 4% PFA in PBS and permeabilized with 0.3% Triton X-100 in PBS. After blocking (PBS containing 0.001% Triton X-100, 1% bovine serum albumin and 1% FCS), cells were incubated overnight at 4 °C with anti-troponin I (1:500). The day after, cells were washed 3× and incubated 1 h at room temperature in the dark with the secondary-conjugated antibody diluted 1:500 (488 goat anti-rabbit A11008; Life Technologies). EdU has been labelled and detected using

a Click-iT EdU Alexa Fluor 594 Imaging Kit (Invitrogen C10339). Nuclei were stained with DAPI (Invitrogen).

Correlated confocal and transmission electron microscopy

Cells were seeded on gridded coverslips (MatTek, P35-1.5-14-CGRD-D) and grown to 50–60% confluence. Cells were fixed at room temperature for 1 h in freshly prepared fixative (2% PFA, 1% glutaraldehyde in PBS 0.1 M, pH 7.4), followed by 10× washing in PBS. Samples were imaged by confocal microscopy on the same day and z-stacks were acquired of whole cells, the pinhole was closed to 0.5 AU and pixel size reduced to 50–100 nm in xy and 100–150 nm in z. Samples were stored overnight, in PBS at 4 °C. They were then stained with osmium and potassium ferrocyanide, followed by osmium alone, each with cacodylate buffer. They were finally stained with 1% uranyl acetate, then washed in water, dehydrated through 15 increasing concentrations of alcohol and infiltrated with Epon resin. This was polymerized over night at 65 °C. Ultra-thin serial sections were then cut of the cell of interest, and the sections were collected on single slot copper grids with a formvar support membrane. Images were recorded in a transmission electron microscope operating at 80 kV (FEI Company, Tecnai Spirit).

Image analysis

All image analysis was performed with the open-source ImageJ/Fiji[51,52] (including Weka Segmentation, EMBL bleach correction plugins). Mitochondrial fissions were defined as events in which a single mitochondrion divided into two independently moving daughter mitochondria in live cells and in fixed cells when a (DRP1-positive) constriction site showed a diameter of <180 nm, measured via FWHM across the constriction. For representation purpose, a 1-pixel Gaussian filter was used and some videos were corrected for bleaching.

Relative position of constriction site. The positioning of constriction site was measured manually by drawing a line along the length axis of the mitochondrion in the frame before fission. For branched mitochondria (~13% of the mitochondrial population), the lengths of individual branches were summed.

Relative fluorescence intensity. Intensity measurements of biosensors were analysed by measuring mean fluorescence intensity on each side of the constriction and in single daughter mitochondria after fission (ROI defined by using Otsu thresholding) on SIM images and subtracting the cytosolic background. For normalization, the mean fluorescence intensity was measured in three non-dividing mitochondria within the same FOV at the same time point. For fixed samples (anti-PDZD8, anti-MFF, anti-FIS1, anti-MiD49), the mean intensity was measured in a 500-nm circle placed at the constriction site and normalized over the fluorescent signal along the non-constricted part of the mitochondrion. For measuring DRP1, LAMP1–mEGFP, MFF–GFP and FIS1–GFP intensities, a 500-nm circle was placed at the constriction site and normalized over the intensity of at a 500-nm circle placed on a non-constricted part of the same mitochondrion.

Fission rate. To measure the fission rate, the total mitochondrial volume was calculated using trainable Weka segmentation (Fiji plugin) followed by binarization of the image. The total mitochondrial length was calculated using the total area in the binarized image divided by the mean mitochondrial diameter. Fission rates were indicated as number of fissions occurring per micrometre length of mitochondrion, per min.

ER or actin contacts. Contacts between mitochondria and ER or actin were measured by placing a line along the length axis of the mitochondrion crossing the constriction site and measuring the intensity profile for both channels. A contact site was defined, if the two signals cross at the constriction site (ER signal increases at least 2× over background) for at least three consecutive frames before fission.

Lysosome–mitochondria contact. A contact between mitochondria and lysosome was categorized as close proximity (<500 nm) between lysosomes and the mitochondrial constriction site for at least three consecutive frames before fission.

BrU quantification. Individual cells were selected manually, using Fiji's rectangular selection tool. Three consecutive slices to focus at the bottom of the cell were then chosen upon inspection and foci were detected automatically in both BrU and FASTKD2 channels using a fixed threshold. Foci that occurred in both channels were then counted as relevant mitochondrial RNA-transcription granules, whereas nuclear transcription, for instance, was excluded from the analysis. Multiple thresholds were tried, where 150 a.u. (a.u.= grey value from a range 0–255) provided the most sensible results in control cells and are represented in Extended Data Fig. 3g, although all other data are provided in the source data files and followed the same trend. The same pipeline was applied to both control and UV-treated samples.

Animal experiments

Mice were housed in a 12-h light/12-h dark cycle at a temperature of 23 °C with 40–60% humidity. All animal experiments were approved by the Government Veterinary Office (Lausanne, Switzerland) and performed according to the University of Lausanne Medical School institutional guidelines.

Statistics and reproducibility

Sample sizes were determined on the basis of previous experience in previous experiments. All statistics were performed using OriginPro software. First, datasets were tested for normal distribution using D'Agostino–Pearson normality test (significance value of 0.05). If a dataset failed this test, a non-parametric test was chosen to compare significance of means between groups (Mann–Whitney test for two samples). For normally distributed datasets, a two-sample t-test was chosen to compare two samples. For a detailed description of statistical tests used and exact P values, please see Supplementary Table 1. Critical comparative datasets (FIS1 and MFF datasets, DRP1 intensity analysis, ER analysis) were partially re-analysed or analysed with an automated analysis pipeline to exclude observer bias. P values <0.05 were considered to be significant and indicated by *; P values <0.01 were indicated by ** and <0.001 by ***.

Reporting summary

Further information on research design is available in the Nature Research Reporting Summary linked to this paper.

Data availability

All imaging as well as numerical data relevant to this study are publicly available on the online repository Zenodo (https://doi.org/10.5281/zenodo.3550643). The data are organized according to their appearance in the main figures and Extended Data figures. The unprocessed western blot gels are provided in Supplementary Fig. 1. Plasmids and cell lines are available from the corresponding authors on request. Source data are provided with this paper.

Code availability

The custom-written Fiji-macro script for BrU quantification is available at https://github.com/TimoHenry/MitochondrialRNAgranules and the custom written Fiji-macro for caspase staining is available at https://github.com/jutziw/mitochondrial_division.

35. Poburko, D., Santo-Domingo, J. & Demaurex, N. Dynamic regulation of the mitochondrial proton gradient during cytosolic calcium elevations. *J. Biol. Chem.* **286**, 11672–11684 (2011).

36. Gutscher, M. et al. Real-time imaging of the intracellular glutathione redox potential. *Nat. Methods* **5**, 553–559 (2008).

37. Suzuki, J. et al. Imaging intraorganellar Ca²⁺ at subcellular resolution using CEPIA. *Nat. Commun.* **5**, 4153 (2014).

38. Minin, A. A. et al. Regulation of mitochondria distribution by RhoA and formins. *J. Cell Sci.* **119**, 659–670 (2006).

39. Narendra, D., Tanaka, A., Suen, D.-F. & Youle, R. J. Parkin is recruited selectively to impaired mitochondria and promotes their autophagy. *J. Cell Biol.* **183**, 795–803 (2008).

40. Jackson, W. T. et al. Subversion of cellular autophagosomal machinery by RNA viruses. *PLoS Biol.* **3**, e156 (2005).

41. Wu, J. et al. Improved orange and red Ca²⁺ indicators and photophysical considerations for optogenetic applications. *ACS Chem. Neurosci.* **4**, 963–972 (2013).

42. Spelbrink, J. N. et al. Human mitochondrial DNA deletions associated with mutations in the gene encoding Twinkle, a phage T7 gene 4-like protein localized in mitochondria. *Nat. Genet.* **28**, 223–231 (2001).

43. Rey, T. et al. Mitochondrial RNA granules are fluid condensates positioned by membrane dynamics. *Nat. Cell Biol.* **22**, 1180–1186 (2020).

44. Ran, F. A. et al. Genome engineering using the CRISPR–Cas9 system. *Nat. Protocols* **8**, 2281–2308 (2013).

45. Marroquin, L. D., Hynes, J., Dykens, J. A., Jamieson, J. D. & Will, Y. Circumventing the Crabtree effect: replacing media glucose with galactose increases susceptibility of HepG2 cells to mitochondrial toxicants. *Toxicol. Sci.* **97**, 539–547 (2007).

46. Eulalio, A. et al. Functional screening identifies miRNAs inducing cardiac regeneration. *Nature* **492**, 376–381 (2012).

47. Kelso, G. F. et al. Selective targeting of a redox-active ubiquinone to mitochondria within cells: antioxidant and antiapoptotic properties. *J. Biol. Chem.* **276**, 4588–4596 (2001).

48. York, A. G. et al. Instant super-resolution imaging in live cells and embryos via analog image processing. *Nat. Methods* **10**, 1122–1126 (2013).

49. Mahecic, D. et al. Homogeneous multifocal excitation for high-throughput super-resolution imaging. *Nat. Methods* **17**, 726–733 (2020).

50. Holmes, T. J. & Liu, Y. H. Richardson-Lucy/maximum likelihood image restoration algorithm for fluorescence microscopy: further testing. *Appl. Opt.* **28**, 4930–4938 (1989).

51. Schindelin, J. et al. Fiji: an open-source platform for biological-image analysis. *Nat. Methods* **9**, 676–682 (2012).

52. Schneider, C. A., Rasband, W. S. & Eliceiri, K. W. NIH Image to ImageJ: 25 years of image analysis. *Nat. Methods* **9**, 671–675 (2012).

Additional information
Supplementary information The online version contains supplementary material available at https://doi.org/10.1038/s41586-021-03510-6.
Correspondence and requests for materials should be addressed to T.K. or S.M.
Peer review information *Nature* thanks Henry Higgs and the other, anonymous, reviewer(s) for their contribution to the peer review of this work.
**Reprints and permissions information** is available at http://www.nature.com/reprints.
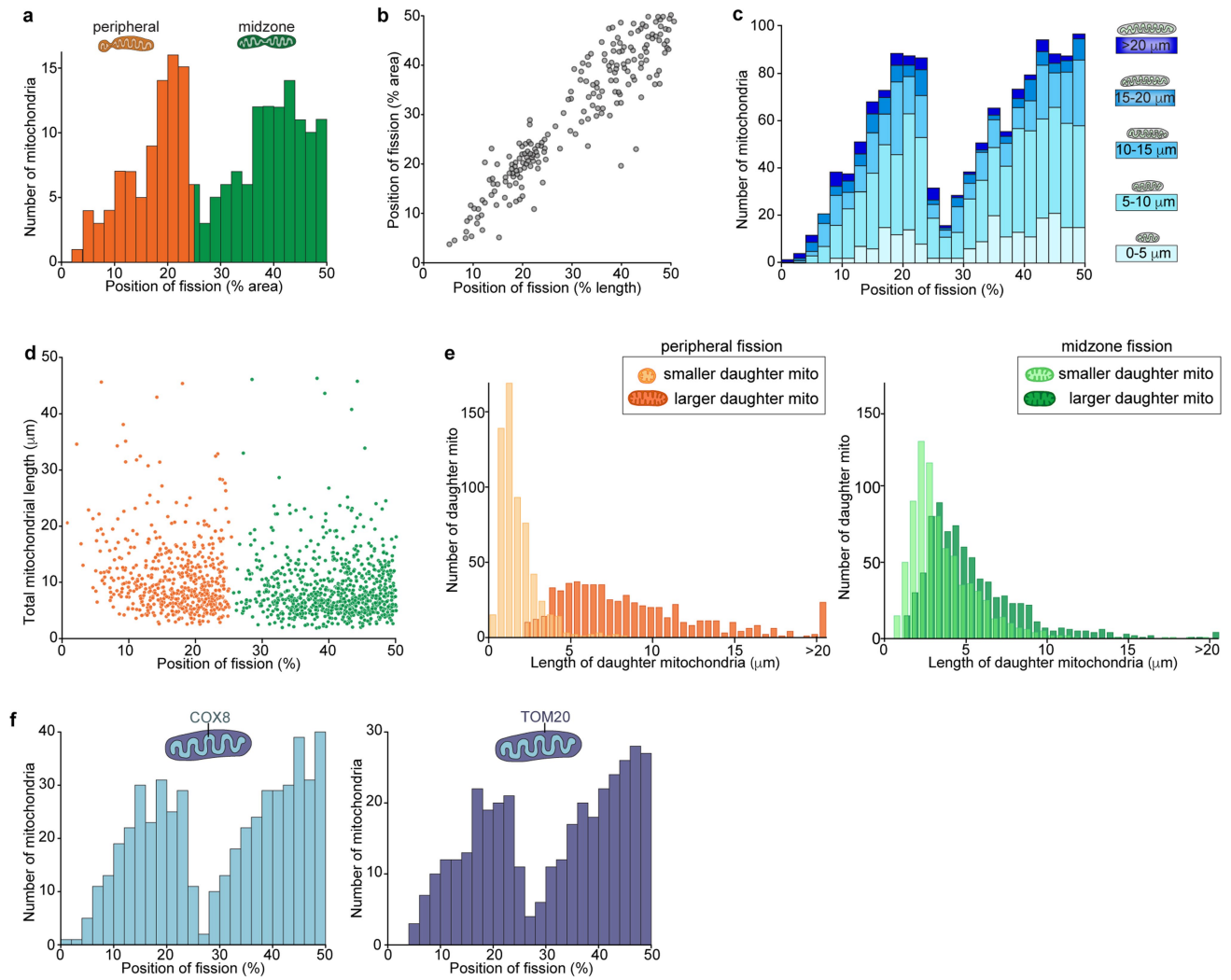
Extended Data Fig. 1 | Distribution of mitochondrial fission sites. a, Histogram of the relative position of constriction/fission measured by mitochondrial volume (*n* = 190 fissions). The two peaks are coloured in orange (0–25 bin; 'peripheral position') and green (25–50 bin; 'midzone position'). **b**, Relative position of mitochondrial fission measured by length versus measured by area (*n* = 190 fissions). **c**, Stacked histogram of the relative position of fission for different bins grouped by the total length of the dividing mitochondria (*n* = 1393). **d**, Scatter plot of the total length of dividing mitochondria versus the relative position of the fission site along the length axis with peripheral fissions (0–25% bin) coloured in orange and midzone fissions (25–50% bin) coloured in green (*n* = 1393 fissions). **e**, Length distribution of the smaller (light colour) and larger (dark colour) daughter mitochondria arising from peripheral left, orange) and midzone (right, green) fissions. **f**, Histogram of relative position of fission in datasets acquired with a mitochondrial inner membrane marker (left, COX8 targeting domain; *n* = 510 fissions) and a mitochondrial outer membrane marker (right, TOM20; *n* = 368 fissions).
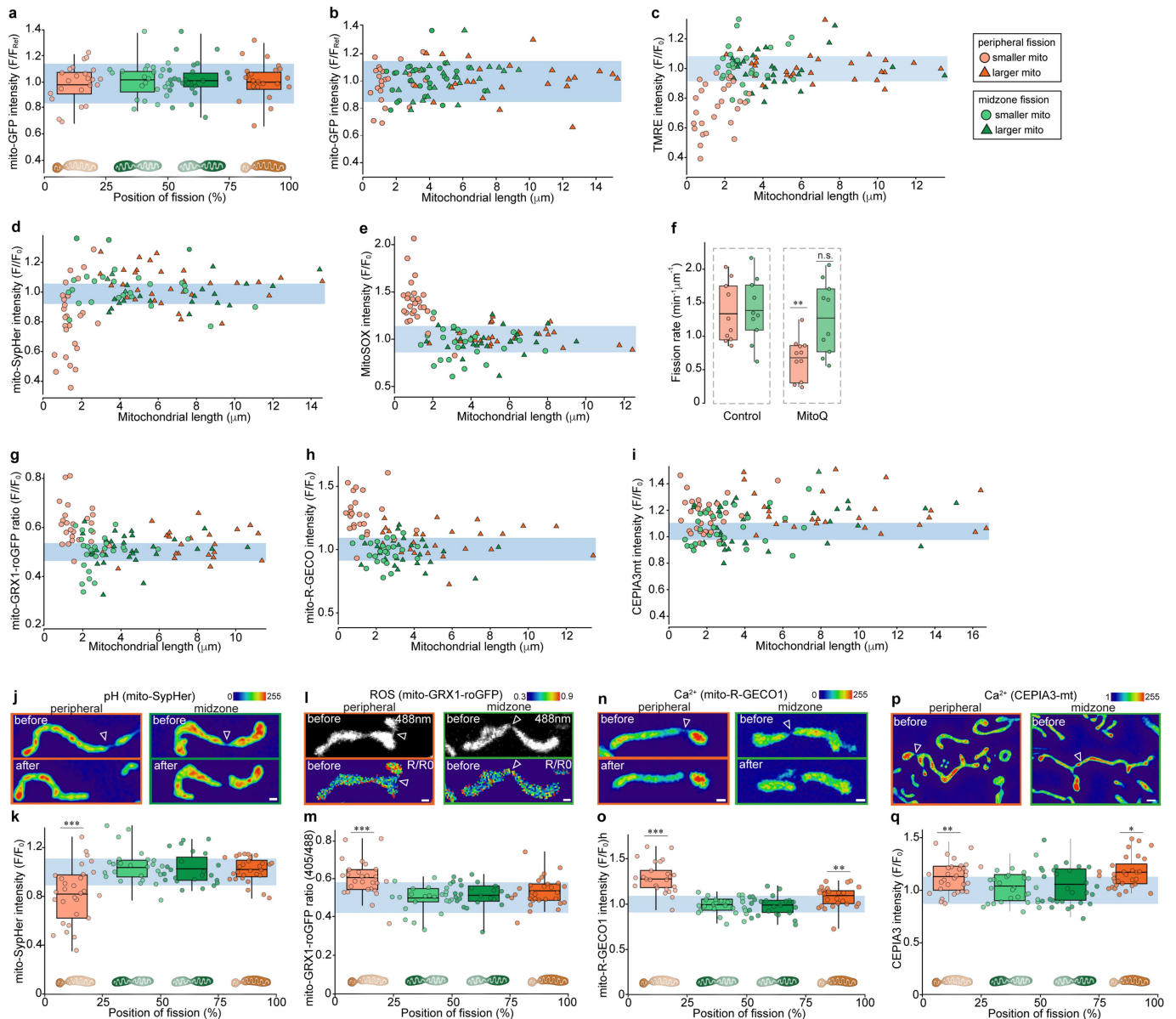
Extended Data Fig. 2 | Physiological changes preceding fission are independent of volume and absolute length. a, Normalized mito–GFP intensity depending on the relative position of fission measured in mitochondria immediately before fission. (*n* = 50 fissions). **b**, Dependence on the length of the daughter mitochondria of normalized mito–GFP intensity immediately before peripheral (orange) or midzone (green) fissions (*n* = 50 fissions). **c**, Dependence on the length of the daughter mitochondria of normalized TMRE intensity immediately before peripheral (orange) or midzone (green) fissions (*n* = 56 fissions). **d**, Dependence on the length of the daughter mitochondria of normalized mito–SypHer intensity before fission (*n* = 53 fissions). **e**, Dependence of the length of the daughter mitochondria on normalized MitoSOX intensity before fission (*n* = 52 fissions). **f**, Rates of peripheral and midzone fissions in control Cos-7 cells (*n* = 10 fields of view) versus cells treated with 500 nM ROS scavenger MitoQ (*n* = 10 fields of view). **g**, Dependence on the length of the daughter mitochondria of ratiometric intensity of mito–GRX1–roGFP immediately before fission (*n* = 52 fissions). **h**, Dependence on the length of the daughter mitochondria of normalized mito–R-GECO1 intensity before fission (*n* = 50 fissions). **i**, Dependence on the length of the daughter mitochondria of normalized CEPIA3–mt intensity before fission (*n* = 61 fissions). **j**, Mitochondrial pH before and after a peripheral

or midzone fission from SIM movies of mito–SypHer transfected Cos-7 cells. **k**, Normalized mito–SypHer intensity as a function of relative position of fission, measured immediately before fission (*n* = 53 fissions). **l**, Mitochondrial ROS before and after a peripheral or midzone fission from ratiometric images of mito–GRX1–roGFP transfected Cos-7 cells. **m**, Ratiometric mito–GRX1–roGFP intensity as a function of relative position of fission, measured immediately before fission (*n* = 52 fissions). **n**, Mitochondrial matrix Ca²⁺ before and after a peripheral or midzone fission from SIM movies of mito–R-GECO1 transfected Cos-7 cells. **o**, Normalized mito–R-GECO1 intensity as a function of relative position of fission, measured immediately before fission (*n* = 50 fissions). **p**, Mitochondrial matrix Ca²⁺ before and after a peripheral or midzone fission from SIM movies of CEPIA3–mt transfected Cos-7 cells. **q**, Normalized CEPIA3–mt intensity as a function of relative position of fission, measured immediately before fission (*n* = 61 fissions). In **a**, **k**, **m**, **o** and **q** circles indicate individual measurements; values of binned groups represented as box plots (line, mean; bounds of box: 25th and 75th percentiles; whiskers, min/max values). Light blue areas indicate mean intensity in non-dividing mitochondria (± s.d.). n.s. >0.05, ***P < 0.001. Number of experiments, statistical tests and exact *P* values are provided in Supplementary Table 1. Scale bars, 0.5 μm. Fission sites are indicated by arrowheads.
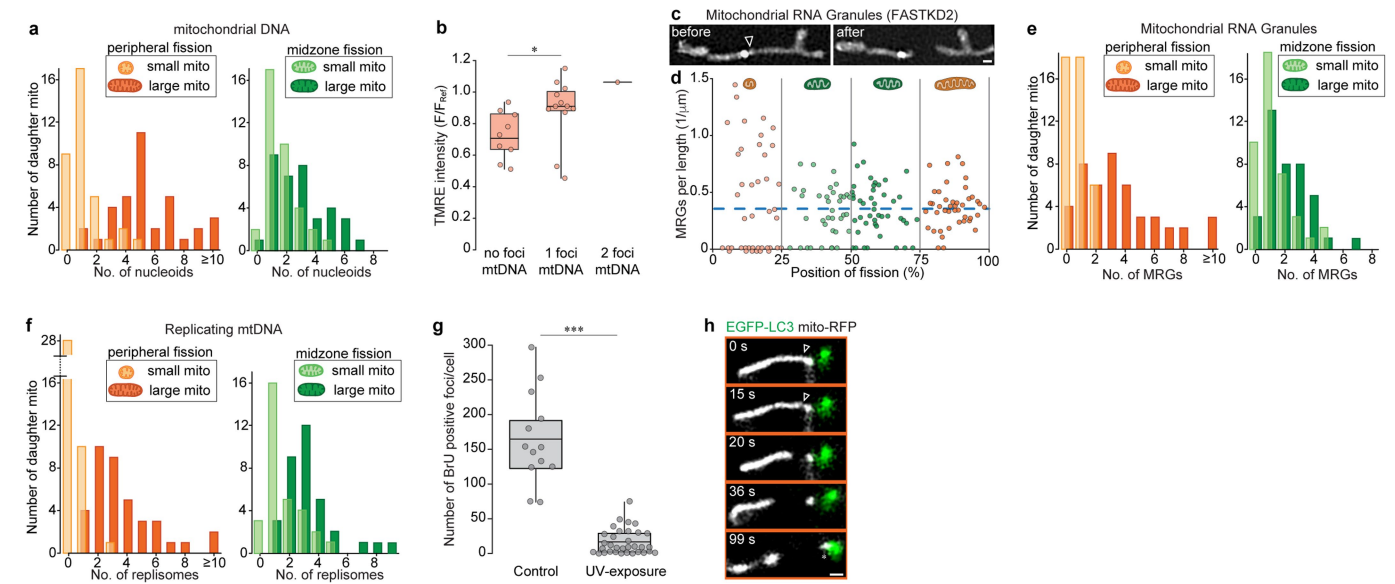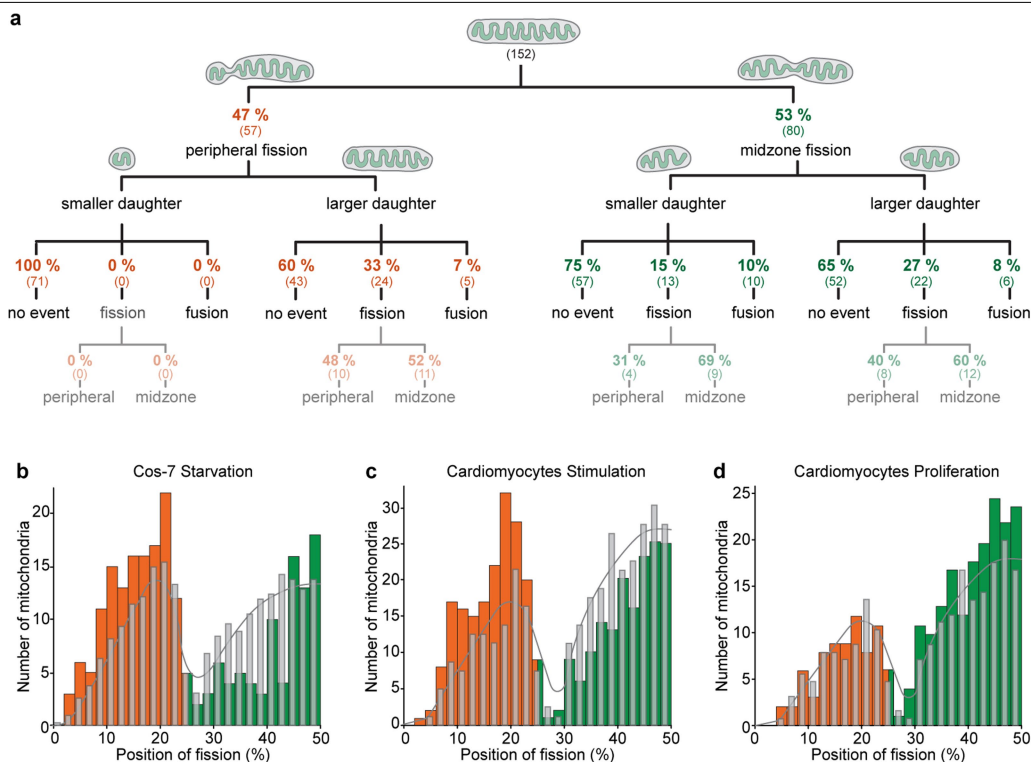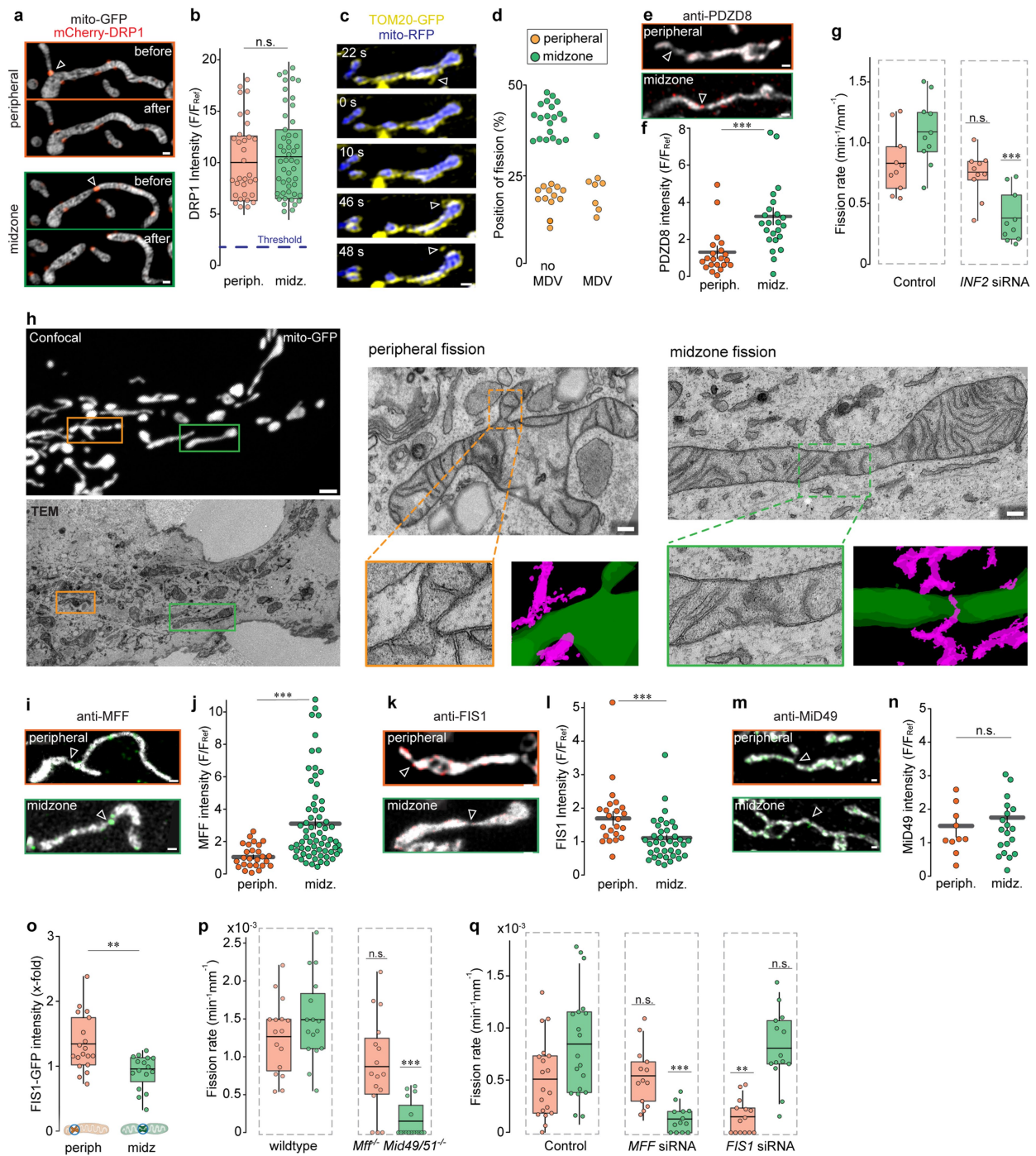
Extended Data Fig. 3 | Redistribution of mitochondrial DNA and RNA granules. a, Distribution of PicoGreen foci in the small and large daughter mitochondrion derived from peripheral and midzone fission (*n* = 78 fissions). **b**, Normalized TMRE intensity in the small daughter mitochondria from peripheral fissions that contain 0, 1 or 2 nucleoids (*n* = 20 fissions). **c**, SIM images of mitochondrial RNA granules (MRGs) (FASTKD2) before and after fission. **d**, Number of MRGs per μm length as a function of fission position (*n* = 84 fissions). Blue line shows average MRG per length in non-dividing mitochondria (*n* = 41). **e**, Distribution of the number of MRGs (FASTKD2; *n* = 84 fissions). **f**, Number of replicating nucleoids (TWINKLE; *n* = 74 fissions) in

smaller (light) and larger (dark) daughter mitochondria from peripheral (orange) and midzone (green). **g**, Number of BrU-positive foci per cell in control Cos-7 cells (*n* = 39) and cells exposed to UV light for 3 min before measurement (*n* = 98). **h**, Time-lapse SIM sequence of Cos-7 mitochondria (mito–RFP, grey) and autophagosomes (EGFP–LC3, green), where the small daughter mitochondrion from a peripheral fission is being taken up by an autophagosome (asterisk). In **b** and **g** circles indicate individual measurements; line, mean; bounds of box, 25th and 75th percentiles; whiskers, min/max values. **P* < 0.05, ****P* < 0.001. Number of experiments, statistical tests and exact *P* values are provided in Supplementary Table 1. Scale bars, 0.5 μm.
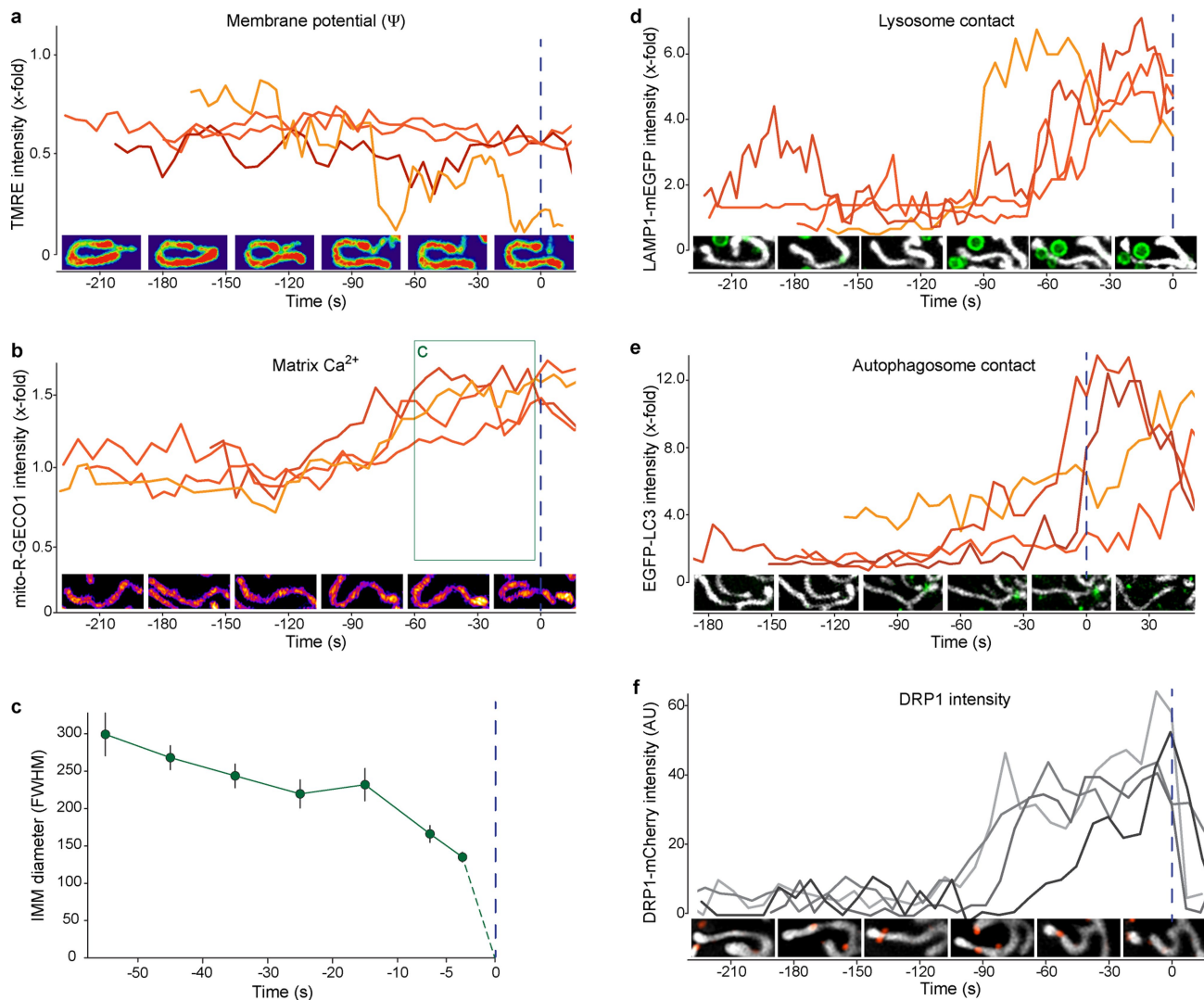
Extended Data Fig. 4 | Time course of physiological changes and recruitment of fission regulators. a, b, Time course of fluorescent signals in four examples of Cos-7 mitochondria displaying normalized TMRE intensity (**a**) and mito–R-GECO1 intensity (**b**) with corresponding SIM images in the mitochondrial compartment giving rise to the smaller daughter mitochondria before a peripheral division. **c,** Average inner membrane diameter at the constriction site at several time points before fission, measured in mito–R-GECO1 transfected Cos-7 cells during the time window where Ca^{2+} is elevated (green box in **b**, n = 10 fission events). **d, e,** Time course of lysosome co-localization (**d**) and autophagosome co-localization (**e**) at constriction sites for peripheral fissions, by measuring LAMP1–mEGFP and EGFP–LC3 intensity, respectively. For EGFP–LC3 measurements, cells were pre-treated with 10 µM CCCP to increase LC3 signals. **f,** Normalized DRP1 intensity at the constriction sites before peripheral fission in four examples of Cos-7 mitochondria with corresponding SIM images. Blue dotted lines (t = 0 s) mark the time point of fission.

Extended Data Fig. 5 | Peripheral and midzone fissions interact differently with the mitochondrial network, and the distribution of the fission positions is regulated independently. a, Schematic diagram depicting the fate ('no event', another 'fission' or 'fusion') of each daughter mitochondrion from peripheral and midzone fissions after the initial division in postnatal cardiomyocytes. Only mitochondria that could be traced for more than 100 s after fission were included in the analysis. **b**, Distribution of the relative position of fission in starved Cos-7 cells, with peripheral (1–25%) fission labelled in orange and midzone fissions (25–50%) in green (n = 212 fissions). The frequency distribution of Cos-7 control samples is superimposed in grey (replotted from Fig. 1c). **c**, **d**, Distribution of the relative position of constriction/fission along the length axis of isoproterenol-treated mouse cardiomyocyte mitochondria (**c**; n = 356 fissions) and miR-199 treated cardiomyocytes (**d**; n = 225 fissions) respectively. The frequency distribution of untreated mouse cardiomyocyte samples is superimposed in grey (replotted from Fig. 1e).

Extended Data Fig. 6 | See next page for caption.

Article

Extended Data Fig. 6 | Peripheral and midzone fissions are both DRP1 mediated but involve distinct upstream mechanisms. a, Two-colour SIM images of mitochondria (mito–GFP, greyscale) and DRP1 (mCherry–DRP1, red) undergoing peripheral or midzone fission. **b**, Normalized DRP1 intensity on the constriction sites of peripheral and midzone divisions. The threshold for a DRP1 accumulation (blue dotted line) was set at a signal >3× over background ($n = 107$ fissions). **c**, Time-lapse sequence of a SIM movie, in which both mitochondrial outer membrane (TOM20–GFP) and inner membrane (mito–RFP) were labelled to detect mitochondria-derived vesicle (MDV) formation (arrowhead). **d**, Quantification of the fission positions for mitochondria undergoing MDV formation or not before or after division ($n = 41$ fissions). **e**, SIM images of peripheral and midzone constrictions in fixed Cos-7 cells labelled with anti-PDZD8 (red). **f**, Distribution of normalized fluorescence intensities of anti-PDZD8 staining in fixed Cos-7 cells for peripheral (orange) and midzone (green) fissions ($n = 38$ fissions). **g**, Rate of peripheral and midzone fissions in control cells ($n = 10$ FOV) versus cells treated with *INF2* siRNA ($n = 10$ FOV). **h**, Correlated confocal and transmission electron microscopy (CLEM) of mitochondria in Cos-7 cells labelled with mito–GFP, fixed 24 h after expression. Zoom-in of two individual mitochondria with a peripheral (orange frame) and a midzone (green frame) constriction in the TEM plane containing the widest diameter of the constriction site. Pseudo-colouring of three consecutive TEM *z*-sections recombined into a single rendering shows mitochondria (green) and ER (magenta). Scale bar represents 2 μm in confocal and 200 nm in TEM images. **i, k, m**, SIM images of peripheral and midzone constrictions in fixed Cos-7 cells labelled with anti-TOM20 (grey) and anti-MFF (green) (**i**), anti-FIS1 (red) (**k**) and anti-MiD49 (green) (**m**). **j, l, n**, Distribution of normalized fluorescent intensities of anti-MFF ($n = 92$ fissions) (**j**), anti-FIS1 ($n = 59$ fissions) (**l**) and anti-MiD49 ($n = 29$ fissions) (**n**) staining in fixed Cos-7 cells for peripheral (orange) and midzone (green) fissions. **o**, Normalized FIS1–GFP intensity at the fission site of peripheral (left) and midzone (right) divisions (orange dots: peripheral, green dots: midzone; $n = 35$ fissions). **p**, Quantification of the peripheral (orange) and midzone (green) fission rates in wild-type ($n = 16$ FOV) and *Mff*$^{-/-}$*Mid49*$^{-/-}$*Mid51*$^{-/-}$ triple-knockout ($n = 16$ FOV) MEFs stained with Mitotracker Green. **q**, Quantification of the peripheral (orange) and midzone (green) fission rates in control Cos-7 cells and cells treated with siRNAs against *MFF* or *FIS1* ($n \geq 13$ FOV per group). n.s. $P > 0.05$, **$P < 0.01$, ***$P < 0.001$. Number of experiments, statistical tests and exact P values are provided in Supplementary Table 1. Scale bars, 0.5 μm. Fission sites are indicated by arrowheads.
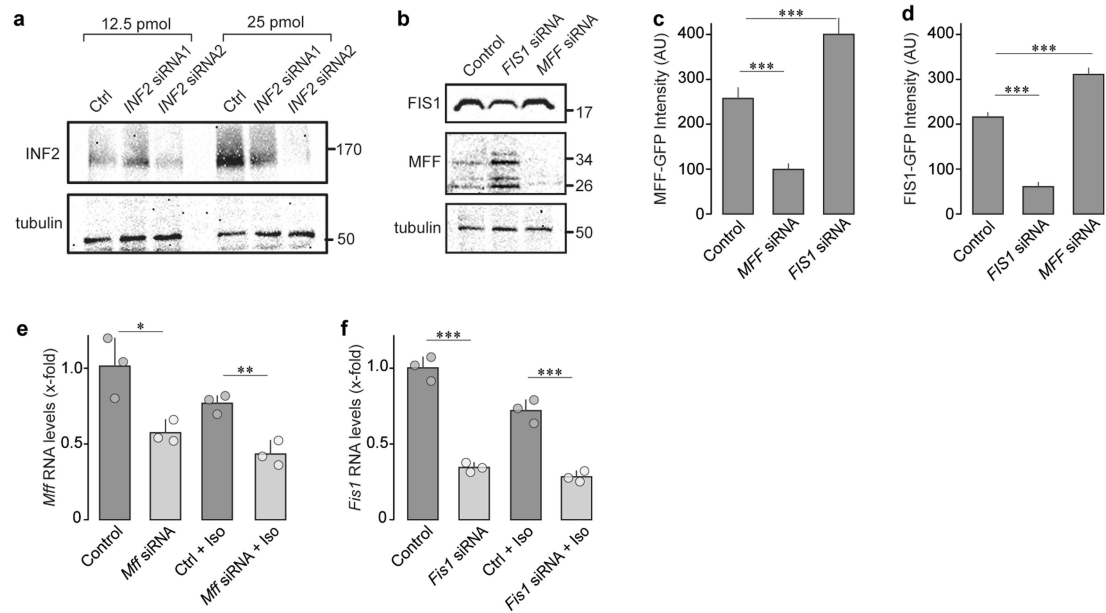
Extended Data Fig. 7 | Silencing efficiency of siRNA against *FIS1*, *MFF* and *INF2* in Cos-7 cells. a, Western blot analysis of protein levels for Cos-7 cells 72 h after transfection with two siRNAs against *INF2* at two different quantities (pmol). Molecular mass is in kilodaltons. **b**, Western blot analysis of protein levels for Cos-7 cells 72 h after transfection with 12.5 pmol of siRNA against *FIS1* or *MFF*. **c**, **d**, Mean fluorescence intensity in U2OS cells endogenously expressing MFF–GFP (**c**) or FIS1–GFP (**d**) in control conditions and 72 h after transfection with siRNA against *FIS1* or *MFF* (*n* > 39 cells per group). **e**, Relative *Mff* RNA expression levels in control cardiomyocytes and in cardiomyocytes 48 h after transfection with si*Mff* and with or without isoproterenol (Iso) treatment. **f**, Relative *Fis1* RNA expression levels in control cardiomyocytes and in cardiomyocytes 48 h after transfection with si*Fis1* and with or without isoproterenol (Iso) treatment. **P* < 0.05, ***P* < 0.01, ****P* < 0.00. Number of experiments, statistical tests and exact *P* values are provided in Supplementary Table 1.

Mitochondrial RNA granules are fluid condensates positioned by membrane dynamics

Timo Rey [1,4] ✉, Sofia Zaganelli [1,2,4], Emilie Cuillery, Evangelia Vartholomaiou [2], Marie Croisier[3], Jean-Claude Martinou [2] ✉ and Suliana Manley [1] ✉

Mitochondria contain the genetic information and expression machinery to produce essential respiratory chain proteins. Within the mitochondrial matrix, newly synthesized RNA, RNA processing proteins and mitoribosome assembly factors form punctate sub-compartments referred to as mitochondrial RNA granules (MRGs)[1–3]. Despite their proposed importance in regulating gene expression, the structural and dynamic properties of MRGs remain largely unknown. We investigated the internal architecture of MRGs using fluorescence super-resolution localization microscopy and correlative electron microscopy, and found that the MRG ultrastructure consists of compacted RNA embedded within a protein cloud. Using live-cell super-resolution structured illumination microscopy and fluorescence recovery after photobleaching, we reveal that MRGs rapidly exchange components and can undergo fusion, characteristic properties of fluid condensates[4]. Furthermore, MRGs associate with the inner mitochondrial membrane and their fusion coincides with mitochondrial remodelling. Inhibition of mitochondrial fission or fusion leads to an aberrant accumulation of MRGs into concentrated pockets, where they remain as distinct individual units despite their close apposition. Together, our findings reveal that MRGs are nanoscale fluid compartments, which are dispersed along mitochondria via membrane dynamics.

RNA in eukaryotic and bacterial cells can be sequestered into ribonucleoprotein granules that exhibit a wide range of forms and functions, under both physiological and stress conditions. For example, in the nucleus, speckles and paraspeckles are involved in RNA splicing and transcriptional regulation[5,6], whereas the nucleolus creates a compartment for ribosomal assembly[7,8]. RNA–protein granules often form by liquid–liquid phase separation (LLPS)[9,10], and multivalent weak interactions between disordered RNA-binding protein (RBP) domains, and RNA itself, have been identified as hallmark factors for the formation of biomolecular condensates in many in vitro and in silico studies[11–13]. However, phase behaviour is sensitive to a number of environmental parameters, such as concentration, ionic strength, pH or crowding, native conditions of which are challenging to reproduce in test tubes[14]. Therefore, studies in living cells are fundamental to understanding the formation mechanisms, which may go beyond LLPS[15], and biological functions of such structures.

In mitochondria, mitochondrial RNA granules (MRGs) comprise newly synthesized mitochondrial RNAs (mtRNAs), transcribed from the 16-kb mitochondrial DNA (mtDNA) as long polycistronic precursors, as well as mitochondrial RBPs[1,2,16].

It was previously demonstrated that mtRNA is essential for MRG formation[3]. However, both the structural organization of and the dynamic interplay between MRG components remain unknown. Mitochondria undergo dramatic shape changes through fission, fusion and branching, of which fission directly impacts the distribution of mtDNA[17,18]. How MRGs respond to this dynamicity and complex architecture is also unknown, due in part to their size (below the diffraction limit). Here, we investigate the molecular organization, distribution and positioning mechanism of MRGs within the mitochondrial network, using super-resolution and correlative fluorescence and electron microscopy. We show that MRGs are ~130-nm, sub-compartmentalized liquid condensates. They associate with the inner mitochondrial membrane (IMM) and mislocalize following perturbation of mitochondrial fission and fusion dynamics.

To assess the MRG dimensions and overall organization, we examined two MRG-associated RBPs—FASTKD2 and GRSF1—along with mtRNA in fixed COS-7 cells. We stained endogenous proteins using immunofluorescence and newly synthesized RNA by incubation with 5 mM bromouridine (BrU) for 1 h, and anti-BrU staining as previously described[2,3]. In conventional immunofluorescence images against FASTKD2, MRGs appear as bright, diffraction-limited punctae against a dim mitochondrial matrix (Fig. 1a). We used similar fluorescence images to identify in-focus MRGs and the corresponding high-throughput stochastic optical reconstruction microscopy (htSTORM)[19] images to compute their size and shape at the nanoscale (Extended Data Fig. 1). We found that the mtRNA within the MRGs occupied a region with a median diameter of 92 nm (±40 nm (s.d.), $n = 431$; Fig. 1b and Supplementary Fig. 1). To assess the MRG shape we determined the ratio between the long and short axes for each granule and measured a median eccentricity of 1.7 (±0.6 s.d.) for mtRNA (Extended Data Fig. 1 and Supplementary Fig. 1). mtDNA is also packaged into punctate structures called nucleoids, which we measured to have a diameter of 88 nm (±32 nm (s.d.), $n = 310$; Fig. 1b and Supplementary Fig. 2), when stained with antibodies against mtDNA. This is consistent with previous reports of ~100-nm nucleoid diameters[20–22], as is our estimated eccentricity of 1.7 (±0.7 s.d.), reflecting a slightly ellipsoidal shape. Thus, mtDNA serves as an internal reference or positive control for our STORM-based size and shape measurements.

We then quantified the nanostructure of MRGs immunolabelled for GRSF1 or FASTKD2 (bona fide MRG markers), where mutations in the latter are associated with severe mitochondrial diseases[23,24]. Our measurements showed that the MRG diameter marked by either protein is significantly larger than that of mtRNA: 139 nm

(±36 nm (s.d.), $n = 297$) for FASTKD2 and 123 nm (±31 nm (s.d.), $n = 338$) for GRSF1 foci in COS-7 cells (Fig. 1b and Supplementary Figs. 3 and 4). Alternative size descriptors, including radius of gyration and convex hull area, showed the same trends (Extended Data Fig. 1). Furthermore, protein punctae are significantly rounder, with an eccentricity of 1.4 (±0.4 s.d.) and 1.5 (±0.5 s.d.) for FASTKD2 and GRSF1, respectively (Extended Data Fig. 1), underlining the differences between RNA and protein organization in MRGs.

To further investigate the MRG architecture and the relationship between mtRNA- and FASTKD2-foci dimensions, we next performed two-colour htSTORM (Fig. 1c and Extended Data Fig. 2). We found no correlation between the size ($R = 0.26$, $n = 26$) or eccentricity ($R = 0.42$) of the protein components and newly synthesized RNA for individual granules (Extended Data Fig. 2). Yet, in 80% of measured MRGs, the projected area of mtRNA was smaller and contained within (>80% overlap) the FASTKD2 area (Fig. 1d–f and Supplementary Table 1). These quantifications led us to schematize the ultrastructure of a typical MRG as compacted RNA surrounded by and commingled with RBPs (Fig. 1f).

Liquid phase properties, such as the ability to rapidly exchange components while maintaining a high local concentration of selected molecules, play a functional role in stress and other RNA granules by enabling mRNA sequestration, enzyme buffering and tuning of reaction kinetics[9]. These roles may apply to MRGs and their function in gene expression, if they are indeed liquid-like. To test this hypothesis, we generated stable FASTKD2-eGFP expressing cell lines and assessed the common hallmarks of fluids: content exchange and droplet fusion[25]. We examined the molecular exchange of MRG components by fluorescence recovery after photobleaching (FRAP). To monitor MRG fluorescence inside highly mobile mitochondria, we developed a software tool for FRAP analysis with motion tracking (Fig. 2a). We found FASTKD2-eGFP molecules within MRGs to recover on average to ~64% of their bleached intensity, with a median half-recovery time of 5.8 s (±3.3 s (s.d.)) and 4.6 s (±11.3 s (s.d.)) in U2OS and COS-7 cells, respectively (Fig. 2c,d, Extended Data

Fig. 3 and Supplementary Videos 1 and 2). To test whether dynamic exchange is generalizable beyond FASTKD2, we created two additional stable cell lines expressing MRG markers—ERAL1 and DDX28[26,27]—both fused to eGFP. Both recovered at a timescale similar to FASTKD2 (half-recovery time of 1.9 s (±0.7 s (s.d.)) for ERAL1 and 3.1 s (±1.9 s (s.d.)) for DDX28) (Fig. 2c, Extended Data Fig. 3 and Supplementary Videos 3 and 4). For comparison, we overex-

Fig. 1 | The nanoscopic architecture of MRGs consists of compacted RNA surrounded by RNA binding proteins. a, Wide-field immunofluorescence of FASTKD2 (left) shows punctate, diffraction-limited MRGs within mitochondria (white dashed lines). Scale bar, 10 μm. Zoomed view (centre) of a representative MRG: overlay of STORM (green) and wide-field images (greyscale). Right: the MRG is segmented by its high density of STORM localizations (right) using DBSCAN[38]. Scale bar, 200 nm. The images are representative of the dataset shown in **b**. **b**, MRG (mtRNA, FASTKD2 or GRSF1) and nucleoid (mtDNA) diameters determined as mean full-width at half-maximum (FWHM) from htSTORM images. The numbers (n) of clusters quantified for each condition are shown in the figure and are pooled from 24, 13, 7 and 14 fields of view (FOVs) and 4, 4, 3 and 2 samples for BrU, GRSF1, FASTKD2 and mtDNA, respectively. The median diameter and number of analysed clusters are noted. Box plots denote the first and third quartiles and the median; the whiskers comprise the rest of the distributions, except outliers. A two-sided Mann–Whitney U-test was used and **** denotes P values < 0.0001; NS, non-significant ($P_{BrU-mtDNA} = 1$, $P_{BrU-FASTKD2} = 1.0 \times 10^{-48}$, $P_{BrU-GRSF1} = 4.5 \times 10^{-30}$, $P_{GRSF1-FASTKD2} = 3.1 \times 10^{-11}$). Representative images are shown on the right. Scale bar, 200 nm. **c**, Example of two-colour htSTORM of MRGs (anti-FASTKD2, green) and mtRNA (anti-BrdU, blue) overlaid on wide-field images (grey). Scale bar, 500 nm. Images are representative of the dataset shown in **f**. **d,e**, Scatter plots of localizations from the clusters marked **d** and **e** in **c**. Areas were estimated using a convex hull (dashed line) and used to find the percent overlap between channels. Diameter and eccentricity were also quantified (Supplementary Information). Scale bars, 100 nm. **f**, Schema of MRG organization and median ± s.d. values for all analysed two-colour htSTORM clusters ($n = 26$ MRGs were examined over eight independent experiments). Statistical source data are provided in Source Data Fig. 1.
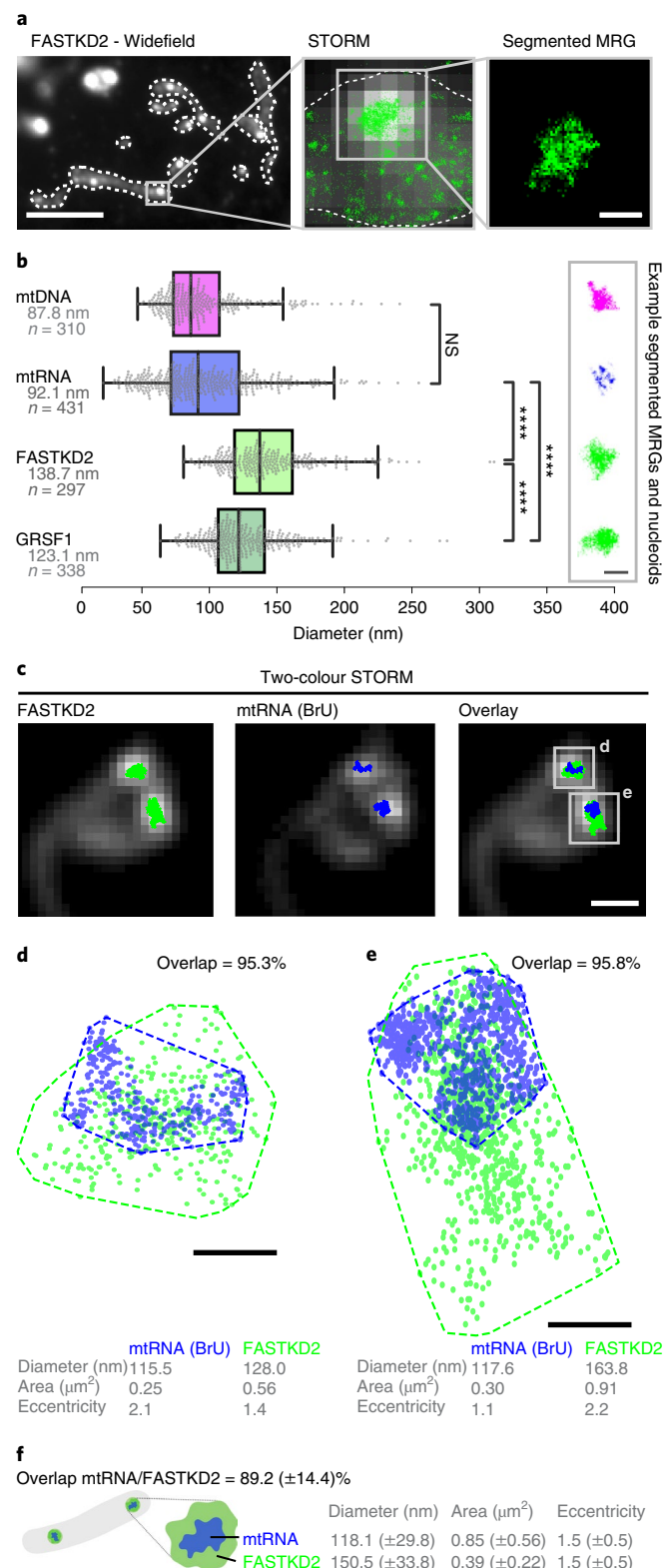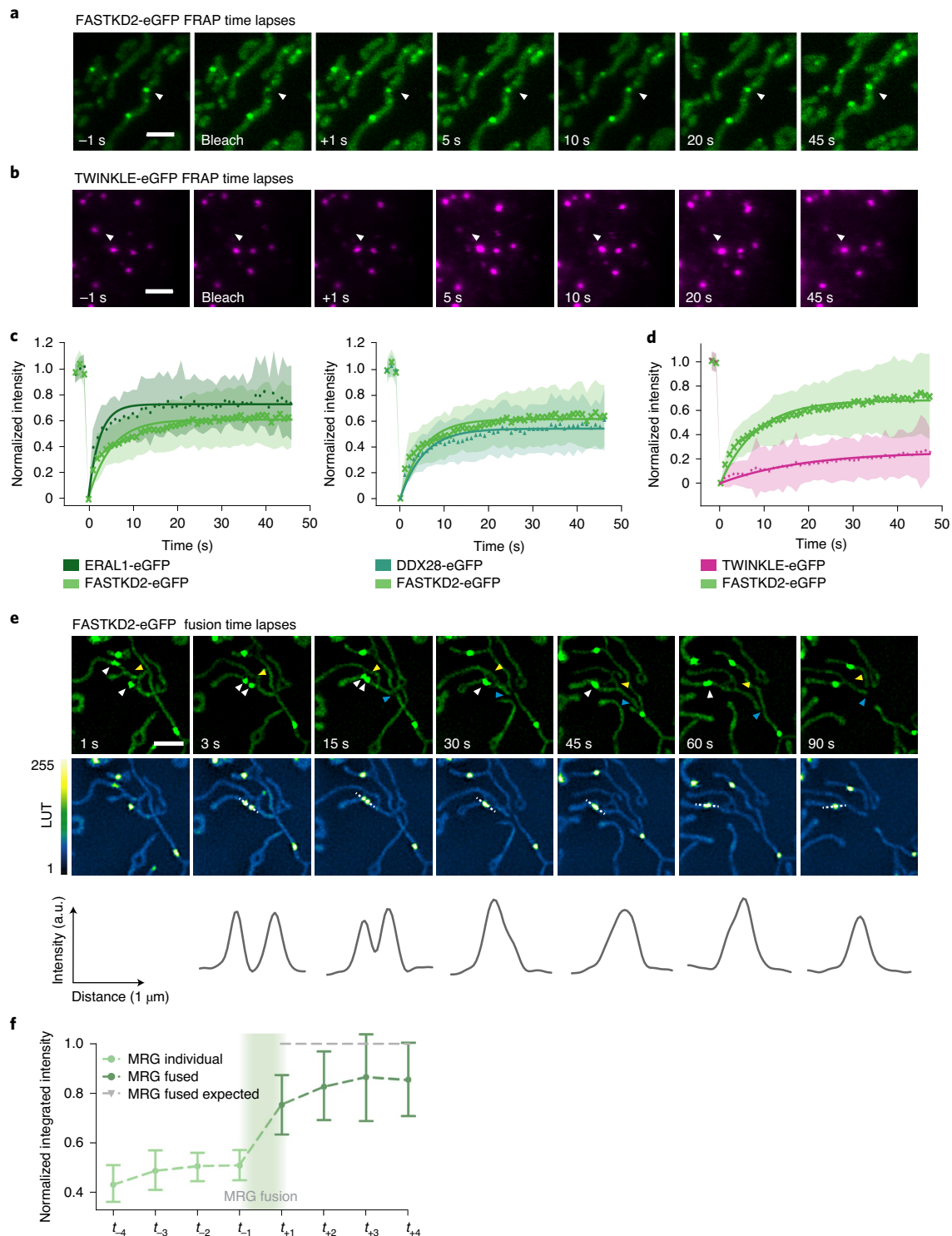
Fig. 2 | MRGs exchange content and undergo fusion in live COS-7 cells. a,b, Examples of FRAP time-lapse series of MRGs (**a**, stable expression, FASTKD2-eGFP, green) or nucleoids (**b**, transient transfection, TWINKLE-eGFP, magenta), from the datasets represented in **c** and **d**, respectively. An individual MRG or nucleoid (arrowhead) was partially photobleached to allow tracking during recovery. Scale bars, 2 μm. **c,d,** FRAP intensity, where symbols represent mean data points, lines are single exponential fits, and shaded areas are standard deviations at each time point, for FASTKD2-eGFP (*n* = 44 MRGs examined over eight independent experiments) and ERAL1-eGFP (*n* = 17 MRGs examined over three independent experiments), DDX28-eGFP (*n* = 17 MRGs examined over three independent experiments) (**c**) and TWINKLE-eGFP (*n* = 50 nucleoids examined over five independent experiments) (**d**). **e,** Representative SIM time-lapse series of an MRG fusion event (white arrowheads) in cells stably expressing FASTKD2-eGFP. Cells were imaged at 1/3 Hz. Yellow and blue arrowheads highlight mitochondrial network dynamics (top). MRGs enriched in FASTKD2-eGFP stand out in yellow; pixel intensity values are shown with a linear Fire lookup table (LUT). Line profiles of MRGs along the mitochondrial axis (middle, dashed lines) show the intensity values at each time point (bottom). Scale bar, 2 μm. **f,** Temporal evolution of the integrated intensity of MRGs in COS-7 cells before and after fusion. Pre-fusion integrated intensities were summed for each granule pair (*n* = 9 biologically independent cells) and the sums were used for normalization (grey dashed line). Data are presented as mean and s.d. for each MRG type for four time points before fusion (light green, t_{-4}–t_{-1}) as well as after fusion (dark green, t_{+1}–t_{+4}). Statistical source data are provided in Source Data Fig. 2.
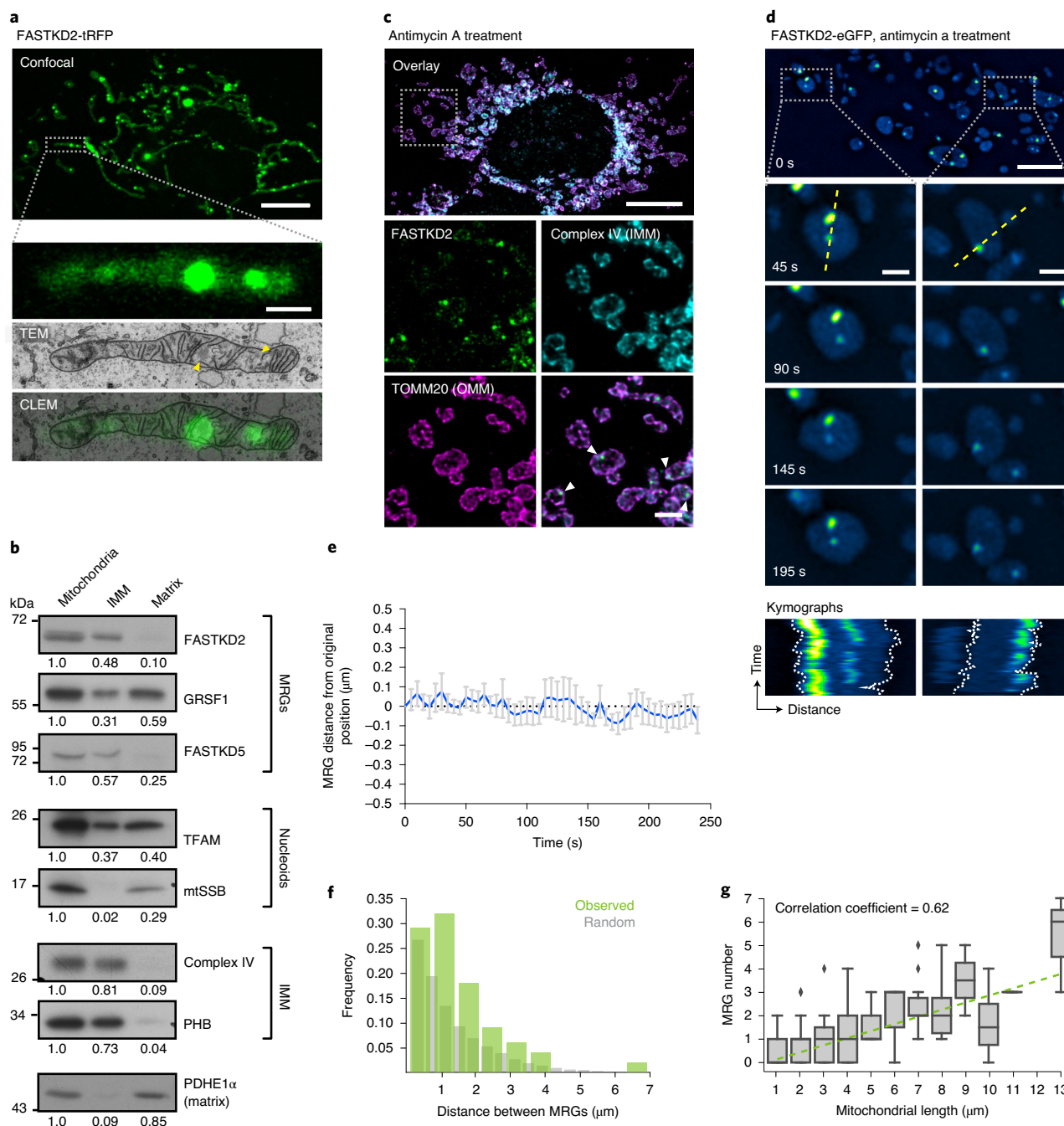
Fig. 3 | MRGs are associated with inner mitochondrial membranes and are randomly spaced along the mitochondrial network. a, Correlated fluorescence (axially projected confocal image, green) and transmission electron micrograph (TEM, greyscale), in a FASTKD2-tRFP expressing COS-7 cell. Electron densities corresponding to MRGs are visible (arrowheads; $n = 7$ MRGs from three mitochondria). Scale bars, 10 μm (top) and 1 μm (bottom). **b**, Western blot of fractionated mitochondria, probed with antibodies against MRG (FASTKD2, GRSF1, FASTKD5) and nucleoid (transcription factor A, mitochondrial (TFAM), mtSSB) components. IMM-integrated proteins (complex IV, prohibitin (PHB)) and soluble matrix protein pyruvate dehydrogenase E1 α (PDHE1α) served as controls. Blots were processed simultaneously and compared quantitatively from the same gel. The experiment was performed twice with similar results.

c, FASTKD2-eGFP expressing HeLa cells treated with 100 μM antimycin A for 1 h, then fixed. IMM (anti-complex IV, cyan) and outer mitochondrial membrane (OMM, anti-TOMM20, magenta), reveal swollen mitochondria with few inner membranes. MRGs appear proximal to the IMM (arrowheads). The experiment was performed twice with similar results. Scale bars, 10 μm (top), 2 μm (bottom). **d**, FASTKD2-eGFP expressing COS-7 cells treated with 100 μM antimycin A for 1 h, imaged live. Pixel intensity values are shown with a linear Fire LUT as in Fig. 2e. Time-lapse series are shown for two exemplary mitochondria (dashed boxes). Kymographs (from the yellow dashed line) highlight the co-mobility of individual granules. Scale bars, 10 μm (top) and 1 μm (bottom). The experiment was performed twice with similar results. **e**, MRG movement over time, measured as the distance between the MRG and the closest membrane, for swollen mitochondria as exemplified in **d** ($n = 20$ MRGs examined from three cells). Data are presented as mean (blue line) ± s.d. (error bars). **f**, Histogram of the distance between neighbouring pairs of MRGs for unbranched mitochondria ($n = 100$ mitochondria over three independent experiments, green) and simulated randomly distributed granules (grey). **g**, Correlation between MRG number and length of unbranched mitochondria ($n = 206$ mitochondria over three independent experiments). Each box plot denotes the median and first and third quartiles, and diamonds show outliers for each bin (for example, bin_1 = 0–1 μm and so on). The linear regression (green dashed line) was computed on non-binned data. Unprocessed blots and statistical source data are provided in Source Data Fig. 3.
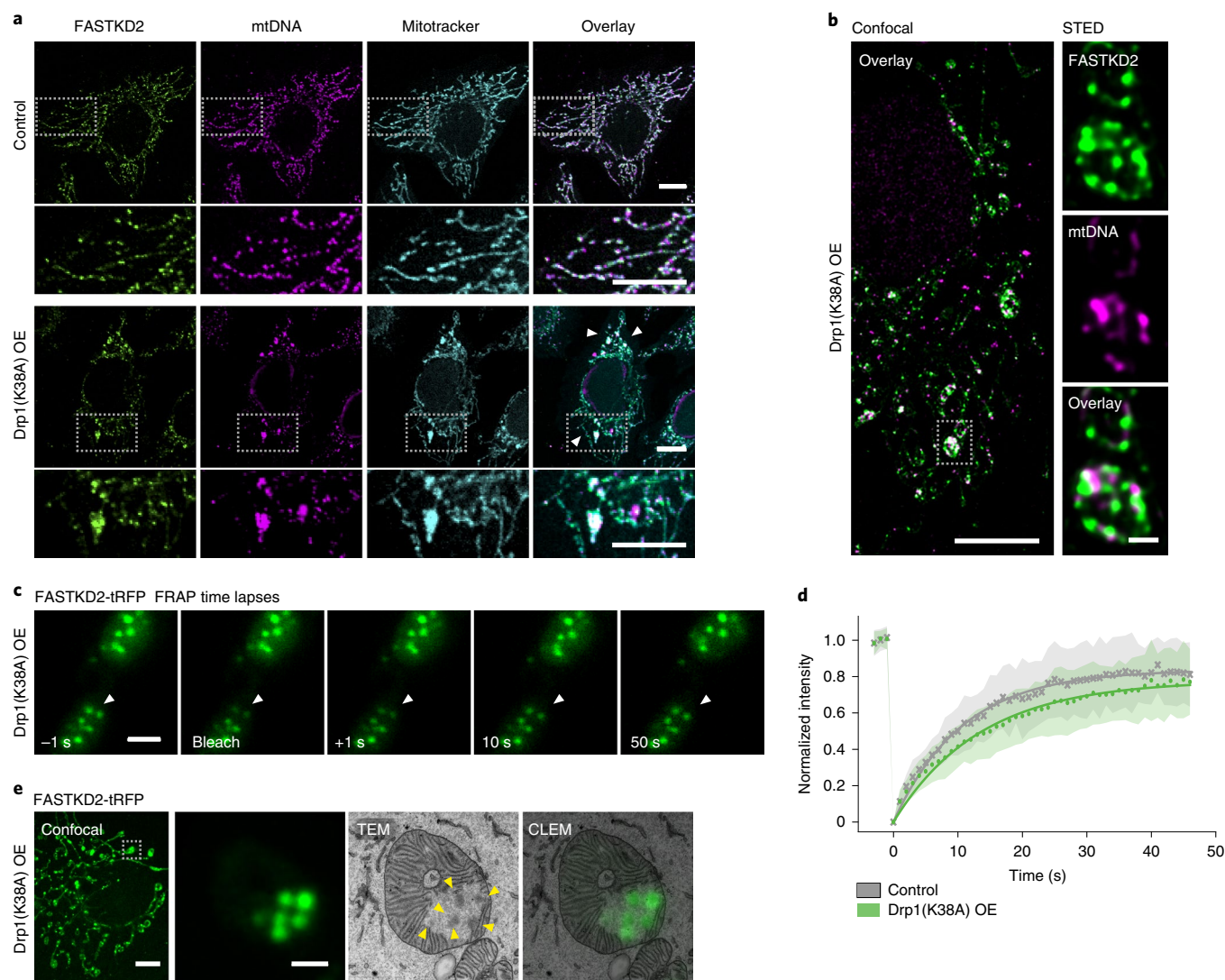
Fig. 4 | Impaired mitochondrial fission leads to aberrant MRG positioning. a, HeLa cells imaged by confocal microscopy in control settings (top) or after 48 h of Drp1[K38A] overexpression (OE, bottom), stained for MRGs (anti-FASTKD2, green), nucleoids (anti-DNA, magenta) and mitochondria (MitoTracker Deep Red, cyan). The second and fourth rows show zoomed views of the regions indicated by grey boxes in the first and third rows. The experiment was performed three times with similar results. Scale bars, 10 μm (first and third rows) and 1 μm (second and fourth rows). **b,** Confocal (left) and STED (right) images of mito-bulbs containing MRGs (anti-FASTKD2, green) and nucleoids (anti-mtDNA, magenta) in fixed Drp1[K38A]-overexpressing COS-7 cells. The experiment was performed twice with similar results. Scale bars, 10 μm (left) and 2 μm (right, zoom). **c,** Example of FRAP time-lapse images from the datasets represented in **d** of mito-bulb-associated MRGs (arrowheads), in FASTKD2-tRFP (green) stably expressing COS-7 cells transiently transfected with Drp1[K38A] for 24 h. Scale bar, 2 μm. **d,** Comparison of FASTKD2-tRFP FRAP between control (n = 31 MRGs examined over four independent experiments) and Drp1[K38A] (n = 40 MRGs examined over three independent experiments) overexpressing cells. Symbols represent mean data points, lines are single exponential fits and shaded areas are s.d. values for each time point. **e,** Confocal fluorescence and TEM (CLEM) of MRGs (stable expression, FASTKD2-tRFP, green) in COS-7 cells, fixed 24 h after Drp1[K38A] transfection. Zoom of a single mitochondrion shows several MRGs (arrowheads), resembling a bunch of grapes (10 MRGs were analysed from three mitochondria). Scale bars, 10 μm (left), 1 μm (right). Grey dashed boxes indicate magnified regions. Statistical source data are provided in Source Data Fig. 4.

pressed the mitochondrial helicase TWINKLE fused to eGFP as a nucleoid marker with high DNA-binding affinity[28]. TWINKLE foci only slightly (~29%) recovered over the course of our FRAP assay (50 s), and served as negative control to highlight that fast protein exchange is particular to MRGs (Fig. 2b,d). Thus, MRG components exchange rapidly, on a fast timescale, even compared to stress granules (recovery half-time, 18.5–35 s)[29].

Whereas liquid drops may fuse upon contact, solid granules will instead remain inert or aggregate while maintaining their shape. We followed FASTKD2 foci by live-cell super-resolved structured illumination microscopy (SIM), which provides the necessary reso-

lution to discern the two cases. We observed MRG fusion in multiple instances in both U2OS and COS-7 cells, where two individual foci merged to form a single spot (Fig. 2e, Extended Data Fig. 4 and Supplementary Videos 5 and 6). We also noted MRG splitting on some occasions (Extended Data Fig. 4 and Supplementary Video 7). Imaging TWINKLE-eGFP by SIM, we observed nucleoid 'kiss-and-runs' and nucleoid splitting, as previously described[30], as well as one fusion event (Extended Data Fig. 4 and Supplementary Videos 8 and 9). We determined the photobleaching-corrected integrated intensity of FASTKD2-eGFP in the merged droplet to be approximately the sum of the initial droplets, as expected if no

material was lost during fusion (Fig. 2f). Notably, 75% of fusion events coincided with visible mitochondrial rearrangements such as fusion, fission or bulging (Supplementary Table 2).

Infoldings of the IMM called cristae densely populate the mitochondrial interior. By correlative fluorescence and electron microscopy (CLEM), we observed that displaced cristae accommodate MRGs in open spaces (Fig. 3a), as was recently reported for nucleoids by live-cell stimulated emission depletion (STED) microscopy[31]. MRGs are clearly distinguishable as round electron-dense granules, with dimensions consistent with our htSTORM data (Figs. 1 and 3a and Extended Data Fig. 5) and an ultrastructure reminiscent of that of stress granules and P-bodies[32].

Noticing their close proximity to the IMM and intrigued by the concurrence between MRG fusion and membrane dynamics, we assessed their association with the membrane using both biochemical and image-based approaches. First, we performed a biochemical fractionation to enrich for IMM or matrix-associated proteins. We found MRG components FASTKD2 and FASTKD5 primarily in the IMM fraction, while GRSF1 was present in both IMM and matrix fractions (Fig. 3b), similar to the nucleoid associated protein TFAM, in accordance with previous reports[33]. Next, we swelled mitochondria by antimycin A treatment of live COS-7 and HeLa cells to test whether MRGs would diffuse freely within the cristae-devoid enlarged lumen[34] or remain associated with the IMM. We observed that most MRGs decorated the perimeter (Fig. 3c) and retained their relative position within mitochondria over time (Fig. 3d,e, Extended Data Fig. 6 and Supplementary Videos 10 and 11), consistent with IMM association. Thus, as nucleoids[33], MRGs appear to be physically attached to the IMM.

We then assessed the distribution of MRGs along the mitochondrial network. A semiregular nucleoid spacing was found to be important in fission yeast to circumvent the problem that random spacing would contribute to binomial errors in genome partitioning and thus a high probability of total mtDNA loss[17]. We used the same method to compare measured inter-MRG distances with those of simulated randomly placed granules (Fig. 3f). Our analysis shows that the positions of individual MRGs within their respective mitochondria are not distinguishable from a random distribution (Extended Data Fig. 6), while the distances between MRGs inside the same mitochondrion are at the borderline of being considered different from random ($P = 0.04997$; Fig. 3f). In the case of a random distribution along the entire mitochondrial network, we would expect an equal probability of finding an MRG anywhere along the network, so that larger mitochondria should have more granules. Indeed, we found on average one MRG for every of $2.00\,\mu m$ ($\pm 1.65\,\mu m$) of mitochondria ($n = 131$) and a positive correlation between MRG number and mitochondrial length (correlation coefficient $= 0.62$; Fig. 3g and Extended Data Fig. 6). Although nucleoids are accurately positioned[18], our data suggest that MRGs are not.

Because MRGs appear relatively immobile within the matrix, yet are randomly distributed, we decided to investigate the interplay between MRG positioning and mitochondrial dynamics. We inhibited mitochondrial fission by overexpression of a dominant negative mutant of the fission factor dynamin-related protein 1 (Drp1), Drp1[K38A]. Under this condition, we observed highly elongated mitochondria with enlarged domains, as previously described and termed 'mito-bulbs'[35]. We found that these domains contain not only nucleoids, but also MRGs (Fig. 4a). With super-resolved STED microscopy, we discovered that mito-bulbs are better described as resembling bunches of grapes, composed of many interspersed MRGs and nucleoids, rather than as a single enlarged and coalesced structure as previously proposed[35] (Fig. 4b). Intrigued by the absence of MRG fusion (illustrated in Fig. 2) in such a confined space, we assessed whether MRGs may have solidified, as stress granules can[36]. We found that fluorescence recovery of stably expressed FASTKD2-tRFP was similar in control and Drp1[K38A]-overexpressing

cells, suggesting that the liquid nature of MRGs within the mito-bulbs had not changed (Fig. 4c,d and Supplementary Videos 12 and 13). Using CLEM, we confirmed that the MRGs remained as distinct individual units, despite their close apposition, and did not observe the presence of cristae that could have formed physical barriers to the fusion of these granules (Fig. 4e and Extended Data Fig. 5). Furthermore, this EM analysis showed that a number of these electron-dense granules were closely apposed to membranes, consistent with the results shown in Fig. 3a–c. Tightly stacked cristae could be seen adjacent to mito-bulbs in affected mitochondria (Fig. 4d). Knockdown of mitochondrial fusion factor Mitofusin 2 (Mfn2) evoked similar MRG clustering, further supporting a role for mitochondrial dynamics in maintaining an even distribution of MRGs along mitochondria (Extended Data Fig. 7).

In conclusion, our data show that MRGs share several properties with phase-separated condensates, albeit the exact mechanism of their formation is not yet fully elucidated. We propose that condensation of mtRNA and RBPs into MRGs may allow mammalian cells to regulate positioning of these components along the mitochondrial network via membrane association (Fig. 3). Mitochondrial dynamics via fission and fusion is critical for maintaining a random positioning of MRGs, and its perturbation leads to their accumulation in small domains, while their individual stability and capacity for molecular exchange is maintained (Fig. 4). Our findings show that changes in positioning can arise, decoupled from changes in the biophysical properties of RNA sub-compartments. This insight could be important for understanding mitochondrial disorders that are reported to feature aberrant mitochondrial RNA and DNA distribution into clusters. Adequate positioning of genetic material and transcripts may be crucial for proper synthesis of the respiratory chain and oxidative phosphorylation[37].

Online content

Any methods, additional references, Nature Research reporting summaries, source data, extended data, supplementary information, acknowledgements, peer review information; details of author contributions and competing interests; and statements of data and code availability are available at https://doi.org/10.1038/s41556-020-00584-8.

References

1. Antonicka, H., Sasarman, F., Nishimura, T., Paupe, V. & Shoubridge, E. A. The mitochondrial RNA-binding protein GRSF1 localizes to RNA granules and is required for posttranscriptional mitochondrial gene expression. *Cell Metab.* **17**, 386–398 (2013).
2. Iborra, F. J., Kimura, H. & Cook, P. R. The functional organization of mitochondrial genomes in human cells. *BMC Biol.* **2**, 9 (2004).
3. Jourdain, A. A. et al. GRSF1 regulates RNA processing in mitochondrial RNA granules. *Cell Metab.* **17**, 399–410 (2013).
4. Hyman, A. A., Weber, C. A. & Jülicher, F. Liquid–liquid phase separation in biology. *Annu. Rev. Cell Dev. Biol.* **30**, 39–58 (2014).
5. Handwerger, K. E., Cordero, J. A. & Gall, J. G. Cajal bodies, nucleoli and speckles in the Xenopus oocyte nucleus have a low-density, sponge-like structure. *Mol. Biol. Cell* **16**, 202–211 (2005).
6. Yamazaki, T. et al. Functional domains of NEAT1 architectural lncRNA induce paraspeckle assembly through phase separation. *Mol. Cell* **70**, 1038–1053 (2018).
7. Feric, M. et al. Coexisting liquid phases underlie nucleolar subcompartments. *Cell* **165**, 1686–1697 (2016).
8. Frottin, F. et al. The nucleolus functions as a phase-separated protein quality control compartment. *Science* **365**, 342–347 (2019).
9. Banani, S. F., Lee, H. O., Hyman, A. A. & Rosen, M. K. Biomolecular condensates: organizers of cellular biochemistry. *Nat. Rev. Mol. Cell Biol.* **18**, 285–298 (2017).
10. Boeynaems, S. et al. Protein phase separation: a new phase in cell biology. *Trends Cell Biol.* **28**, 420–435 (2018).
11. Langdon, E. M. et al. mRNA structure determines specificity of a polyQ-driven phase separation. *Science* **360**, 922–927 (2018).

12. Maharana, S. et al. RNA buffers the phase separation behavior of prion-like RNA binding proteins. *Science* **360**, 918–921 (2018).

13. Wang, J. et al. A molecular grammar governing the driving forces for phase separation of prion-like RNA binding proteins. *Cell* **174**, 688–699 (2018).

14. Alberti, S., Gladfelter, A. & Mittag, T. Considerations and challenges in studying liquid–liquid phase separation and biomolecular condensates. *Cell* **176**, 419–434 (2019).

15. McSwiggen, D. T. et al. Evidence for DNA-mediated nuclear compartmentalization distinct from phase separation. *eLife* **8**, e47098 (2019).

16. Jourdain, A. A. et al. A mitochondria-specific isoform of FASTK is present in mitochondrial RNA granules and regulates gene expression and function. *Cell Rep.* **10**, 1110–1121 (2015).

17. Jajoo, R. et al. Accurate concentration control of mitochondria and nucleoids. *Science* **351**, 169–172 (2016).

18. Lewis, S. C., Uchiyama, L. F. & Nunnari, J. ER-mitochondria contacts couple mtDNA synthesis with mitochondrial division in human cells. *Science* **353**, aaf5549 (2016).

19. Douglass, K. M., Sieben, C., Archetti, A., Lambert, A. & Manley, S. Super-resolution imaging of multiple cells by optimized flat-field epi-illumination. *Nat. Photon.* **10**, 705–708 (2016).

20. Alán, L., Špaček, T. & Ježek, P. Delaunay algorithm and principal component analysis for 3D visualization of mitochondrial DNA nucleoids by Biplane FPALM/dSTORM. *Eur. Biophys. J.* **45**, 443–461 (2016).

21. Brown, T. A. et al. Superresolution fluorescence imaging of mitochondrial nucleoids reveals their spatial range, limits and membrane interaction. *Mol. Cell. Biol.* **31**, 4994–5010 (2011).

22. Kukat, C. et al. Super-resolution microscopy reveals that mammalian mitochondrial nucleoids have a uniform size and frequently contain a single copy of mtDNA. *Proc. Natl Acad. Sci. USA* **108**, 13534–13539 (2011).

23. Ghezzi, D. et al. FASTKD2 nonsense mutation in an infantile mitochondrial encephalomyopathy associated with cytochrome c oxidase deficiency. *Am. J. Hum. Genet.* **83**, 415–423 (2008).

24. Yoo, D. H. et al. Identification of FASTKD2 compound heterozygous mutations as the underlying cause of autosomal recessive MELAS-like syndrome. *Mitochondrion* **35**, 54–58 (2017).

25. Brangwynne, C. P. et al. Germline P granules are liquid droplets that localize by controlled dissolution/condensation. *Science* **324**, 1729–1732 (2009).

26. Tu, Y. T. & Barrientos, A. The human mitochondrial DEAD-Box protein DDX28 resides in RNA granules and functions in mitoribosome assembly. *Cell Rep.* **10**, 854–864 (2015).

27. Zaganelli, S. et al. The pseudouridine synthase RPUSD4 is an essential component of mitochondrial RNA granules. *J. Biol. Chem.* **292**, 4519–4532 (2017).

28. Farge, G. et al. The N-terminal domain of TWINKLE contributes to single-stranded DNA binding and DNA helicase activities. *Nucleic Acids Res.* **36**, 393–403 (2008).

29. Wheeler, J. R., Matheny, T., Jain, S., Abrisch, R. & Parker, R. Distinct stages in stress granule assembly and disassembly. *eLife* **5**, e18413 (2016).

30. Garrido, N. et al. Composition and dynamics of human mitochondrial nucleoids. *Mol. Biol. Cell* **14**, 1583–1596 (2003).

31. Stephan, T., Roesch, A., Riedel, D. & Jakobs, S. Live-cell STED nanoscopy of mitochondrial cristae. *Sci. Rep.* **9**, 12419 (2019).

32. Souquere, S. et al. Unravelling the ultrastructure of stress granules and associated P-bodies in human cells. *J. Cell Sci.* **122**, 3619–3626 (2009).

33. Gerhold, J. M. et al. Human mitochondrial DNA–protein complexes attach to a cholesterol-rich membrane structure. *Sci. Rep.* **5**, 15292 (2015).

34. Hytti, M. et al. Antimycin A-induced mitochondrial damage causes human RPE cell death despite activation of autophagy. *Oxid. Med. Cell. Longev.* **2019**, 1583656 (2019).

35. Ban-Ishihara, R., Ishihara, T., Sasaki, N., Mihara, K. & Ishihara, N. Dynamics of nucleoid structure regulated by mitochondrial fission contributes to cristae reformation and release of cytochrome c. *Proc. Natl Acad. Sci. USA* **110**, 11863–11868 (2013).

36. Jain, S. et al. ATPase-modulated stress granules contain a diverse proteome and substructure. *Cell* **164**, 487–498 (2016).

37. Durigon, R. et al. LETM1 couples mitochondrial DNA metabolism and nutrient preference. *EMBO Mol. Med.* **10**, e8550 (2018).

38. Ester, M., Kriegel, H.-P., Sander, J. & Xu, X. A density-based algorithm for discovering clusters in large spatial databases with noise. In *Proceedings of the 2nd International Conference on Knowledge Discovery and Data Mining* 226–231 (AAAI, 1996).

Methods

Plasmids and reagents. All cell culture reagents and chemicals were purchased from Sigma unless stated otherwise.

The following plasmids were cloned in the laboratory, using pWPT lentiviral vector (Addgene 12255) as a backbone: FASTKD2-eGFP, FASTKD2-tRFP, DDX28-eGFP, ERAL1-eGFP and TWINKLE-eGFP. CFP-Drp1(K38A) plasmid was a gift from A. Van der Bliek. Plasmids for lentiviral production pMD2.G and psPAX2 were gifts from D. Trono (Addgene 12259 and 12260, respectively).

Cell culture and transfection. HeLa (ATCC, CCL-2), HEK293T (ATCC, CRL-11268), COS-7 (ECACC, 87021302) and U2OS (ATCC, HTB-96) cells were cultured in 5% CO_2 at 37 °C in Dulbecco's modified Eagle medium (DMEM) supplemented with 10–25 mM glucose, 4 mM GlutaMAX (Gibco) or 2 mM L-glutamine, 10% heat-inactivated fetal bovine serum (FBS), 100 U ml^{-1} penicillin and 100 mg ml^{-1} streptomycin. All cells were maintained in culture for a maximum of 20 passages, and routinely assessed for mycoplasma contamination. CRISPR-engineered HeLa Cox8a-SNAP cells were a gift from T. Stephan and S. Jakobs[31].

Plasmid transfection of cells was performed using Lipofectamine LTX (Invitrogen) or FuGENE 6 (Promega) according to the manufacturer's instructions (typically 4–6 µl FUGENE reagent and 100–500 ng of plasmid DNA were used per well of a six-well plate). Cells were analysed 12–48 h after transfection. siRNA transfection was performed using Lipofectamine RNAi Max (Invitrogen) and cells were analysed 72 h after transfection.

For Drp1 and Mfn2 silencing, ON-TARGETplus SMARTpool (Dharmacon, GE Healthcare) were used following the manufacturer's instructions (siDrp1, cat. no. L-012092-00; siMfn2, cat. no. L-012961-00; ON-TARGETplus non-targeting pool (negative control), cat. no. D-001810-10).

Stable cell line generation. We used a second-generation lentiviral system to transform individual cell lines. In brief, gene sequences of interest were cloned into lenti-expression vector pWPT (as described above). Co-transfection of HEK293T cells was performed with packaging plasmids pMD2.G and psPAX2 using calcium phosphate precipitation. Medium containing virus was collected 48 h after transfection and filtered using membranes with a pore size of 0.45 µm. The viral supernatant and polybrene were added to 70% confluent recipient cells, and culture medium was replaced 24 h after infection. For FASTKD2-, ERAL1- and DDX28-eGFP cell lines, FACS sorting was performed with the help of the Flow Cytometry Core Facility at EPFL, to enrich cells expressing eGFP at the desired level.

Live-cell treatments. *Bromouridine tagging of RNA.* When a bromouridine pulse assay was performed, cells were incubated with 5 mM 5-bromouridine (BrU) in complete culture medium for 1 h before fixation, as previously described[1,2]. BrU was stored at −20 °C as 250 mM aliquots, and was heated and vortexed before dilution in culture medium when used.

Antimycin A treatment. For antimycin A treatment, cells were incubated with 25 or 100 µM antimycin A (Abcam) in complete culture medium for 24 h or 1 h, respectively, before fixation or live imaging. Live imaging was performed in Leibovitz L-15 Medium (Gibco) for SIM microscopy or Live Cell Imaging Solution (Thermo Fisher Scientific) for STED microscopy, supplemented with adequate amount of antimycin A. Antimycin A was resuspended in EtOH at 1 mM and stored at −20 °C.

Immunofluorescence. Cells were seeded on glass coverslips and grown to a confluence of 40–80%. Following live-cell treatments if indicated, fixation of cultured cells was performed in warm 4% paraformaldehyde (PFA) in phosphate-buffered saline (PBS) for 15 min. Then, cells were rinsed with PBS, and cell permeabilization and blocking were co-executed by incubating the fixed cells in PBS containing 0.3% Triton X-100 and 10% pre-immune goat serum for 15 min. The same buffer was used to incubate cells with the specified primary antibody (see antibody list below). After incubation with primary antibodies overnight in a humid chamber and at 4 °C or 2 h at room temperature, the cells were washed with PBS and incubated with the appropriate secondary antibody conjugated with a fluorophore. Where indicated, the mitochondrial network was stained before fixing the cells using MitoTracker Deep Red FM (Thermo Fisher Scientific), according to the manufacturer's instructions.

Antibodies used for immunofluorescence. The following primary antibodies were used for immunofluorescence: anti-FASTKD2 (Proteintech, 17464-1-AP; 1:250 dilution), anti-bromodeoxyuridine (Roche, 11170376001; 1:250 to 1:500 dilution), anti-GRSF1 (Sigma, HPA036985; 1:250 dilution), anti-DNA (ProGen, 61014; 1:250 to 1:400 dilution), anti-TOMM20 (Abcam, ab186734; Santa Cruz Biotech, SC-17764; 1:200 dilution for both antibodies), anti-OxPhos Complex IV subunit IV (clone 20E8C12, Thermo Fisher Scientific, A21348; 1:200 dilution) and anti-mtHSP70 (Thermo Fisher Scientific, MA3-028; 1:250 dilution).

The secondary antibodies differed depending on the microscopy technique applied and are detailed in the following. All secondary antibodies for immunofluorescence were diluted 1:500–1:1,000.

htSTORM. htSTORM experiments were performed as previously described[19,39], using the same hardware. Microscope acquisitions were controlled by Micromanager software (v. 2.0 beta), interfaced with the Thorlabs APT software (v. 3.21.4) to control the piezo stage. Immunofluorescence was performed as described above. The following primary antibodies were combined for one- or two-colour imaging, as stated in the figures: anti-FASTKD2, anti-bromodeoxyuridine, anti-GRSF1 and anti-DNA. For one-colour htSTORM we used Alexa Fluor 647 coupled anti-rabbit or anti-mouse secondary antibodies (Invitrogen); the respective number of foci analysed are stated in Fig. 1. To verify mitochondrial localization of the analysed foci, we co-stained the mitochondrial proteins TOMM20 or mtHSP70 using the respective primary antibodies and Alexa Fluor 488 coupled secondary antibody (Invitrogen). For two-colour htSTORM, we used Alexa Fluor 647 for BrU coupled with DyLight 755 (Invitrogen) to label FASTKD2 and we analysed 12 FOVs from four distinct imaging days. To allow lateral drift-correction, 100-nm gold nanospheres coated with poly-L-lysine were incubated on each sample for 5 min before the sample was mounted on the microscope with fresh imaging buffer. Before acquiring each raw STORM stack (10-ms exposure, 20,000–40,000 frames), we collected a 50-ms wide-field reference image at low laser power. Manually incrementing the 405 nm activation laser power allowed prolonged imaging. Imaging conditions (excitation illumination powers of 500–1,500 mW) were adjusted according to sample type.

We analysed and plotted the obtained localizations by adapting published MATLAB[39] and new Python scripts (Supplementary Fig. 1). In brief, adaptations of data processing encompassed manual selection of regions of interest (ROIs) around MRGs that were in focus. For two-colour experiments, this selection was applied very restrictively, verifying the presence of a bright wide-field signal in both channels. For two-colour experiments, additional care was paid to reduce effects due to chromatic aberrations. For this, the localizations of every selected ROI were visually inspected, and ROIs were rejected from further analysis unless no visually detectable systematic shift was visible following DBSCAN clustering[38].

All descriptors were computed from localizations belonging to each particular cluster. We calculated the FWHM from the summed eigenvalues as the diameter for each granule using a Python script provided here. The eccentricity was determined as the ratio between the long axis and the short axis. Axis lengths are the eigenvalues of the covariance matrix of clustered localizations in the x and y dimension as described in ref. 40. We used the MATLAB function 'convexHull' to compute granule area and identify the hull-defining edge points. Three data points >0.25 µm^2 were omitted for the creation of Supplementary Fig. 1, but kept for all statistical analysis. The radius of gyration was computed as the sum of variances in x and y, divided by the number of localizations. Sigma was computed as the sum of the eigenvalues in x and y.

SIM live-cell microscopy. SIM was performed on a three-dimensional (3D) NSIM Nikon microscope with a CFI Apochromat TIRF objective (×100, numerical aperture (NA) 1.49, Nikon). The microscope was equipped with 400-mW, 561-nm and 480-mW, 488-nm lasers (Coherent Sapphire) and a back-illuminated electron-multiplying charge-coupled device camera (iXon 3, Andor Technology). Live-cell imaging was performed at 37 °C, using 488- and 561-nm lasers for eGFP and tRFP excitation, respectively. Imaging settings were adapted to yield the best image quality with minimal photobleaching at a laser power between 2 and 10% and 3–10 s per frame. Per field of view, 15 raw images were acquired in 3D-SIM imaging mode to ensure the highest signal-to-noise ratio and resolution. Final, super-resolved SIM images were reconstructed using the commercial Nikon NIS-Elements software (v. 3.2.2) and analysed in Fiji (ImageJ 2.0.0.-rc-69/1.52p). Open-source MicrobeJ software[41], originally developed for analysis of bacteria, was used for supervised automatic segmentation of mitochondria and location of their associated foci (Supplementary Fig. 4).

FRAP and confocal microscopy. For FRAP assays, cells were seeded on coverslips and grown to 60–80% confluence. Coverslips were mounted on a Zeiss LSM 700 inverted confocal microscope with a Plan-Apochromat oil objective (×63, NA 1.40). Microscope acquisitions were controlled by the Zen (2009 v. 6.0.0) software from Zeiss. The microscope was equipped with 488-nm and 555-nm solid-state lasers and three photomultipliers for simultaneous transmission and epifluorescence recording. A sliding prism and green and red bandpass filters were used to ensure clean fluorescence emission. For live assays, an Okolab stage top incubator H301 was used to maintain the sample temperature at 37 °C. Cells were maintained in CO_2-independent Leibovitz L-15 medium (Gibco). For FASTKD2- ($n_{eGFP} = 44$, $n_{tRFP} = 31$, $n_{tRFP-Drp1KD} = 40$), ERAL1- ($n = 17$) and DDX28- ($n = 16$) FRAP, the pixel size was reduced to 70 nm (zoom = 12) and line scans were recorded at a pixel dwell time of 2.55 µs (maximum speed), resulting in a scan time of 97.75 ms per 128 × 128-pixel FOV. The pinhole was opened for FRAP recording. The 10 × 10-pixel ROIs were manually drawn around single MRGs for FRAP and two or three pre-bleach time points were acquired for normalization. FASTKD2-eGFP in COS-7- ($n = 75$) and U2OS- ($n = 38$), and TWINKLE-eGFP ($n = 50$) FRAP were acquired with twice as many pixels (254 × 254 and 20 × 20 ROI) but for the same sample region (zoom = 12). A different FOV was chosen for every FRAP experiment and multiple different cells could be imaged per sample, but samples

were exchanged after ~1 h of imaging and when low mitochondrial motility was noticeable, to avoid confounding effects of deteriorating cell health. If MRGs had left the ROI before bleaching, the assay was aborted and a different MRG was chosen. Recovery was monitored over 50–60 s at 1 f.p.s.

For confocal microscopy of fixed cells, samples were prepared as described above. Alexa Fluor 488, 594 or 647 secondary conjugated antibodies (Invitrogen) were used to visualize the immunolabelled targets. Imaging was performed using a Leica TCS SP8 inverted microscope with a Plan-Apochromat oil objective (×63, NA 1.4), using the Lightning mode (Leica) to generate deconvolved images. Microscope acquisitions were controlled by LAS X (v. 3.5.2) software from Leica. The microscope was equipped with 405-, 488-, 552- and 638-nm lasers. Imaging for Extended Data Fig. 7 was performed using a Molecular Devices ImageXpress Micro XL automated wide-field microscope, equipped with an air objective (×60).

FRAP analysis and software. For FRAP recording of moving objects, a custom Fiji script was co-developed with O. Burri from the Bioimaging and Optics Platform (BIOP) at EPFL. In brief, this script, 'TrackFRAP', is based on the Fiji plugin TrackMate and automatically follows the bleaching ROI during recovery. It allows the user to choose other foci as FRAP references for overall bleaching correction and outputs both a list of intensity values and metadata to allow reproducible data analysis. All tracks were manually inspected to ensure the bleached granule was recorded correctly over the full course of acquisition. If no reference granule could be tracked over the full acquisition period, the dataset was excluded from analysis. We then developed a Python script to load and analyse TrackFRAP data, which we termed FRAPtrackAnalyser (FRAPtA) and which is based on the FRAPAnalyser tool[42]. Single or double exponentials were fit and plotted for each dataset, as well as used to extract recovery times.

Correlative confocal light and electron microscopy. Cells were seeded on a gridded coverslip (MatTek, P35-1.5-14-CGRD-D), transfected with CFP-Drp1(K38A) plasmid if applicable, and grown to 50–60% confluence. Cells were then fixed at room temperature for 1 h in fresh fixative (2% PFA, 1% glutaraldehyde in PBS 0.1 M pH 7.4), washed in PBS and imaged by confocal microscopy the same day. Z-stacks were acquired of whole cells, with the pinhole closed to 0.5 Airy units (AU) and the pixel size reduced to 50–100 nm in the x–y dimensions and 100–150 nm in the z dimension. Samples were then stored overnight in PBS, at 4 °C. They were then stained with osmium and potassium ferrocyanide, followed by osmium alone, each with cacodylate buffer. They were finally stained with 1% uranyl acetate, then washed in water, dehydrated with increasing concentrations of alcohol, and infiltrated with EPON resin. This was polymerized overnight at 65 °C. Serial, ultra-thin sections were then cut of the cell of interest and the sections were collected on single-slot copper grids with a formvar support membrane. Images were recorded in a transmission electron microscope operating at 80 kV (FEI Company, Tecnai Spirit).

Mitochondrial sub-fractionation and western blotting. To perform mitochondrial sub-fractionation experiments, HeLa cells were grown to ~60% confluency in four 150-mm Petri dishes. Cells were washed in PBS and collected by mechanical scraping. For a first mitochondrial extraction, cells were broken in cold mannitol buffer (MB) (210 mM mannitol, 70 mM sucrose, 10 mM HEPES-KOH pH 7.4, 1 mM EDTA) in the presence of protease inhibitors (Roche), using a syringe with a G25 n18 needle. Cell passage through the needle was repeated 20 times. Unbroken cells and nuclei were discarded in the pellet after centrifugation for 5 min at 1,000g at 4 °C, followed by a second centrifugation for 5 min at 2,500g at 4 °C. The mitochondria-rich fraction was pelleted by centrifugation for 10 min at 6,000g at 4 °C, then the pellet was washed in 1 ml of fresh MB buffer and centrifuged again for 15 min at 13,000g at 4 °C.

To further proceed with sub-mitochondrial fractionation and remove the OMM, mitoplasts were prepared by gently resuspending the mitochondria in cold 10 mM HEPES buffer pH 7.4 in the presence of protease inhibitors (Roche) and 1 U μl^{-1} of RNAsin (Promega), at a final concentration of 0.5 μg of mitochondria per μl. After incubation for 20 min on ice, mitoplasts were recovered in the pellet by centrifugation for 15 min at 15,000g at 4 °C. Finally, to obtain the IMM and matrix fractions, mitoplasts were resuspended in MB buffer (in the presence of protease and RNAse inhibitors) and sonicated using a water bath sonicator Bioruptor TM Twin with 30-s pulses for 15 cycles at 4 °C. After sonication, the samples were ultra-centrifuged for 30 min at 45,000g at 4 °C, to obtain a pellet corresponding to the IMM-rich fraction and a supernatant corresponding to the matrix-rich fraction. Mitochondria-, IMM- and matrix-rich fractions were analysed by SDS-PAGE using 4–20% gradient Novex TM Tris-glycine gels (Thermo Fisher Scientific).

For immunoblotting, proteins were transferred electrophoretically to PVDF membranes (GE Healthcare) and exposed to the primary antibodies listed below, diluted in 5% non-fat dry milk in Tris buffered saline with Tween 20 (TBST). The blots were further incubated with anti-mouse or anti-rabbit horseradish peroxidase-conjugated secondary antibodies (Dako, P0447 and P0448 respectively; used at 1:5,000–1:10,000 dilution), and visualized using an ECL system (GE Healthcare). Where required, images of western blots were treated for contrast enhancement and band intensities were quantified using ImageJ.

Primary antibodies used for western blots. The primary antibodies used for western blots were anti-FASTKD2 (Proteintech, 17464-1-AP), anti-GRSF1 (Sigma, HPA036985), anti-FASTKD5 (Sigma, SAB2700438), anti-TFAM (Proteintech, 22386-1-AP), anti-mtSSB (Proteintech, 12212-1-AP), anti-PHB (Thermo Fisher Scientific, MS-261-PO), anti-OxPhos Complex IV subunit IV (clone 20E8C12, Thermo Fisher Scientific, A21348) and anti-PDHE1α (GeneTex, GTX104015). All primary antibodies were diluted 1:2,000.

Stimulated emission depletion microscopy. STED microscopy was performed on a Leica TCS SP8 STED 3X inverted microscope equipped with an HC PL-APO glycerol motC STED W objective (×93, NA 1.30) for fixed samples or an HC PL-APO oil objective (×100, NA 1.40) for live samples. The microscope was equipped with a white light laser (470–670 nm) and 592-nm and 775-nm (pulsed) depletion lasers for STED.

For fixed-cell STED microscopy, samples were prepared following the immunofluorescence protocol described above. Abberior STAR 580 and Abberior STAR RED secondary antibodies (Abberior) were used in combination to label the primary antibodies. Coverslips were mounted on slides using Prolong Gold Antifade mounting agent (Thermo Fisher Scientific). STED depletion lasers were set to 70% of maximum power. The pinhole was opened to 1 AU for image acquisition. The LIGHTNING mode (Leica) was used to deconvolve STED images.

For live-cell STED microscopy, we followed the sample preparation and adapted the imaging protocol as recently published in ref. [31]. In brief, HeLa Cox8a-SNAP cells were seeded onto coverslips the day before imaging. Following antimycin A treatment, cells were incubated at 37 °C for 15–30 min with 1 μM SNAP-Cell SiR fluorescent substrate (New England Biolabs), followed by a 15–30-min washing step in dye-free medium. Cells were imaged at 37 °C in Life cell imaging solution (Thermo Fisher Scientific). For live-cell STED acquisitions, the pinhole was set to 1 AU, the zoom was set to ×5–9 and the pixel size automatically adapted. The SiR was excited at 640 nm with 775-nm depletion at 60–70%. Fine-tuning the gating (1–5 ns) and emission-filter bandwidths proved vital. Dwell times were around 8 μs, and 8× line-accumulation was used to obtain the best images. The FASTKD2-eGFP signal to visualize the MRGs was acquired in confocal mode and each line was scanned once. No deconvolution was used. The presented images are raw data, adjusted for brightness and contrast using Fiji software.

Statistics and reproducibility. All plotting and statistical analysis was performed using Python 3, with Jupyter Notebook 6.0 used to document analyses. Mann–Whitney U, Students t and Kolmogorov–Smirnov tests were used as indicated, and computed using the Python scipy-library. seaborn- and matplotlib-libraries were used to plot the figures, and to add statistical significance indicators we used the statannot-library[43]. To avoid conflicts with non-Gaussian distributions we report the median values, unless stated otherwise. Correlation coefficients are calculated as Pearson's R using numpy-library. Analysis is reproducible through automated analysis scripts.

Reporting Summary. Further information on research design is available in the Nature Research Reporting Summary linked to this article.

Data availability

All imaging as well as numerical data relevant to this study are publicly available in the online repository Zenodo (https://doi.org/10.5281/zenodo.3747143) or upon reasonable request. A README-file on Zenodo will guide the reader. All remaining other data supporting the findings of this study are available from the corresponding author on reasonable request. Plasmids and cell lines are available; please contact the corresponding authors. Source data are provided with this paper.

Code availability

All code including adapted STORM-analysis code, TrackFRAP, FRAPtA and other python scripts and Fiji macros for analysis and figure generation are available in the online repository GitHub (https://github.com/TimoHenry/MitochondrialRNAgranules), or upon reasonable request. Jupyter Notebooks are available in the data repository on Zenodo to trace the application of the code to the data in our manuscript.

References

39. Sieben, C., Banterle, N., Douglass, K. M., Gonczy, P. & Manley, S. Multicolor single-particle reconstruction of protein complexes. *Nat. Methods* **15**, 777–780 (2018).
40. Spruyt, V. *A Geometric Interpretation of the Covariance Matrix* (Computer Vision for Dummies, 2014); https://www.visiondummy.com/2014/04/geometric-interpretation-covariance-matrix/
41. Ducret, A., Quardokus, E. M. & Brun, Y. V. MicrobeJ, a tool for high throughput bacterial cell detection and quantitative analysis. *Nat. Microbiol* **1**, 16077 (2016).

42. Halavatyi, A., Yotskou, M. & Friederich, E. FRAPAnalyser (OMICtools, 2008); https://omictools.com/frapanalyser-tool

43. Weber, M. 'statannot' (GitHub, 2019); https://github.com/webermarcolivier/statannot

Acknowledgements

Author contributions

S.Z., T.R., J.-C.M. and S.M. conceived and designed the study and wrote the manuscript. All authors reviewed and edited the manuscript. T.R. and S.Z. designed, executed, analysed and validated the experiments. E.C. executed and coded FRAP experiments and analysis. E.V. performed fractionation and western blotting. M.C. embedded, sectioned and acquired transmission electron microscopy samples. T.R. and S.Z. prepared the figures and plots. S.M. and J.-C.M. supervised the project.

Competing interests

The authors declare no competing interests.

Additional information

Extended data is available for this paper at https://doi.org/10.1038/s41556-020-00584-8.

Supplementary information is available for this paper at https://doi.org/10.1038/s41556-020-00584-8.

Correspondence and requests for materials should be addressed to T.R., J.-C.M. or S.M.

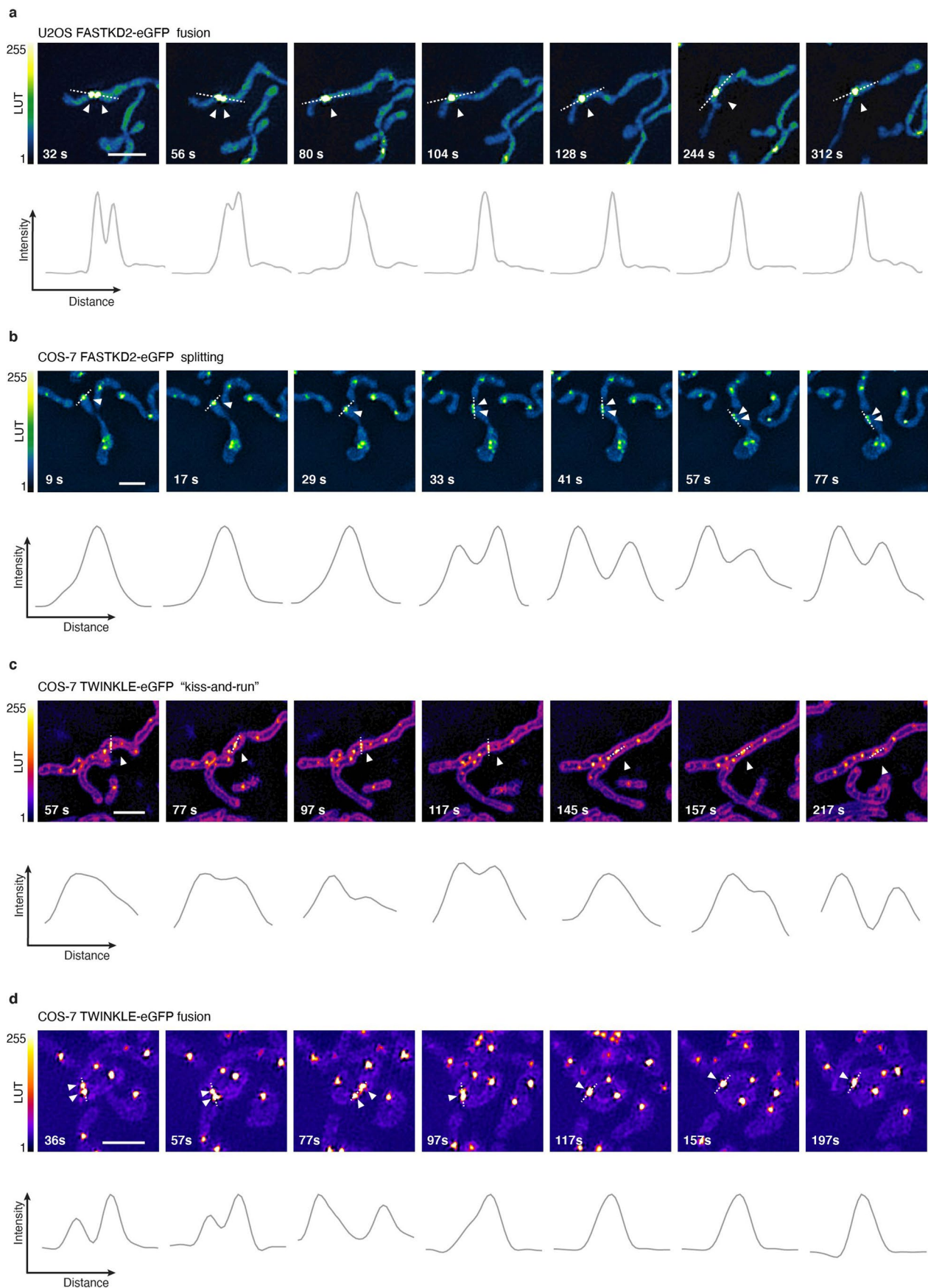**Reprints and permissions information** is available at www.nature.com/reprints.
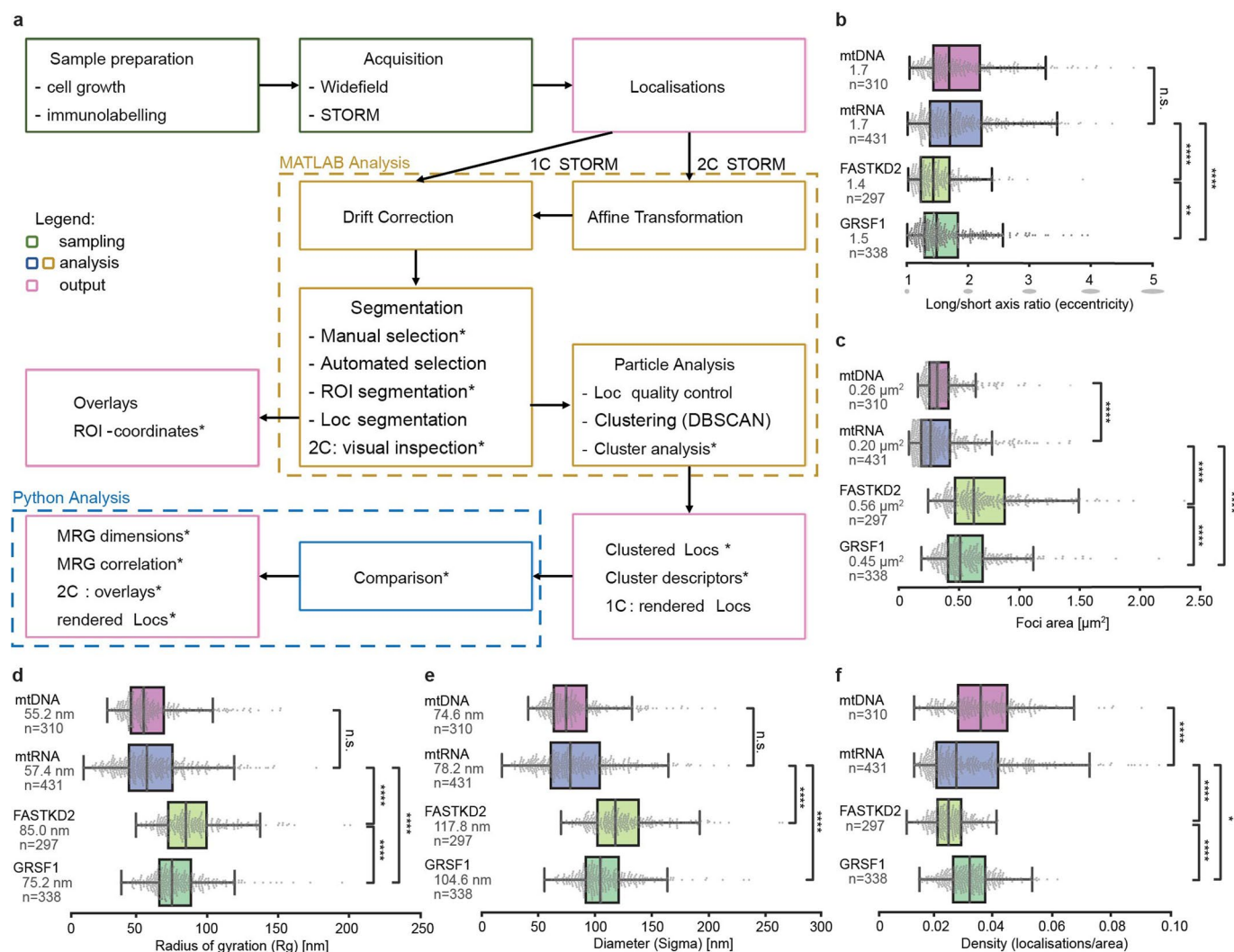
Extended Data Fig. 1 | Workflow and quantification of nanoscopic architecture of MRGs. a, Workflow used for this study. Previously unpublished parts of the analysis are highlighted by asterisks, while other parts were previously published[17,36]. **b**–**f** Additional quantification of MRG and nucleoid (mtDNA) architecture from htSTORM data. Markers (mtRNA, FASTKD2 and GRSF1), number of granules n and median values are indicated for each condition; n.s. denotes p-values > 0.05, * denotes p-values ≤ 0.05, ** denote p-values ≤ 0.01, *** denote p-values ≤ 0.001,**** denote p-values ≤ 0.0001 of two-sided Mann-Whitney-U test. Individual data points are plotted grey, box plots denote first and third quartiles, and the median, whiskers comprise rest of distributions except outliers. Multiple acquisitions, samples and imaging days were pooled. **b**, Median eccentricity of both MRG-proteins differ slightly ($p = 5.1e^{-3}$), with largely overlapping boxes and can be approximated by spheres. Nucleoids and nascent RNA components of MRGs are more elongated ($p_{BrU-FASTKD2} = 1.4e^{-15}$, $p_{BrU-GRSF1} = 1.7e^{-6}$). **c**, Comparison of areas described by convex hull. MRG-protein foci are significantly larger than nascent-RNA foci ($p_{BrU-FASTKD2} = 2.7 \times 10^{-61}$, $p_{BrU-GRSF1} = 6.5 \times 10^{-49}$), yet less different from one another ($p_{GRSF1-FASTKD2} = 6.9 \times 10^{-7}$). The distribution of mtRNA- and mtDNA-foci areas strongly overlap, though their medians are significantly different with $p_{mtRNA-mtDNA} = 1.2 \times 10^{-6}$. Three outliers for FASTKD2 (> 2.5 μm²) were removed for better visualisation, but included in all quantitative analysis. **d**, and **e**, Comparison of alternative standard point-cloud descriptors Radius of gyration (R_g), and Sigma as the average of the eigenvalues in two dimensions, and multiplied by two to yield a diameter. **f**, Density of localisations was also compared, and both GRSF1 and FASTKD2-foci follow a narrow normal distribution, while mtDNA & BrU show a larger variance of density. Number (n) of clusters quantified for each condition is represented in the figure and is pooled from 24, 13, 7, and 14 FOVs, and 4, 4, 3, and 2 samples for BrU, GRSF1, FASTKD2, and mtDNA respectively. Statistical source data are provided in Source data Extended data Fig. 1.
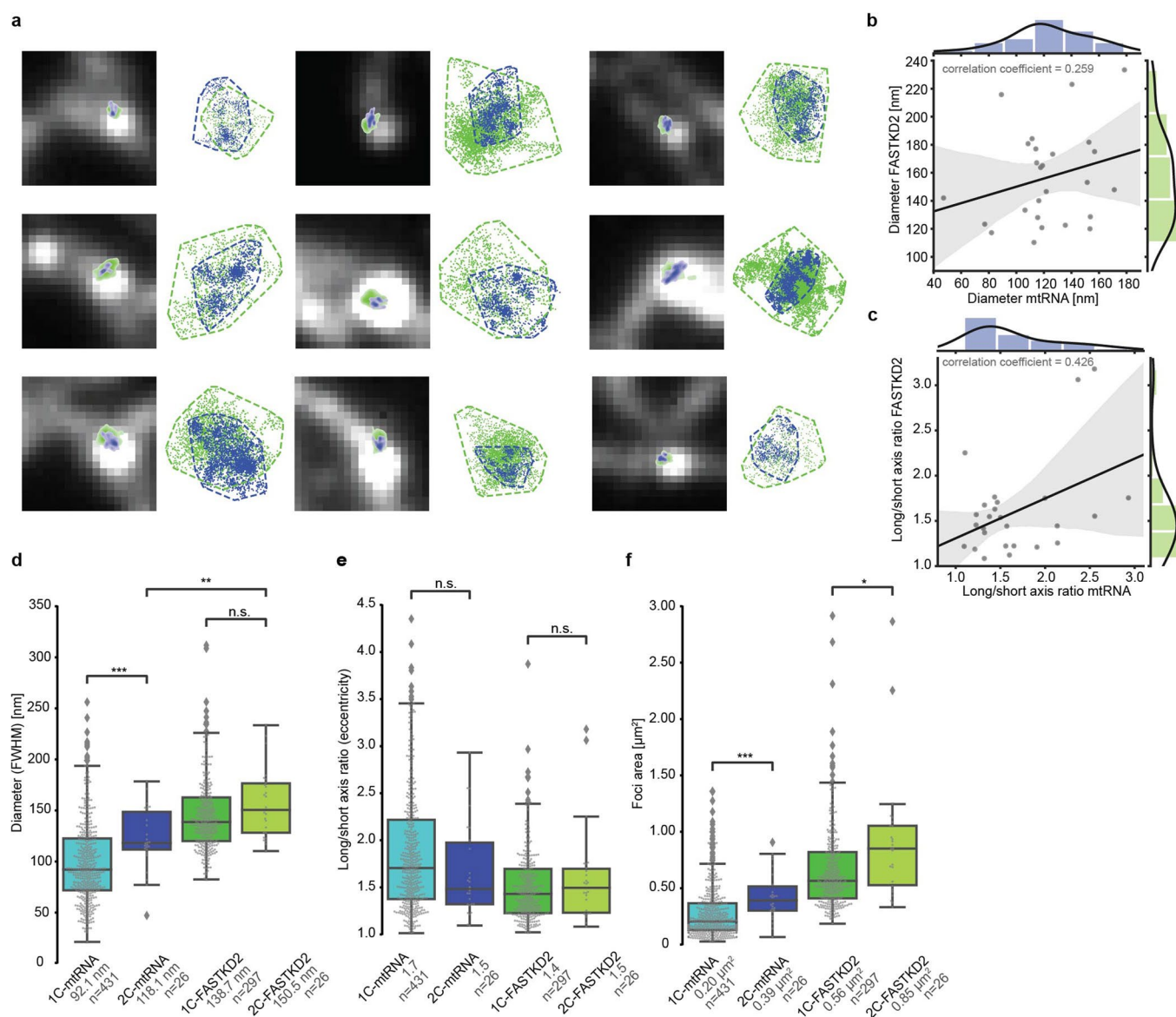
Extended Data Fig. 2 | Comparison and correlation of two-colour htSTORM data. a, Nine additional examples of two-colour htSTORM of MRGs. Scatter plots of localisations (right) are shown next to corresponding clusters of FASTKD2 (green) and mtRNA (BrU, blue) overlaid on widefield images (left). Convex hull areas are represented with dashed lines. **b**, and **c**, Scatter plots of all FASTKD2-mtRNA (BrU) pairs with regression-fit (black) and standard deviation (grey). Histograms of the distribution for FASTKD2 (y-axis, right, green), and mtRNA (x-axis, top, blue), including a kernel density estimate are shown. No correlation of Diameter (FWHM) (R = 0.26) or eccentricity (length/width, R = 0.43) was found between FASTKD2 and BrU foci from individual granules (n=26 MRGs over 4 independent experiments). **d-f**, Comparison of foci characteristics for one- versus two-colour htSTORM by Two-sided Mann-Whitney-U test from two-colour to one-colour data. Number of granules n (pooled from 20 FOVs, and 8 samples) and median values are indicated for each condition; n.s. denotes p-values > 0.05, * denotes p-values ≤ 0.05, ** denote p-values ≤ 0.01, *** denote p-values ≤ 0.001,**** denote p-values ≤ 0.0001. **d**, FWHM is not significant for FASTKD2 (p = 0.22) but two-colour BrU foci were significantly larger (p = 8.8e^{-4}), and two-colour FASTKD2 were also larger than two-colour-mtRNA (p = 0.0014) **e**, Eccentricity is not significantly different (p$_{mtRNA}$ = 0.36, p$_{FASTKD2}$ = 1.0) **f**, Size determined by convex hull, differed between one-colour and two-colour BrU (p = 2.4e^{-4}) as well as FASTKD2 (p = 0.017). This may in parts be due to the heavy weight of two outliers as visible in the plot. Statistical source data are provided in Source data Extended data Fig. 2.
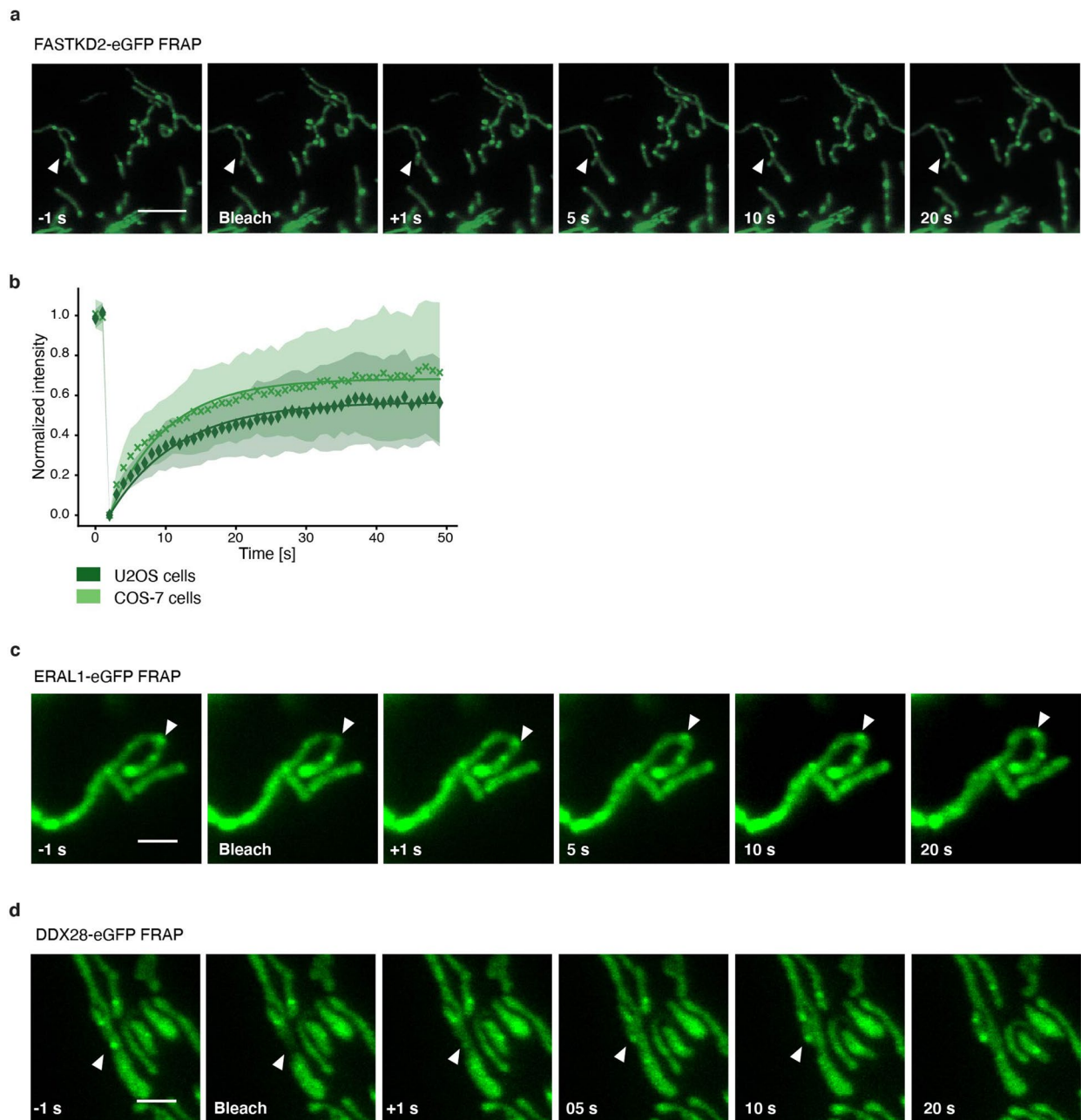
Extended Data Fig. 3 | FRAP of MRG-associated proteins. a, Representative time-lapse images of MRGs FRAP experiments in U2OS cells stably expressing FASTKD2-eGFP (green) (n= 39 MRGs examined over 3 independent experiments). White arrowheads indicate the photobleached structures. Scale bar: 5 μm. **b**, FRAP analysis of FASTKD2-eGFP in U2OS (n= 39 MRGs examined over 3 independent experiments) and COS-7 cells (n = 44 MRGs examined over 8 independent experiments). Symbols in the graph represent mean data points. Single exponential fits (lines) and standard deviations for each time point (shaded area) are shown. **c, d**, Representative time-lapse images of ERAL1- (n = 17 MRGs examined over 3 independent experiments) and DDX28-eGFP (n = 17 MRGs examined over 3 independent experiments) FRAP experiments in COS-7 cells. White arrowheads indicate the photobleached structures. These images correspond to the data plotted in Fig. 2c. Scale bar: 2 μm.

a U2OS FASTKD2-eGFP fusion

b COS-7 FASTKD2-eGFP splitting

c COS-7 TWINKLE-eGFP "kiss-and-run"

**d** COS-7 TWINKLE-eGFP fusion

Extended Data Fig. 4 | See next page for caption.

**Extended Data Fig. 4 | MRG and nucleoid dynamics in live cells. a**, Representative time-lapse images of an MRG fusion event in a live U2OS cell, monitored by SIM. MRGs are visualized by stable expression of FASTKD2-eGFP (n= 7 cells). **b**, Representative time-lapse images of an MRG splitting event in a live COS-7 cell, monitored by SIM. MRGs are visualized by stable expression of FASTKD2-eGFP (n= 6 cells). **c, d**, Representative time-lapse images of nucleoid "kiss-and-run" (n=1 cell) and splitting events (n=2 cells), respectively, in COS-7 cells, monitored by SIM. Nucleoids are visualized by transient expression of TWINKLE-eGFP and mitochondrial outlines are highlighted by TOMM20-eGFP expression. **a–d**, Cells were imaged at 1/5 Hz. White arrowheads indicate the dynamic events. Dashed lines indicate the segments used to measure the intensity (grey values) represented in the plots below. Linear Fire LUTs are used to represent pixel intensity values. Scale bars: 2 μm. Statistical source data are provided in Source data Extended data Fig. 4.
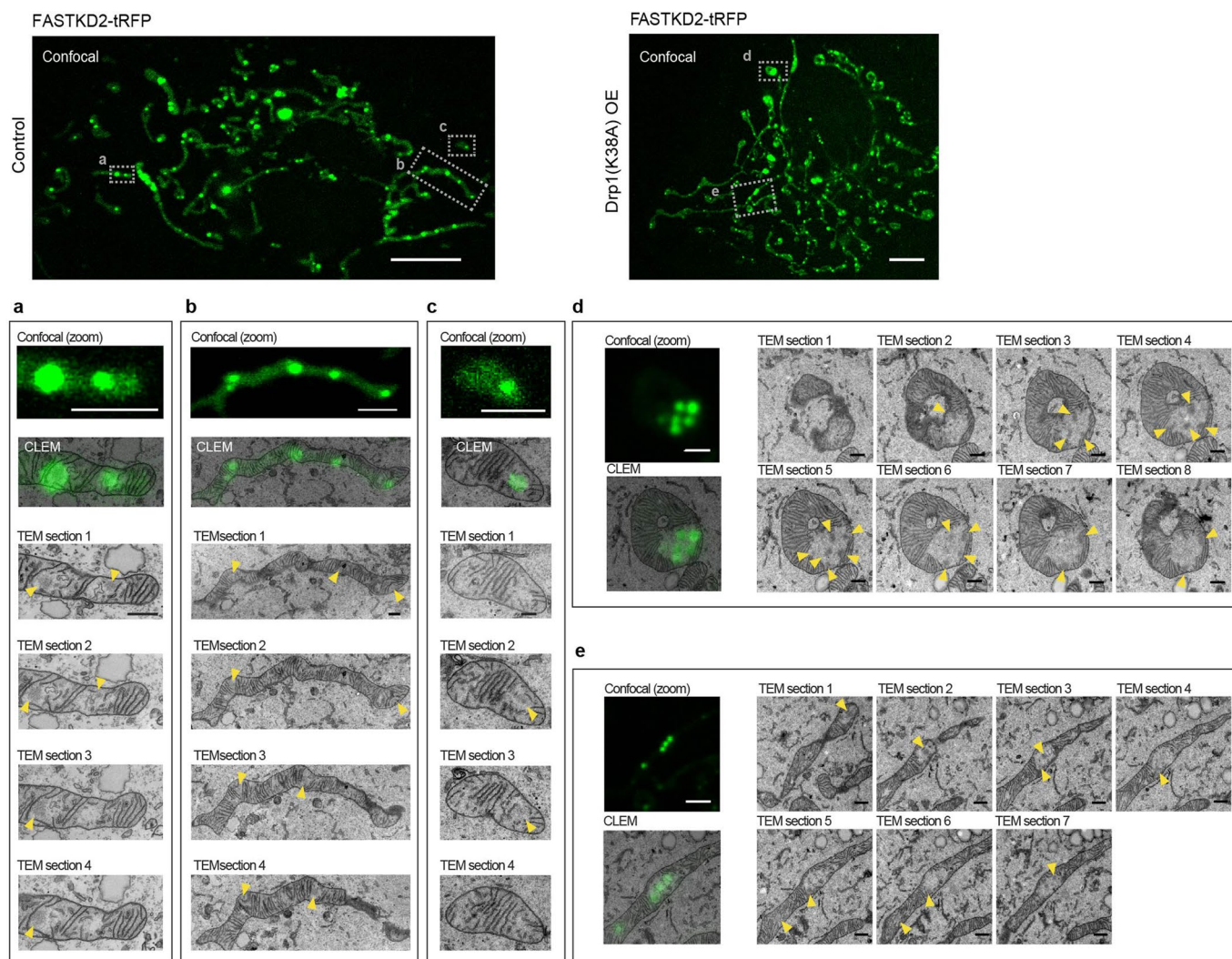
Extended Data Fig. 5 | CLEM of FASTKD2-tRFP and MRG electron densities. Correlative confocal fluorescence micrograph of FASTKD2-tRFP and transmission electron micrograph (TEM) in COS-7 control (**a** - **c**) (7 MRGs were examined from 3 mitochondria of a single cell) and Drp1[K38A]-CFP positive (**d**, **e**) (10 MRGs were examined from 2 mitochondria of a single cell) cells. TEM-highlights correspond to the data presented in Figs. 3a and 4e respectively, and show additional examples. Contiguous 50 nm TEM microtome sections show electron densities corresponding to the MRGs visualized by fluorescence microscopy (yellow arrowheads). Scale bars: Confocal: 10 μm; Confocal zoom: 2 μm; CLEM and TEM sections: 500 nm.
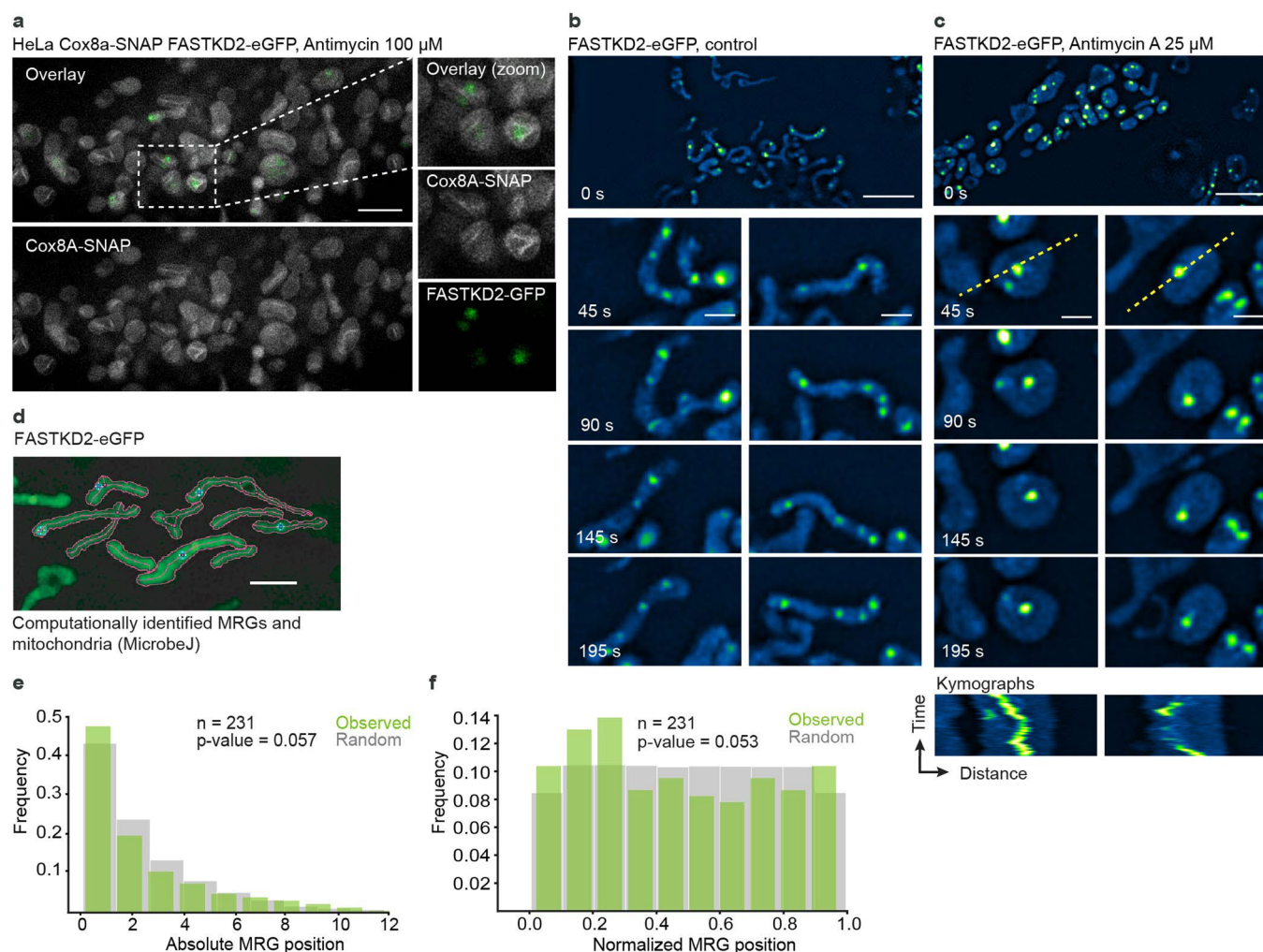
Extended Data Fig. 6 | Membrane association and distribution of MRGs within mitochondria. a, STED microscopy of HeLa cells stably expressing Cox8a-SNAP (grey) and FASTKD2-eGFP (green), treated with 100 μM antimycin A for 1 hour, prior to labelling with SIR-SNAP dye and live cell imaging (The experiment has been performed twice with similar results). A zoomed field of view on the right (dashed box). Scale bar: 2 μm. **b-c**, FASTKD2-eGFP expressing COS-7 cells untreated (**b**) or treated with 25 μM antimycin A for 24 hours (**c**), imaged live using SIM microscopy. The same linear Fire LUT is used for pixel intensity values as in Fig. 2e. Zoomed time-lapse series are shown for two mitochondria (dashed boxes) (The experiment has been performed twice with similar results). Kymographs below (plotted lines are represented on the analysed mitochondria as yellow dashed lines). Scale-bar: 2 μm. **d**, Example FOV of semi-automated mitochondria segmentation and MRG-association with their parent organelle with the ImageJ plugin, MicrobeJ. (The experiment has been performed three times with similar results). **e**, and **f**, Histograms of absolute or relative position of MRGs (n = 231 MRGs examined over 3 independent experiments) within their host mitochondria (green) and simulated, randomly positioned granules (grey). The observed distribution of MRG positions is not significantly different from the simulated random distribution (Kolmogorov-Smirnov test: $p_{abs} = 0.057$, $p_{norm} = 0.053$). Statistical source data are provided in Source data Extended data fig. 6.
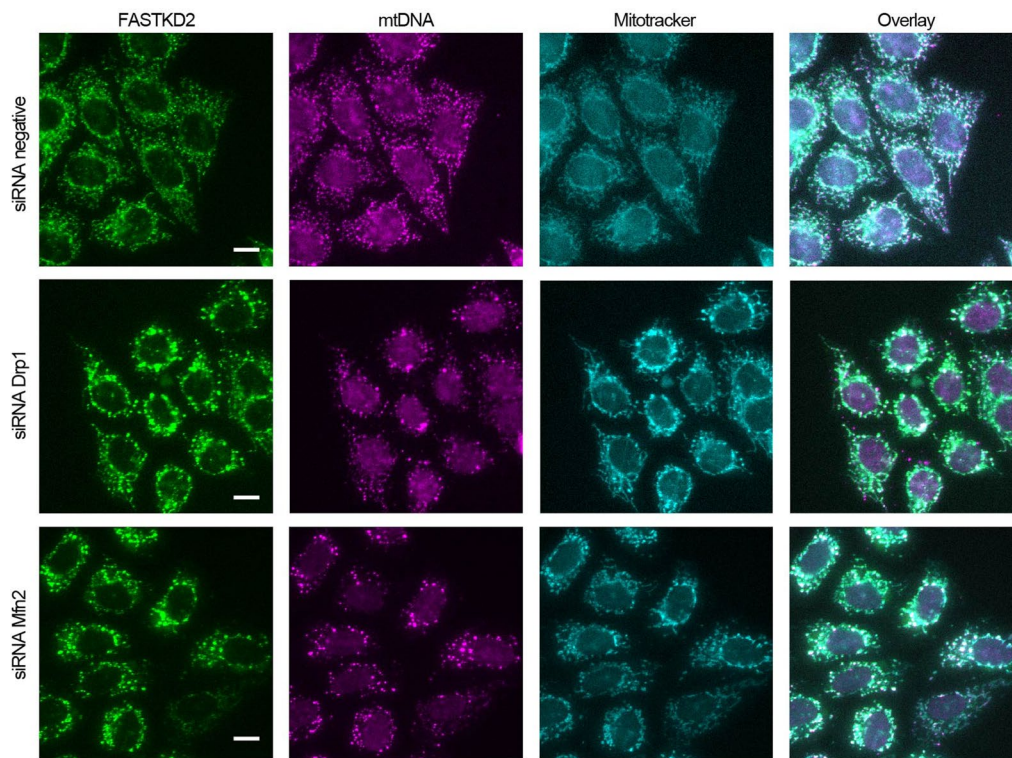
Extended Data Fig. 7 | Effect of perturbations to mitochondrial dynamics on MRG distribution. Representative widefield-microscopy images of HeLa cells silenced using siRNAs against Drp1 (second row) or Mfn2 (third row). Cells were fixed after 72 hours of silencing. A negative control siRNA was used in parallel, and is shown in the first row. MRGs and nucleoids were immunolabeled using anti-FASTKD2 (green) and anti-DNA (magenta), respectively. Mitochondria were labelled using MitoTracker Deep Red staining (cyan) (The experiment has been performed twice with similar results). Scale-bar: 10 µm. Disrupted MRG and nucleoid positioning, and clumped appearance as described for mito-bulbs is apparent when either Drp1 and Mfn2 are silenced, but the negative control shows well-dispersed MRGs and nucleoids.